GDAŃSK UNIVERSITY OF TECHNOLOGY

The author of the doctoral dissertation: Malwina Kroczewska-Gnatowska
Scientific discipline: Chemical Sciences

DOCTORAL DISSERTATION

Title of doctoral dissertation: Modified Metal-Organic Frameworks for selective adsorption and photoconversion of CO_2

Title of doctoral dissertation (in Polish): Modyfikowane Struktury Metaloorganiczne do selektywnej adsorpcji oraz fotokonwersji CO_2

Supervisor *signature*	Second supervisor - *signature*
Justyna Łuczak, PhD, DSc, University professor	n.a.
Auxiliary supervisor - *signature*	Cosupervisor - *signature*
n.a.	n.a.

Gdańsk, year 2026

GDAŃSK UNIVERSITY OF TECHNOLOGY

STATEMENT

The author of the doctoral dissertation: Malwina Kroczewska-Gnatowska

I, the undersigned, declare that I am aware that in accordance with the provisions of Art. 27 (1) and (2) of the Act of 4th February 1994 on Copyright and Related Rights (Journal of Laws of 2021, item 1062), the university may use my doctoral dissertation entitled:

Modified Metal-Organic Frameworks for selective adsorption and photoconversion of CO_2

for scientific or didactic purposes.

Gdańsk,..... .....

signature of the PhD student

Aware of criminal liability for violations of the Act of 4th February 1994 on Copyright and Related Rights and disciplinary actions set out in the Law on Higher Education and Science(Journal of Laws 2021, item 478), as well as civil liability, I declare, that the submitted doctoral dissertation is my own work.

I declare, that the submitted doctoral dissertation is my own work performed under and in cooperation with the supervision of Justyna Łuczak, PhD, DSc, University professor.

This submitted doctoral dissertation has never before been the basis of an official procedure associated with the awarding of a PhD degree.

All the information contained in the above thesis which is derived from written and electronic sources is documented in a list of relevant literature in accordance with Art. 34 of the Copyright and Related Rights Act.

I confirm that this doctoral dissertation is identical to the attached electronic version.

Gdańsk,..... .....

signature of the PhD student

I, the undersigned, agree~~/do not agree*~~ to include an electronic version of the above doctoral dissertation in the open, institutional, digital repository of Gdańsk University of Technology.

Gdańsk,..... .....

signature of the PhD student

[1] Art 27. 1. Educational institutions and entities referred to in art. 7 sec. 1 points 1, 2 and 4–8 of the Act of 20 July 2018 – Law on Higher Education and Science, may use the disseminated works in the original and in translation for the purposes of illustrating the content provided for didactic purposes or in order to conduct research activities, and to reproduce for this purpose disseminated minor works or fragments of larger works.

2. If the works are made available to the public in such a way that everyone can have access to them at the place and time selected by them, as referred to in para. 1, is allowed only for a limited group of people learning, teaching or conducting research, identified by the entities listed in paragraph 1.

GDAŃSK UNIVERSITY OF TECHNOLOGY

DESCRIPTION OF DOCTORAL DISSERTATION

The Author of the doctoral dissertation: Malwina Kroczewska-Gnatowska

Title of doctoral dissertation: Modified Metal-Organic Frameworks for selective adsorption and photoconversion of CO_2

Title of doctoral dissertation in Polish: Modyfikowane Struktury Metaloorganiczne do selektywnej adsorpcji oraz fotokonwersji CO_2

Language of doctoral dissertation: English

Supervisor: Justyna Łuczak, PhD, DSc, University professor

Date of doctoral defense:

Keywords of doctoral dissertation in Polish: Szkielety metaloorganiczne, adsorpcja gazu, fotokonwersja CO_2, modyfikacja strukturalna, ciecze jonowe, inżynieria defektów **.**

Keywords of doctoral dissertation in English: Metal-Organic Frameworks, gas adsorption, CO_2 photoconversion, structural modification, ionic liquids, defect engineering.

Summary of doctoral dissertation in Polish:

W niniejszej rozprawie doktorskiej zweryfikowano skuteczność metod modyfikacji szkieletów metaloorganicznych (MOF) ukierunkowanych na zwiększenie ich efektywności w procesach zagospodarowania tlenku węgla(IV). Zaproponowano trzy główne strategie modyfikacji struktur metaloorganicznych: celowe wprowadzanie cieczy jonowych, inżynierię defektów wspomaganą zastosowaniem metali nieszlachetnych oraz wytwarzanie kompozytów typu MOF-MOF z udziałem cieczy jonowych. Uwzględniono wprowadzanie modulatorów do środowiska syntezy szkieletów metaloorganicznych, jak modyfikacji gotowych materiałów po zakończeniu procesu syntezy. Zweryfikowano możliwość zastosowania wybranych struktur metaloorganicznych, różniących się zarówno rodzajem centrum metalicznego, jak i zastosowanym linkerem, w procesach adsorpcji CO_2 oraz fotokatalitycznej redukcji tego gazu w układzie ciało stałe-ciecz. Oceniono skuteczność zastosowanych metod modyfikacji i wykorzystanych modulatorów, a także wskazano perspektywiczne kierunki dalszych badań oraz aspekty wymagające szczególnej uwagi.

Summary of doctoral dissertation in English:

The hereby presented doctoral dissertation evaluates the effectiveness of modification methods for metal-organic frameworks (MOFs) aimed at enhancing their performance in carbon dioxide (CO_2) utilization processes. Three primary strategies for modifying these structures were proposed: the intentional incorporation of ionic liquids, defect engineering assisted by non-noble metals, and the synthesis of MOF-MOF composites incorporating ionic liquids. The study considered both the introduction of modulators during the MOF synthesis process and the modification of the materials after the synthesis. The applicability of selected MOF structures – varying in terms of both the metallic center and the organic linker – was assessed for CO_2 adsorption and its photocatalytic reduction in solid-liquid system. Finally, the effectiveness of the modification methods and modulators was evaluated, and promising directions for future research, along with aspects requiring particular attention, were identified.

From the bottom of my heart I would like to thank hereby:

My supervisor, Professor Justyna Łuczak, for her substantive guidance and for providing the research framework.

My furry friends – Rudi (I miss you so much Buddy) and Mini – for being the most cozy purring emotional support.

My Parents – Kasia and Marek – for always being there for me and lifting my spirit up.

Ania, Szymon and Bartek for experiencing this scientific adventure together and for the friendship outside of the University.

My dearest colleagues from Fluffy Friends Lab for believing in my wisdom and being a super supportive team, I have never dreamt of.

The workers and colleagues from the Department of Process Engineering and Chemical Technology for your kindness.

My international co-workers: Isabel, José and Thiago from Nova University of Lisbon for giving me the opportunity to spend 3 scientifically wonderful months in beautiful Portugal; Azahara and Vicent from Eindhoven University of Technology for the contribution in widening my research.

The workers and colleagues from the Department of Environmental Technology of the University of Gdańsk, especially Mateusz for the cooperation, crazy research ideas and all the tips.

Last, but not least, I would like to sincerely thank my beloved husband, Przemysław. My best friend. My biggest inspiration and source of power. The most clever and humble person I know. Thank you for everything.

Melancholy, never over it
Editors – Call it in

That's a glory
deep in my soul
Dave Gahan, Soulsavers – My sun

Table of contents

STATEMENT 2

DESCRIPTION OF DOCTORAL DISSERTATION 3

Table of contents 5

Abbreviations 7

1. Introduction 12

2. Research hypothesis and aims of dissertation 15

3. Thesis scope and novelty 17

4. Literature review 18

4.1. Global problem of increasing CO_2 emission and current counter measurements 18

4.2. Metal-organic frameworks 26

4.3. Modification of metal-organic frameworks 31

4.4. Application of MOFs 40

5. Materials and methods 68

5.1. Materials 68

5.2. Synthesis of MOFs 69

5.3. Synthesis of AAILs 72

5.4. Methods of MOFs modification 73

5.5. Activation of MOFs 75

5.6. Characterization of the samples 75

5.7. CO_2 photoreduction experiments 81

6. The influence of the synthesis conditions on properties and performance of Cu-TDPAT MOF 84

6.1. Synthesis in primary conditions 86

6.2. Synthesis in different solvents 93

6.3. The influence of the reaction vessel 96

6.4. Influence of the modulator presence and its type 97

6.5. Influence of the time and temperature of the reaction 100

6.6. Influence of precursors molar ratio 103

6.7. Influence of the copper precursor 105

6.8. Analysis of synthesis conditions influence on Cu-TDPAT 109

6.9. Stability of Cu-TDPAT in liquid environment of CO_2 photoconversion 112

6.10. Summary 114

7. HKUST-1 modified with heterocyclic amino acid ionic liquids for selective CO_2 adsorption 116

7.1. Characterization of materials 118

7.2. Sorption properties 126

7.3. Gas Adsorption/Desorption Equilibrium Measurements 129

7.4. Summary 134

8. The influence of defect induction by introduction of non-noble metals on the photocatalytic performance of UiO-66(Zr) and NH_2-UiO-66(Zr) 136

8.1. Structure of the pristine and modified MOFs 138

8.2. Sorption properties 147

8.3. Photocatalytic performance 148

8.4. Mechanism of CO_2 photoreduction 158

8.5. Summary 160

9. UiO-67(Zr)-NH_2-MIL-125(Ti) composites modified with ionic liquid for CO_2 photoreduction 161

9.1. Structure of the MOF-MOF composites 161

9.2. Sorption properties 166

9.3. Photocatalytic performance 173

9.4. Discussion over the possible mechanism of CO_2 photoreduction 175

9.5. Summary 177

10. Conclusions and future outlook 179

11. SCIENTIFIC ACHIEVEMENTS 184

12. REFERENCES 187

List of Figures 226

List of Tables 232

Abbreviations

2ABA – 3,5-diaminobenzoic acid

4,4'-bpy – 4,4'-bipyridinine

AAIL – amino acid ionic liquid

[Ac] – acetate anion

ACF – activated carbon fiber

[Ala] – L-alanate anion

[AMIM] – 1-allyl-3-ethylimidzaole cation

[AOT] – dioctylsulfosuccinate anion

APTES – (3-Aminopropyl)triethoxysilane

AQE – apparent quantum efficiency

[Arg] – L-arginate anion

BA – butanedioic acid

BDC – 1,4-benzenedicarboxylic acid, terephtalic acid

BET – Brunauer-Emmett-Teller

[BF_4] – tetrafluoroborate anion

[BMIM] – 1-butyl-3-ethylimidzaole cation

[BMMIM] – 1-butyl-2,3-dimethylimidazolium cation

BNAH – 1-benzyl-1,4-dihydronicotinamide

[Br] – bromide anion

[C_3NH_2BIM] – 1-(3-aminopropyl)-3-butylimidazolium cation

[Cap] – caprate anion

[Cho] – choline cation

[Cl] – chloride anion

CMS – carbon molecular sieves

CNT – carbon nanotubes

COF – covalent organic frameworks

CTAB – cetyltrimethylammonium bromide

[DBP] – dibutylphosphate anion

[DCA] – dicyanamide anion

dcbpy – 2,2’-bipyridine-4,4’-dicarboxylate

DEA – diethylamine

DEF – *N,N*-diethylformamide

DETA – diethylenetriamine

DFT – density functional theory

DMA – *N,N*-dimethylacetamide

DMF – *N,N*-dimethylformamide

[DMIM] – 1-decyl-3-methylimidazolium cation

DMSO – dimethyl sulfoxide

DPE – 1,2-di(4-pyridyl)ethylene

DRIFTS – diffuse reflectance infrared Fourier transform spectroscopy

DRS – diffuse reflectance spectroscopy

[EDDA] – ethylenediamine-N,N'-diacetate anion

EDX – energy dispersive X-ray spectroscopy

EIS – electrochemical impedance spectroscopy

[EMIM] – 1-ethyl-3-ethylimidzaole cation

EN – ethylenediamine

[E(OH)MIM] – 1-(2-hydroxyethyl)-3-methylimidazolium cation

EPR – electron paramagnetic resonance

EtOH – ethanol

FTIR – Fourier Transform infrared spectroscopy

FTO – fluorine-doped tin oxide

[Glu] – glutarate anion

[Gly] – L-glycinate anion

HAD – adenine

[H-IDA] – protonated iminodiacetate anion

[His] – L-histidinate anion

[HMIM] – 1-hexyl-3-methylimidazolium cation

HMP – halide metal perovskite

HOCO – highest occupied crystal orbital

[I] – iodide anion

IA – isobutyric acid

IC – ionic chromatography

[IDA] – iminodiacetate anion

IL – ionic liquid

[Ile] – L-isoleucinate anion

iPrOH – isopropanol

IR – infrared

L – 4,4'-(anthracene-9,10-diylbis(ethyne-2,1-diyl))dibenzoic acid

LA – lauric acid

[Lev] – levulinate anion

LLCT – linker-to-linker charge transfer

LMCT – linker-to-metal charge transfer

[Lys] – L-lysininate anion

LUCO – lowest unoccupied crystal orbital

MC – missing-cluster defect

MeCN – acetonitrile

MeOH – methanol

mIm – 2-methylimidazole

ML – missing-linker defect

MMCT – metal-to-metal charge transfer

[MOBMIM] – 1-methoxylbutyl-3-methylimidazolium

MOF – metal-organic frameworks

[$N_{1(2OH)(2OH)(2OH)}$] – N-methyl-N,N,N-tris(2-hydroxyethyl)ammonium cation

[N_{2114}] – N-butyl-N,N-dimethyl-N-ethylammonium cation

[NAIM] – 1-(3-Aminopropyl)-3-ethylimidazole cation

NMR – nuclear magnetic resonance

NP - nanoparticle

[NTA] – nitrilotriacetate anion

NTB – 4,4',4''-nitrilotribenzoic acid

OMS – open-metal sites

[Oxa] – oxalate anion

PEI – polyethylenimine

[Phe] – phenylalanate anion

PhIM – benzimidazole

[P_{4442}] – tributylethylphosphonium cation

[P_{4444}] – tetrabutylphosphonium cation

[$P_{666(14)}$] – trihexyl(tetradecyl)phosphonium cation

[PF_6] – Hexafluorophosphate anion

PL – photoluminescence

[PMIM] – 1-propyl-3-methylimidazolium cation

[Pro] – L-Prolinate anion

PSE – post-synthetical exchange

PSM – post-synthetical metalation/modification

PTPA – Poly(triphenylamine)

PVP – Polyvinylpyrrolidone

PXRD – powder X-ray diffraction

RT – room temperature

[Sar] – sarcosinate anion

[SCN] – thiocyanate anion

SDS – sodium dodecyl sulfate

SEM – scanning electron microscopy

[SO_3] – sulfite anion

[Tau] – taurinate anion

TCA – 4,4′,4″-nitrilotribenzoic acid

[TCB] – tetracyanoborate anion

TCPP – 4',4'',4'''-(porphyrin-5,10,15,20-tetrayl)tetrabenzoate

TEM – Transmission electron microscopy

[Tf_2N] - bis(trifluorometanosulfonylo)imide anion

TEOA – triethanolamine

TEPA – tetraethylenepentamine

TETA – triethylenetetramine

TGA – thermogravimetric analysis

TIPA – triisopropanolamine

TMA – trimethylamine

TSIL – task-specific ionic liquid

UV – ultraviolet

[Val] – valerate anion

VOC – volatile organic compounds

XPS – X-ray Photoelectron Spectroscopy

ZIF – zeolitic imidazolate framework

1. Introduction

Recent years have clearly shown that the Earth's climate is unstoppably changing due to human's activity. The growth of industry, undeniably needed for the functioning and development of societies all over the world, leads to emission of gases and dust, resulting in degradation of the environment. It also affects the number of forests and green areas, which are successively removed for the construction of new facilities. Additionally, growing industry results in the continuous surge in carbon dioxide emissions, as this compound is a primary constituent of industrial flue gases. While CO_2 naturally existed only in trace concentrations within the Earth's atmosphere [1], human's activity not only accelerated the already rapid pace of global warming but also contributed to the severe acidification of aquatic ecosystems. Moreover, the natural sequestration of CO_2 *via* photosynthesis is increasingly compromised. This is largely due to the global reduction of plant biomass, driven by urban and industrial expansion, as well as extreme weather events and widespread wildfires. Consequently, developing methods to neutralize anthropogenic carbon dioxide is critical for preserving the natural environment for future generations. One promising strategy is the efficient valorization of CO_2, transforming it into alternative fuels or value-added chemicals, such as short-chain hydrocarbons.

The two novel paths considering reduction of carbon dioxide can be distinguished. The first one involves electrochemical conversion. In order to assure, that the method is ecological and relatively harmless the electricity should come from renewable sources. Alternatively, catalysis employing light as driving force, namely photocatalysis, is widely considered as the second promising development direction. However, both technologies still require a lot of effort and work to bring them to the industrial level of utility. The rising potential of metal-organic frameworks (MOFs) is reported by scientists in terms of carbon dioxide selective adsorption and photoreduction, which can be utilized in both pathways [2,3].

This novel group of organic-inorganic crystalline compounds is characterized by high crystallinity, designable structure with nanometric pores and both organic (linkers), and inorganic (metals) components. The significant advantages of these structures lays in their high specific surface area, susceptibility for post-synthetical modifications and significant affinity for CO_2 adsorption [4]. Potentially, MOFs can also act as photocatalysts, co-catalysts or as photocatalytic hosts in carbon dioxide reduction reactions (Figure 1.1), leading to formation of short hydrocarbons (i.e. CH_4, CH_3OH, HCOOH, etc.) being relevant substances used in industry [5]. A big advantage of MOFs is their designable structure. By choosing suitable constituents of the structure and synthesis conditions, products with varying characteristics can be obtained [5]. It ensures the possibility of producing MOF with targeted properties and performance, which can be even further improved by modification with varying moieties *via* either introduction to the synthesis process itself or by conjugation with the finished MOF material in the post-synthetical way. Several potential pathways of tailored MOF-based materials development currently exist, of which two main branches of modifications were adapted for this work.

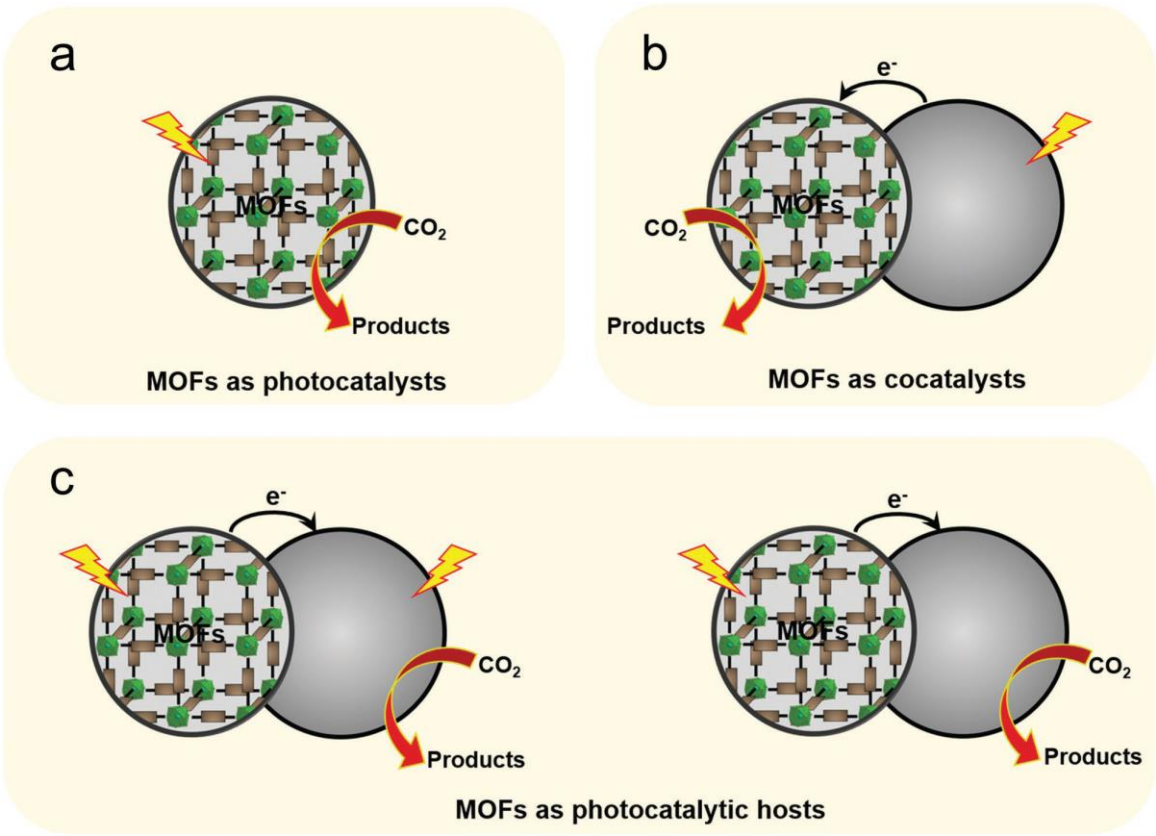


Figure 1.1 Schematic representation of the roles that can be performed by MOFs in the light-driven CO_2 reduction: a) photocatalysts, b) cocatalysts and c) photocatalytic hosts. Gray balls denote materials of other type in MOF-based photocatalysts (reproduced with permission from [6]).

The first explored branch aimed at improving the MOFs efficiency towards CO_2 utilization is defect engineering. This term covers the intentional creation of structural defects (missing clusters or linkers in the case of MOFs) by adapting the synthesis conditions, introduction of dopants or post-synthetical treatment to optimize the properties of resulting material. The targeted disarrangement may be beneficial due to the exposure of open-metal sites (OMS), development of the surface area or adjustment of the electronic structure [7,8]. Such approach is a relatively simple and cost-efficient method, and additionally can be precisely adjusted, to maintain the structural stability and at the same time to improve the applicational performance.

The second selected MOFs modification method focuses on introduction of peculiar compound, that is characterized with high affinity to CO_2, increasing the overall adsorption capacity of the modified MOF. From among various groups of such compounds, ionic liquids (ILs) were selected as promising modifiers, as like MOFs, ILs are also designable, meaning there exist a wide range of possibilities of anions and cations to be paired. What is more, several ILs are characterized by equimolar sorption capacity of CO_2 [9]. ILs are widely known to be an alternative to volatile organic compounds in the chemical industry. To maximize the affinity of ionic liquids to CO_2, incorporation of amino acids as anions was designated as the most promising as they are naturally occurring, with potential for biodegradability and biocompatibility [10]. Therefore, the influence of their introduction to MOFs structure was investigated herein.

The following thesis aims at validation of the possible pathways of MOFs modification and verification of their potential to achieve a material with stable characteristics and satisfactory performance. Thanks to unique properties of MOFs, their targeted modification – by introduction of ILs, non-noble metals coupled with creation of structural defects or linkage with other materials – could potentially bring a solution contributing to limitation of the worldwide excessive CO_2 emission problem. Precise selection of modifier type, amount and the approach of its introduction to MOF structure is crucial in terms of preserving structural stability, boosting the efficiency and maintaining extensive surface area as well as unclogged pores.

The novelty of the herein presented work lays in employment of few different and facile modification methods of the MOF-based materials to enhance their performance in the field of CO_2-related applications. The four cost-efficient and simple modification methods were proposed. First of them concerned the manipulation with the primary conditions of the synthesis to seek for and alternative conditions allowing to maximize the characteristics of the product. The second approach utilized the intentional incorporation of ionic liquids to the structure of MOF in order to assess their potential of improving gas-related properties of the chosen MOF. In turn the photocatalytic properties of MOFs were adjusted *via* either non-noble metal-assisted defect engineering approach or for the first time by ionic liquid-assisted creation of a MOF-MOF composite.

2. Research hypothesis and aims of dissertation

The aim of the doctoral dissertation was the selection and characterization of different MOF materials capable of efficiently capture carbon dioxide and act as photocatalyst of its reduction reaction to obtain short hydrocarbons (methanol, formic acid, methane etc.) or carbon monoxide.

The main hypothesis of the presented research was that MOF properties – especially related to carbon dioxide selective adsorption and its reduction under light illumination – can be tuned by subjecting the material (or the pathway of its synthesis) to different modifications. It was also postulated that depending on the type of modifying agent used, the method of its introduction will have a crucial influence on the final properties of as-obtained MOFs.

To verify the correctness of the hypothesis and achieve the assumed aim, the work was divided into four main stages:

- the investigation over the possibility of tuning MOFs CO_2 sorption capacity by changing synthesis conditions;
- modification of chosen MOF with different ionic liquids *via* different methods and verification of their influence on the material and their photocatalytic activity;
- utilization of defect engineering by introduction of additional non-noble metals *via* different methods and verification of their influence on the material and its photocatalytic activity;
- preparation of a MOF-MOF composite with the use of ionic liquid introduced *via* different approaches and verification of their influence on the material and their photocatalytic activity.

The first task was exploited on the Cu-TDPAT MOF. Different synthesis conditions were indicated as potentially critical regarding the characteristics of the obtained material. Among them, time and temperature of the reaction, molar ratio and type of precursors, type and amount of modulating acid, type of solvent or solvents mixture acting as reaction medium, as well as the type of the reaction vessel were identified as the most influential.

The second task, materials based on HKUST-1 (a copper-based MOF) were obtained using several types of ionic liquids (including four bio-based amino acid ionic liquids) and *via* two different approaches – addition of ILs to MOF synthesis and post-synthetical impregnation of MOF with ILs. Resulting materials were investigated in terms of the influence of ILs structure (type of paired anion and cation) and amount (different weight or molar ratio in relation to MOF precursors) on the properties of the resulting MOFs.

For the third task, two zirconium-based MOFs – UiO-66(Zr) and its aminated analogue NH_2-UiO-66(Zr) – were subjected to defect engineering procedure. Cobalt, nickel and copper were chosen to be introduced *via* two different methods namely: synthetical incorporation and post-synthetical photodeposition. The efficiency of defect engineering was investigated in terms of morphology, sorption properties and photocatalytic application. The mechanism of light-driven

excitation and following reduction reactions will be examined. Stability of the best material was investigated.

The last task involved attempt of creation of MOF-MOF composite by addition of UiO-67(Zr) to the synthesis environment of NH_2-MIL-125(Ti). 1-ethyl-3-methylimidazole chloride [EMIM][Cl] IL was employed as a modulator during MOF-MOF composite synthesis *via* either synthetical, post- or mid-synthetical way. The impact of obtainment method on the resulting morphology and properties was explored together with mechanisms of light-driven excitation and following reduction reactions.

3. Thesis scope and novelty

The scope of this research encompasses the investigation over the influence of different aspects of synthesis and modification methods on varying MOF-based materials. By identifying the potential ways to improve the gas sorption and photocatalytic performance, different pathways were selected for different MOFs.

This work covers both synthetical approaches of MOFs modifications as well as post-synthetical ways. The structure of the herein presented dissertation starts with the wide-ranging literature review on the topic of MOFs modification, through the selection of modification conditions and methods, ending with verifying the impact of such approaches on the properties of resulting MOFs. The structure of the thesis was organized to provide a detailed insight into the outcome of all of the branches of the proposed pathways of MOFs modification. The work was arranged as follows:

- Chapter 4 provides the literature review exploring the knowledge on metal-organic frameworks, their structure, modification methods and the possible applications in CO_2 storage and utilization. This chapter partially incorporates findings published in [11]
- Chapter 5 covers the detailed description of materials and methods utilized throughout the experimental research.
- Chapter 6 evaluates the influence of the synthesis conditions on properties and performance of Cu-TDPAT MOF.
- Chapter 7 provides an insight into the possibility of HKUST-1 modification with ionic liquids and verifies its impact on the morphology and application of as-obtained materials.
- Chapter 8 focuses on the defect engineering by introduction of non-noble metals to UiO-66(Zr) and NH_2-UiO-66(Zr). The properties of photocatalysts are correlated with the method of modification and the type of introduced metal. This chapter incorporates findings published in [12].
- Chapter 9 refers to the creation of UiO-67(Zr)-NH_2-MIL-125(Ti) MOF-MOF composites and assesses its effectiveness. The role of ionic liquid in obtainment of the material and in the photocatalytic reaction is also discussed.
- Chapter 10 depicts a conclusion of the presented research, summarizing the results and suggesting future perspectives towards industrial MOF applications.

4. Literature review

4.1. Global problem of increasing CO_2 emission and current counter measurements

Carbon dioxide is one of the major components of flue gas emitted in large quantities by various industries and its concentration in the atmosphere is consistently growing [1]. According to Global Carbon Budget 2024, the preliminary estimation of the total emission of anthropogenic CO_2 to the atmosphere in 2024 reached the appalling level of 41.6 $GtCO_2 \cdot yr^{-1}$, which gives over 2.5% growth rate comparing to year 2023 [13]. What seems even more disturbing is the fact, that the confirmed amount for year 2024 was even higher, reaching 42.4 $GtCO_2 \cdot yr^{-1}$ (increase of almost 4.4%), and the expected number for 2025 was estimated at almost identical level of 42.2 $GtCO_2 \cdot yr^{-1}$ [14]. Compared to the pre-industrial period, the current concentration of CO_2 in the air's atmosphere – 425.6 ppm in 2025 – raised already by 53% and is prognosed to increase further. Such phenomenon is caused by the constant growth of total population and ongoing technological advancement. Various industries are constantly developing, and civilization is consuming ever-larger areas, more and more often at the expense of nature. Approaches to environmental protection and awareness of the threats posed by climate change vary widely around the world. Although many countries are tightening gas emission limits, prioritizing the use of renewable energy sources, and restoring green vegetation, other parts of the world ignore all warnings by they use of fuels of questionable purity and continuedly issuing permits for clearing another forest lands.

Despite the fact that the use of renewable energy sources is becoming more and more popular, especially in the European Union region, and the amount of green energy produced is increasing [15], these statistics are insufficient to start displacing the conventional energy sources from the market. This means that mankind still needs an effective solution that will help reduce the CO_2 emissions into the Earth's atmosphere and prevent its harmful effects. Currently, several technologies of CO_2 capturing and separation are widely utilized. However, they are still not sufficient in terms of planned by European Commission decarbonization of industry and new target of net greenhouse gas emissions reduction by 90% within the European Union by 2040 compared to year 1990 [16]. The solution of the problem may lie in technologies that include not only CO_2 capture and storage but also ensure its conversion into valuable chemical compounds like short-chained hydrocarbons. Minimization of the industrially emitted CO_2 effects on the environment are put into practice by development of a process called *Carbon Capture and Sequestration* (CCS) or *Carbon Capture and Utilization* (CCU), or merged together as *Carbon Capture, Utilization and Storage* (CCUS) [17]. This term covers such steps of proceeding as carbon dioxide capture, transport and, respectively, direct storage or application.

4.1.1. Carbon capture

In the industry, three routes of CO_2 capture from the gas streams can be distinguished [18]. For the first route, called post-combustion, CO_2 is acquired from the flue gas, therefore in the

industrial processes it is implemented at the ending stage. In this approach both the partial pressure of CO_2 (4-15 mol%, depending on the source) and the gas stream pressure (nearly ambient) are relatively low, which makes this process challenging and requires strictly dedicated methods aimed at strongly interacting with diluted CO_2 in the stream [19]. In other approach, CO_2 is captured prior the combustion (termed pre-combustion capture) from the synthesis gas formed by fuel conversion [19]. The as-acquired CO is then treated with steam to obtain CO_2 and pure H_2, which is subsequently burnt. Compared to the flue gas, in this route the partial pressure of CO_2 is higher and ranges between 15 and 40 mol%, and at the same time the pressure of gas stream is relatively high reaching the value of 15-40 bar. In contrast to the first described route, the third possibility employs O_2 as a factor responsible for fuel combustion in the exchange of air, therefore it is called oxy-fuel combustion [18]. Such approach leads to obtainment of flue gas rich in CO_2.

4.1.2. Carbon dioxide separation

Depending on the route of the gas capture, CO_2 can be separated from the gas streams *via* different methods basing on absorption, membrane separation, phase separation or adsorption [20]. The choice of a specific CO_2 separation method is mainly determined by factors such as gas mixture composition and pressure, especially the concentration of CO_2 and properties of the other gases.

For post-combustion capture, the most wide-spread technique of carbon dioxide separation is gas absorption using amines. Aqueous solution of monoethanolamine (MEA) with concentration of 30% is commonly used in industry to absorb CO_2, thanks to the highest efficiency in comparison with other amines [21]. After the cycle of scrubbing, the solution have to be purified by stripping, which significantly increases the energy consumption. Additionally, because of relatively low chemical stability of MEA (in relation to other amines) and its corrosive character, there is still need to search for better method of trapping the CO_2. Even though new amines were investigated in terms of this problem, no suitable substitute of absorbent was found yet [22]. As a promising alternative amino acid ionic liquids (AAILs) were also indicated. However, the research shows that with increasing gas saturation, the viscosity of AAILs also increases drastically limiting their use in practice [23–26].

In turn, the cryogenic air separation is the elemental technique for the oxy-fuel combustion [27]. It involves distillation of oxygen and nitrogen at drastically reduced temperature, as their boiling points are at level of -196 and -183 °C, respectively. To reduce the energy expense, additionally the pressure is increased to move the boiling points towards higher, yet still negative temperatures [18]. Even though, this method enables obtainment of purity exceeding 99% and does not require the use of any hazardous chemicals (like in case of absorption), the deep refrigeration is still too unprofitable to become more widespread.

Membranes are made of solids capable of separating mixture components by passing one component and blocking another. Typically, membranes are polymeric, but porous silica, zeolites or porous ceramics are also effective, especially when operating in harsh conditions. This specific

separation route may be based on the phenomenon of solution-diffusion (for non-porous membranes) or molecular sieving (for porous structures) [18]. Even though this approach of CO_2 separation is of reasonable cost, characterized by simple construction and accessible way of implementation, provides chemical neutrality, this method still did not find the actual application in large-scale installations [28].

Next to absorption, adsorption, is considered as another promising technique for both pre- and post-combustion capture [18]. The advantage of gas adsorption can be clearly indicated considering the fact that adsorption is usually conditioned with the weak interactions (steric, kinetic or equilibrium effects), thus efficiently limiting the energetic cost of regeneration. Additionally, adsorption decreases the use of chemicals like in the case of the classic method of amine scrubbing for CO_2 absorption. By controlling the pressure or temperature CO_2 can be effectively separated *via* pressure swing adsorption (PSA) or temperature swing adsorption (TSA), respectively [28].

4.1.3. Materials for CO_2 adsorption

To attract CO_2, a material should possess favorable functional moieties (specific metals or pending groups) and preferably developed specific surface. Among wide variety of materials that could be potentially used for CO_2 adsorption (Figure 4.1), the most popular representatives include zeolites, carbon-based materials, mesoporous silica and metal-organic frameworks.

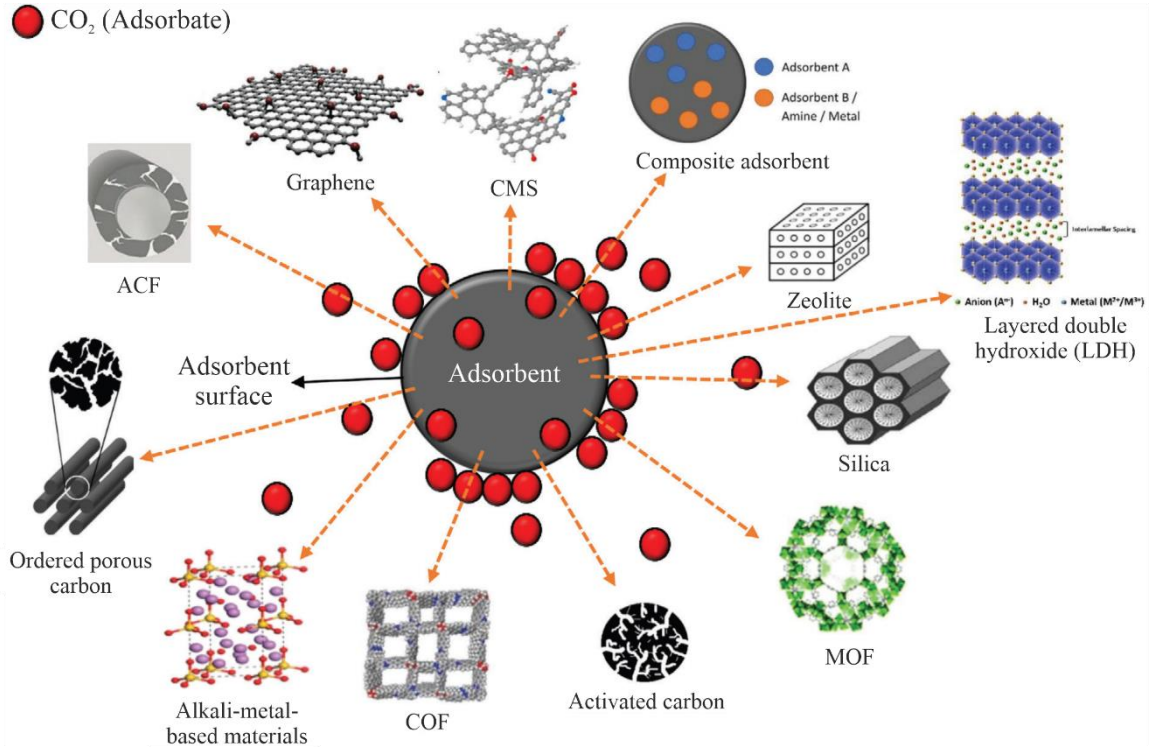


Figure 4.1 Different materials for potential use in CO_2 adsorption (reproduced with permission from [29]*); ACF – activated carbon fiber, CMS – carbon molecular sieves, COF – covalent-organic frameworks.*

Zeolites are a class of aluminosilicates characterized by highly ordered crystalline structure with a net of microporous channel to which zeolites owe their second name – molecular sieves [30]. Apart from Al, Si and water molecules, zeolites contain in their structure charge-balancing cations

in form of alkali metal or alkaline earth metal. Such specific structure allows zeolites to interact with CO_2 and adsorb them by using the quadrupole moment of the gas particles to attract it. However due to hydrophilic character of most zeolites, their industrial use for CO_2 capture is limited. It is due to the fact that usually the flue gas streams contain moisture or impurities like sulfur or nitrogen oxides, reducing the efficiency of CO_2 separation [31,32].

Another very broad group of materials capable of effective CO_2 adsorption are porous carbonaceous materials such as active carbons, nanotubes or graphene [20]. These materials can attract CO_2 *via* either physical and chemical interactions depending on the functionalization of the surface of the specific sorbent [33]. In contrast to zeolites, most of carbon materials is characterized with hydrophobic character, therefore limiting competing interactions with moisture and facilitating regeneration of the active surface. However, the domination of the adsorption mechanism by weak interactions with gas molecules leads to a significant reduction in the sorption capacity especially at elevated temperatures and in the case of low adsorbate concentrations. Another drawback of carbon materials concerns the fact that these materials possess low selectivity towards CO_2 [34].

Mesoporous silica is a particular type of amorphous silica *i.e.* silicon dioxide, with porosity in the range of 2-50 nm, resulting in relatively large specific surface area and porosity. Mesoporous silica, like the most popular MCM-41 or SBA15 [35], themselves are not attractive CO_2 sorbents [36]. However, these materials can act as a reasonable substrate for functionalization with amines like polyethylenimine (PEI) [35], tetraethylenepentamine (TEPA) [35] or (3-aminopropyl)triethoxysilane (APTES) [37]. Such approach results in obtaining materials capable of selective CO_2 chemisorption [35,37], but at the same time, the process itself becomes more complex and expensive in large scale, especially that its implementation requires the use of amines, considered as harmful for the environment.

In recent years, metal-organic frameworks dominated the different research fields, especially the one of gas adsorption. MOFs have attracted attention due to their characteristic organic-inorganic porous crystalline structure, which results in obtaining a material with a large specific surface area [4]. Their structure can be handily modified at different stages of obtaining the material to adjust their properties. MOFs can possess open-metal sites and/or different functional moieties in the structure, which, combined with their huge specific surface area, makes them capable of adsorbing significant amounts of gas [20]. Despite many undeniable advantages, the synthesis of many MOFs is accompanied by high costs (both in terms of components prices and energy costs) and the resulting materials often possess limited resistance to operation in aggressive environments.

4.1.4. Carbon dioxide storage

Even though, several efficient methods of CO_2 separation exist, it is more problematic to store the acquired gas for long-term. In practice it is not possible to enclose each portion of the obtained gas in a cylinder, therefore different ideas are under investigation.

One of the fundamental ideas is to pump the gas to the deepest levels of the seas and oceans. However, it was very fast realized and proven, that when uncontrolled in proper way, such interference with the aquatic environments would be very harmful [38]. The potential acidification was found to drastically affect not only the fauna and flora of the water depths, but as a result also the top layers (being already the great reservoir of the anthropogenic CO_2). The uncompensated progressive acidification would lead to extinction organisms living in the gas storage area or their migration to subsequent water layers. This in turn would disturb the ecosystem homeostasis of the subsequent biomes, therefore the implementation of this idea should be explored with particular caution and attention to safety of living organisms [39].

The second main idea – geological sequestration – involves injection of the compressed CO_2 gas deep underground to trap it. For this purpose niches with saline aquifers could be adapted as the storage site or alternatively, fossil fuel deposits like unmineable coal seams or depleted oil and gas fields as a starting point of the fuels formation renewal [40]. Such installations could be built near large industrial plants to be able to directly dispose of the captured and separated CO_2. However, the concept is burdened with a high risk of geological fractures generation (especially in areas of high geological activity) and installation leakage, affecting the efficiency of the method in an undesired trend [41]. Additionally, such events could be potentially very dangerous to human and animal habitats exposed to destroying influence of eventual incidents.

At the moment, both ideas are intensely investigated by the researchers around the world. Since real-scale research is very limited, a significant part of the research is based on calculations and modeling. As the fossil fuels formation processes are estimated to take thousands of years, development of methods of CO_2 storage would only provide short-term relief and as a result we, the mankind, would quickly return to the starting point. Taking into consideration the up-to-date knowledge and being aware of the pros-and-cons balance of CO_2 storage, it would be more beneficial to find a straightforward utilization method for the captured CO_2 and treat its storage as a supplementary method.

4.1.5. Carbon dioxide utilization

The development of methods that would allow for the ongoing use of CO_2 produced would be a major step forward in the context of "healing" the Earth's environment. For that reason various pathways are intensively investigated to mitigate the climate changes and at the same time to benefit from the CO_2 derivatives obtained.

Polymerization is currently one of the potential way to consume the generated CO_2. Homopolymerization of the gas itself is very complicated and extremely ineffective in practice [42]. Nevertheless, CO_2 particles can be indirectly incorporated into the structure of various polymers *via* copolymerization. For example heterocyclic molecules as epoxides, episulfides or aziridines (Figure 4.2) to obtain different polycarbonate derivatives [42]. Alternatively, CO_2 can be combined with propylene oxide to synthesize polyethercarbonate polyols, which can further act as feedstock for polyurethane manufacture [43]. However, taking into account the current trend of moving away from

the production of excess amounts of plastics, especially those that cannot be safely and effectively recycled or reused, the question arises whether such a problem solution will be beneficial for the environment overall. Another concern refers to the fact that once bound in the polymeric chain, as the material wears out and degrades, the gas will be released back into the atmosphere.

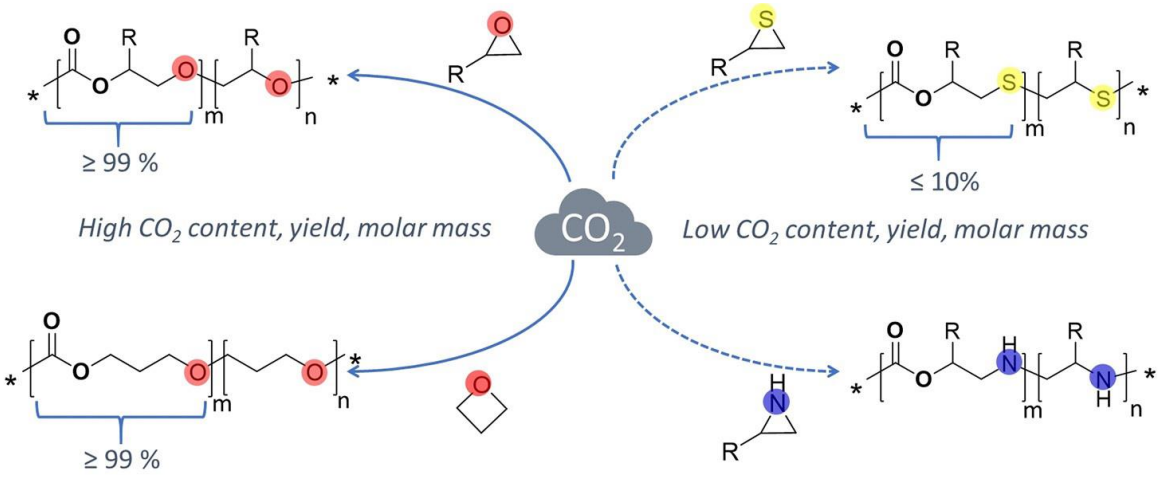


Figure 4.2. Possible pathways of CO_2 copolymerization (reproduced with permission from [42]*)*

Another potential pathway to dispose the anthropogenic CO_2 uses the natural process of photosynthesis. In comparison with chemical bonding of CO_2 in different materials, the biological approach seems as a more sustainable solution employing chosen autotropic microorganisms and flora representatives. The research has shown that thanks to its miniature size, ability to reproduce quickly and great ability to adapt to different conditions, microalgae would be the most promising organisms capable of utilizing great amounts of carbon dioxide [44]. However, severe obstacles like microalgae poisoning of the with flue gas components (e.g. nitrogen and sulfur oxides) or not efficient enough method of the dissolution of CO_2 in the microalgae environment are significantly impeding the large-scale development of such method [45].

The third branch of CO_2 utilization considers the chemical conversion of the gas to obtain valuable chemicals and fuels *i.e.* short-chain hydrocarbons, alcohols, carbon monoxide, formic acid or urea among others [46]. In this regard, apart from thermocatalytic approach two main novel pathways for CO_2 reduction are currently investigated – namely photocatalytic and electrocatalytic methods [47]. These methods requires the use of materials being able to facilitate the reaction of CO_2 transition to other compounds *via* impacting with specific force like light irradiation in the case of photocatalysis. Each of these approaches of CO_2 utilization encounters severe obstacles on the way to developing a large-scale method [46]. Scientists' reports mention various problems such as discrepancies between theory and practice, problems with the long-term stability of the catalysts and maintaining steady performance or expensive regeneration. The source of energy used to power such a process should also be taken into account and provide the sustainability, so that the amount of CO_2 converted is more favorable than the amount of CO_2 produced during supplying the necessary energy.

The literature review clearly indicates multiplicity of potential solutions of the efficient CO_2 utilization problem. However, most of the ideas are still in the relatively early stages of research or their efficiency requires a lot of work to boost it for industrial requirements. Therefore it is important to anticipate possible development paths and potential inhibiting factors from the very first stages of material development. Considering that in the future photocatalysis could be energetically cost-free method, it is very important to pay special attention to it and invest in the development of materials which will be able to accomplish.

4.1.6. Materials for light-driven CO_2 conversion

Among the different materials for the targeted photocatalysis of CO_2 conversion, next to the classic titanium(IV) oxide, examples as bismuth compounds, halogen perovskites, graphitic carbon nitride or metal-organic frameworks or their composites can be listed.

Titanium(IV) oxide is the most wide-spread photocatalytic material. Apart from CO_2 photoconversion it is also known in the field of light-driven water splitting and degradation of organic pollutants, as well as is an important structural element of solar cells [48]. Its popularity is mainly due to its low price, relatively low toxicity, and resistance to external factors, especially corrosive environments [49]. On the other hand, TiO_2 is characterized by wide bandgap of about 3.2 eV (designated for anatase) This makes the compound unsuitable for use as a photocatalyst under solar irradiation (or its artificial imitation) without appropriate modification of the structure. Additionally, the photogenerated electron-hole charge pairs recombine very quickly reducing the efficiency of process. To adjust the bandgap size and shift the range of absorbed light towards longer wavelengths, TiO_2 can be modified by doping with different elements [50,51], creating oxygen vacancies [52] or introducing noble metals as co-catalysts [53]. However such interference with material electronic structure can lead to deterioration of its activity in specific type of reaction.

Another promising photocatalyst is g-C_3N_4 – graphitic carbon nitride a 2D polymeric structure composed of carbon and nitrogen with no metal [54]. It is commonly obtained by thermal decomposition of nitrogen-rich organic compounds like urea or melamine. Compared to TiO_2, g-C_3N_4 possess narrower bandgap (about 2.7 eV), therefore it absorbs light from wider wavelength range [55]. Despite this, the photogenerated charge carriers undergo recombination shortly after excitation [56]. To compensate its relatively low surface area and overcome the relatively low efficiency of photocatalytic process, g-C_3N_4 is usually combined with other semiconductors to create a heterojunction [57,58].

Graphitic carbon nitride is often coupled with different bismuth-based compounds, which are also show promising photoconversion capabilities themselves. Among them Bi-based oxyhalides, vanadates and tungstates can be listed as the ones that are getting the most attention [59]. In comparison with the classic photocatalyst – TiO_2 – in the case of these compounds, two distinct orbitals *i.e.* O 2p and Bi s6, are responsible for the charge transfer (as they constitute the valence band) making it more effective than in O 2p orbital alone (characteristic for TiO_2) [59]. The band gaps of the corresponding compounds are within the range of 2.6-2.9 eV, 2.4-2.9 eV, 1.8-

3.3 eV (depending on the introduced halide, highest for Cl, lowest for I), respectively [60]. Despite the large variety of bismuth compounds providing wide variety of properties that can be selected for the specific conditions as potential photocatalysts of CO_2 reduction, researchers report several difficulties. Apart from the very rapid recombination of charges generated as a result of light excitation, the progressive defecting of the structure during irradiation was observed, which may consequently lead to the deactivation or total breakdown of such a photocatalyst [60].

Over the past several years, perovskites have been gaining enormous popularity in many applications related to their broadly understood optical properties, especially in photovoltaics. Currently these compounds, especially the sub-group of metal halide perovskites (MHP), are gaining more and more interest in the field of photocatalysis, including photoreduction of CO_2 [61]. The structure of MHPs has a common formula of ABX_3, where X stands for halide atom (Cl, Br or I), A for monovalent metal (alkali metals like Cs, Na, K etc., alkaline earth or rare earth metals alternatively), while B refers to divalent metal (usually transition metals like Pb, Ge, Sn etc.) [62]. In general, the composition designates the properties of the specific perovskite material influencing its band gap width and the location of conduction and valence band, this in turn allows to adapt them to the needs of, for example, visible light absorption [61]. Comparing to the previously described photocatalysts, electron-hole pairs created in HMPs are characterized by relatively longer lifetime which increases the efficiency of the overall photocatalytic process. Nevertheless, many reports indicate that several perovskites of this type are very sensitive to water, which may significantly limit their applications, especially in solid-liquid environment since it is common to replace organic CO_2 photoreduction media with aqueous solutions or water [61].

As in the case of adsorption, MOFs are gaining more and more interest as photocatalysts. It is especially owed to the simultaneous high affinity towards CO_2 adsorption, making them very versatile materials for either capturing and further utilizing the gas. Herein, the significant porosity and development of the specific surface area are crucial in terms of maximizing the photocatalytic performance of MOFs [63]. In terms of this application, many MOFs possess favorably located highest occupied (HOCO) and lowest unoccupied (LUCO) crystalline orbitals (*i.e*. the equivalents of the valence and conduction bands), and the resulting optical gap, which can be customized even further by modifying their structure *via* different approaches. Additionally, these structures may be adapted in a way enabling the use in solid-gas or solid-liquid environments of the reaction [64,65]. Taking into account the possibility of such dual use of carbon capture and straightforward utilization, the cost of producing such a material could be compensated and in a way justified with the positive aspects resulting from their practical application. However, a lot of substantial work is still needed to be carried out before such advancement will be achieved.

The versatility and duality of MOFs use in the context of CO_2 makes them very promising candidates for the developing technologies of CCUS. Therefore this work shows focuses on the use of different MOFs for CO_2 adsorption and light-driven conversion and tries to maximize their performance by different modification methods.

4.2. Metal-organic frameworks

Metal-organic frameworks are materials of rather short, but intensive history and undoubtedly great interest from scientists and engineers. Along with covalent-organic frameworks (COFs), MOFs visibly dominate the field of reticular chemistry, which focuses on materials characterized by very specific geometry [5]. The ordered crystalline nets of both MOFs and COFs are the result of combination of polynuclear clusters with a type of struts between them, and linked together with strong bonds. In the case of MOFs, organic molecules play the role of linkers between the neighboring metal clusters, what distinguishes them from COFs for which the distinct structure is owed to the organic clusters linked with organic struts. The components of MOFs are connected with each other by coordination bonds, creating one-, two- or three-dimensional networks with voids. Thanks to the particular architecture, by customization of the chemical identity, MOFs can be tailor-made according to the application with customized characteristics like good thermal, chemical or mechanical stability, as well as extensive specific surface area and significant porosity.

The development crystalline porous networks such as MOFs and COFs was mainly pioneered and spread around the world by Professor Omar M. Yaghi, who, along with Professor Richard Robson and Professor Susumu Kitagawa, was honored with the Nobel Prize in Chemistry in the year 2025 for his contribution and discoveries. Undeniably, it was the research on varying other coordination compounds with metals in their structure that contributed to the discovery followed by exploration and dissemination of MOFs. Among such structures Werner complexes, Hofman clathrates and wide variety of coordination networks can be distinguished. The observation made and employed for the synthesis of organometallic compounds, led Yaghi to differentiate a new group of compounds and call it with the name of “metal-organic frameworks”.

Due to the great interest that MOFs arouse, many of the specific structures have been named differently depending on their origin. Three different types of names for MOFs may be given. First considers the abbreviation “MOF” itself and a number, like for example MOF-5 or MOF-808. The other type of short denotation symbols the name of the institution, which was first to report the obtainment of the structure. Among them institutions like ***U**niversitetet i **O**slo* (UiO), **H**ong **K**ong **U**niversity of **S**cience and **T**echnology (HKUST) or ***M**atériaux de l'**I**nstitut **L**avoisier* (MIL) can be distinguished. The last type of naming uses the initials of components – metal and linker – or the chemical formula. As an example, the name of Cu-TDPAT stands for MOF containing copper nodes and 4,6-**t**ris(3,5-**d**icarboxyl**p**henyl**a**mino)-1,3,5-**t**riazine as linker [66]. Several MOFs can be recognized by many names – for instance, UiO-66 can be also found as Zr-BDC (1,4-**b**enezene**d**i**c**arboxylic acid) or $Zr_6O_4(OH)_4(BDC)_6$ [67], while different names for MOF-5 are IMROF-1 (**i**so**r**eticular **m**etal-**o**rganic **f**ramework), Zn-BDC or $Zn_4O(BDC)_3$ [68,69].

4.2.1. Structure of MOFs

To act as linker, the organic molecule is required to possess at least two functional groups in its structure. Among them, the most widespread are linkers with carboxylic functionalities, for example ditopic 1,4-benzenedicarboxylic acid (H_2BDC). The number of extension points i.e. number

of functional groups determines the topicity of the strut. Units with more than two branches – containing in total three, four, six, eight or even twelve extension points – can be successfully introduced. Linkers containing other binding groups like: phosphates [70], pyrazolates [71], tetrazolates [72], catecholates [73] and imidazolates [74] are also known.

Another feature that dominates most MOFs is the presence of an aromatic ring in the structure of linkers as core and/or extending units. The unsaturated hydrocarbon fragments are controlling the rigidity of the whole structure and influence the mechanical stability. Apart from the binding functionalities, the organic struts can be functionalized with additional single or multiple groups (amino, bromide, chloride, hydroxyl etc.), which are not taking part in the formation of coordination bonds. Examples of such linkers include 2-amino-1,4-benzenedicarboxylic acid (NH_2-H_2BDC) or 2,5-dihydroxy-1,4-benzenedicarboxylic acid (H_4DOBDC). The diversity of linkers is not limited to the type of possessed functional groups. The amount of binding groups and their mutual position can be customized. It is the most common case, where the linker is symmetrical and planar. Additionally, struts can combine extending units of different length and type, which influences the overall geometry. The symmetry of the organic compound can be affected by implementation of angled (bent or offset) core units. Examples of various linkers structures are shown in Figure 4.3.

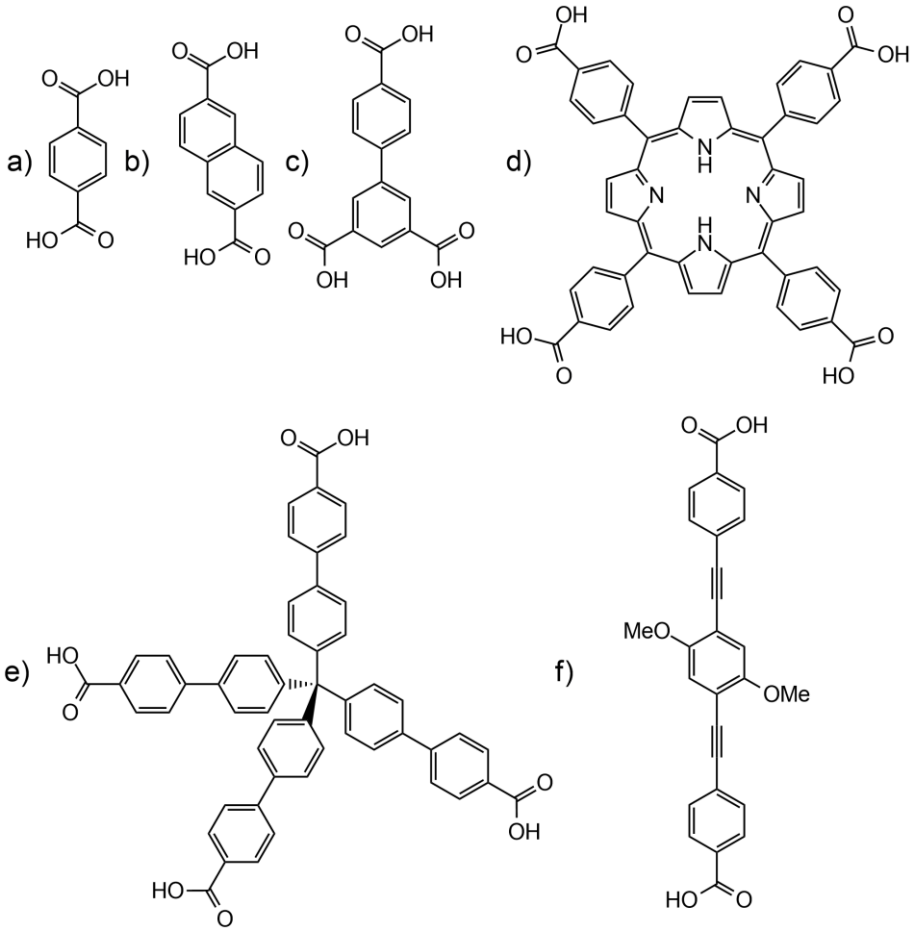


Figure 4.3. Examples of carious carboxylate linkers with different topology: a) 1,4-benzenedicarboxylic acid, b) naphthalene-2,6-dicarboxylic acid, c) [1,1'-biphenyl]-3,4',5-tricarboxylic acid, d) 4,4',4'',4'''-(porphyrin-5,10,15,20-tetrayl)tetrabenzoic acid, e) 4',4''',4''''',4'''''''-methanetetrayltetrakis (([1,1'-biphenyl]-4-carboxylic acid)), f) 4,4'-((2,5-dimethoxy-1,4-phenylene)bis(ethyne-2,1-diyl))dibenzoic acid

Like in the case of linkers, wide variety of metal atoms can be incorporated into MOFs secondary building units (SBUs) – the polynuclear clusters. The divalent metals (like zinc, magnesium or copper) are most commonly introduced [75,76]. Aluminum, gallium, iron or indium are the examples of trivalent elements [77,78], while titanium or zirconium represent the tetravalent ones [79,80]. The above listed elements can be directly built in MOF network during the synthesis. Due to their expensiveness and chemical nature, MOFs based on noble metals are not popularized, but it is possible to obtain them [81–83].

So many variables mean that MOFs can be practically freely designed according to specific requirements. However, choice of linker with sophisticated, original structure or rare elements as nodes can lead to some difficulties. Firstly, this can significantly affect the price of the final product. Secondly, such structure may require elongated time or more stages in the procedure, probably dictating the utilization of greater amount of different components and solvents, which may be unfavorable for the environment. A general tendency of using the simpler or easier to achieve precursors for MOFs synthesis is observed in order to diminish the harmful side effects of creating these structures.

4.2.2. Synthesis of metal-organic frameworks

Several approaches can be employed to obtain different MOFs. Among them, solvothermal [66,79] route is the most popular, but approaches like electrochemical [84,85], sonochemical [86], microwave-assisted [87], ionothermal [88], spray-drying [89] or even mechanochemical methods [90] can be utilized. The general scheme of MOFs preparation of most procedures can be shortly outlined. The starting point includes the dissolution of the linker and a metal precursor (separately or together at once) in suitable solvent. In the case of the electrochemical synthesis, the metal ions are provided by anode dissolution to the electrolyte which contains dissolved linker [91]. The combined solutions are placed in one vessel, sealed and treated in suitable conditions. For example, solvo- and hydrothermal synthesis demand a vessel, which can be tightly sealed – like scintillation vials [66], Schott bottles [92] with sealed caps or stainless steel autoclaves with Teflon liners [93]. The as-prepared solution containing both precursors is subjected to the thermal treatment, usually not exceeding 220°C. The chosen synthesis method determines the duration of the synthesis which can last several minutes (in case of microwave methods [87]), hours [75] or even few days [94]. The as-synthesized material is then purified and activated prior the measurements. The term of activation will be described in detail in following subsection.

The specific structure of linkers i.e. the presence of aromatic rings and multiple carboxyl functionalities, makes them hardly soluble in water and alcohols. This compels the use of appropriate solvent to completely dissolve them. The structures of the most commonly utilized organic solvents for MOFs synthesis are shown in Figure 4.4. Examples of such solvents include – above all – amides, like for example *N,N*-dimethylformamide (DMF) [79], *N,N*-diethylformamide (DEF) [95] or *N,N*-dimethylacetamide (DMA) [96]. This fact is inseparably connected with the mechanism of MOFs formation. During the heating of solution containing precursors, amides partially decompose to adequate amines and acids. The first of them is responsible for the

deprotonation of linker particles, while the second acts as a modulator. Deprotonated carboxyl groups of struts react with metal cations to form SBU, then multiple SBUs are forming the expanded network. At the same time, the modulator is responsible for control of reaction rate. It can be attached to the SBU – instead of a linker – thus will not contribute to further growth of a framework in contact with metal [11]. Owing to the reversibility of bond formation, any errors in the net can be corrected and hence contribute to generation of highly crystalline MOF. Other organic solvents, like for example *N*-Methyl-2-pyrrolidone (NMP) [97] or dimethyl sulfoxide (DMSO) [98] can be also used. Due to potential hazardous effects of amides on human's health and on the natural environment, their use tends to be limited by mixing with co-solvents as water [75], ethanol [75] or DMSO [66]. Syntheses in which successful utilization of acetone [99,100] or acetonitrile [101] as reaction medium were reported as well.

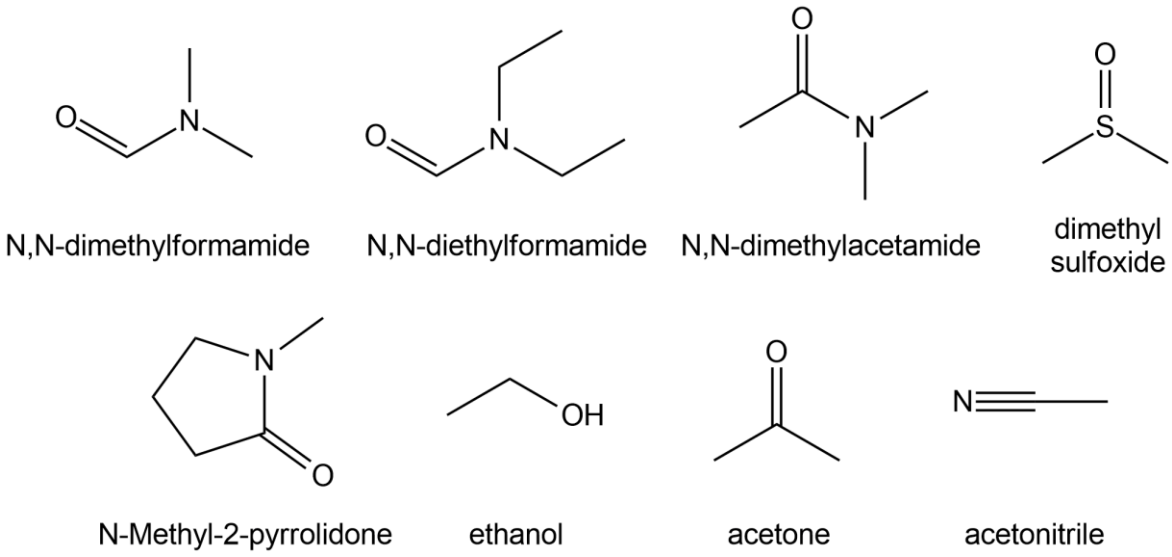


Figure 4.4. Structures of organic solvents used in MOFs synthesis

Next to the linker, the second main compound used for the synthesis are metal salts, rather hydrated than non-hydrated. The question of using salts with water particles in the structure finds an explanation in providing good solubility in the synthesis environment and crystal growth control basing on the competition of linker with the coordinated water [102]. Additionally, as it was mentioned above, in solvothermal approach at elevated temperatures water enables amides hydrolysis, products of which contribute the modulation of the crystal net growth by altering the protonation-deprotonation equilibrium [11]. Hydrated nitrates, acetates or chlorides are commonly used as the precursors of di- and trivalent metal atoms [66,103,104]. In the case of tetravalent examples – like hafnium or zirconium – chlorides or oxychlorides are more convenient to use [79,105]. Apart from that, titanium requires the use of alkoxides [80]. It is also possible to use metal oxide as a precursor in solvothermal approach, however it usually results in obtainment of product contaminated with the unreacted substrate [106]. Apart from salts, the electrochemical approach may also use the pure metal to act as an anode [107]. The advantage of such method is the lack of contamination of product with the remaining salt anions, as well as the possibility of depositing thin MOFs layers directly on the substrate.

4.2.3. Activation of MOFs

The characteristic feature of MOFs is their exceptionally high porosity, and hence the specific surface area exceeding 1000 $m^2 \cdot g^{-1}$. However, usually after the synthesis the pores of formed MOF are usually clogged with the remaining precursors or solvents, especially amides. In this regard it is therefore necessary to unblock the inner surfaces before the product characterization and application. In general, the elemental MOF cleansing procedure takes place straight after the synthesis and includes washing several times with the primary solvent in order to dissolve any unreacted linkers or metal salts. This may be followed by washing with a lower boiling point solvent as ethanol, tetrahydrofuran or methanol. Product treated this way can be then dried in temperature not exceeding 100 °C, usually under reduced pressure. This process is commonly called purification and is distinguished as a preface of the activation process. To perform the proper MOF cleansing, which is synonymous with full exposition of MOF's whole surface, the actual process called activation should be performed (Figure 4.5). This is especially important prior to the analysis of gas sorption properties and catalytic performance to provide the highest efficiency of the material. Activation releases the surfaces within the pores and provides more adsorption or specific reaction sites enabling the use of the full capability of MOFs. There exist several approaches to effectively remove the residues from MOF pores. The typical activation protocol starts with immersing the sample in the chosen solvent and its further simple exchange. Methanol [66], acetone [108], dichloromethane [109], chloroform [68] and tetrahydrofuran [79] are widely applied for this purpose, as in comparison with DMF, DMSO or even water are characterize by relatively low boiling point. Procedure of solvent exchange typically lasts several days – from two or three days to even ten days – and employs utilization of at least one solvent. Typically solvent is removed (by decantation or filtration) and exchanged with fresh portion multiple times a day after. The procedure ends with vacuum drying in temperature ranging from 25 °C [68] even up to 300 °C [79], depending on the thermal stability of the specific MOF.

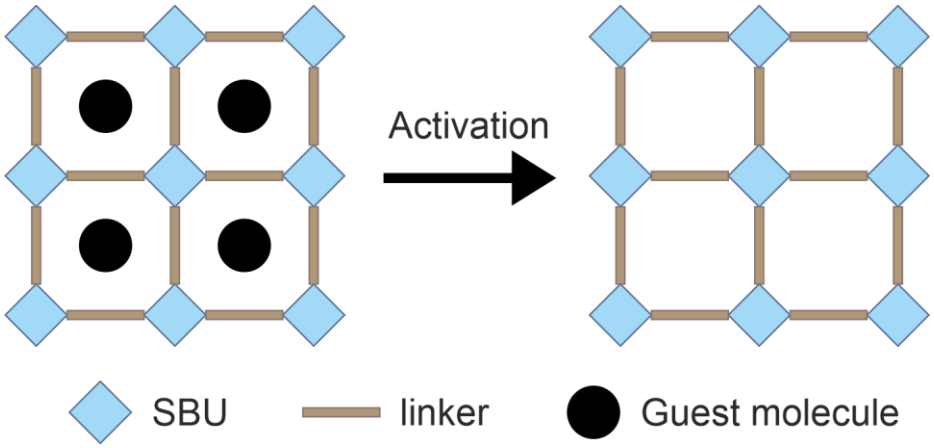


Figure 4.5. Schematical representation of MOF activation

Several modifications of the activation procedure can be introduced. To reduce the large amount of utilized solvent and shorten the time of the process, Soxhlet extraction can be also successfully performed as an alternative to multiple manual exchanges [110]. Alternatively, to

speed up the procedure of washing out the guest molecules the procedure can be assisted with ultrasound treatment [111], but this method is not suitable for several MOFs characterized by fragile structure due to the possibility of structure collapse. Activation methods using microwaves [112] or UV-Vis light [113] as supporting factors are also known. Even though, both of them can efficiently reduce the time needed for activation procedure, similarly to ultrasonic-assisted approach, structure of MOF can be damaged by sudden overheating (in the case of microwaves) or by photodegradation caused by absorption of highly energetic UV irradiation (in the case of light treatment). The use of the supporting methods and their influence on the structure of MOFs, should be investigated carefully to fully indicate the real advantages and limitations in practice.

To limit the undesirable influence of the high surface tension and capillary forces generated during the vacuum drying related to the solvent liquid-to-gas phase transition, other approaches were also explored. For example, the use of supercritical CO_2 instead of thermal treatment is reported increasingly as less destructive for the framework and more beneficial for industrial applications due to accessible scalability [114,115]. Although this method effectively removes the contaminants and solvent residues, there is concern that the advantages of this method do not outweigh the disadvantages, especially considering the environmental impact and greenhouse gas emission. As another alternative for MOF activation method, freeze drying technique can be considered. This approach can use for example benzene [116] or cyclohexane [117] as sublimating agents, which are removed from the pores of MOF by treatment at suitable temperature and pressure for the chosen solvent to enable its direct transformation from solid to gas. Though, to maximize the effects of cleaning, a few cycles of solvent exchange (using for example methanol), should be conducted prior the freeze drying to increase the efficiency of the process.

4.3. Modification of metal-organic frameworks

There exist multiple possible pathways to find the convenient approach of obtaining the optimal structure with the tailored characteristics for specific requirements. For example the change of MOFs particles size can be achieved by simply varying the elementary synthesis conditions like temperature and time of reaction or the molar ratio of the precursors. In turn, the complete change of MOFs morphology or characteristics (affinity to different gases, electronic structure, thermal stability, etc.) can be achieved by further adapting of the broadly understood synthesis process [11]. In connection to this, basing on the moment of modifying factor application, general term of modifications can be divided into three different groups. The first one concerns the modification of the components before conducting the synthesis (pre-synthetic modification), addition of modulators or other additives to the synthesis environment (*in situ* modification) and the modification of as-synthesized MOFs (post-synthetical modification). Combined methods are also known in the literature, which may include selected modifications at different stages of MOF preparation.

4.3.1. Pre-synthetic modification of MOFs

The pre-synthetic MOF structure modification regards modification of the synthesis components. The simplest approach concern the modification of linker's structure with additional pending functionalities. This method of MOF modification also includes the use of different types of a given precursor at once – two or more metals (mixed-metal approach) or linkers (mixed-linker approach).

As an example of simple linker functionalization the complete replacement of 1,4-benzedicarboxylic acid with its aminated version can be used. In suitable conditions the reaction of H_2BDC with zirconium cations, leads to formation of UiO-66 [79]. In the same conditions, when the linker is exchanged with 2-amino-1,4-benzedicarboxylic acid (NH_2-H_2BDC) NH_2-UiO-66 is formed. In the same way different combination can be also obtained by simple change of metal. By utilization of hafnium salt, in reaction with mentioned H_2BDC, UiO-66(Hf) is synthesized [118]. The replacement of one type of precursor does not have to be complete. In such a scenario, when introducing two or more compounds acting as linker or metal source, the obtained products can be defined as Mixed MOF. Combination of two or more structurally analogous linkers for example H_2BDC and X_y-H_2BDC, where X can be $–NH_2$, -Cl, -Br, -OH, etc. [99,119] and y has value of 1, 2 or 4 [120] (Figure 4.6), effects in creation of mixed-linker MOF. In turn, Mixed-metal MOF in created when two or more metals of the same valence (like for example zirconium and titanium [121]) or different valence are combined (like zirconium with europium, cerium or terbium [122,123]). Another specific type of pre-synthetic modification is the introduction of an additional metal (usually different from the one forming the SBU) into the structure linker. In such a way porphyrin linker (H_4TCPP), which is facilitated by its peculiar structure with functionalized void in the middle [124]. This approach is usually beneficial in terms of obtaining additional sorption or catalytic sites.

Introduction of functionalized linkers leads to decrease of the specific surface area (S_{BET}) of MOF in comparison with the parent structure. For example, Katz *et al.* reported that the introduction of one or two amine groups to linker of UiO-66(Zr) causes 25% and 65% S_{BET} decrease, respectively for NH_2-UiO-66(Zr) and $(NH_2)_2$-UiO-66(Zr) [125]. A similar relationship was observed after the introduction of one and two hydroxyl groups to the H_2BDC linker. The presence of additional functional groups also influences the crystallinity of the product, In consequence the modification of the synthesis conditions is usually required to maintain the crystallinity of the product [79]. At the same time the presence of chosen functional groups can positively influence for example the gas adsorption properties and the selectivity of the uptake. For example, the presence of the amine group in UiO-66(Zr) facilitates the total CO_2 uptake and the increased affinity towards this gas makes it effectively separated from the mixture with methane and nitrogen [126]. Another property that is influenced by the type of functional group attached to the linker is the range of light absorbed [127].

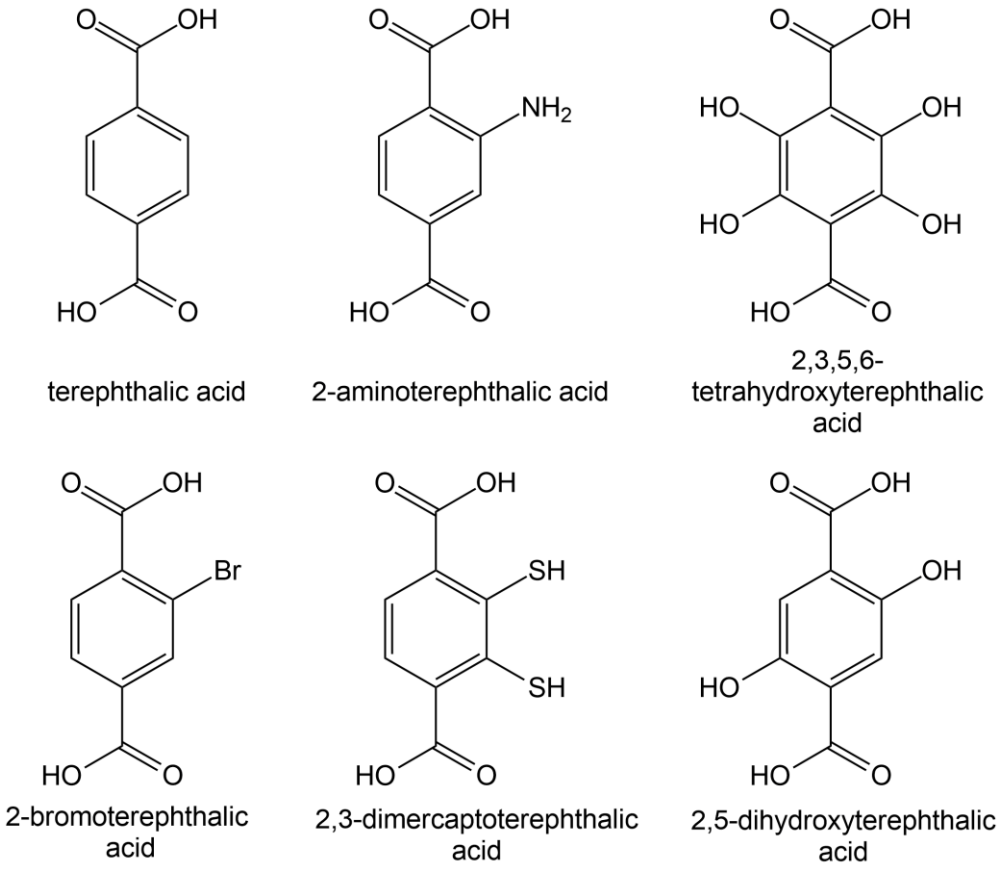


Figure 4.6. Structures of H_2BDC and different H_2BDC-derived linkers

Particular type of the mixed-linker MOF can be also obtained by using two (or more) completely varying struts. In such a case a new MOF with distinct type of SBUs can be obtained. UMCM-1 is an example of structure which is formed as a result of uniformly spread out ditopic H_2BDC and tritopic 4,4',4''-benzene-1,3,5-triyltribenzoate connected with zinc nodes [128]. When applied separately, these linkers lead to the creation of MOF-5 and MOF-177 respectively. It is worth to underline that synthesis of mixed-linker MOF can be unpredictable in some way, due to possible formation of multiple building blocks. It means that for different relative concentration of linkers, not only the mentioned UMCS-1 will be formed, but some extra amounts of MOF-5 and MOF-177 can be observed as well. Mixed linker systems can also regard MOFs with different connecting functionalities, like in the case of $M_2(BDC)_2(DABCO)$ [129]. In this kind of structure the single 2D planes consisting of the metallic clusters connected by H_2BDC linker are stacked one above another and additionally linked by the additional amino functionalized struts – 1,4-diazabicyclo[2.2.2] octane (DABCO), creating a MOF of characteristic pillared-layer architecture.

In several cases the pre-synthetical approach of MOFs modification can be combined with a post-synthetical approach, as a method of the preliminary preparation of structure for the further modification. For example, in this manner, 4,4′-biphenyl dicarboxylic acid (H_2BPDC) – linker of UiO-67 – can be partially replaced with its pyridine derivative. The particular structure of 2,2′-bipyridine-5,5′-dicarboxylic acid (H_2BPYDC) allows for coordinative functionalization using the additional nitrogen atoms present in the aromatic rings of single linker. After the synthesis, different metal

complexes like for example ruthenium or iridium pentamethylcyclopentadienyl can be conjugated with the structure [130] targeting the widening of the range of absorbed light by the resulting MOF.

4.3.2. Synthetical modification

Like in the case of different materials, the appropriately selected conditions of the synthesis can influence the resulting material, especially the size of the forming particles, their shape or polydispersity. In addition to changing the elementary synthesis parameters (temperature, time, solvent, molar ratio of precursors or the type of precursors), in the case of MOFs, different modulating substances can also be also introduced into its environment.

As it was aforementioned, the reaction time varies greatly from several minutes [87], hours [75] or even few days [94]. Individually selected time of the reaction may significantly influence the morphology of forming structure of MOF. For example, with the increasing time of reaction, the structure's shape and size can change from narrow nanobelts, *via* nanosheets, to finally take a form of the microscopic crystals [131]. Another essential factor is the temperature of the reaction. In many cases, the crystallization temperature window is very wide, ranging room temperature (RT) [132] to different elevated temperatures between 70 and 185 °C [106,133]. For several MOFs the synthesis performed at higher temperatures, can lead to formation of product with disturbed morphology (for example visible as evident rounding of edges and corners) and the formation of by-products can be observed [106,133]. In turn, the change of the solvents often results in the variation of the MOF morphology, and, in some cases, formation of MOF with different crystal structure than original [134]. The type of the metal precursor and its ratio with linker is also a significant factor. The type of metal precursor can affect the overall formation of the product, its crystallinity, as well as phase purity and its morphology as well as the development of surface area and the resulting application potential [76,106]. Usually, the molar excess of metal precursor to linker is more beneficial in terms of increasing the surface area of MOF than the inverse molar ratio [135].

In case of wide variety of MOFs, addition of small amount of modulator has a positive effect on the formation of crystalline particles instead of amorphous solid. The essential modulators are monocarboxylic acids as well as strong inorganic acids. Among the first mentioned group of acidic modulators, acetic [79], benzoic [79], formic [136] or trifluoroacetic acid [137] can be effectively used (structures shown in Figure 4.7a). Different inorganic mineral acids like hydrochloric acid [138], hydrofluoric acid [139] or nitric acid [94] can also act as strong modulators (Figure 4.7b). Apart from increasing the crystallinity and developing the specific surface area, the presence of balanced amount of acidic modulator in the synthesis environment of MOFs can positively influence the morphology of the forming crystals and prevent their aggregation [79].

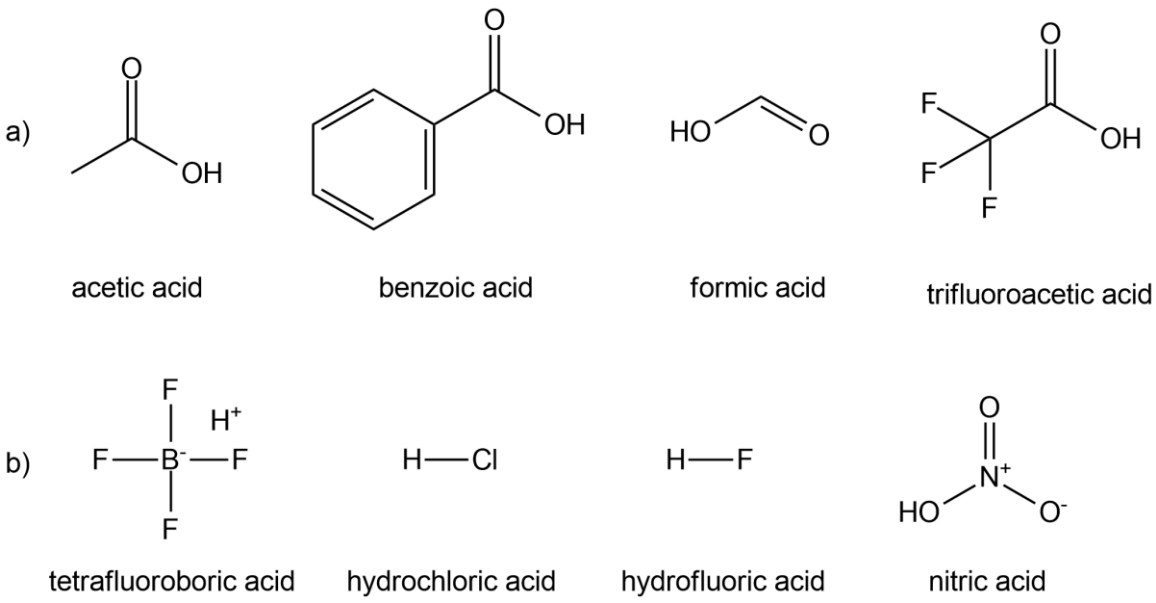


Figure 4.7. Structure of acetic modulators: a) organic, b) inorganic

MOFs morphology can be also controlled by using modulators of alkaline character like sodium salts (formate, acetate [140] etc.), amines (triethylamine (TEA) [140], n-butylamine [141] etc.) or other N-rich organic species (like pyridine [142] or 1-methylimidazole [141]). The presence of such moieties regulates the acid-base balance and interacts with linkers leading to their deprotonation. Similarly to acidic modulators, basic modulators in limited amount can prevent the aggregation of growing crystals and limit their size. The growing content of alkaline modulator, and thus growing pH of the synthesis environment can lead to changes in the morphology of MOFs, however, after crossing a certain limit, it starts to negatively affect the product, making it more amorphous due to very high nucleation rate [143].

Furthermore, the morphology of MOFs can be adjusted by introduction bigger and more complex compounds like surfactants [144–147] or ionic liquids [84,85] to the reaction environment. Depending on the type of the moiety different effects can be expected. Cetyltrimethylammonium bromide (CTAB) [144], polyvinylpyrrolidone (PVP) [145], sodium dodecyl sulfate (SDS) [147] or lauric acid (LA) [146] can be listed as examples of most commonly used surfactants. Selection of a compound with the appropriate structure and properties, as well as its appropriate quantity can affect such aspects as formation of specific crystalline facets, change the shape of forming crystal or alter its size as the nucleation rate gets affected and competitive interactions with the metal precursor occur. Similarly to surfactants, presence of small amounts of ILs in the synthesis medium can affect the morphology and crystallinity of the resulting MOF [148]. By appropriate selection of anion and cation that create the IL, different results can be observed. For example formation of Co-MOF particles with decreasing length-to-width ratio was observed when the side chain length in the cation increased from two carbon atoms ([EMIM]) to sixteen ([HDMIM]) [149]. In turn the use of IL as an emulsion phase for the synthesis can notably increase the S_{BET} (even double it) of forming MOF compared to product obtained by typical hydrothermal approach [150]. Due to high viscosity ILs can be effectively used for ionothermal [88] or electrochemical [84] approach of MOF synthesis,

and thus significantly influence the change in the shape and size of the formed particles. Both surfactants and ILs can also prevent agglomeration of the forming particles as a result of reaction medium viscosity adjustment and creation of the steric hindrance.

A special type of modification, which is defect engineering, concerns intentional formation of defects in the crystal structure. Either missing linker (ML) and missing cluster (MC) defects can be purposely induced [151,152] (Figure 4.8). Such approach is an easy method to influence the structure of MOF especially in terms of modifying the electronic band structure [7]. In order to cause deficiency selected modulators like simple organic acids can be intentionally added to the synthesis medium. Such approach may not only influence the porosity and specific surface area [93], but can also affect the position of HOCO and LUCO, as well as the related width of optical gap [7]. Defects can be also introduced by addition of linker isomers. For example *para*-substituted H_2BDC can be partially exchanged with *meta*-substituted isomer, providing functional cavities, which can be further utilized in post-synthetical modification to bind additional moieties [153].

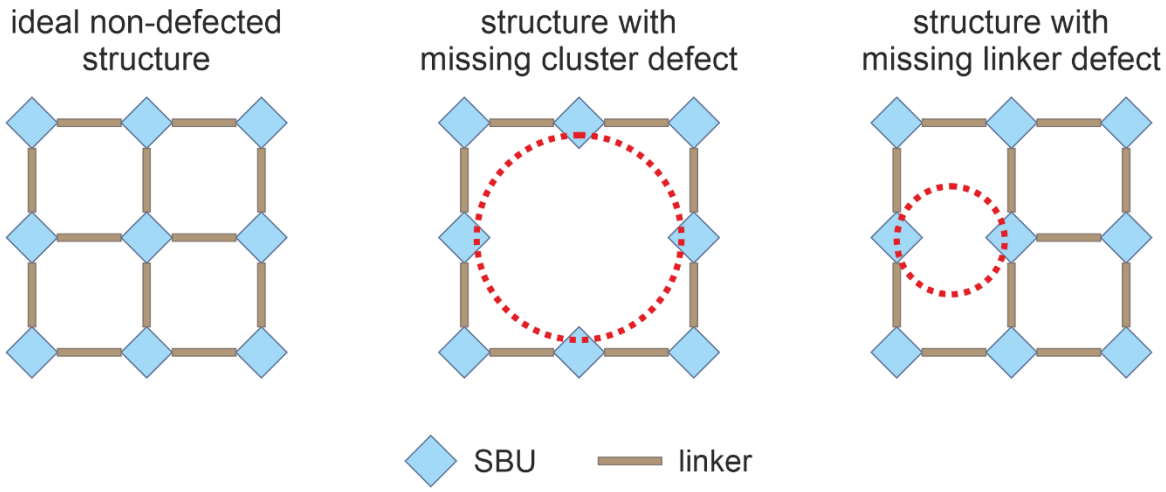


Figure 4.8 Schematical representation of MOF with ideal and defected structure

To modify the properties of MOFs, different nanoparticles (NPs) can be closed inside the pores during synthesis, leading to creation of a composite material of new characteristics. When the guest molecule possesses bigger kinetic diameter than the MOF pores outlets, it can be closed inside of pores of the forming MOF. For example, copper NPs added to the synthesis medium of UiO-66(Zr) can be successfully trapped inside [154]. Such approach however demands using Zr source that will not dissolve the NPs during synthesis and additionally, the before the synthesis the environment should be purged with inert gas. Different approach concerns the encapsulation of metal NPs deposited on metal oxide surface inside MOF [155]. The substrate can simultaneously act as a source of metal for MOF creation, which leads to encapsulation of NPs in the growing MOF. Additionally, by careful selection of synthesis conditions, the NP position can either remain near the interface between the MOF and the substrate or be moved deeper into the MOF (Figure 4.9). This approach was successfully applied for combinations of ZIF-8(Zn) and MIL-53(Al) with Au and Pt NPs and HKUST-1 with Au NPs [155].

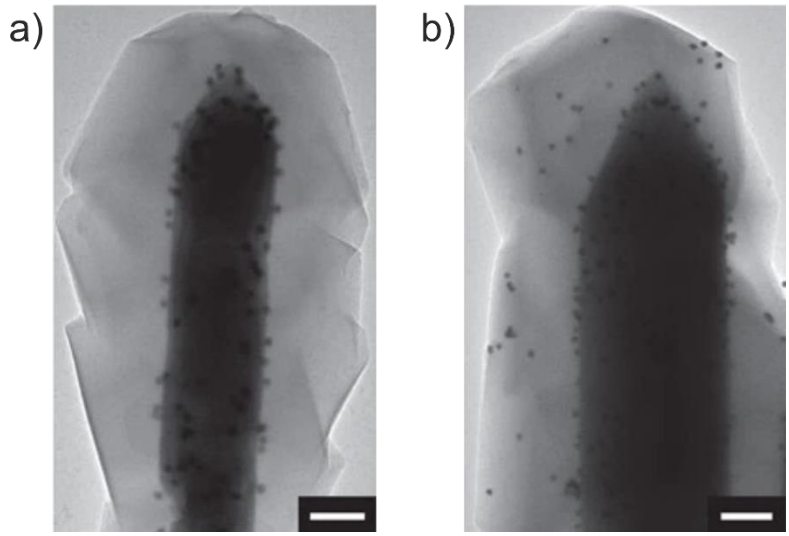


Figure 4.9. TEM images of different location of Au NPs incorporated into ZIF-8(Zn) supported on ZnO depending on synthesis conditions: a) high concentration of linker, b) low concentration of linker. Scale bar represents 100 nm (adapted from [155] under CC-BY-4.0 license).

In turn, when the particles have significantly bigger size than the framework pores the surface of the introduced NPs can be enveloped with net of MOF [156]. Among the few reports MOFs can be combined together with other MOFs *via* synthetical approach to obtain core-shell structures [157–160], Janus particles [161], layered structures [162] or epitaxial materials [163–166].

4.3.3. Post-synthetic modification

The post-synthetical modification of MOFs can include changes of the structure *via* a chemical interaction as well as simple physical binding with other materials. It can be used alone, but can also benefit from the effects of both pre-synthetic and synthetic modifications, and in some cases such prior modification is necessary to carry out the post-synthetical one.

When the pre-synthetical modification of MOF in form of linker functionalization cannot be successfully employed, for example due to competing metal-chelating properties of functional groups attached to adjacent carbon atoms (like hydroxyl [167] or thiol [168], example of which is shown in Figure 4.6), the post-synthetic exchange (PSE) of linkers can be applied instead. In such a case, MOF is dispersed in the solution containing the new linker and further treated as in the case of solvothermal treatment, including the process of purification and activation performed afterwards. Post-synthetic modifications allow also for incorporation of various linkers into the structure of already existing MOF leading to create a new one. For example, the arrangement of PCN-700 framework allows to customize it in three different ways [169]. The mentioned MOF possesses in its structure enough space to build in two additional linkers. PCN-701 and PCN-702 are formed after treatment in appropriate conditions with 1,4-benzedicarboxylic acid and 2',5'-dimethyl-[1,1':4',1''-terphenyl]-4,4''-dicarboxylic acid respectively. Additionally, third MOF – PCN-703 – can be synthesized by addition of H_2BDC to PCN-702, but not the other way around.

Similar PSE procedure as for linker can be also utilized for metals the SBUs, which can be replaced after the synthesis [170]. PSE is especially beneficial for introduction of metals that are problematic to be incorporated directly to the specific MOF. Such a case is, among others, the formation of NH_2-UiO-66 with titanium instead of zirconium [171]. The straightforward creation of NH_2-UiO-66(Ti) is impossible, as other structure is formed instead *i.e.* NH_2-MIL-125(Ti). The post-synthetical exchange usually does not change the morphology or the crystallinity of the MOF, but may result in adjustment of the chosen applicational performance. According to Kim *et al.* it is also possible to exchange both – metals or linkers – between two different MOFs *via* solid-solid interaction [172].

Another modification using chemical interaction with the ready-made MOF is the reaction with the pending functionalities of MOFs. Some of the SBUs, for example in UiO-66 or MOF-808, contain terminal –OH and $–OH_2$ ligands in their structure. These groups can be efficiently exchanged with different organic molecules. L-histidine, 4-imidazole acrylic acid or 5-benzimidazolecarboxylic acid can effectively replace the mentioned functionalities in MOF-808 [173]. In turn, the incorporated pendant molecules can react with metal complexes and thus create an internal subnet. Alternatively, for several MOFs with suitably tight architecture, such complexation with metal can be created directly between two neighboring struts, like in the case of MOF-303(Al) (Figure 4.10). Different metal complexes can be also incorporated directly in place of –OH and $–OH_2$ ligands of SBU [174].

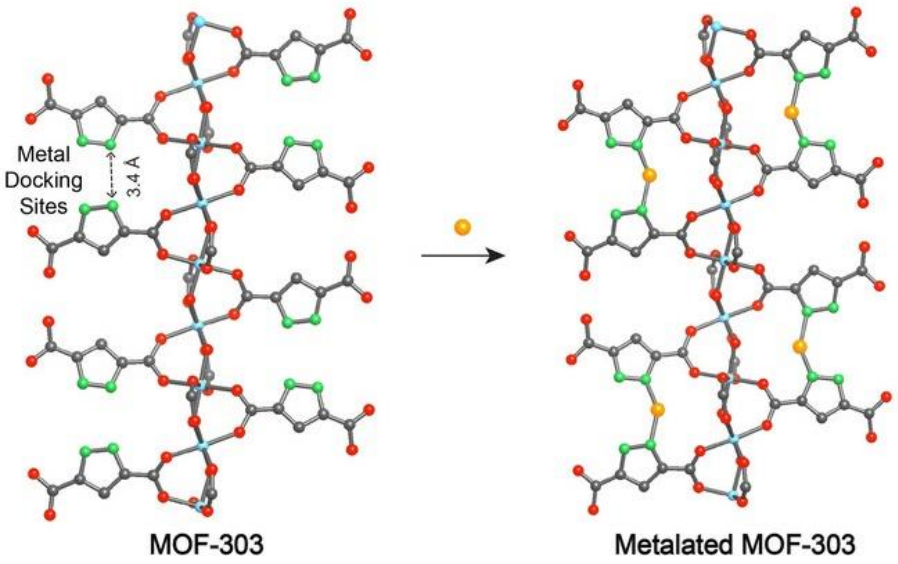


Figure 4.10. Scheme of MOF-303 modification with Cu atoms (reproduced with permission from [175]*)*

Post-synthetical modification can be the continuation of the changes in the structure introduced with previous steps. When portion of the primary linker, for example H_2BDC, possessing carboxylic functionalities in 1,4 position, is replaced with its 1,3 analogue (Figure 4.11), the pending non-coordinated –COOH groups can be further utilized for incorporation of metal complexes [153,176,177]. New coordination sites may also be provided in other manner. For this purpose, amine functionalized linkers of MOFs can be covalently modified during organic reactions. Addition

of for example salicylaldehyde, cyanuric chloride or 2-thiophenecarboxaldehyde to NH_2-UiO-66 can facilitate complexation of molybdenum [178] or copper compounds [179–181]. As an another example of similar approach the pyridine moieties introduced to the structure of UiO-67(Zr) [182,183] or pyrazole moiety in MOF reported by Huxley *et al.* [184] may be also used to bin additional metal site.

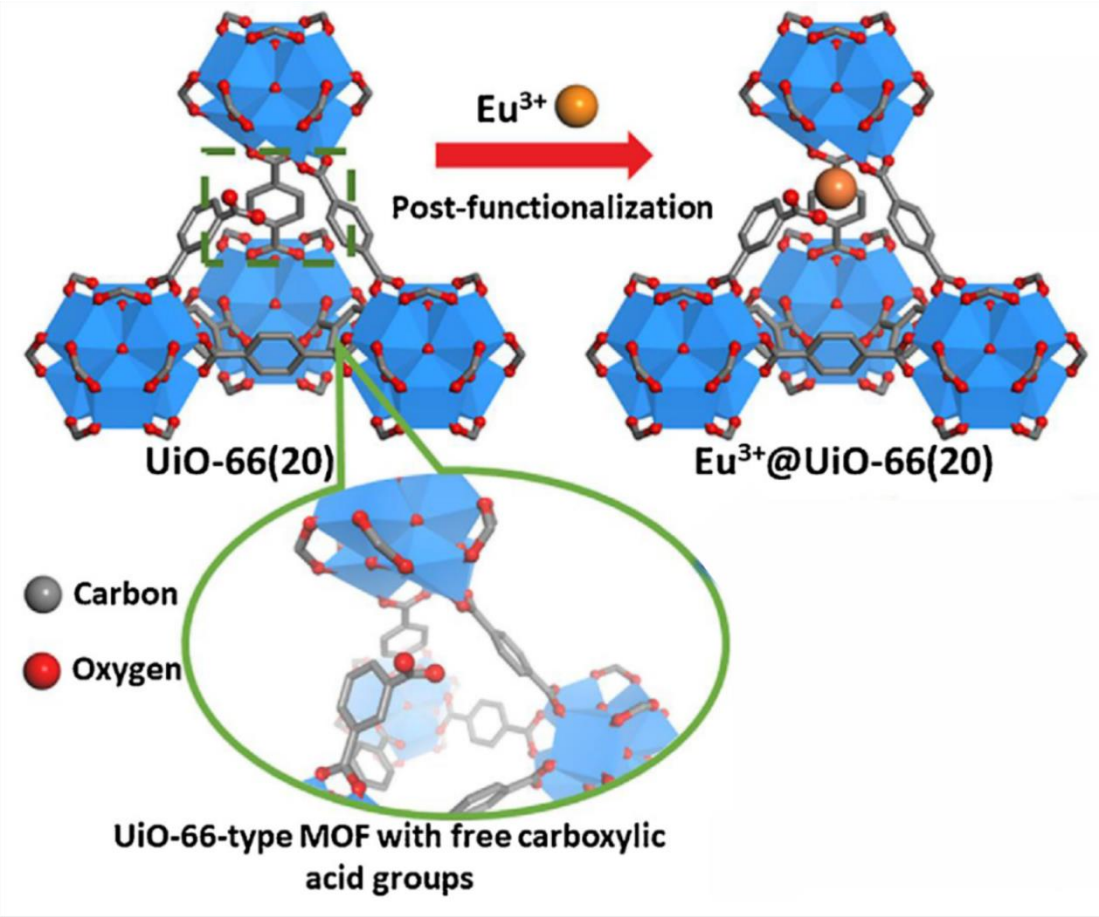


Figure 4.11. Structure of UiO-66(Zr) with intentionally incorporated defects of structure and its post-synthetic metalation with Eu^{3+} (reproduced with permission from [153]*)*

Similarly to synthetical approach of modification, MOF can be combined with NPs. It can result in deposition of smaller particles on MOFs surface (Figure 4.12) [154,185] or with guest entrapment inside the framework [186]. The second possibility is only achievable when the open pores are wide enough to fit guest molecules inside. This type of trapping is useful when the molecule is disturbing the *in situ* formation of MOF. Hybrid materials can be also created by post-synthetical introduction of ILs [187–189]. The ILs can be deposited on the surface and inside of the MOF pores by simple impregnation method. Such approach involves dissolution of IL in low-boiling medium and dispersion of MOF in as prepared mixture. The slurry is stirred at first at RT, followed by slow stirring at temperature enabling the slow evaporation of solvent. Depending on the character of the introduced IL, the as-prepared material can demonstrate alternated applicational properties especially considering sorption properties [190,191].

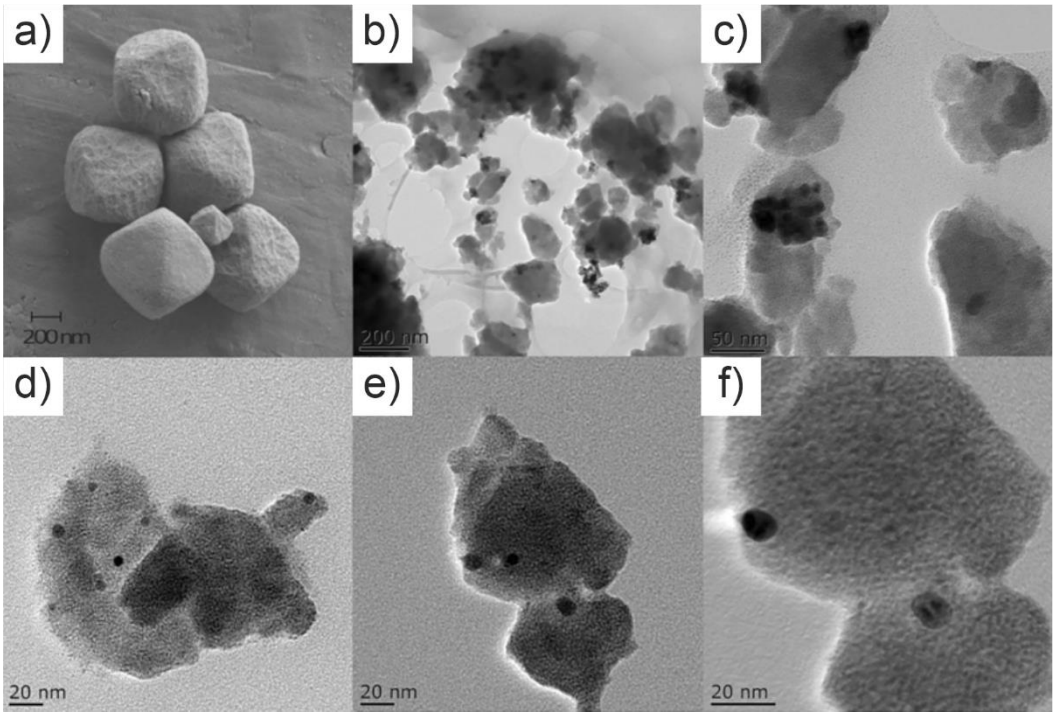


Figure 4.12 MOF-808(Zr): a) pristine (SEM image), b)-f) with embedded Pt NPs (TEM images) (reproduced with permission from [185]*)*

4.4. Application of MOFs

The original and most widespread application of MOFs was the sorption and sensing of gases, not only CO_2, but also for hydrogen, short hydrocarbons, noble gases and others [192]. However, with the growing knowledge about MOFs and the exploration of possibilities of modifying their properties, many new application paths have emerged. Thanks to their unique properties and extraordinary porosity, MOFs are useful in wide variety of applications like capture and degradation of pollutants [193], hydrogen generation [194], drug delivery [195] or energy harvesting and storage [196].

Apart from the light-driven conversion of CO_2, the photocatalytic abilities of MOFs are explored to find an efficient method of capture and degradation of different organic and inorganic pollutants to purify aquatic environments [193]. Next to the topic of limiting the global CO_2 emission, this is an another extremely important issue that needs attention form the science, especially taking into consideration very limited drinking water resources in the world. The problem includes in particular chemicals such as plant protection products, drugs and their metabolites, dyes and surfactants.

The field of medicine and pharmacy is still searching for the drug delivery agents which will be adapted to the individual active substances and that will limit the side effects [195]. Thanks to the possibility of MOF composition selection and further modification of the structure, this group of materials is widely studied. The MOFs would be not only to transport the drug in unchanged state to the target organ, but also to provide the release of the active substance in a regulated manner.

Thanks to the crystalline structure uniformly distributed metallic centers and presence of the aromatic rings, MOFs have also attracted interest in the energy field. Research towards using MOFs for construction of electrodes, batteries or supercapacitors is extensively carried out in order to provide the development of renewable energy sources and lossless storage of the produced current [196]. Apart from that, generation [194] and storage [197] of hydrogen as an alternative fuel is also spreading as a hot topic.

Even a short exploration of literature clearly indicates that there are many research areas that could potentially use MOFs, but they still require research. The topic that deserves a special attention is the development of CO_2. Therefore, a more detailed discussion will be given in terms of CO_2 sorption and photoconversion in the following subsections. An overview of the most important works on these topics is presented in Table 4.1.

Table 4.1. Application of MOFs for CO_2 sorption and photoconversion

Material	Chemical composition and morphology	Preparation method	BET/CO_2 adsorption	Reaction environment	Light source (λ range)	Main product(s)	Efficiency	AQE [%] (λ)	Band gap [eV]	Ref.
UiO-66	Zr-BDC octahedrons	solvothermal	BET=1268 $m^2 \cdot g^{-1}$ CO_2 = 98.9 $cm^3 \cdot g^{-1}$ (0 °C, 1bar)	H_2O vapour V_R = 500 mL m_{cat} = 50 mg gas-solid system	300 W Xe lamp	CH_4 CO	0.6 $\mu mol \cdot g^{-1} \cdot h^{-1}$ 1.0 $\mu mol \cdot g^{-1} \cdot h^{-1}$	n.d.	3.86	[198]
UiO-66/TiO_2	Zr-BDC octahedrons covered with TiO_2 NPs	solvothermal, electrostatic self-assembly process	BET=452 $m^2 \cdot g^{-1}$ CO_2 = 78.9 $cm^3 \cdot g^{-1}$ (0 °C, 1bar)				17.9 $\mu mol \cdot g^{-1} \cdot h^{-1}$ 1.9 $\mu mol \cdot g^{-1} \cdot h^{-1}$		3.32	
UiO-66	Zr-BDC octahedrons	solvothermal	BET=1322 $m^2 \cdot g^{-1}$ CO_2 = 2.22 $mmol \cdot g^{-1}$ (25 °C, 0-100 kPa)	H_2O vapour m_{cat} = 300 mg T = 25 °C gas-solid system	70 W Hg lamp 85 $mW \cdot cm^{-2}$	CH_4 CH_3OH	n.d.	n.d.	3.88	[199]
UiO-66/TiO_2	TiO_2 nanoflower covered with Zr-BDC		BET=410 $m^2 \cdot g^{-1}$ CO_2 = 0.91 $mmol \cdot g^{-1}$ (25 °C, 0-100 kPa)				41.81 $\mu mol \cdot g^{-1} \cdot h^{-1}$ 1.49 $\mu mol \cdot g^{-1} \cdot h^{-1}$	0.075 (n.d.) 0.002 (n.d.)	3.43	
UiO-66	Zr-BDC spheres	solvothermal	L_{SSA}=1610 $m^2 \cdot g^{-1}$ CO_2 = 38.4 $cm^3 \cdot g^{-1}$ (25 °C, 1 bar)	5 mL MeCN, TEOA (4:1 by volume) V_R = 330 mL sample on porous quartzose film	300 W Xe lamp (400 nm > λ > 800 nm)	CO	n.d.	n.d.	n.d.	[200]
UiO-66/C_3N_4	C_3N_4 nanosheets on Zr-BDC	solvothermal, electrostatic self-assembly process	L_{SSA}=1315.3 $m^2 \cdot g^{-1}$ CO_2 = 32.7 $cm^3 \cdot g^{-1}$ (25 °C, 1 bar)				9.9 $\mu mol \cdot g^{-1} \cdot h^{-1}$	n.d.	C_3N_4 2.78	
UiO-66	Zr-BDC rhombic dodecahedrons	solvothermal	BET = 1228.9 $m^2 \cdot g^{-1}$ CO_2 = 2.96 $mmol \cdot g^{-1}$ (25 °C, 1 bar)	5% water vapour V_R = 206 mL m_{cat} = 40 mg (on fiberglass membrane)	UV–vis-IR 650 $mW \cdot cm^{-2}$	CO CH_4	~6 $\mu mol \cdot g^{-1} \cdot h^{-1}$ ~0.25 $\mu mol \cdot g^{-1} \cdot h^{-1}$	n.d.	3.05	[201]
UiO-66/B_2S_3	Zr-BDC rhombic dodecahedrons covered with B_2S_3		BET = 1309.4 $m^2 \cdot g^{-1}$ CO_2 = 2.6 $mol \cdot g^{-1}$ (25 °C, 1 bar)				25.60 $\mu mol \cdot g^{-1} \cdot h^{-1}$ 0.25 $\mu mol \cdot g^{-1} \cdot h^{-1}$	n.d.	B_2S_3 1.31	
UiO-66	Zr-BDC octahedrons	solvothermal	BET = 1353.5 $m^2 \cdot g^{-1}$	50 mL H_2O m_{cat} = 30 mg T = 5 ºC liquid-solid system	300 W Xe lamp	CO	3.88 $\mu mol \cdot g^{-1} \cdot h^{-1}$	n.d.	3.82	[202]
UiO-66/$Bi_4O_5Br_2$	$Bi_4O_5Br_2$ stereoscopic flowers covered with Zr-BDC octahedrons	electronic assembly	BET = 211.12 $m^2 \cdot g^{-1}$				8.35 $\mu mol \cdot g^{-1} \cdot h^{-1}$		$Bi_4O_5Br_2$: 2.44	
UiO-66	Zr-BDC cubic plates	solvothermal	n.d..	15 mL MeCN, TEOA (5:1 by volume) V_R = 44 mL m_{cat} = 25 mg 3 cycles of freeze–pump–thawed liquid-solid system	Xe 200 W Arc lamp	$HCOO^-$	2.9 µmol (after 12 h)	n.d.	n.d.	[203]
NH_2-UiO-66	Zr-(BDC-NH_2) spheres		n.d.				9.5 µmol (after 12 h)	n.d.	n.d.	

Material	Chemical composition and morphology	Preparation method	BET/CO_2 adsorption	Reaction environment	Light source (λ range)	Main product(s)	Efficiency	AQE [%] (λ)	Band gap [eV]	Ref.
			n.d.	15 mL MeCN, DEA (5:1 by volume) V_R = 44 mL m_{cat} = 25 mg 3 cycles of freeze–pump–thawed liquid-solid system			16.9 μmol (after 12 h)	n.d.	n.d.	
NH_2-UiO-66	Zr-(BDC-NH_2) octahedrons with no defects	solvothermal	BET = 517.53 $m^2 \cdot g^{-1}$ CO_2 = 38.53 $cm^3 \cdot g^{-1}$ (25 °C, 1 bar)	2 mL TEOA m_{cat} = 2 mg (on glass fiber) gas-solid system	300 W Xe lamp (λ > 400 nm)	CO	~6.5 $\mu mol \cdot g^{-1} \cdot h^{-1}$	n.d.	2.78	[7]
NH_2-UiO-66-LV	defected Zr-(BDC-NH_2) octahedrons		BET = 920.59 $m^2 \cdot g^{-1}$ CO_2 = 63.46 $cm^3 \cdot g^{-1}$ (25 °C, 1 bar)				30.5 $\mu mol \cdot g^{-1} \cdot h^{-1}$	0.9 (n.d.)	2.70	
NH_2-UiO-66	Zr-(BDC-NH_2)	solvothermal	BET = 778 $m^2 \cdot g^{-1}$ CO_2 ~ 68 $cm^3 \cdot g^{-1}$ (1 atm, 0 °C)	60 mL MeCN, TEOA (5:1 by volume) m_{cat} = 50 mg liquid-solid system	500 W Xe lamp (800 nm > λ > 400 nm)	$HCOO^-$	26.4 $\mu mol \cdot g^{-1} \cdot h^{-1}$	n.d.	n.d.	[127]
Mixed-NH_2-UiO-66	Zr-(BDC-NH_2)-(BDC-$(NH_2)_2$)		BET = 734 $m^2 \cdot g^{-1}$ CO_2 = 71 $cm^3 \cdot g^{-1}$ (1 atm, 0 °C)				41.4 $\mu mol \cdot g^{-1} \cdot h^{-1}$	n.d.	n.d.	
NH_2-UiO-66(Zr/Ti)	Zr-(BDC-NH_2)-(BDC-$(NH_2)_2$) octahedrons	solvothermal, post-synthetic exchange	BET = 1004 $m^2 \cdot g^{-1}$	5 mL MeCN, TEOA (4:1 = by volume)+0.1M BNAH m_{cat} = 5 mg liquid-solid system	300 W Xe lamp (420 nm < λ < 800 nm)	HCOOH	1058 $\mu mol \cdot g^{-1} \cdot h^{-1}$	n.d.	2.67	[171]
NH_2-UiO-66	Zr-(BDC-NH_2)	solvothermal	BET = 778 $m^2 \cdot g^{-1}$ CO_2 = 68 $cm^3 \cdot g^{-1}$ (0 °C, 1 bar)	60 mL MeCN, TEOA (5:1 by volume) m_{cat} = 50 mg liquid-solid system	300 W Xe lamp (420 nm > λ > 800 nm)	HCOOH	0.34 $mmol \cdot mol^{-1} \cdot h^{-1}$	n.d.	n.d.	[110]
NH_2-UiO-66(Zr/Ti)	Zr/Ti-(BDC-NH_2)	post-synthetic exchange	BET = 787 $m^2 \cdot g^{-1}$ CO_2 = 83 $cm^3 \cdot g^{-1}$ (0 °C, 1 bar)				0.58 $mmol \cdot mol^{-1} \cdot h^{-1}$	n.d.	n.d.	
NH_2-UiO-66	Zr-(BDC-NH_2) octahedrons	solvothermal	BET = 860 $m^2 \cdot g^{-1}$	5.1 mL MeCN, TEOA (50:1 by volume) V_R = 10 mL m_{cat} = 50 mg liquid-solid system	450 W Xe lamp (Solar Simulator)	$HCOO^-$	99 μmol after 17 h	n.d.	2.79	[121]
$(Zr_{0.87}/Ti_{0.13})$ UiO-66-NH_2	Zr/Ti-(BDC-NH_2) octahedrons	post-synthetic exchange	BET = 750 $m^2 \cdot g^{-1}$				145 μmol after 17 h	n.d.	2.75	
$(Zr_{0.41}/Ti_{0.59})$ UiO-66-NH_2		solvothermal	BET = 650 $m^2 \cdot g^{-1}$				151 μmol after 17 h	n.d.	2.61	
NH_2-UiO-66	Zr-(BDC-NH_2) octahedrons	solvothermal	BET = 774 $m^2 \cdot g^{-1}$	H_2O vapour	300 W Xe lamp	CO	1.3 $\mu mol \cdot g^{-1} \cdot h^{-1}$	0.05 (420 nm)	2.79	[204]

Material	Chemical composition and morphology	Preparation method	BET/CO_2 adsorption	Reaction environment	Light source (λ range)	Main product(s)	Efficiency	AQE [%] (λ)	Band gap [eV]	Ref.
15% NH_2-UiO-66 /TTCOF	Zr-(BDC-NH_2) octahedrons embedded on the surface of TTCOF nanofibers		CO_2 = 70 $cm^3 \cdot g^{-1}$ (1 bar) BET = 900 $m^2 \cdot g^{-1}$ CO_2 = 60 $cm^3 \cdot g^{-1}$ (1 bar)	V_R = 250 mL m_{cat} = 5 mg	(λ > 420 nm)		6.56 $\mu mol \cdot g^{-1} \cdot h^{-1}$	0.21 (420 nm)	2.74	
NH_2-UiO-66	Zr-(BDC-NH_2) octahedrons	solvothermal	n.d.	150 µL H_2O m_{cat} = 1 mg (coated glass)	LED	CO	71 $\mu mol \cdot g^{-1} \cdot h^{-1}$	0.140 (350 nm)	2.74	[205]
NH_2-UiO-66/CdS	Zr-(BDC-NH_2) octahedrons mixed with spherical CdS		CO_2 = 7.3 $cm^3 \cdot g^{-1}$ (25 °C, 1 bar)				280.5 $\mu mol \cdot g^{-1} \cdot h^{-1}$	0.472 (350 nm)	2.37	
NH_2-UiO-66	chitosan membrane containing Zr-(BDC-NH_2) octahedrons	solvothermal, casting and evaporation	n.d.	18 mL MeCN, H_2O, TEOA (3:2:1 by volume)+10 mg bipyridine V_R = 100 mL m_{cat} = 16.5 mg liquid-solid system	300 W Xe lamp (400 nm > λ > 760 nm)	CO HCOOH	21.25 $\mu mol \cdot g^{-1} \cdot h^{-1}$, HCOOH not detected	n.d.	n.d.	[206]
CdS/NH_2-UiO-66	chitosan membrane containing Zr-(BDC-NH_2) octahedrons and CdS rods		powder: CO_2 = 28.1 $cm^3 \cdot g^{-1}$ (25 °C, 1 bar) membrane: CO_2 = 37.7 $cm^3 \cdot g^{-1}$ (25 °C, 1 bar)				87 $\mu mol \cdot g^{-1} \cdot h^{-1}$, HCOOH not detected	n.d.	n.d.	
NH_2-UiO-66	Zr-(BDC-NH_2) octahedrons	solvothermal	BET = 820 $m^2 \cdot g^{-1}$ CO_2 = 28 $cm^3 \cdot g^{-1}$ (1 bar)	2 mL H_2O m_{cat} = 15 mg (on glass microfiber) T = 25 °C	300 W Xe lamp (λ > 420 nm)	CO	~14 $\mu mol \cdot g^{-1} \cdot h^{-1}$	n.d.	2.89	[207]
NH_2-UiO-66/In	In/Zr-(BDC-NH_2) octahedrons		BET = 689 $m^2 \cdot g^{-1}$ CO_2 = 26 $cm^3 \cdot g^{-1}$ (1 bar)				37.58 $\mu mol \cdot g^{-1} \cdot h^{-1}$	0.21 (420 nm)	2.77	
NH_2-UiO-66	Zr-(BDC-NH_2)	solvothermal	BET = 871 $m^2 \cdot g^{-1}$ CO_2 = 1.3 $mmol \cdot g^{-1}$ (25 °C, 1 bar)	V_R = 132 mL gas-solid system	150 W Xe arc lamp (λ > 325 nm)	CO	1.5 $\mu mol \cdot g^{-1} \cdot h^{-1}$	n.d.	2.70	[208]
NH_2-UiO-66/TiO_2	composite of Zr-(BDC-NH_2) and TiO_2	solvothermal	BET = 202 $m^2 \cdot g^{-1}$ CO_2 = 0.36 $mmol \cdot g^{-1}$ (25 °C, 1 bar)				4.24 $\mu mol \cdot g^{-1} \cdot h^{-1}$	n.d.	TiO_2: 3.20	
UiO-66-NH_2	Zr-(BDC-NH_2) octahedrons	solvotermal	BET = 1268 $m^2 \cdot g^{-1}$ CO_2 = ~30 $cm^3 \cdot g^{-1}$ (25 °C, 1 bar)	2 mL TEOA m_{cat} = 3 mg (on glass fiber) T = 50 °C	300 W Xe lamp (λ > 400 nm) 400 $mW \cdot cm^{-2}$	CO	6.1 $\mu mol \cdot g^{-1} \cdot h^{-1}$	n.d.	2.6	[156]
Cu_2O@Cu@ UiO-66-NH_2	Cu_2O@Cu nanocubes covered with Zr-(BDC-NH_2)		BET = 212 $m^2 \cdot g^{-1}$ CO_2 = ~7 $cm^3 \cdot g^{-1}$ (25 °C, 1 bar)			CO CH_4	20.9 µ $mol \cdot g^{-1} \cdot h^{-1}$ 8.3 $\mu mol \cdot g^{-1} \cdot h^{-1}$	0.101 (n.d.) 0.161 (n.d.)	Cu_2O: 2.18	
UiO-66-NH_2-2ABA	Zr-(BDC-NH_2)(2ABA)	solvothermal	BET = 740.24 $m^2 \cdot g^{-1}$ CO_2 = 47.46 $cm^3 \cdot g^{-1}$ (25 °C, 1 bar)	m_{cat} = 2 mg (on glass fibre) gas-solid system	300 W Xe arc lamp (λ > 400 nm) 400 $mW \cdot cm^{-2}$	CO	17.5 $\mu mol \cdot g^{-1} \cdot h^{-1}$	$1.63 \cdot 10^{-4}$ (450 nm) $1.87 \cdot 10^{-4}$ (700 nm)	2.12	[8]
UiO-66-NH_2	Zr-(BDC-NH_2)	solvothermal	BET = 618.5 $m^2 \cdot g^{-1}$ CO_2 = ~25 $cm^3 \cdot g^{-1}$ (0 °C, 1 bar)	48 mL DMF, H_2O, TEOA	300 W Xe arc lamp (λ > 400 nm)	HCOOH	23.13 $\mu mol \cdot g^{-1} \cdot h^{-1}$	n.d.	2.94	[209]

Material	Chemical composition and morphology	Preparation method	BET/CO_2 adsorption	Reaction environment	Light source (λ range)	Main product(s)	Efficiency	AQE [%] (λ)	Band gap [eV]	Ref.
30 wt % PTPA/UiO-66-NH_2	Zr-(BDC-NH_2) hexahedrons distributed on PTPA		BET = 333.5 $m^2 \cdot g^{-1}$ CO_2 = ~85 $cm^3 \cdot g^{-1}$ (0 °C, 1 bar)	(40:3:5 by volume) m_{cat} = 20 mg liquid-solid system			38.25 $\mu mol \cdot g^{-1} \cdot h^{-1}$	n.d.	2.87	
UIO-66-NH_2/2 wt% CNTs	Zr-(BDC-NH_2) octahedrons on CNT tubes	solvothermal	BET = 642.5 $m^2 \cdot g^{-1}$	48 mL DMF, H_2O, TEOA (40:3:5 by volume) liquid-solid system	500 W Xe lamp (λ > 400 nm)	HCOOH	18.2 μmol	n.d.	n.d.	[210]
NUZ/HGN-35%	Zr-(BDC-NH_2) crystals dispersed on holey g-C_3N_4	solvothermal	BET = 335 $m^2 \cdot g^{-1}$	21 mL TEOA, H_2O (1:20 by volume) m_{cat} = 10 mg liquid-solid system	300 W Xe arc lamp (cutoff 400 nm) 70 $mW \cdot cm^{-2}$	CO	31.6 $\mu mol \cdot g^{-1} \cdot h^{-1}$	0.26 (380 nm)	NUZ: 2.58 HGN: 2.1	[211]
UiO-66-NH_2	Zr-(BDC-NH_2) crystals	microwave-assisted	BET = 968.9 $m^2 \cdot g^{-1}$	48 mL DMF, H_2O, TEOA (40:3:5 by volume) m_{cat} = 20 mg liquid-solid system	300 W Xe lamp (λ > 410 nm)	HCOOH	38.75 $\mu mol \cdot g^{-1} \cdot h^{-1}$	n.d.	2.73	[212]
UiO-66-NH_2/GR	Zr-(BDC-NH_2) crystals dispersed on graphene	microwave-assisted	BET = 791.2 $m^2 \cdot g^{-1}$ CO_2 = 73 $cm^3 \cdot g^{-1}$ (0 °C, 1 bar)				418.75 $\mu mol \cdot g^{-1} \cdot h^{-1}$	n.d.	2.64	
		hydrothermal	n.d.				201.25 $\mu mol \cdot g^{-1} \cdot h^{-1}$	n.d.	n.d.	
		mechanical	n.d.				118.75 $\mu mol \cdot g^{-1} \cdot h^{-1}$	n.d.	n.d.	
NU66	Zr-(BDC-NH_2) octahedrons	solvothermal	BET = 712.08 $m^2 \cdot g^{-1}$ CO_2 = 2.25 $cm^3 \cdot g^{-1}$ (0 °C, 1 bar)	100 mL H_2O m_{cat} = 50 mg T = 25 °C liquid-solid system	300 W Xe-arc lamp 3 AM 1.5 G filter (solar light)	CO CH_4	~10 $\mu mol \cdot g^{-1}$ ~3.5 $\mu mol \cdot g^{-1} \cdot h^{-1}$	n.d.	2.81	[213]
8% NU66/CIS	porous octahedrons of Zr-(BDC-NH_2) anchored on flowerlike 3D-microspheres of $CdIn_2S_4$	solvothermal, hydrothermal	BET = ~29.16 $m^2 \cdot g^{-1}$ CO_2 = ~1.0 $cm^3 \cdot g^{-1}$ (0 °C, 1 bar)				11.24 $\mu mol \cdot g^{-1} \cdot h^{-1}$ 2.92 $\mu mol \cdot g^{-1} \cdot h^{-1}$	n.d.	CIS: 2.05	
UiO-66-NH_2	Zr-(BDC-NH_2)	solvothermal	BET = 823 $m^2 \cdot g^{-1}$	50.1 mL H_2O, TEOA (500:1 by volume) m_{cat} = 100 mg T = 10 °C liquid-solid system	300 W Xe lamp (λ > 400 nm)	CH_3OH CH_3CH_2OH	trace	n.d.	n.d.	[214]
Cu SAs/UiO-66-NH2	Cu single atoms on Zr-(BDC-NH_2)	photodeposition	BET = 856.5 $m^2 \cdot g^{-1}$				5.33 $\mu mol \cdot g^{-1} \cdot h^{-1}$ 4.22 $\mu mol \cdot g^{-1} \cdot h^{-1}$	n.d.	n.d.	
Cu NPs/UiO-66-NH2	Cu NPs on Zr-(BDC-NH_2)	mixing (impregnation)	BET = 828.7 $m^2 \cdot g^{-1}$				~ 2 $\mu mol \cdot g^{-1} \cdot h^{-1}$ ~ 1 $\mu mol \cdot g^{-1} \cdot h^{-1}$	n.d.	n.d.	
Ir/UiO-66-NH_2	Ir single atoms on Zr-(BDC-NH_2)	hydrothermal	n.d.	50 mL H_2O, iPrOH (4:1 by volume) m_{cat} = 15 mg liquid-solid system	300 W Xe lamp (λ > 420 nm)	HCOOH	0.51 $mmol \cdot g^{-1} \cdot h^{-1}$	2.51 (420 nm)	n.d.	[215]

Material	Chemical composition and morphology	Preparation method	BET/CO_2 adsorption	Reaction environment	Light source (λ range)	Main product(s)	Efficiency	AQE [%] (λ)	Band gap [eV]	Ref.
UiO-66-CAT-Cr	$Zr_6O_4(OH)_4(BDC)_6$ partially exchanged with H_2-(BDC-$(OH)_2$) metalated with Cr	PSE and PSM	n.d.	MeCN, TEOA (4:1 by volume)+0.1 M BNAH V = 5 mL m_{cat} = 5 mg liquid-solid system	300 W Xe lamp (420 nm < λ < 800 nm) 100 $mW·cm^{-2}$	HCOOH	~8.6 $μmol·h^{-1}$	1.83 (450 nm)	n.d.	[167]
UiO-66-CAT-Ga	$Zr_6O_4(OH)_4(BDC)_6$ partially exchanged with H_2-(BDC-$(OH)_2$) further metalated with Ga		n.d.				~4.8 $μmol·h^{-1}$	1.17 (450 nm)	n.d.	
MOF-525	$Zr_6O_4(OH)_4(TCPP\text{-}H_2)_3$	-	BET = 2127.7 $m^2·g^{-1}$ CO_2 = 25.3 $cm^3·g^{-1}$ (1 bar)	MeCN, TEOA (4:1 by volume) V = 2 mL m_{cat} = 2 mg on porous quartzose	300 W Xe lamp (400 nm < λ < 800 nm)	CO, CH_4	64.02 $μmol·g^{-1}·h^{-1}$ 6.2 $μmol·g^{-1}·h^{-1}$	n.d.	n.d.	[216]
MOF-525-Co	$Zr_6O_4(OH)_4(TCPP\text{-}H_2)_3$ modified with Co	Post-metalation	BET = 1317.8 $m^2·g^{-1}$ CO_2 = 33.6 $cm^3·g^{-1}$ (1 bar)				200.6 $μmol·g^{-1}·h^{-1}$ 36.76 $μmol·g^{-1}·h^{-1}$	n.d.	n.d.	
MOF-525-Zn	$Zr_6O_4(OH)_4(TCPP\text{-}H_2)_3$ modified with Zn		BET = 1264.2 $m^2·g^{-1}$ CO_2 = 28.1 $cm^3·g^{-1}$ (1 bar)				111.7 $μmol·g^{-1}·h^{-1}$ 11.635 $μmol·g^{-1}·h^{-1}$	n.d.	n.d.	
AD-MOF-1	$[Co_2(HAD)_2(AD)_2(BA)]·DMF·2H_2O$	solvothermal	CO_2 = 52.15 $cm^3·g^{-1}$ (25 °C, 1 bar)	30 mL MeCN, H_2O, 2 mL TIPA m_{cat} = 5 mg T = 30 °C	300 W Xe lamp (420 nm < λ < 800 nm)	HCOOH	179 $μmol·g^{-1}·h^{-1}$	n.d.	1.76	[217]
AD-MOF-2	$[Co_2(HAD)_2(AD)_2(IA)_2]·DMF$		CO_2 = 41.75 $cm^3·g^{-1}$ (25 °C, 1 bar)				443.2 $μmol·g^{-1}·h^{-1}$	n.d.	1.52	
NNU-28	$Zr_6O_4(OH)_4(L)_6$	solvothermal	BET = 1490 $m^2·g^{-1}$ CO_2 = 33.4 $cm^3·g^{-1}$ (25 °C, 1 atm), 63.4 $cm^3·g^{-1}$ (0 °C, 1 atm)	60 mL MeCN, TEOA (30:1 by volume) m_{cat} = 50 mg	300 W Xe lamp (420 nm < λ < 800 nm)	$HCOO^-$	183.3 $μmol·mmol_{MOF}^{-1}·h^{-1}$	n.d.	~5	[218]
NNU-29	$TBA_5[P_2Mo_{16}{}^{V}Mo_8{}^{VI}O_{71}(OH)_9Zn_8(L)_4$ modified by Ru-based photosensitizer	solvothermal	n.d.	50 mL H_2O, TEOA (4:1 by volume) m_{cat} = 10 mg V_R = 100 mL T = 20 °C	300 W Xe lamp (420 nm < λ < 800 nm)	$HCOO^-$	220 $μmol·g^{-1}·h^{-1}$	n.d.	1.67	[219]
MOF-Co	$\{Co_3(TCA)_2(DPE)_3(H_2O)_6\}_n$	solvothermal	CO_2 = 40.35 $cm^3·g^{-1}$ (25 °C, 1 bar)	MeCN, H_2O, TIPA (13:1:1 by volume) Ru-based photosensitizer V_R = 100 mL m_{cat} = 5 mg T = 25 °C	300 W Xe lamp (420 nm ≤ λ ≤ 800 nm)	CO, H_2	1140 $μmol\ g^{-1}·h^{-1}$	n.d.	2.02	[220]
MOF-Cu	$\{Cu_3(TCA)_2(DPE)_3(H_2O)_3\}_n$		CO_2 = 34 $cm^3·g^{-1}$ (25 °C, 1 bar)				68 $μmol\ g^{-1}·h^{-1}$	n.d.	1.77	
MOF-Ni	$\{Ni_3(TCA)_2(DPE)_3(H_2O)_6\}_n$		CO_2 = 38.87 $cm^3·g^{-1}$ (25 °C, 1 bar)				371 $μmol\ g^{-1}·h^{-1}$	$5.3·10^{-3}$ (420 nm)	1.50	
ZIF-8	$Zn_6(mIm)_{12}$ nanocrystals	solvothermal	BET = 1160.1 $m^2·g^{-1}$ CO_2 = 34.5 $cm^3·g^{-1}$ (0 °C, 1 bar),	100 mL of 0.1M Na_2SO_3 aqueous solution m_{cat} = 200 mg	500 W Xe lamp	CH_3OH	0.14 $μmol·g^{-1}·h^{-1}$	n.d.	n.d.	[221]
ZIF-8/Zn_2GeO_4	Zn_2GeO_4 nanorods decorated with $Zn_6(mIm)_{12}$	ZIF-8 growth on Zn_2GeO_4	BET = 319.5 $m^2·g^{-1}$				0.22 $μmol·g^{-1}·h^{-1}$	n.d.	n.d.	

Material	Chemical composition and morphology	Preparation method	BET/CO_2 adsorption	Reaction environment	Light source (λ range)	Main product(s)	Efficiency	AQE [%] (λ)	Band gap [eV]	Ref.
			CO_2 = 15.5 $cm^3 \cdot g^{-1}$ (0 °C, 1 bar)							
Co-ZIF-9	$Co(PhIM)_2$ modified by Ru-based photosensitizer	solvothermal	n.d.	6 mL MeCN, H_2O, TEOA (4:1:1 by volume) T = 20 °C V_R = 80 mL	Xe lamp (>420 nm)	CO	41.8 µmol (after 30 min)	1.48 (420 nm)	n.d.	[222]
NH_2-MIL-125(Ti)	$Ti_8O_8(OH)_4(BDC\text{-}NH_2)_6$	solvothermal	BET = 1302 $m^2 \cdot g^{-1}$ CO_2 = 132.2 $cm^3 \cdot g^{-1}$ (0 °C, 1 bar)	30 mL MeCN, TEOA (5:1 by volume) m_{cat} = 50 mg	500 W Xe lamp (420 nm < λ < 800 nm)	$HCOO^-$	16.3 $\mu mol \cdot g^{-1} \cdot h^{-1}$	n.d.	n.d.	[223]
MIL-101(Fe)	$Fe_3OH(H_2O)_2O[(BDC)]_3$	hydrothermal	CO_2 = 26.4 $cm^3 \cdot g^{-1}$ (0 °C, 1 bar)	60 mL MeCN, TEOA (5:1 by volume) m_{cat} = 50 mg	300W Xe lamp (420 nm < λ < 800 nm)	$HCOO^-$	147.5 $\mu mol \cdot g^{-1} \cdot h^{-1}$	0.8 (450 nm)	n.d.	[224]
NH_2-MIL-101(Fe)	$NH_2\text{-}Fe_3OH(H_2O)_2O[(BDC)]_3$		CO_2 = 34.0 $cm^3 \cdot g^{-1}$ (0 °C, 1 bar)				445 $\mu mol \cdot g^{-1} \cdot h^{-1}$	1.3 (450 nm)	n.d.	
MIL-53(Fe)	Fe(OH)(BDC)		CO_2 = 13.5 $cm^3 \cdot g^{-1}$ (0 °C, 1 bar)				74.25 $\mu mol \cdot g^{-1} \cdot h^{-1}$	n.d.	n.d.	
NH_2-MIL-53(Fe)	$Fe(OH)(NH_2\text{-}BDC)$		CO_2 = 20.0 $cm^3 \cdot g^{-1}$ (0 °C, 1 bar)				116.5 $\mu mol \cdot g^{-1} \cdot h^{-1}$	n.d.	n.d.	
MIL-88B(Fe)	$Fe_3O(BDC)_3(OH) \cdot nH_2O$		CO_2 = 10.4 $cm^3 \cdot g^{-1}$ (0 °C, 1 bar)				22.5 $\mu mol \cdot g^{-1} \cdot h^{-1}$	n.d.	n.d.	
NH_2-MIL-88B(Fe)	$Fe_3O(NH_2\text{-}BDC)_3(OH) \cdot nH_2O$		CO_2 = 14.4 $cm^3 \cdot g^{-1}$ (0 °C, 1 bar)				75 $\mu mol \cdot g^{-1} \cdot h^{-1}$	n.d.	n.d.	
MIL-101(Cr)	$Cr_3OH(H_2O)_2O(BDC)_3$	hydrothermal	BET = 3126.5 $m^2 \cdot g^{-1}$ CO_2 = 3.03 $mmol \cdot g^{-1}$ (0 °C, 1 bar)	3 mL H_2O, TEOA (1:1 by volume) m_{cat} = 5 mg on a quartz membrane T = 20 °C	n.d.	CO, CH_4	8.3 $\mu mol \cdot g^{-1} \cdot h^{-1}$ 1.7 $\mu mol \cdot g^{-1} \cdot h^{-1}$	n.d.	n.d.	[225]
MIL-101(Cr)-SO_3H	$Cr_3OH(H_2O)_2O(SO_3H\text{-}BDC)_3$		BET = 1936.9 $m^2 \cdot g^{-1}$ CO_2 = 2.07 $mmol \cdot g^{-1}$ (0 °C, 1 bar)				21.7 $\mu mol \cdot g^{-1} \cdot h^{-1}$ 1.3 $\mu mol \cdot g^{-1} \cdot h^{-1}$	n.d.	n.d.	
MIL-101(Cr)-DETA	DETA impregned $Cr_3OH(H_2O)_2O(SO_3H\text{-}BDC)_3$	PSM (impregnation)	CO_2 = 1.73 $mmol \cdot g^{-1}$ (0 °C, 1 bar)				n.d.	n.d.	n.d.	
MIL-101(Cr)-TETA	TETA impregned $Cr_3OH(H_2O)_2O(SO_3H\text{-}BDC)_3$		CO_2 = 1.51 $mmol \cdot g^{-1}$ (0 °C, 1 bar)				n.d.	n.d.	n.d.	
MIL-101(Cr)-EN	EN impregned $Cr_3OH(H_2O)_2O(SO_3H\text{-}BDC)_3$		BET = 839.7 $m^2 \cdot g^{-1}$ CO_2 = 3.57 $mmol \cdot g^{-1}$ (0 °C, 1 bar)				47.2 $\mu mol \cdot g^{-1} \cdot h^{-1}$ 1.8 $\mu mol \cdot g^{-1} \cdot h^{-1}$	n.d.	n.d.	
Ni-MOF layers	$Ni_2(OH)_2BDC$ layers and Ru-based photosensitizer	Ultrasonic precipitation	BET = 48.9 $m^2 \cdot g^{-1}$	6 mL MeCN, H_2O, TEOA (3:2:1 by volume) V_R = 60 mL m_{cat} = 1 mg	5 W white LED (400 nm ≤ λ ≤ 800 nm)	CO	12.5 $\mu mol \cdot h^{-1}$	2.2 (420 nm)	n.d.	[226]

Material	Chemical composition and morphology	Preparation method	BET/CO_2 adsorption	Reaction environment	Light source (λ range)	Main product(s)	Efficiency	AQE [%] (λ)	Band gap [eV]	Ref.
PCN-222	$Zr_6(\mu_3\text{-}OH)_8(OH)_8\text{-}(TCPP)_2$ rods	solvothermal	BET = 1728 $m^2 \cdot g^{-1}$ CO_2 = 58 $cm^3 \cdot g^{-1}$ (0 °C, 1 bar), 35 $cm^3 \cdot g^{-1}$ (25 °C, 1 bar)	60 mL MeCN, TEOA (10:1 by volume) m_{cat} = 50 mg	300 W Xe lamp (420 nm < λ < 800 nm)	HCOO	60 $\mu mol \cdot g^{-1} \cdot h^{-1}$	n.d.	1.77	[227]
PCN-224(Cu)	$Zr_6O_{12}(OH)_8[TCPP\text{-}Cu]_{1.5}$ cubes	solvothermal	BET = 2285 $m^2 \cdot g^{-1}$	2 mL H_2O V_R = 50 mL m_{cat} = 100 mg	500 W Xe lamp (λ > 300 nm)	CO, CH_4	3.72 $\mu mol \cdot g^{-1} \cdot h^{-1}$ 1.36 $\mu mol \cdot g^{-1} \cdot h^{-1}$	n.d.	1.68	[228]
15% PCN-224(Cu)/TiO_2	TiO_2 on $Zr_6O_{12}(OH)_8[TCPP\text{-}Cu]_{1.5}$ cubes		BET = 178 $m^2 \cdot g^{-1}$				37.21 $\mu mol \cdot g^{-1} \cdot h^{-1}$ 0.21 $\mu mol \cdot g^{-1} \cdot h^{-1}$	n.d.	1.78	
Al-PMOF	$Al_2(OH)_2(H_2TCPP)$ cubes	solvothermal	BET = 1142 $m^2 \cdot g^{-1}$	60 mL MeCN, TEOA (5:1 by volume) m_{cat} = 50 mg T = 30 °C	125 W Hg lamp (λ > 420 nm)	HCOO	165.3 $\mu mol\ g^{-1} \cdot h^{-1}$	n.d.	1.89	[229]
NH_2-rGO (5 wt%)/Al-PMOF	$Al_2(OH)_2(H_2TCPP)$ platelets and NH_2-rGO sheets		BET = 1180 $m^2 \cdot g^{-1}$				685.6 $\mu mol\ g^{-1} \cdot h^{-1}$	n.d.	1.85	
Co_6-MOF	$[Co_3(OH)_3(NTB)(4,4'\text{-}bpy)_{1.5}]$ DEF and Ru-based photosensitizer	solvothermal	BET = 1957.5 $m^2 \cdot g^{-1}$ CO_2 = 55.2 $cm^3 \cdot g^{-1}$ (0 °C, 1 atm), 38.2 $cm^3 \cdot g^{-1}$ (25 °C, 1 atm)	5 mL MeCN, H_2O, TEOA (4:1:1 by volume) T = 30 °C	150 W Xe lamp (420 nm ≤ λ ≤ 780 nm)	CO	~13 $\mu mol \cdot g^{-1}$	0.76 (420 nm)	n.d.	[230]
Ru-MOF	$\{Cd_2[Ru(dcbpy)_3] \bullet 12H_2O\}_n$ 3D flowers	solvothermal	BET = 8.1 $m^2 \cdot g^{-1}$	60 mL MeCN, TEOA (20:1 by volume) V_R = 100 mL m_{cat} = 40 mg	500 W Xe lamp (420 nm ≤ λ ≤ 800 nm)	HCOO	77.2 $\mu mol\ g^{-1} \cdot h^{-1}$	0.67 (n.d.)	n.d.	[231]
SIFSIX-3-Ni	n.d.	RT synthesis	BET = 356 $m^2 \cdot g^{-1}$ CO_2 = 64.5 $cm^3 \cdot g^{-1}$ (25 °C, 1 bar)	n.d.	n.d.	n.d.	n.d.	n.d.	n.d.	[158]
HKUST-1	octahedrons		BET = 1869 $m^2 \cdot g^{-1}$ CO_2 = 91 $cm^3 \cdot g^{-1}$ (25 °C, 1 bar)							
SIFSIX-1-Cu	n.d.		BET = 1294 $m^2 \cdot g^{-1}$ CO_2 = 110 $cm^3 \cdot g^{-1}$ (25 °C, 1 bar)							
SIFSIX-3-Ni@HKUST-1	HKUST-1 core with SIFSIX-3-Ni shell	Layer-by-layer deposition of secondary MOF on primary MOF	BET = 1098 $m^2 \cdot g^{-1}$ CO_2 = 101 $cm^3 \cdot g^{-1}$ (25 °C, 1 bar)							
SIFSIX-3-Ni@SIFSIX-1-Cu	SIFSIX-1-Cu core with SIFSIX-3-Ni shell		BET = 748 $m^2 \cdot g^{-1}$ CO_2 = 86 $cm^3 \cdot g^{-1}$ (25 °C, 1 bar)							
UiO-66(Zr)	cubic-shaped crystals	solvothermal	BET = 1272 $m^2 \cdot g^{-1}$ CO_2 = 19.1 $cm^3 \cdot g^{-1}$ (25 °C, 1 bar)	n.d.	n.d.	n.d.	n.d.	n.d.	n.d.	[232]
Cu-BTC	octahedral-shaped microcrystals		BET = 1116 $m^2 \cdot g^{-1}$							

Material	Chemical composition and morphology	Preparation method	BET/CO_2 adsorption	Reaction environment	Light source (λ range)	Main product(s)	Efficiency	AQE [%] (λ)	Band gap [eV]	Ref.
UiO-66(Zr)/Cu-BTC	octahedral-shaped microcrystals	Two-step synthesis	CO_2 = 23.9 $cm^3 \cdot g^{-1}$ (25 °C, 1 bar) BET = 693 $m^2 \cdot g^{-1}$							
Cu-BTC/UiO-66(Zr)	cubic-shaped crystals		CO_2 = 31.8 $cm^3 \cdot g^{-1}$ (25 °C, 1 bar) BET = 255 $m^2 \cdot g^{-1}$							
NH_2-MIL-125(Ti)	octahedral crystals	solvothermal	CO_2 = 29.6 $cm^3 \cdot g^{-1}$ (25 °C, 1 bar) BET = 928 $m^2 \cdot g^{-1}$ CO_2 = 2.23 $mmol \cdot g^{-1}$ (25 °C, 1 bar)	60 mL MeCN, TEOA (5:1 by volume) V_R = 240 mL m_{cat} = 50 mg T = 25 °C	500 W Xe lamp (λ ≥ 420 nm)	$HCOO^-$	15.20 $\mu mol\ g^{-1} \cdot h^{-1}$	0.13 (430 nm)	2.68	[233]
NTU-9(Ti)	chunks of layered nanosheets		BET = 123 $m^2 \cdot g^{-1}$ CO_2 = 0.63 $mmol \cdot g^{-1}$ (25 °C, 1 bar)				18.77 $\mu mol\ g^{-1} \cdot h^{-1}$	0.16 (430 nm)	1.90	
NH_2-MIL-125(Ti)@NTU-9(Ti)	NH_2-MIL-125(Ti) partly decorated with random layered NTU-9(Ti) nanosheets	Two-step synthesis	BET = 414 $m^2 \cdot g^{-1}$ CO_2 = ~1 $mmol \cdot g^{-1}$ (25 °C, 1 bar)				72.46 $\mu mol\ g^{-1} \cdot h^{-1}$	0.67 (430 nm)	1.97	
UiO-66(Zr)	n.d.	solvothermal	n.d.	2 mL H_2O V_R = 50 mL m_{cat} = 100 mg	300 W Xe lamp (λ > 300 nm)	CO	> 0.5 $\mu mol \cdot g^{-1} \cdot h^{-1}$	n.d.	3.87	[234]
CuTCPP⊂UiO-66(Zr)	Octahedral microcrystal morphology	Two-step synthesis	BET = 1023 $m^2 \cdot g^{-1}$ CO_2 = ~30 $cm^3 \cdot g^{-1}$ (25 °C, 1 bar)				1.09 $\mu mol \cdot g^{-1} \cdot h^{-1}$		1.66	

4.4.1. Mechanism of CO_2 adsorption

The high values of MOFs surface area, extraordinary porosity and their prone for modification structures are the reasons of potential application in terms of CO_2 adsorption, storage and in separation from different gases mixtures like model flue gas (CO_2/N_2 = 15:85) or biogas (CO_2/CH_4 = 40:60). However, before MOFs will find the large-scale utilization in industry, the detailed investigation concerning single gases and their elementary mixtures have to be carried out. When designing such a material, it is also be important to determine and eliminate (or at least limit to neutral level) the influence of other factors that are not usually included in basic research on a laboratory scale, but which may prove crucial on an industrial scale (like humidity, pollution with other gases, harsh conditions).

The activity of MOFs in gas adsorption is related with their structure. As polar components of the net, SBUs are capable of interacting with the molecules of gas by formation of hydrogen bonds between the -OH groups in the metal cluster and the gas moiety [235]. Additionally, the organic linkers, especially the ones containing aromatic rings in its structure, may also contribute increased sorption, as a result of interaction between a quadrupole of CO_2 and delocalized electrons of benzene rings [236]. The overall capacity can be improved by adding more polarized centers (i.e. incorporation of functionalized linkers with pending amino groups able to interact chemically with CO_2) [237] or by existence of OMS [5]. OMS are generated by removal of terminal solvent molecules from SBUs by simple thermal treatment under reduced pressure.

The molecule of carbon dioxide contain electrophilic carbon atom and two oxygen atoms. Both of this species can interact with particular components of MOFs. Electrophilic character of C atom in CO_2 allows the molecule to undergo an attack of Lewis bases like amine groups. These functionalities can be incorporated to the structure of linker. Weak interactions, thus physisorption can be observed, which can be concluded from the distance between carbon and nitrogen atoms and not bended CO_2 molecule [238,239]. In turn, the oxygen atoms can interact with Lewis acids like OMSs, which are present in wide variety of MOFs [240]. Strong polarizing character of various metals leads to coordination of CO_2 molecules, as evidenced by deflection of carbon dioxide particle and short distance between metal and oxygen [240]. This kind of interaction can be disrupted by presence of other polarizable molecules, especially when possessing strong dipole moment (like in case of water molecules) [241].

Specific phenomenon called breathing of MOF, can also contribute increased CO_2 capacity. Only MOFs possessing specific net topologies can show this effect, especially for the ones with rod-shaped SBUs. By the term of MOFs breathing, particular structural changes can be defined. Before saturation with gas, pores of MOF are narrow, but at certain pressures and CO_2 concentration, the voids dramatically increase their volume. This effect can be reversed – pores are becoming narrow again after evacuation of CO_2 [242].

4.4.2. Application of MOF-based materials for CO_2 adsorption

Gas sorption properties of many pristine MOFs are already very satisfying, especially in terms of the CO_2 adsorption. For example, at 25 °C and pressure of 1 bar MIL-101(Cr) shows adsorption capacity of 1.22 mmol·g^{-1} [243], UiO-66(Zr) of 2.11 mmol·g^{-1} [244], MIL-53(Al) of ~2.4 mmol·g^{-1} [245], HKUST-1 of 3.84 mmol·g^{-1} [246] and rht-MOF-7 (known also as Cu-TDPAT) – ~3.8 mmol·g^{-1} [94]. In comparison, in the same conditions zeolite 13X and activated carbon can adsorb 3.7 mmol·g^{-1} [247] and 1.8-5.6 mmol·g^{-1} [248,249] CO_2, respectively.

In general, to effectively boost the affinity of the material to CO_2 pending functionalities acting as Lewis basic sites can be introduced [94,250]. Since structure of MOFs can be easily modified, different approaches have been implemented by researchers to improve sorption capacity of MOFs. For example, three Fe-based MOFs, MIL-101(Fe), MIL-53(Fe) and MIL-88B(Fe), which are obtained by using the same metal in linker, but coupled in different synthetical conditions, are characterized not only with varying chemical structure, but also with differing CO_2 uptake [224]. However, sorption capacities of all of them can be increased by introduction of amine groups into the linker structure giving respectively about 30, 50 and 40% improvement (measured at 0 °C and 1 bar). Similarly, the CO_2 uptake of UiO-66(Zr) can be boosted by 20-30% (depending on the temperature of measurement) when linker with amino groups is introduced instead of the original H_2BDC [12,127]. Increased sorption capacity was also achieved when linker with -Br or -NO_2 functionalities were used to obtain the MOF [251]. However, this increase was smaller than that owed to the introduction of amino groups. In turn, Vo *et al.* reported even better improvement of CO_2 uptake at 25 °C and 1 bar, when two hydroxyl groups were introduced to the structure of UiO-66(Zr) and additionally, significant deficiency was induced by synthesis in rapid conditions [252]. Balanced, moderate amount of structural defects (missing linkers) contributed to the designated adsorption of 6.23 mmol·g^{-1} at 25 °C and 1 bar. A similar dependence was observed for the UiO-66(Hf) – introduction of single amino group and two hydroxyl groups to the linker structure led respectively to 87 and 171% increase of CO_2 uptake measured at 25 °C and 1 bar [118].

The previous example (replacement of Zr with Hf) also shows that the type of metal introduced to the SBU of MOF is important as well. In other study, Queen *et al* have shown that depending on the metal type, the sorption capacity of M_2(DOBDC)-based structures can be growing with following order Cu<Zn<Mn<Co<Ni<Fe<Mg reaching from ~2.9 mmol·g^{-1} to ~7.1 mmol·g^{-1} at 1 bar and 25 °C [253]. In turn, Wang and co-workers obtained a small series of MOFs containing two distinct linkers in the structure, namely 4,4′,4″-nitrilotribenzoic acid (TCA) and 1,2-di(4-pyridyl)ethylene (DPE), and combined them with three transition metals – cobalt, copper and nickel [220]. The CO_2 uptake was dependent from the introduced metal – the highest result measured at 25 °C and 1 bar was achieved for Co-based MOF (40.35 cm^3·g^{-1}) , and lowered further for Ni (38.87 cm^3·g^{-1}) and the lowest for Cu (34 cm^3·g^{-1}).

Regardless of the type of MOF modification, increased CO_2 sorption capacity is often accompanied by a reduced specific surface area. For example, the PSM of porphyrin -based MOF-525(Zr) with Co and Zn brought to the decrease of specific surface area by about 40% in both cases

[216]. However, the resulting CO_2 sorption capacity at 1 bar (the measurement temperature was not specified) was increased by 30 and 10%, respectively, compared to pristine MOF-525(Zr).

In turn, the post-synthetical impregnation of MIL-101(Cr)-SO_3H, showing the CO_2 uptake of 2.07 mmol·g^{-1} at 0 °C and 1 bar, led to different consequences after introduction of amines of different length [225]. Introduction of ethylenediamine (EN), with the smallest particle size among the selected amines, led to increased CO_2 sorption capacity by 72.5%, surpassing even the uptake measured for pristine MIL-101(Cr) (3.03 mmol·g^{-1}), despite the fact of reduced specific surface area by almost 53 and 75% compared to MIL-101(Cr)-SO_3H and MIL-101(Cr), respectively. In turn diethylenetriamine (DETA) and triethylenetetramine (TETA) had the opposite effect and lowered the performance by about 16 and 30% respectively compared to MIL-101(Cr)-SO_3H. This example underlines that the size of the particle introduced into the MOF pores is important in the context of the final properties. Despite promising abilities as an individual sorbent, too large modifying particles may lead to pore clogging and thus bring about a different effect than intended.

A large group of purposely modified MOFs aiming at increase of their CO_2 sorption and separation performance are MOFs modified with ionic liquids, in particular amino acid ionic liquids. Therefore, to better introduce the topic and to emphasize the role of ILs, a separate subsection is further dedicated to get a deeper insight to this specific type of modification.

4.4.3. Mechanism of CO_2 photoreduction

Recent studies over application of MOFs revealed that some of these materials can be potentially utilized in photocatalytic carbon dioxide reduction [6]. This process requires an appropriate band structure to occur and either visible light or UV radiation as driving force. The CO_2 reduction reaction leads to creation of simple hydrocarbons (i.e. formic acid, methane, formaldehyde, methanol) or carbon oxide, with simultaneous generation of oxide from water [254]. Depending on the product, either two, four, six or eight electrons are consumed and corresponding number of protons take part in the reaction, but processes requiring more electrons are also known (Table 4.2). The light irradiation excites MOFs structure, which lead to generation of photoinduced electrons and holes, which are involved in reactions of reduction and oxidation respectively.

Table 4.2 Standard potentials of CO_2 reduction in aqueous solution at 25 °C

Half-reaction	E° (V vs. NHE)
single carbon products	
$CO_2 + 2H^+ + 2e^- \rightarrow HCOOH$	-0.61
$CO_2 + 2H^+ + 2e^- \rightarrow CO + H_2O$	-0.53
$CO_2 + 4H^+ + 4e^- \rightarrow HCHO + H_2O$	-0.48
$CO_2 + 6H^+ + 6e^- \rightarrow CH_3OH + H_2O$	-0.38
$CO_2 + 8H^+ + 8e^- \rightarrow CH_4 + 2H_2O$	-0.24
products with two carbon atoms	
$2CO_2 + 12H^+ + 12e^- \rightarrow C_2H_4 + 4H_2O$	-0.34
$2CO_2 + 12H^+ + 12e^- \rightarrow C_2H_5OH + 3H_2O$	-0.33
$2CO_2 + 14H^+ + 14e^- \rightarrow C_2H_6 + 4H_2O$	-0.27

In accordance with molecular orbital method, it has been assumed that, LUCO energy level of the MOF is identified as redox potential energy level of the metal–oxo cluster, and at the same time the HOCO energy level is recognized as the one of linker. These are corresponding respectively with conduction and valence band in conventional semiconductor, thus being the place

of reduction and oxidation reactions [255]. It follows that the electrons induced by the light are transferred at short-range distance from the linker to metal nodes, what was schematically summed up in Figure 4.13.

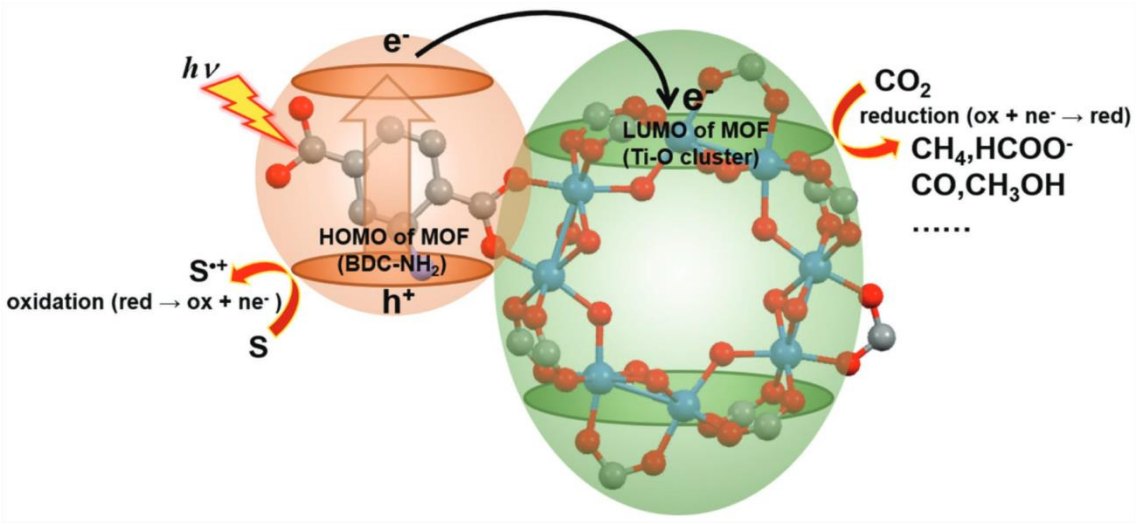


Figure 4.13. Exemplary scheme of CO_2 photoreduction reaction over NH_2-MIL-125(Ti) (reproduced with permission from [6])

To ensure the optimal efficiency of carbon dioxide photoreduction, MOFs should meet different requirements. Apart from being photoactive, to obtain the MOF with optimally broad light absorption – from the range of full UV-vis – the width of HOCO-LUCO gap must be most favorably tight. In practice this means, that the value of LUCO energy should be higher (more positive) than the oxidation potential of the oxidation of H_2O to O_2. Simultaneously, the level of HOCO energy should exceed (be more negative) the value of reduction potential of CO_2 conversion to solar fuels. Another desirable feature refers to linkers. Their structure should provide suitable amount of photoinduced absorption centers and thus allowing the generated electrons transfer smoothly towards metal-oxo clusters. This can be obtained by incorporation of electron-rich struts possessing the level of LUMO energy higher the redox potential energy level of metal nodes [256–258]. The overall efficiency of CO_2 photocatalytic reduction can be also increased by incorporation of metal ions, that may serve as additional catalytic sites [259,260].

MOFs may also act as cocatalysts or photocatalytic hosts. As cocatalyst, the metal-organic frameworks are supposed to prevent the recombination of electron-hole pairs. Thanks to high CO_2 capacity, these materials are significantly increase the total sorption ability, and thus, activate the carbon dioxide molecules due to presence of active sites [222,261]. In case of photocatalytic hosts, MOFs acts inversely i.e. they are working as photosensitizers, while the photoreduction reaction occurs due to the presence of the main catalyst [208,262]. However, the highly developed MOFs surface and high adsorption ability are also significant as well.

Aqueous solution is highly desirable for photocatalytic environment and thus MOFs for this application should be stable under this conditions. The water stability of MOFs is regulated by two factors – Lewis acidity of metal clusters and on the pKa values of linkers [263]. The structures of

some MOFs are prone to the presence of water molecules, which can lead to collapse of the framework due to impact on SBUs and their coordination to linkers [264,265]. Therefore MOFs from the families of UiO, ZIF or MIL are indicated as the most promising [266]. Importantly, MOF decomposition may also occur due to light illumination, thus it is important to neutralize this effect by for example utilization of sacrificial agents during photoconversion process. Usage of chemical compounds like triethylamine (TEA) or triethanolamine (TEOA) results in interception of photo generated holes.

4.4.4. Application of MOF-based materials for CO_2 photoconversion

Among the most promising MOFs for photoconversion of CO_2, materials basing on NH_2-UiO-66(Zr) [127], PCN-222(Zr) [267], NH_2-MIL-125(Ti) [80,268], PCN-601 [269] can be listed as examples. The porous structure of these materials enables to use them both in solid-liquid and solid-gas photocatalytic systems.

Among the reported approaches to improve the photocatalytic performance, partial replacement of linkers [8,127] or metals [110,121,171] to other than the original ones can extend the spectrum of absorbed light, adjust the optical gap or to increase surface area. Alternatively MOF can be merged with semiconductors like TiO_2 [198,199,208], g-C_3N_4 [200], CdS [205,206] $Bi_4O_5Br_2$ [202], B_2S_3 [201] or Cu_2O [156] to create a composite that uses the advantages of both materials. Aside of that, the introduction of transition metals, like Cu, Co and Ni, have shown significant potential of use in terms of CO_2 reduction [270]. Non-noble transition metals usually do not suffer from competing hydrogen evolution reactions or overly strong intermediate binding, and additionally, they introduce optimal d-orbital configuration for CO_2 photoreduction. The incorporation of Ni to NH_2-MIL-125(Ti) was proved to increase the CO generation in comparison with unmodified MOF [271]. Similar boosting effect was observed when MIL-101(Cr) was loaded with CoO_x species [272]. In turn, efficient generation of methanol and ethanol was reported after introduction of Cu single atoms onto NH_2-UiO-66(Zr) [214].

How much can be achieved by functionalizing the linker itself is perfectly demonstrated by the example of UiO-66(Zr) and it aminated analogue – NH_2-UiO-66(Zr). It is worth to mention, that the optical gap of UiO-66(Zr) reaches the value of about 4 eV, which destinates this form of MOF to work only under the illumination of UV light, while the introduction of -NH_2 moiety causes the optical gap to narrow to approx. 2.6 eV, which allows to partially absorb the light from visible range. The pristine UiO-66(Zr) is mainly reported to produce CH_4 [198,201], CO [198,200] or CH_3OH [199] under light irradiation. One of the few reports on HCOOH generation was presented by Bhattacharya *et al*. [203] who have reached the efficiency of 9.7 $\mu mol \cdot g^{-1} \cdot h^{-1}$ HCOOH for pristine UiO-66. Similar result was achieved by the research group of Łuczak *et al.* [12] achieving the efficiency of 13.65 $\mu mol \cdot g^{-1} \cdot h^{-1}$. The additional cycles of freeze–pump–thaw preceding the photocatalytic reaction of CO_2 reduction let to produce 13.5 $\mu mol \cdot g^{-1} \cdot h^{-1}$of HCOOH by the non-modified NH_2-UiO-66(Zr) [203]. Ethanol and methanol were reported as products of CO_2 photoconversion by Wang *et al.* [214]. To achieve that, NH_2-UiO-66(Zr) was modified with Cu and the photocatalytic process was carried out in an aqueous environment under visible light irradiation.

In turn, NH_2-UiO-66(Zr) decorated with copper(0) and copper(I) oxide more than tripled the CO production rate at 50 °C and enabled additional generation of CH_4, which was not observed in the same conditions for unmodified MOF. Similar boost of CO production was observed by Su *et al.* [207], who have incorporated In *via* synthetical approach to the structure of NH_2-UiO-66(Zr). The other method of raising the photocatalytic abilities of NH_2-UiO-66(Zr) was an exchange of the elementary metal with titanium by either synthetical and post-synthetical approaches, reaching extraordinary level of HCOOH generation of 1 $mmol \cdot g^{-1} \cdot h^{-1}$ [171] and 180 $\mu mol \cdot g^{-1} \cdot h^{-1}$ [121], respectively.

In terms of efficient CO_2 photoreduction, the defect engineering was proven to be an important method of MOF modification. The structure that is relatively frequently subjected to such alternation of structure are MOFs from UiO family, especially NH_2-UiO-66(Zr) [7,8,273]. Defectivity can be introduced during the synthetical approach by adjusting the synthesis temperature [67], by using a modulator in the form of small organic acids, by suitable thermal treatment after the synthesis or combination of these methods [7]. Moderate linker deficiency was found to increase the efficiency of CO_2-to-CO photoreduction by about 4.5-times compared to the ideal MOF [7] and about 2.2-times more than MOF with missing-cluster defects [273]. Alternatively, chemical compounds with a similar structure to the linker or its isomers can be also introduced [8]. When added to the synthesis environment of NH_2-UiO-66(Zr), NH_2-UiO-67(Zr) and NH_2-UiO-68(Zr), 3,5-diamino-benzoate (2ABA) acted as competing agent for the linkers during structure crystallization. Its incorporation led not only to the creation of defects of the structure, but also to a favorable change of the electronic structure, which in turn increased the efficiency of the photocatalytic process for all MOFs modified with 2ABA, compared to the respective structures modulated with benzoic acid [273].

Introduction of different metals to the structure of MOFs *via* varying approaches may lead to obtaining photocatalyst of increased photocatalytic abilities. Differences can be noticed when changing the metal creating the SBU. For example, depending from the chosen metal – Co, Cu or Ni – the obtained structure of the mixed-linker MOF gave different photocatalytic outcome[220]. In the case of $\{Co_3(TCA)_2(DPE)_3(H_2O)_6\}_n$ and $\{Cu_3(TCA)_2(DPE)_3(H_2O)_6\}_n$ the photocatalytic CO_2 reduction competed with hydrogen generation. Even though the amount of generated CO was relatively high for the Co-based MOF (reaching the production rate of 1140 $\mu mol \cdot g^{-1} \cdot h^{-1}$), it was accompanied with similarly high rate of H_2 production (1265 $\mu mol \cdot g^{-1} \cdot h^{-1}$). Selectivity was almost completely changed in favor of CO photogeneration by using $\{Ni_3(TCA)_2(DPE)_3(H_2O)_6\}_n$ at the expense of the side reaction. However, it simultaneously decreased the rate of CO_2-to-CO light-driven conversion by about 77%. In turn, the introduction of coordinatively unsaturated single atoms of Co and Zn to the porphyrin-based linker of MOF-525(Zr) significantly decreased the rate of photogenerated pairs recombination compared to the pristine MOF [216]. Modification with Zn almost doubled the amount of photogenerated CO and CH_4, while presence of Co more than tripled. Interestingly, while for MOF-525(Zr) and the material with Zn, the amount of produced CH_4

constituted approximately 10% of the amount of generated CO. In turn, for CO-modified MOF the relative amount was almost doubled and reached 18.3%.

Construction of heterojunction is another method of boosting photocatalytic efficiency of MOFs. Even though the porphyrin-based Cu-modified PCN-224(Zr) absorbs light from UV-Vis spectrum, its photocatalytic activity is relatively low [228]. The photogeneration rate reached only 3.7 and 1.4 $\mu mol \cdot g^{-1} \cdot h^{-1}$ of CO and CH_4 respectively. *In situ* growth of TiO_2 on the surface of MOF led to obtainment of Z-scheme heterojunction and 10-fold increase of CO photocatalytic generation. At the same time the CH_4 creation significantly limited (to level of 0.2 $\mu mol \cdot g^{-1} \cdot h^{-1}$) thereby increasing the selectivity of the process. Sadeghi *et al.* reported obtainment of Al/PMOF combined with amine-functionalized reduced graphene oxide (NH_2-rGO) for efficient CO_2 photoreduction to HCOOH under visible light irradiation [229]. Addition of only 5 wt% of NH_2-rGO resulted in obtainment of platelet-like morphology and preserved the primarily high level of specific surface area similar to the unmodified MOF. Boosted product generation rate by four times was observed (compared to the pristine MOF) that can be explained by significantly elongated lifetime of electron-hole pairs in the synthesized material. Improvement of photocatalytic properties was also observed when the solid MOF – precisely MIL-101(Cr)-SO_3H – was impregned with ethylenediamine [225]. The increased affinity to attract CO_2 (via either physical and chemical interactions) in combination with reduced rate of charge carriers recombination enabled 2.2-times fold increase of the amount of photogenerated CO and 1.4-fold increase of CH_4 by the obtained material in comparison with pristine MIL-101(Cr)-SO_3H.

The above subsection clearly indicates multiplicity of potential pathways of developing MOF-based material characterized by satisfactory photocatalytic abilities. It is possible to modify the structure itself (different linkers and metals, structure defects), modify both the finished MOF and the process of obtaining it, and also combine MOFs with other materials that compensate their shorcomings. However, it should be underlined that each MOF should be treated individually and not all methods may affect one MOF in the same way as another. This should be taken into account when selecting the appropriate modification method. Special attention should also be paid to the environment in which the CO_2 photoreduction process is carried out.Ionic Liquids and their role in MOFs modification

Ionic liquids are a class of peculiar salts – characterized by extremely low vapor pressure and consisting of organic bulky cation and relatively small organic or inorganic anion [274]. Their composition versatility allows them to simply maneuver the properties of ILs to comply with particular requirements, just like MOF structures can be tailor-made according to the application [275]. ILs show high thermal stability and the possibility of remaining in a liquid state in the temperature range of about 400°C. The special properties of ionic liquids are also very low vapor pressure and non-flammability. By introduction of additional functional groups to the structure of regular IL, the chosen features of the compound can be modified. Such specific group is referred to as TSILs, among them ILs having increased affinity towards CO_2 uptake can be distinguished if possess dedicated moieties.

Two different types of CO_2 absorption by ILs can be distinguished. First of them is physical mode in which the weak interactions (electrostatic interactions, van der Waals interactions [276], hydrogen bonds [277]) are responsible for trapping the CO_2 molecules in gap spaces between ILs molecules. The bigger the voids are, the higher solubility can be observed, thus incorporation of longer side chains to the cations is crucial [278,279]. Similar effect can be reached by incorporation of fluorine atoms to the anion [279,280]. The second type – chemical absorption, characteristic for TSILs, concerns binding CO_2 molecules by functionalities like amino [281], hydroxyl [282,283], carbonyl [85] or fluoric [285] groups. Depending on the localization of the functionality, the type of reaction taking place is different. On the example of amino group, if the functionality is incorporated into cation structure (Figure 4.13a), the reaction with CO_2 will lead to creation of carbamate zwitterion [286]. It means, that one molecule of CO_2 will bind two cations. In turn, if the anion possesses the functionality (Figure 4.13b), one molecule of CO_2 will attach to only one anion, leading to formation of a carbamic acid [287]. When chemisorption capacity reaches its maximum, the physisorption can additionally occur and thus, the sorption will exceed the value of one mole of carbon dioxide per one mole of IL.

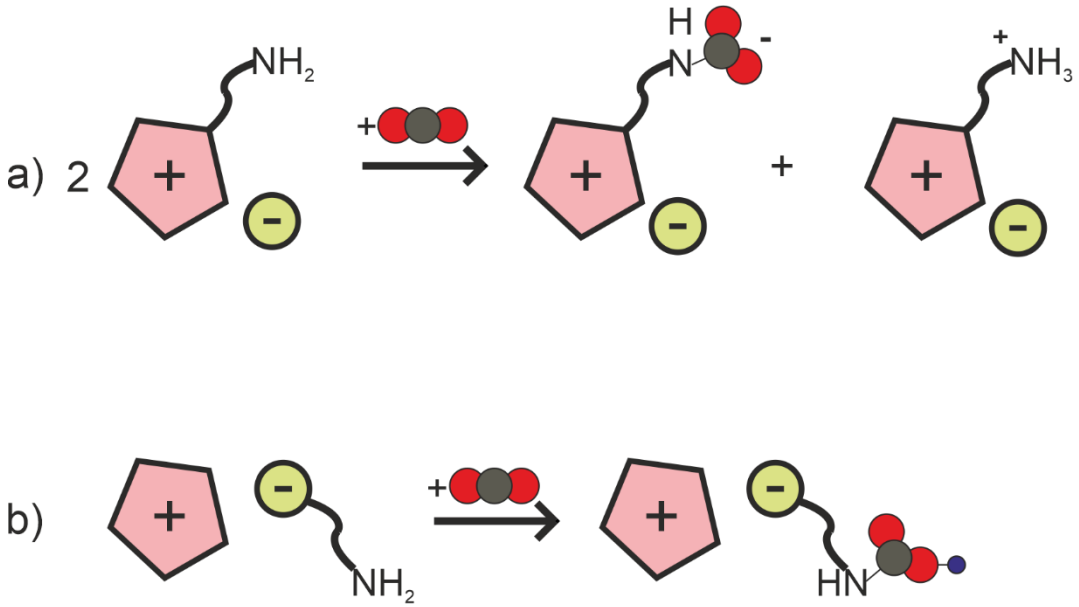


Figure 4.14. Chemical absorption of CO_2 by ILs with NH_2-functionalized: a) cation, b) anion.

Amino acid ionic liquids are a special sub-class of bio-based and task-specific ionic liquids, first obtained and characterized by Fukumoto and co-workers [288]. The unique structure of amino acids – presence of amino- and carboxylic group – enables to use them as both anion and cation of ILs (Figure 4.15) [10]. The biodegradability and biocompatibility of amino acids and their IL-derivatives would potentially allow to drastically limit the risk of toxicity [10,288].

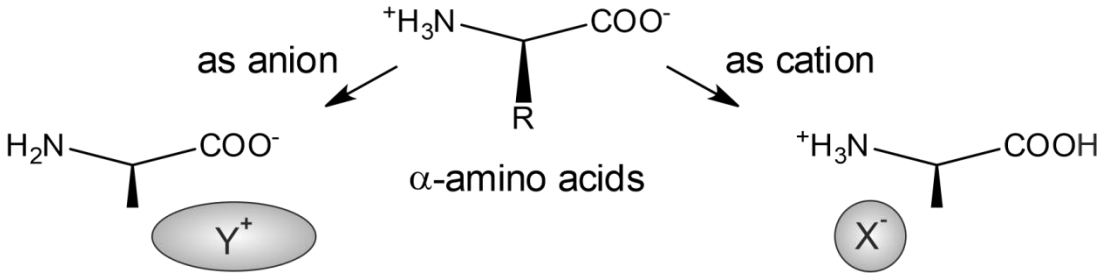


Figure 4.15. Possible structures of AAILs

Introduction of amino acids into IL's structure as an anion with pending amino groups (especially like L-lysine or L-arginine, possessing more than one amino groups), contributes to significantly improved CO_2 sorption capacity (Table 4.3). Phosphonium and ammonium cations are used apart from the most popular imidazolium-based ILs. To boost the sorption properties of AAILs, in case of using imidazolium cations different moieties like ether [24], hydroxyl [289] or vinyl [290] can be introduced to the side chains. For example, the exchange of tetrafluoroborate (BF_4^-) or bis(trifluoromethylsulfonyl)imide (Tf_2N^-) in 1-butyl-3-methylimidazolium ([BMIM])-based ILs to L-arginine resulted in an increase from 0.1 $mmol_{CO2}\cdot(mmol_{IL})^{-1}$ and 0.2 $mmol_{CO2}\cdot(mmol_{IL})^{-1}$ to 0.8 $mmol_{CO2}\cdot(mmol_{IL})^{-1}$ at 10 bars and 25 °C [291], respectively. Nevertheless, the use of the potential laying in AAILs for efficient CO_2 absorption is greatly limited by their viscosity increasing by at least two orders of magnitude during the CO_2 capture process [24–26].

Table 4.3. Absorption capacity of CO_2 in different AAILs and values of viscosity before and after saturation with the gas

Amino Acid Ionic Liquid	CO_2 absorption		Viscosity (mPa•s)		Ref.
	Uptake ($mole_{CO2}\cdot mole_{IL}^{-1}$)	Measurement conditions	Before saturation	After saturation	
$[P_{666(14)}][Gly]$ trihexyl(tetradecyl)phosphonium glycinate	1.26	T = 25 °C p = 1 bar	360	17 000	[23]
$[P_{666(14)}][Ala]$ trihexyl(tetradecyl)phosphonium alanate	0.66		450	53 000	
$[P_{666(14)}][Sar]$ trihexyl(tetradecyl)phosphonium sarcosinate	0.91		440	83 000	
$[P_{666(14)}][Ile]$ trihexyl(tetradecyl)phosphonium isoleucinate	0.97		430	100 000	
[MOBMIM][Lys] 1-methoxylbutyl-3-methylimidazolium lysinate	2.12	T = 50 °C p = 0.5 MPa t = 30 min	3201	-	[24]
[MOBMIM][His] 1-methoxylbutyl-3-methylimidazolium histidinate	2.28		2987	-	
[MOBMIM][Arg] 1-methoxylbutyl-3-methylimidazolium arginate	2.09		5631	-	
[MOBMIM][Gly] 1-methoxylbutyl-3-methylimidazolium glycinate	2.36		536	-	
[BMIM][Gly] 1-butyl-3-methylimidazolium glycinate	1.75		767	-	
$[P_{666(14)}][Pro]$ trihexyl(tetradecyl)phosphonium prolinate	0.96	T = 25 °C p = 1 bar	720	1 200	[25]

Amino Acid Ionic Liquid	CO_2 absorption		Viscosity (mPa•s)		Ref.
	Uptake ($mole_{CO2}$ ·$mole_{IL}^{-1}$)	Measurement conditions	Before saturation	After saturation	
$[P_{666(14)}]$[Lys] trihexyl(tetradecyl)phosphonium lysinate	1.37		730	160 000	
$[P_{666(14)}]$[Tau] trihexyl(tetradecyl)phosphonium taurinate	0.80		670	19 000	
$[P_{4442}]_2$[IDA] Di(tributylethylphosphonium) iminodiacetate	1.69		66.2	961.6	
$[P_{4442}]_3$[NTA] Tri(tributylethylphosphonium) nitrilotriacetate	0.44		68.2	1 367	
$[P_{4442}]_2$[EDDA] Di(tributylethylphosphonium) ethylenediamine-N,N'-diacetate	1.65	T = 40 °C p = 1 bar	74.4	2 140	[26]
$[P_{4442}]$[H-IDA] tributylethylphosphonium iminodiacetate	0.70		1 069	11 357	
$[BMIM]_2$[IDA] di(1-butyl-3-methylimidazolium) iminodiacetate	0.99		627.7	17 346	

4.4.5. The role of ionic liquids in synthesis and modification of MOFs

Thanks to the unique properties of ILs they were applied in MOF field, aiming at morphology and crystal structure control, improvement of sorption capabilities or development of new synthesis methods. A summary of IL-modified MOFs including the method of their introduction and the CO_2 sorption performance of the modified structures is presented in Table 4.4

Table 4.4. Application of ionic liquids for MOFs modification (to enhance CO_2 binding); the full names of the listed ILs symbols are listed below the table in alphabetical order.

Modified MOF	Ionic liquid	Amount of added IL	Method of IL introduction	Efficiency of CO_2 binding	Application	Ref.
ZIF-8(Zn)	-	-	Post-synthetical impregnation	~0.7 mmol·g^{-1} at 1 bar, 30 °C ~6 mmol·g^{-1} at 10 bar, 30 °C	CO_2/N_2 separation	[187]
	[EMIM][Ac]	12.9 mol%		0.67 mmol·g^{-1} at 1 bar, 30 °C 4.53 mmol·g^{-1} at 10 bar, 30 °C		
	[DMIM][Ac]	12.9 mol%		0.63 mmol·g^{-1} at 1 bar, 30 °C 3.31 mmol·g^{-1} at 10 bar, 30 °C		
ZIF-8(Zn)	-	-	Post-synthetical impregnation	~0.7 mmol·g^{-1} at 1 bar, 30 °C ~6 mmol·g^{-1} at 10 bar, 30 °C	CO_2/CH_4 and CO_2/N_2 separation	[188]
	$[N_{2114}][Ac]$	9.3 mol%		0.56 mmol·g^{-1} at 1 bar, 30 °C 4.55 mmol·g^{-1} at 10 bar, 30 °C		
	$[N_{1(2OH)(2OH)(2OH)}][Ac]$	9.3 mol%		0.57 mmol·g^{-1} at 1 bar, 30 °C 4.83 mmol·g^{-1} at 10 bar, 30 °C		
	$[N_{1(2OH)(2OH)(2OH)}][Tf_2N]$	9.3 mol%		0.55 mmol·g^{-1} at 1 bar, 30 °C 4.94 mmol·g^{-1} at 10 bar, 30 °C		
ZIF-8(Zn)	-	-	Post-synthetical impregnation	~0.6 mmol·g^{-1} at 1 bar, 30 °C ~6 mmol·g^{-1} at 10 bar, 30 °C	CO_2/CH_4 separation	[189]
	$[P_{66614}][Tf_2N]$	9.3 mol%		0.41 mmol·g^{-1} at 1 bar, 30 °C 4.28 mmol·g^{-1} at 10 bar, 30 °C		
	$[EMIM][Tf_2N]$	9.3 mol%		0.43 mmol·g^{-1} at 1 bar, 30 °C 3.97 mmol·g^{-1} at 10 bar, 30 °C		
	$[E(OH)MIM][Tf_2N]$	9.3 mol%		0.41 mmol·g^{-1} at 1 bar, 30 °C 3.81 mmol·g^{-1} at 10 bar, 30 °C		
	$[HMIM][Tf_2N]$	9.3 mol%		0.40 mmol·g^{-1} at 1 bar, 30 °C 3.44 mmol·g^{-1} at 10 bar, 30 °C		
	$[DMIM][Tf_2N]$	9.3 mol%		0.45 mmol·g^{-1} at 1 bar, 30 °C 2.85 mmol·g^{-1} at 10 bar, 30 °C		
ZIF-8(Zn)	-	-	Post-synthetical impregnation	0.62 mmol·g^{-1} at 1 bar, 30 °C 5.73 mmol·g^{-1} at 10 bar, 30 °C	CO_2/N_2 separation	[292]
	[EMIM][Val]	12.9 mol%		0.65 mmol·g^{-1} at 1 bar, 30 °C 3.97 mmol·g^{-1} at 10 bar, 30 °C		
	[EMIM][Cap]	12.9 mol%		0.57 mmol·g^{-1} at 1 bar, 30 °C 3.20 mmol·g^{-1} at 10 bar, 30 °C		
	[EMIM][Lev]	12.9 mol%		0.66 mmol·g^{-1} at 1 bar, 30 °C 4.10 mmol·g^{-1} at 10 bar, 30 °C		
	[EMIM][Oxa]	12.9 mol%		0.59 mmol·g^{-1} at 1 bar, 30 °C 4.09 mmol·g^{-1} at 10 bar, 30 °C		
	[EMIM][Glu]	12.9 mol%		0.70 mmol·g^{-1} at 1 bar, 30 °C 3.38 mmol·g^{-1} at 10 bar, 30 °C		
ZIF-8(Zn)	-	-	Post-synthetical impregnation	~0.6 mmol·g^{-1} at 1 bar, 25 °C ~5.5 mmol·g^{-1} at 10 bar, 25 °C	CO_2/CH_4 and CO_2/N_2 separation	[293]
	$[BMIM][PF_6]$	30 wt%		~0.5 mmol·g^{-1} at 1 bar, 25 °C ~2.7 mmol·g^{-1} at 10 bar, 25 °C		

Modified MOF	Ionic liquid	Amount of added IL	Method of IL introduction	Efficiency of CO_2 binding	Application	Ref.
ZIF-8(Zn)	- [BMIM][Tf_2N]	- 60 mL [BMIM][Tf_2N]	Ionothermal synthesis	~0.75 mmol·g^{-1} at 1 bar, 25 °C ~0.68 mmol·g^{-1} at 1 bar, 25 °C	CO_2/CH_4 and CO_2/N_2 separation	[294]
ZIF-8(Zn)	- [BMIM][BF_4]	- 5, 20, 30 wt%	Post-synthetical impregnation	~0.5 mmol·g^{-1} at 1 bar, 25 °C ~5.5 mmol·g^{-1} at 10 bar, 25 °C ~0.7 mmol·g^{-1} at 1 bar, 25 °C (5 wt%) ~5.4 mmol·g^{-1} at 10 bar, 25 °C (5 wt%)	CO_2/CH_4 and CO_2/N_2 separation	[295]
ZIF-8(Zn)	- [BMIM][Ac] [EMIM][Ac]	- 10, 20, 30 wt% 10, 20, 30 wt%	Post-synthetical impregnation	~0.6 mmol·g^{-1} at 1 bar, 30 °C ~6 mmol·g^{-1} at 10 bar, 30 °C ~0.7 mmol·g^{-1} at 1 bar, 30 °C (10 wt%) ~5 mmol·g^{-1} at 10 bar, 30 °C (10 wt%) ~0.7 mmol·g^{-1} at 1 bar, 30 °C (10 wt%) ~4 mmol·g^{-1} at 10 bar, 30 °C(10 wt%)	CO_2 sorption, CO_2/N_2 separation	[296]
ZIF-8(Zn)	- [BMIM][SCN]	- 30 wt%	Post-synthetical impregnation	~0.53 mmol·g^{-1} at 1 bar, 25 °C ~0.40 mmol·g^{-1} at 1 bar, 25 °C	CO_2/N_2, CO_2/CH_4 separation	[297]
ZIF-8(Zn)	- [P_{4444}][Lev] [P_{66614}][Tf_2N]	- ~5 wt% MOF in IL ~5 wt% MOF in IL	Suspension of MOF in IL (porous liquid)	~2.7 mmol·g^{-1} at 5 bar, 30 °C ~1.8 mmol·g^{-1} at 5 bar, 30 °C ~0.3 mmol·g^{-1} at 5 bar, 30 °C	CO_2 sorption	[298]
ZIF-8(Zn)	- [EMIM][Gly] [EMIM][Ala]	- 10, 20, 30 wt% 10, 20, 30 wt%	Post-synthetical impregnation	0.12 mmol·g^{-1} at 0.2 bar, 30 °C ~0.6 mmol·g^{-1} at 1 bar, 30 °C 0.89 mmol·g^{-1} at 0.2 bar, 30 °C (30 wt%) ~1.4 mmol·g^{-1} at 1 bar, 30 °C (30 wt%) 0.91 mmol·g^{-1} at 0.2 bar, 30 °C (30 wt%) ~1.8 mmol·g^{-1} at 1 bar, 30 °C (30 wt%)	CO_2 sorption, CO_2/N_2 separation	[191]
ZIF-67(Co)	- [NAIM][Br]	- 0.119 g_{IL}/1.232 g_{linker}/ 1.096 g_{Co}	Present in synthesis environment	~0.8 mmol·g^{-1} at 1 bar, 25 °C ~1.1 mmol·g^{-1} at 1 bar, 25 °C	CO_2 sorption,	[299]
HKUST-1(Cu)	- [BMIM][BF_4]	- 5, 20, 30 wt%	Post-synthetical impregnation	~14.5 mmol·g^{-1} at 10 bar ~12.5 mmol·g^{-1} at 10 bar (5 wt%)	CO_2/CH_4, CO_2/N_2, CO_2/H_2 separation	[300]
HKUST-1(Cu)	- [BMIM][PF_6] [BMIM][Tf_2N]	- 1, 5, 10 wt% in relation to mass of used MOF 1, 5 wt% in relation to mass of used MOF	Post-synthetical impregnation	~4.7 mmol·g^{-1} at 1 bar, 25 °C ~13 mmol·g^{-1} at 10 bar, 25 °C ~4.5 mmol·g^{-1} at 1 bar, 25 °C (5 wt%) ~1.5 mmol·g^{-1} at 1 bar, 25 °C (10 wt%) ~12 mmol·g^{-1} at 10 bar, 25 °C (5 wt%) ~3 mmol·g^{-1} at 10 bar, 25 °C (10 wt%) ~4 mmol·g^{-1} at 1 bar, 25 °C (5 wt%) ~11 mmol·g^{-1} at 8 bar, 25 °C (5 wt%)	CO_2 sorption	[301]
HKUST-1(Cu)	- [BMIM][PF_6] [BMIM][BF_4]	- 20 wt% 20 wt%	Post-synthetical impregnation	~3.7 mmol·g^{-1} at 1 bar, 25 °C ~2.2 mmol·g^{-1} at 1 bar, 25 °C ~1.9 mmol·g^{-1} at 1 bar, 25 °C	CO_2 sorption	[302]
HKUST-1(Cu)	- [BMIM][DCA] [BMIM][DBP]	- 30 wt% 30 wt%	Post-synthetical impregnation	~11.2 mmol·g^{-1} at 10 bar, 25 °C ~3.3 mmol·g^{-1} at 10 bar, 25 °C ~3.6 mmol·g^{-1} at 10 bar, 25 °C	CO_2/N_2, CO_2/CH_4 separation	[303]

Modified MOF	Ionic liquid	Amount of added IL	Method of IL introduction	Efficiency of CO_2 binding	Application	Ref.
HKUST-1(Cu)	- [BMIM][PF_6] [BMMIM][PF_6]	- 30 wt% 30 wt%	Post-synthetical impregnation	~ 5.3 mmol·g^{-1} at 1 bar, 25 °C ~ 2.2 mmol·g^{-1} at 1 bar, 25 °C ~ 2.0 mmol·g^{-1} at 1 bar, 25 °C	CO_2/N_2, CH_4/N_2 separation	[304]
MOF-177(Zn)	- [EMIM][Gly] [EMIM][Ala]	- 10, 20, 30 wt% 10, 20, 30 wt%	Post-synthetical impregnation	~0.7 mmol·g^{-1} at 1 bar, 30 °C ~10 mmol·g^{-1} at 10 bar, 30 °C ~1.2 mmol·g^{-1} at 1 bar, 30 °C (20 wt%) ~4 mmol·g^{-1} at 10 bar, 30 °C (20 wt%) ~1.2 mmol·g^{-1} at 1 bar, 30 °C (20 wt%) ~3 mmol·g^{-1} at 10 bar, 30 °C (20 wt%)	CO_2/N_2, CO_2/CH_4 separation	[305]
MIL-100(Al)	- [EMIM][DCA] [EMIM][TCB]	- m_{MOF}:m_{IL} = 1:1 m_{MOF}:m_{IL} 1:1 or 1:0.5	Post-synthetical impregnation	~2.5 mmol·g^{-1} at 1 atm, 25 °C ~3.8 mmol·g^{-1} at 1 atm, 25 °C ~3.2 mmol·g^{-1} at 1 atm, 25 °C (both)	CO_2 sorption, CO_2/N_2 separation	[190]
NH_2-MIL-101(Cr)	- [C_3NH_2BIM][Tf_2N]	- m_{MOF}:m_{IL} = 1:1	Post-synthetical impregnation	~0.67 mmol·g^{-1} at 1 bar, 25 °C ~0.53 mmol·g^{-1} at 1 bar, 25 °C	CO_2/N_2 separation	[306]
UiO-66(Zr)	- [EMIM][Gly] [EMIM][Phe]	- 5, 10, 30 % by pore volume 5, 10, 30 % by pore volume	Post-synthetical impregnation	~2.6 mmol·g^{-1} at 1 bar, 25 °C ~2.5 mmol·g^{-1} at 1 bar, 25 °C (5%) ~2.2 mmol·g^{-1} at 1 bar, 25 °C (5%)	CO_2 sorption	[307]
NU-1000(Zr)	- [EMIM][Gly] [EMIM][Phe]	- 5, 10, 30 % by pore volume 5, 10, 30 % by pore volume		~2.2 mmol·g^{-1} at 1 bar, 25 °C ~1.9 mmol·g^{-1} at 1 bar, 25 °C (5%) ~1.3 mmol·g^{-1} at 1 bar, 25 °C (5%)		
NH_2-UiO-66(Zr)	- [BMIM][Gly] [BMIM][Arg]	- 10, 30, 50, 70 wt% 10, 30, 50, 70 wt%	Post-synthetical impregnation	3.13 mmol·g^{-1} at 1 bar, 40 °C 6.13 mmol·g^{-1} at 1 bar, 40 °C (70 wt%) 7.05 mmol·g^{-1} at 1 bar, 40 °C(70 wt%)	CO_2/N_2 separation	[308]
NH_2-MIL-125(Ti)	- [BMIM][Gly] [BMIM][Arg]	- 10, 30, 50, 70 wt% 10, 30, 50, 70 wt%		~2 mmol·g^{-1} at 1 bar, 40 °C 6.34 mmol·g^{-1} at 1 bar, 40 °C (70 wt%) 5.74 mmol·g^{-1} at 1 bar, 40 °C (70 wt%)		
UiO-67(Zr)	- [PMIM][SO_3] [PMIM][Cl]	- $n_{UiO\text{-}67\text{-}MIMS}$:$n_{Na2SO3}$ = 1:1 $n_{UiO\text{-}67\text{-}MIMS}$:$n_{NaCl}$ = 1:1	IL-modified linker added to synthesis environment	~1.7 mmol·g^{-1} at 1 atm, 25 °C ~3 mmol·g^{-1} at 1 atm, 25 °C ~3.8 mmol·g^{-1} at 1 atm, 25 °C	CO_2 sorption, CO_2/N_2 separation	[309]
UiO-67(Zr)	- [AMIM][Br]	- N_{linker}:n_{ZrCl4} = 1:1	IL-modified linker added to synthesis environment	~1.02 mmol·g^{-1} at 1 atm, 25 °C ~1 mmol·g^{-1} at 1 atm, 25 °C	CO_2 sorption	[310]
ZIF-8(Zn)	- [Cho][AOT]	- n_{EOAF}:$n_{[Cho][AOT]}$ = 2:1	Present in synthesis environment (reverse microemulsion, R-limonene, [Cho][AOT], ethanolammonium formate EOAF)	n.a. 1.78 mmol·g^{-1} at 1 bar	CO_2 sorption	[311]
HKUST-1(Cu)	- [Cho][AOT]	- n_{EOAF}:$n_{[Cho][AOT]}$ = 2:1		n.a. 0.88 mmol·g^{-1} at 1 bar		
NH_2-UiO-66(Zr)	- [Cho][AOT]	- n_{EOAF}:$n_{[Cho][AOT]}$ = 2:1		n.a. 0.66 mmol·g^{-1} at 1 bar		

Modified MOF	Ionic liquid	Amount of added IL	Method of IL introduction	Efficiency of CO_2 binding	Application	Ref.
NH_2-MIL-53(Al)	-	-		n.a.		
	[Cho][AOT]	n_{EOAF}:$n_{[Cho][AOT]}$ = 2:1		1.4 mmol·g^{-1} at 1 bar		

[AMIM][Br] – 1-allyl-3-ethylimidzaole bromide; [BMIM][Ac] – 1-butyl-3-ethylimidzaole acetate; [BMIM][Arg] – 1-butyl-3-ethylimidzaole L-arginate; [BMIM][BF_4] – 1-butyl-3-ethylimidzaole tetrafluoroborate; [BMIM][DBP] – 1-butyl-3-ethylimidzaole dibutylphosphate; [BMIM][DCA] – 1-butyl-3-ethylimidzaole dicyanamide; [BMIM][Gly] – 1-butyl-3-ethylimidzaole L-glycinate; [BMIM][PF_6] – 1-butyl-3-ethylimidzaole hexafluorophosphate; [BMIM][SCN] – 1-butyl-3-ethylimidzaole thiocyanate; [BMIM][Tf_2N] – 1-butyl-3-ethylimidzaole bis(trifluorometanosulfonylo)imide; [BMMIM][PF_6] – 1-butyl-2,3-dimethylimidazolium hexafluorophosphate; [C_3NH_2BIM][Tf_2N] – 1-(3-aminopropyl)-3-butylimidazolium bis(trifluorometanosulfonylo)imide; [Cho][AOT] – choline dioctylsulfosuccinate; [DMIM][Ac] – 1-decyl-3-methylimidazolium acetate; [DMIM] [Tf_2N] – 1-decyl-3-methylimidazolium bis(trifluorometanosulfonylo)imide; [EMIM][Ac] – 1-ethyl-3-ethylimidzaole acetate; [EMIM][Ala] – 1-ethyl-3-ethylimidzaole L-alanate; [EMIM][Cap] – 1-ethyl-3-ethylimidzaole caprate; [EMIM][DCA] – 1-ethyl-3-ethylimidzaole dicyanamide; [EMIM][Glu] – 1-ethyl-3-ethylimidzaole glutarate; [EMIM][Gly] – 1-ethyl-3-ethylimidzaole L-glycinate; [EMIM][Lev] – 1-ethyl-3-ethylimidzaole levulinate; [EMIM][Oxa] – 1-ethyl-3-ethylimidzaole oxalate; [EMIM][Phe] – 1-ethyl-3-ethylimidzaole phenylalanate; [EMIM][TCB] – 1-ethyl-3-ethylimidzaole tetracyanoborate; [EMIM][Tf_2N] – 1-ethyl-3-ethylimidzaole bis(trifluorometanosulfonylo)imide; [EMIM][Val] – 1-ethyl-3-ethylimidzaole valerate; [E(OH)MIM][Tf_2N] – 1-(2-hydroxyethyl)-3-methylimidazolium bis(trifluorometanosulfonylo)imide; [HMIM][Tf_2N] – 1-hexyl-3-methylimidazolium bis(trifluorometanosulfonylo)imide; [$N_{1(2OH)(2OH)(2OH)}$][Ac] – -methyl-N,N,N-tris(2-hydroxyethyl)ammonium acetate; [$N_{1(2OH)(2OH)(2OH)}$][Tf_2N] – -methyl-N,N,N-tris(2-hydroxyethyl)ammonium bis(trifluorometanosulfonylo)imide; [N_{2114}][Ac] – N-butyl-N,N-dimethyl-N-ethylammonium acetate; [NAIM][Br] – 1-(3-Aminopropyl)-3-ethylimidazole bromide; [P_{4444}][Lev] – tetrabutylphosphonium levulinate; [P_{66614}][Tf_2N] – trihexyl(tetradecyl)phosphonium bis(trifluorometanosulfonylo)imide; [PMIM][Cl] – 1-propyl-3-methylimidazolium chloride; [PMIM][SO_3] – 1-propyl-3-methylimidazolium sulfite.

Among different MOFs that were already treated with ILs during synthesis UiO-67 [309,310], HKUST-1 [312], ZIF-8 [150], ZIF-67 [88], MOF-5 [84,85] or MOF-74 [149] can be distinguished. Mainly, the studies involved the investigation over the morphology-affecting properties of ILs towards MOFs. The use of ILs in solvothermal or ionothermal synthesis approaches [88,313] (as a solvent or co-solvent) as well as in the emulsion-based method [149,150] is owed to the undeniable advantage of ILs, which is their liquidity persisting at different temperatures. ILs can also be utilized in the electrochemical processes to act as the electrolyte thanks to the specific ionic structure and stability in wide range of applied current [84,85]. Additionally, syntheses using IL-modified linker precursors were reported [310,314,315]. IL-containing solutions can be used to conduct the post-synthetical procedure called impregnation or encapsulation. Such approach includes simple dipping and soaking the MOFs in solution with IL. The open pores of MOFs are penetrated and filled by IL moieties, what is usually indicated by the reduced value of specific surface area [149,314]. To minimize the risk of clogged pores subsequent washing procedure after impregnation can be implemented to minimize the IL amount to leave just a thin layer [299]. Apart from physical attachment, ILs can be grafted to the pending groups attached to the linker of MOF [316].

Liu and co-workers studied the possibility to obtain HKUST-1 in ionothermal process, using pure IL – 1-butyl-3-methyl-imidazolium tetrafluoroborate [BMIM][BF_4] [313]. It was very quickly established that such approach is very time consuming, but facilitates obtainment of uniform NPs of MOF. In order to shorten the reaction time, authors proposed the pressure increase inside the reactor by providing high gas pressure and introducing a factor that interacts with the forming structure, to compensate the great viscosity of ILs limiting the nucleation rate. On one hand, such approach enabled elimination of using volatile organic compounds (VOCs) or amides as reaction medium and facilitated the obtainment of very fine NPs. However, on the other hand, the most effective gas able to shorten the time necessary for the synthesis was found to be the CO_2. This is an ideal example showing that the positive effects resulting from changing a given factor will not always be equally positive overall and that we need to look at it from a broader perspective, especially considering the CO_2-related topics .

As an another example of IL utilization in MOF synthesis electrochemical approach can be listed. The 1-butyl-3-methyl-imidazolium bromide [BMIM][Br] [84] and 1-allyl-3-methylimidazolium bis(trifluoromethylsulfonyl) imide [AMIM][Tf_2N] [85] were introduced to the solution containing dissolved linker (H_2BDC) and placed zinc anode. In both cases, it resulted in obtaining MOF-5(Zn) of peculiar flower-like morphology, which was owed to the IL acting as a template. The coordination of BDC and zinc cations can be achieved by arrangement ILs moieties arranged by π- π stacking of imidazole-based cations and thus induction of anion interaction with zinc in enforced way. Similar observation of IL acting as a soft template was made for 1-dodecyl-3-methylimidazolium chloride [DDMIM][Cl] which was added as a co-solvent mixed with glycerol for the synthesis of Zn-BTC [148]. The increasing content of IL in relation to zirconium precursor was visibly changing the shape of MOF particles from rough spheres, which gradually began to flatten and at some point also to

reduce in width, leading to the formation of needle-like structures. Interestingly, the highest crystallinity was observed in materials obtained when the largest amount of ionic liquid was introduced.

Playing the role of structure directing agents, ILs can determine the shape and size of resulting particles, which may significantly influence the other properties of forming structure. This may be the basis for ILs use in emulsion-based synthesis. For example, depending on the length of side chain the properties of forming MOF can be modified. Huang *et al.* used this method to successfully control the morphology of Co-MOF, possessing H_4DOBDC linker in its structure [149]. In the mixture with Triton TX-100, DMF and water four different [PF_6]-based ILs were introduced, possessing ethyl- [EMIM], butyl- [BMIM], octyl- [OMIM] or hexadecyl- [HDMIM] sidechains attached to the imidazolium-based cation. The microemulsion approach let to obtain uniform nanometric Co-MOF with differing specific surface area and shape od particles, depending on the type of IL used. This confirms that by selecting the appropriate structure of the ionic liquid and the method of its introduction to the synthesis medium, diverse morphologies of MOFs and differing performance can be obtained. Additionally, such approach of the synthesis can solve the problem of limited solubility of some chemical compounds in different reaction media. ILs can act as emulsifiers and create structures like for example micelles in the solution [317]. By closing the non-soluble compound inside of the created micelle, the given molecule can be efficiently dissolved. This could potentially be exploited in the synthesis of MOFs in an aqueous medium instead of an amide medium. Such approach is problematic due to the fact that most linkers containing aromatic rings in the structure are not soluble in water.

Additionally, ILs are gaining the interest as reactive precursors of metals in the synthesis of metal-based NPs. The desired metals can be introduced into the structure of a cation, like in $[Zn(CH_3NH_2)_4][Tf_2N]_2$ to obtain hierarchical ZnO nanostructures [318], or an anion – like in case of [BIM][$AuCl_4$] [319] or [OMIM][$FeCl_4$] [320] to obtain Au nanosheets or hierarchical $FeWO_4$ structures. Such approach was not yet reported in the case of MOFs, but could be potentially a very interesting route of synthesis pathway development.

4.4.6. IL-supported synthesis of MOFs dedicated for CO_2 sorption

In the context of improving the sorption properties of MOFs, the vast majority of the reports concerns the post-synthetical use of ILs rather than its introduction to the MOF synthesis environment. This approach is still less popular in the case of MOFs compared to impregnation method, but still can be useful when the synthesis conditions are chosen carefully.

One of the few works on this topic describes the synthesis of ZIF-8(Zn), HKUST-1(Cu), NH_2-UiO-66(Zr) and NH_2-MIL-53(Al) in reverse microemulsion system containig choline dioctylsulfosuccinate [Cho][AOT] together with ethanolammonium formate and R-limonene [311]. The molar ratio of the precursors and IL added was roughly 1.5:8.1:3.75 for n_{Cu}:n_{linker}:n_{IL}. The measured values of CO_2 adsorption at 1 bar reaching respectively 1.78, 0.88, 0.66 and 1.40 mmol·g^{-1}. The work however did not provide the comparison of obtaining these MOFs in conditions

without using IL, therefore it is not possible to clearly state what role the IL played in this particular system.

As an example of MOF which was obtained by the ionothermal method is ZIF-8 prepared at RT in 1-butyl-3-methylimidazolium bis(trifluoromethylsulfonyl) imide [BMIM][Tf_2N] [294]. Even though the specific surface area measured for the IL-obtained MOF was reduced by about 73% compared to pristine ZIF-8, the designated ideal selectivity was increased by over five times in the case of both considered equimolar gas mixtures *i.e.* CO_2/N_2 and CO_2/CH_4. Additionally, the permeability study carried out after attaching the material to polymeric membrane, have shown satisfying permeability especially for CO_2/CH_4 mixture. Such performance was ascribed to the IL moieties remaining after the synthesis in the pores of ZIF-8 simultaneously increasing the sorption performance.

During the synthesis, the molecules of ILs can be also anchored on the additional functionalities of linkers of pristine MOF. IL-functionalized linker was utilized to synthesize UiO-67(Zr). The H_2BPDC linker was modified with 3-metyl-1-propylimidazolium sulfonate and added to the synthesis environment in different ratios with the un-modified linker [309]. With the decreasing content of built H_2BPDC, thus increasing content of IL-modified struts, the specific surface area was gradually decreasing from 2407 $m^2 \cdot g^{-1}$ for pure UiO-67(Zr) to about 325 $m^2 \cdot g^{-1}$ when the ordinary linker was fully replaced. However, the when the linkers were introduced with the ratio of 1:3 (of IL-modified to H_2BPDC), almost doubled CO_2 uptake was observed. Additional post-synthetical binding of sodium salt with the pending IL moieties resulted in even more increased CO_2 sorption capacity, with slight decrease of the surface area. Similar approach using UiO-67 was applied by Ding *et al.* [310] who introduced 1-allyl-3-methylimidazolium bromide. Even though the specific surface area was reduced by almost 60% and the CO_2 sorption properties were practically unchanged compared to pristine UiO-67(Zr), the catalytic performance of the IL-modified UiO-67(Zr) in reaction of cycloaddition of CO_2 to epichlorohydrin was improved, even without using a co-catalyst.

The data regarding the synthetical introduction of ILs in order to improve the CO_2 sorption properties is ambiguous. Even though the research indicates that some properties may deteriorate in such environment, it does not mean that other properties will do as well. Therefore there is a need for further research on this topic.

4.4.7. Post-synthetical IL introduction to MOFs dedicated for CO_2 sorption

Post-synthetic modification of MOF surfaces with ILs gained interest, especially in the context of modifying sorption properties [300]. Several reports describing the use of the classical ILs for the post-synthetical modification of MOFs were found in the literature in the context of altering CO_2 sorption properties, but the works considering the use of AAILs for this purpose are gaining more and more interest.

Xia *et al.* reported simultaneous decrease of S_{BET} (by 60-70%) and CO_2 uptake (by 40-50%) for HKUST-1 modified after the synthesis with 20 wt% of [BMIM][PF_6] and [BMIM][BF_4] [302].

Comparable changes were also observed by Nozari and co-workers for HKUST-1 modified with 30 wt% of [BMIM][PF_6] and [BMMIM][PF_6] [304]. In another study, da Silva *et al.* [301] had used 10 wt% of [BMIM][PF_6] to modify HKUST-1. This resulted in decrease of S_{BET} and CO_2 uptake (at 1 bar, 25 °C) by respectively about 80% and 70%. In the work of Aijaz *et al.*, impregnation of MIL-100(Al) with 1-ethyl-3-methylimidazolium dicyanamide [EMIM][DCA] has increased the CO_2 uptake at 1 bar and 25 °C from 2.5 mmol·g^{-1} to 3.8 mmol·g^{-1} [190].

Promising properties of both materials created by combination of MOFs and TSILs is very limited and ambiguous. However, compared to regular ILs, still AAILs show more promising performance. Philip and Henni modified ZIF-8 [191] and MOF-177 [305] with 10, 20 and 30 wt% of two AAILs, namely [EMIM][Gly] and [EMIM][Ala]. The CO_2 uptake measured at 1 bar and 30 °C nearly doubled for the 30 wt%-modified samples compared to both pristine MOFs. Additionally, gradual decrease of the specific surface area from about 1650 $m^2 \cdot g^{-1}$ for unmodified ZIF-8 to 718 and 635 $m^2 \cdot g^{-1}$ for samples impregned with 30 wt% of [EMIM][Ala] and [EMIM][Gly] respectively was observed. Additionally, in comparison with pristine ZIF-8, [EMIM][Gly]-modified samples achieved higher CO_2 sorption capacity at 30, 40 and 50 °C. Interestingly, the effect was differing depending on the pressure range – up to 1 bar the highest uptake was observed for sample ZIF-8(Zn) impregned with 30 wt% [EMIM][Gly], while above 1 bar for ZIF-8 impregned with 10 wt% [191]. The authors also found that the introduction of AAILs to ZIF-8 have improved the selectivity of MOF towards separation of CO_2 from mixture with N_2 at pressure range below 1 bar [191]. Similar tendency regarding surface area as in the case of Philip and co-workers study was reported by Xia *et al*. However, impregnation of UiO-66(Zr) and NU-1000(Zr) with [EMIM][Gly] and [EMIM][Phe] resulted in decreasing CO_2 uptake at 25 °C at 1 bar (even by about 70%) with increasing amount of AAIL (5, 10 and 30% by volume) [307]. In turn, opposite observations to the studies described by Phillip, were made by Mohamedali *et al.*. Increase of CO_2 uptake at 1 bar and 30 °C from 0.6 to about 0.7 mmol·g^{-1} was observed for ZIF-8 impregnated with 10 wt% of 1-butyl-3-methylimidazolium acetate [BMIM][Ac] and 1-ethyl-3-methylimidazolium acetate [EMIM][Ac]. The same samples at 10 bar have shown values lower by 1 and 2 mmol·g^{-1} compared to pristine ZIF-8 (uptake of about 6 mmol·g^{-1}), respectively [296].

Increase of CO_2 sorption capacity at 40 °C with increasing IL loading (even up to 70 wt%). was reported in the literature for NH_2-UiO-66(Zr) and NH_2-MIL-125(Ti) modified with [BMIM]-based AAILs, with L-glycine and L-arginine acting as anions [308]. Thus, unlike regular ionic liquids (without functional groups), the particular composition of AAILs, possessing pending amino groups, can provide significant improvement fo CO_2 uptake (even up to 317% in comparison with the bare MOF [308]).

This proves that by careful selection of AAIL composition, the excessive pore occupation by ILs (regardless of its introduced amount) leading to decrease of gas sorption uptake of the material can be omitted.

5. Materials and methods

5.1. Materials

The chemicals were purchased and used without further purification. All chemicals were categorized and appear in the order of their first mention in the work. It was noted in details, if products of different purities or suppliers were used in different Chapters.

a) Solvents*: N,N*-dimethylacetamide, DMA (Acros Organics, 99%, pure), dimethylsulfoxide, DMSO (POCH, pure p.a.), 1,4-dioxane (POCH, pure p.a.), *N,N*-dimethylformamide, DMF (POCh, pure p.a., ACS), methanol (POCh, pure p.a.), ethanol (POCh, pure p.a., 99.8%), acetonitrile, MeCN (Merck, LiChrosolv®);

b) Metal precursors: copper(II) nitrate trihydrate (Chempur, pure p.a. (in Chapter 6) or Supelco, for analysis EMSURE® (in Chapters 7 and 8)), copper(II) acetate hydrate (Sigma-Aldrich, ACS reagent, ≥98%), copper(II) tetrafluoroborate hydrate (Sigma-Aldrich, Cu(II) 19-22%), zirconium(IV) chloride (Sigma-Aldrich, for synthesis), cobalt(II) chloride (Sigma-Aldrich, 97%), nickel(II) nitrate hexahydrate (Chempur, pure p.a.), titanium(IV) isopropoxide TTIP (Sigma-Aldrich, 97%);

c) Linkers: trimesic acid, H_3BTC (Sigma Aldrich, 95%), terephthalic acid, H_2BDC (Acros Organics, 99+%), 2-aminoterephtalic acid, NH_2- H_2BDC (Sigma-Aldrich, 99%), biphenyl-4,4′-dicarboxylic acid H_2BPDC (Sigma-Aldrich, 97%);

d) Modulators: acetic acid (POCh, pure p.a., 99.5-99.9%), hydrochloric acid (POCh, 35-38%), tetrafluoroboric acid (Sigma-Aldrich, 48 wt.% in water), nitric acid (POCH, 65%);

e) Ionic liquids: 1-ethyl-3-methylimidazolium chloride [EMIM][Cl] (Acros Organics, 97%), 1-butyl-3-methylimidazolium bromide [BMIM][Br] (IOLI-Tec, 99%);

f) Deuterated solvents: deuterated dimethyl sulfoxide d_6-DMSO (Deutero, 99.8%), deuterated acetonitrile d_3-MeCN (Deutero, 99.8%);

g) Other chemicals: 5-aminoisophtalic acid (Acros Organics, 98%), sodium hydroxide (StanLab, pure p.a.), sodium bicarbonate (POCH, pure p.a.), sodium carbonate (Chempur pure p.a.), sodium sulfite (Chempur pure p.a.), cyanuric chloride (Acros Organics, 99%), trimethylamine TMA (Sigma-Aldrich, 43.0-49.0% in H_2O), L-proline (Pol-Aura, 99.0-101.0%), L-histidine (Pol-Aura, 99.0-101.0%), Amberlite™ IRN-78 hydroxide form (Acros Organics), triethanolamine, TEOA (Chempur, pure p.a.), Nafion D-521 dispersion (Alfa Aesar, 5% w/w in water and 1-propanol), sodium sulfate (Chempur, pure p.a.);

h) Gases: He (Air Liquide, >99.999%), N_2 (Air Liquide, purity grade ≥99.999%), CH_4 (Air Liquide, 99.95%), and CO_2 (Air Liquide, 99.998%), isotopic carbon dioxide $^{13}CO_2$ (Merck, 99%).

5.2. Synthesis of MOFs

5.2.1. Synthesis of H_6TDPAT

2,4,6-tris(3,5-dicarboxylphenylamino)-1,3,5-triazine (H_6TDPAT) – linker for Cu-TDPAT – was prepared according to the literature [66]. 5-aminoisophthalic acid (0.084 mol), sodium hydroxide (0.134 mol), and sodium bicarbonate (0.104 mol) were added to 140 ml water. The mixture was stirred in an ice bath at about 0°C for 30 min, followed by dropwise addition of cyanuric chloride (0.02 mol) solution in 1,4-dioxane (70 mL). The mixture was then heated at 100ºC for 24h. The resulting solution was adjusted to pH=2 with HCl solution. The solid was collected by filtration, rinsed several times with distilled water, centrifuged and dried at 80°C to give H_6TDPAT. Successful synthesis of linker was confirmed by NMR.

H_6TDPAT 400 MHz ^{1}H-NMR (DMSO, δ/ppm): 8.12(s, 3H), 8.47(s, 6H), 9.68(s, 3H), 13.01(s, 3H)

5.2.2. Synthesis of Cu-TDPAT

The general procedure of Cu-TDPAT synthesis was adapted from [66]. First, the chosen copper(II) hydrate (2.04, 0.441 or 0.147 mmol, according to the molar ratio n_{Cu}:n_{linker} equal to 13.9:1, 3:1 or 1:1, respectively) was dissolved in 12 mL of the chosen solvent mixture (pure DMF, DMA/DMSO, DMF/DMSO, DMF/EtOH/water, DMF/water; the volumes of individual solvents were equal) and 0.3 mL of water (only if it was not included in the solvent mixture). After that, 0.147 mmol of H_6TDPAT was added and dissolved by using ultrasounds. Upon adding acid (20.4, 10.2 or 0 mmol), the mixture was sealed in a 100 mL PBT-capped glass Schott bottle and heated at chosen temperature and time. After cooling down to RT, the product was filtered, centrifuged and washed with the specific amide and methanol twice. After that, powders were dried in a vacuum oven for 24 hours at 85 °C. Activation of MOF prior to the measurements was described in Supporting Information. The content of all reagents was scaled up proportionally in larger vessels. The labels of all products with full synthesis parameters were shown in Table 5.1.

The yield was calculated taking into consideration product before activation in respect to the theoretical Cu-TDPAT yield based on the amount of added linker. $[Cu_3(TDPAT)(H_2O)_3]\cdot 10H_2O\cdot 5DMA$ (M_w = 1472.67 g·mol^{-1}) and $[Cu_3(TDPAT)(H_2O)_3]\cdot 10H_2O\cdot 5DMF$ (M_w = 1402.52 g·mol^{-1}) chemical formulas were used for calculations for samples obtained in DMA- and DMF-based environments respectively [66].

Table 5.1 Details of synthesis reagents calculated per 100 mL of the reaction vessel volume

Entry	Synthesis parameters										
	Solvents	Volume of water (mL)	Time (h)	Temp. (°C)	Vessel (mL)[a]	Molar ratio n_{Cu}:n_{linker}	Copper source	n_{Cu} (mmol)	n_{inker} (mmol)	Acid	Volume of acid (mL)
DD-65C	6 mL DMA, 6 mL DMSO	0.3	72	65	SB (100)	13.9:1	$Cu(NO_3)_2•3H_2O$	2.04	0.147	HBF_4	2.7
DD-65C-120h	6 mL DMA, 6 mL DMSO	0.3	120	65	SB (100)	13.9:1	$Cu(NO_3)_2•3H_2O$	2.04	0.147	HBF_4	2.7
DD-65C-120h-3/1	6 mL DMA, 6 mL DMSO	0.3	120	65	SB (100)	3:1	$Cu(NO_3)_2•3H_2O$	0.441	0.147	HBF_4	2.7
DD-75C	6 mL DMA, 6 mL DMSO	0.3	72	75	SB (250)	13.9:1	$Cu(NO_3)_2•3H_2O$	2.04	0.147	HBF_4	2.7
Cu-TDPAT(DD)	6 mL DMA, 6 mL DMSO	0.3	72	85	SB (500)	13.9:1	$Cu(NO_3)_2•3H_2O$	2.04	0.147	HBF_4	2.7
DD-R	6 mL DMA, 6 mL DMSO	0.3	72	85	R (200)	13.9:1	$Cu(NO_3)_2•3H_2O$	2.04	0.147	HBF_4	2.7
DD-3/1	6 mL DMA, 6 mL DMSO	0.3	72	85	SB (100)	3:1	$Cu(NO_3)_2•3H_2O$	0.441	0.147	HBF_4	2.7
DD-1/1	6 mL DMA, 6 mL DMSO	0.3	72	85	SB (50)	1:1	$Cu(NO_3)_2•3H_2O$	0.147	0.147	HBF_4	2.7
DD-AcO	6 mL DMA, 6 mL DMSO	0.3	72	85	SB (250)	13.9:1	$Cu(AcO)_2•H_2O$	2.04	0.147	HBF_4	2.7
DD-AcO-R	6 mL DMA, 6 mL DMSO	0.3	72	85	R (200)	13.9:1	$Cu(AcO)_2•H_2O$	2.04	0.147	HBF_4	2.7
DD-AcO-3/1	6 mL DMA, 6 mL DMSO	0.3	72	85	SB (250)	3:1	$Cu(AcO)_2•H_2O$	2.04	0.147	HBF_4	2.7
DD-BF_4	6 mL DMA, 6 mL DMSO	0.3	72	85	SB (100)	13.9:1	$Cu(BF_4)_2•H_2O$	2.04	0.147	HBF_4	2.7
DD-BF_4-HNO_3	6 mL DMA, 6 mL DMSO	0.3	72	85	SB (100)	13.9:1	$Cu(BF_4)_2•H_2O$	2.04	0.147	HNO_3	1.44
DD-95C	6 mL DMA, 6 mL DMSO	0.3	72	95	SB (250)	13.9:1	$Cu(NO_3)_2•3H_2O$	2.04	0.147	HBF_4	2.7
DD-95C-AcO	6 mL DMA, 6 mL DMSO	0.3	72	95	SB (250)	13.9:1	$Cu(AcO)_2•H_2O$	2.04	0.147	HBF_4	2.7
DMF-65C	12 mL DMF	0.3	72	65	SB (100)	13.9:1	$Cu(NO_3)_2•3H_2O$	2.04	0.147	HBF_4	2.7
DMF-75C	12 mL DMF	0.3	72	75	SB (250)	13.9:1	$Cu(NO_3)_2•3H_2O$	2.04	0.147	HBF_4	2.7
Cu-TDPAT(DMF)	12 mL DMF	0.3	72	85	SB (500)	13.9:1	$Cu(NO_3)_2•3H_2O$	2.04	0.147	HBF_4	2.7
DMF-R	12 mL DMF	0.3	72	85	R (200)	13.9:1	$Cu(NO_3)_2•3H_2O$	2.04	0.147	HBF_4	2.7
DMF-0A	12 mL DMF	0.3	72	85	SB (100)	13.9:1	$Cu(NO_3)_2•3H_2O$	2.04	0.147	-	-
DMF-0.5A	12 mL DMF	0.3	72	85	SB (100)	13.9:1	$Cu(NO_3)_2•3H_2O$	2.04	0.147	HBF_4	1.35
DMF-3/1	12 mL DMF	0.3	72	85	SB (250)	3:1	$Cu(NO_3)_2•3H_2O$	0.441	0.147	HBF_4	2.7
DMF-AcO	12 mL DMF	0.3	72	85	SB (250)	13.9:1	$Cu(AcO)_2•H_2O$	2.04	0.147	HBF_4	2.7
DMF-AcO-3/1	12 mL DMF	0.3	72	85	SB (100)	3:1	$Cu(AcO)_2•H_2O$	0.441	0.147	HBF_4	2.7
DMF-3/1-HNO_3	12 mL DMF	0.3	72	85	SB (250)	3:1	$Cu(NO_3)_2•3H_2O$	0.441	0.147	HNO_3	1.44
DMF-95C	12 mL DMF	0.3	72	95	SB (250)	13.9:1	$Cu(NO_3)_2•3H_2O$	2.04	0.147	HBF_4	2.7
Cu-TDPAT(DMF/DMSO)	6 mL DMF, 6 mL DMSO	0.3	72	85	SB (250)	13.9:1	$Cu(NO_3)_2•3H_2O$	2.04	0.147	HBF_4	2.7
DMF/DMSO-0A	6 mL DMF, 6 mL DMSO	0.3	72	85	SB (100)	13.9:1	$Cu(NO_3)_2•3H_2O$	2.04	0.147	-	-
Cu-TDPAT(DWE)	4 mL DMF, 4 mL ethanol, 4 mL water	-	72	85	SB (250)	13.9:1	$Cu(NO_3)_2•3H_2O$	2.04	0.147	HBF_4	2.7
Cu-TDPAT(DW)	6 mL DMF, 6 mL water	-	72	85	SB (100)	13.9:1	$Cu(NO_3)_2•3H_2O$	2.04	0.147	HBF_4	2.7

[a]R – reactor (steel autoclave with Teflon liner), SB - Schott bottle, (V) - volume of vessel in mL;

5.2.3. Synthesis of HKUST-1

HKUST-1 was prepared according to the literature with minor modifications [75]. Copper(II) nitrate trihydrate (2.19 g) and trimesic acid (1.18 g) was completely dissolved in 30 mL DMF/H_2O/EtOH mixture (1:1:1 by volume) in a 100 mL Schott bottle tightly sealed with PBT cap and kept in an oven at 85 °C for 20 h to yield small, blue octahedral crystals. After cooling the flask to room temperature, the mother liquor was decanted. The crystals were rinsed and centrifuged with fresh DMF (thrice) and with methanol (twice), finishing with vacuum drying for 24 hours at 85 °C.

5.2.4. Synthesis of UiO-66(Zr)

UiO-66(Zr) was prepared based on Schaate et al. work [79]. Zirconium(IV) chloride (1.715 mmol) and acetic acid (51.45 mmol) were dissolved in 100 mL of DMF by using ultrasounds. Terephthalic acid (1.715 mmol) was added to the clear solution and fully dissolved by using ultrasounds again. The molar ratio of added $ZrCl_4$, H_2BDC and acetic acid was equal 1:1:30. The tightly capped 500 mL Schott bottles were kept in an oven at 120°C under static conditions for 24 h. Then the solutions were cooled to room temperature. The precipitates were isolated by centrifugation and washed with DMF three times, twice with methanol and then vacuum dried for 24 hours at 85°C.

5.2.5. Synthesis of NH_2-UiO-66(Zr)

NH_2-UiO-66 was prepared based on Schaate et al. work [79]. Zirconium(IV) chloride (1.715 mmol) and 2.96 mL of acetic acid (51.45 mmol) were dissolved in 100 mL DMF by using ultrasounds. 2-aminoterephthalic acid (1.715 mmol) was added to the clear solution and fully dissolved by using ultrasounds again. Next, 0.125 mL of deionized water was added to the solution. The tightly capped 500 mL Schott flasks were kept in an oven at 120°C under static conditions for 24 h. Then the solutions were cooled to room temperature. The precipitates were isolated by centrifugation and washed with DMF three times, twice with methanol and then vacuum dried for 24 hours at 85°C.

5.2.6. Synthesis of UiO-67(Zr)

UiO-67(Zr) was prepared based on Schaate *et al*. work [79]. In 500 mL Schott bottle, zirconium(IV) chloride (2.57 mmol) and acetic acid (4.41 mL) were dissolved in 50 mL DMF by using ultrasounds for about 3 minutes. Biphenyl-4,4’-dicarboxylic acid (2.57 mmol) was added to the clear solution. After addition of 50 mL of DMF, the solution was treated with ultrasounds until fully dissolved. The tightly capped bottle was kept in an oven at 120°C under static conditions for 24 h. Then the solution was cooled to room temperature. The precipitate was isolated by centrifugation, washed with DMF three times and then washed two times with methanol. The product was vacuum dried at 80 °C for 24 h.

5.2.7. Synthesis of NH_2-MIL-125(Ti)

NH_2-MIL-125(Ti) was prepared based on Cheng *et al.* work [321]. In a 200 mL Teflon liner, 2-aminoterephtalic acid (12 mmol) and acetic acid (8 mL) were dissolved in 80 mL DMF/methanol mixture (9:1 by volume) by using magnetic stirring. 8 mmol of titanium(IV) isopropoxide (TTIP) was added to the clear solution. After homogenization, the stirring bar was taken out. The tightly closed stainless-steel autoclave with the Teflon liner was kept in an oven at 150 °C under static conditions for 24 h. The solution was cooled to room temperature. The precipitate was isolated by centrifugation, washed with DMF three times and then washed two times with methanol. The product was vacuum dried at 80 °C for 24 h.

5.3. Synthesis of AAILs

AAILs were prepared according to the literature with minor modifications [291]. The chosen commercial ionic liquid was dissolved in water to obtain 2 $mol \cdot L^{-1}$ solution. Then, the ion-exchange resin was added to the solution (molar ratio 2:1 of resin to IL) to obtain [cation][OH] form. The amount of resin was divided into two equal portions, allowing 1 day of reaction for each addition. A 1.1 mol equivalent of the appropriate amino acid – L-histidine or L-proline – was added in portions to the filtered solution and stirred for 24 hours. Excess water was later removed with a rotary evaporator equipped with heating bath. Cold methanol and acetonitrile mixture (1:9 by volume) was used to crystallize remaining unreacted amino acid, which was further removed by vacuum filtration. The washing-filtration cycle was repeated in case amino acid presence was confirmed. Solvent and water residues were eliminated by pulling a moderate vacuum at 60 °C for approximately one week. Successful synthesis of the amino acid ionic liquids was confirmed by FTIR-ATR and ^{1}H NMR:

[EMIM][His] 400 MHz ^{1}H-NMR (DMSO, δ/ppm): 1.41 (t, 3H, J=7.3Hz), 2.43(dd, 1H, J=14.7, 7.2Hz), 2.83(d, 1H, J=9.7), 3.01(bs, 1H), 3.85(s, 3H), 4.20 (q, 2H, J=7.3Hz), 6.58(s, 1H), 7.39(s, 1H), 7.71(s, 1H), 7.79(s, 1H), 9.33(s, 1H).

[EMIM][Pro] 400 MHz ^{1}H-NMR (DMSO, δ/ppm): 1.41(t, 3H, J=7.3Hz), 1.47(dd, 1H, J=13.4, 5.9 Hz), 1.61-1.50(m, 1H), 1.68(bs, 1H), 1.79(ddd, 1H, J=15.9, 12.2, 7.7 Hz), 2.64(bs, 1H), 2.96(ddd, 1H, J=10.7, 7.0, 5.3 Hz), 3.17(bs, 1H), 3.86(s, 3H), 4.20(q, 2H, J=7.3Hz), 7.72(s, 1H), 7.81(s, 1H), 9.38(s, 1H).

[BMIM][His] 400 MHz ^{1}H-NMR (DMSO, δ/ppm): 0.90 (t, 3H, J=7.4Hz), 1.32-1.18(m, 2H), 1.83-1.68(m, 2H), 2.44(dd, 1H, J=14.7, 7.2Hz), 2.83(d, 1H, J=12.0), 3.02(bs, 1H), 3.86(s, 3H), 4.17 (t, 2H, J=7.3Hz), 6.59(s, 1H), 7.39(s, 1H), 7.72(s, 1H), 7.79(s, 1H), 9.35(s, 1H).

[BMIM][Pro] 400 MHz ^{1}H-NMR (DMSO, δ/ppm): 0.90(t, 3H,J=7.4), 1.31-1.21(m, 2H), 1.45-1.35(m, 2H), 1.56-1.46(m, 2H), 1.81-1.69(m, 2H), 2.98-2.87(m, 1H), 3.25-3.16(m, 1H), 3.10(bs, 1H), 3.86(s, 3H), 4.17(t, 2H, J=7.2), 7.72(s, 1H), 7.79(s, 1H), 9.36(s, 1H).

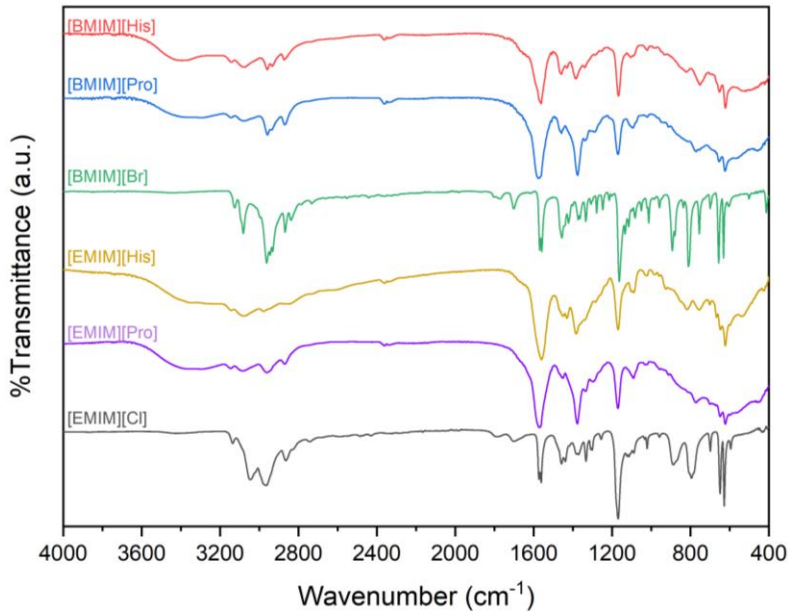


Figure 5.1 FTIR spectra of prepared AAILs in comparison with primary commercial ILs; methodology was described in Subsection 5.6.9;

5.4. Methods of MOFs modification

5.4.1. Preparation of HKUST-1 in presence of AAILs (incorporation)

Incorporation of AAILs to HKUST-1 was performed in analogous way as the synthesis of the pristine sample (described in details in Subsection 5.2.3). For modification, [BMIM][Br] was used as received and the AAILs were synthesized as described in details in ection 5.3. Molar ratios between substrates were $n_{Cu}:n_{linker}:n_{IL}$ = 1.6:1:0.25 or 1.6:1:0.1. Briefly, copper(II) nitrate trihydrate (2.19 g) and trimesic acid (1.18 g) were completely dissolved in 25 mL DMF/H_2O/EtOH mixture (1:1:1 by volume) and the suitable amount of IL was dissolved in 5 mL of the same mixture. The solutions were then mixed and tightly sealed in 100 mL Schott bottle with PBT cap and kept in an oven at 85 °C for 20 h. After cooling the flask to RT, the mother liquor was decanted. The obtained modified MOF crystals were rinsed and centrifuged with fresh DMF (thrice) and with methanol (twice), finishing with vacuum drying for 24 hours at 85 °C. After synthesis, samples were kept in desiccator.

5.4.2. Preparation of IL@HKUST-1 (post-synthetical impregnation)

In a glass vial, 500 mg of pre-activated MOF was dispersed in 10 mL of absolute ethanol containing 5 mg (1% in relation to MOF mass) or 50 mg (10% in relation to MOF mass) of the chosen IL in relation to HKUST-1. The sealed vial with dispersion was first mixed at RT with a magnetic stirrer for 8 hours. After that, to let the solvent evaporate slowly, the glass vial was kept uncapped and its content was gently stirred at 100 rpm overnight at 80 °C. The as-prepared sample was then dried in the oven at 150 °C under vacuum for 24 hours.

5.4.3. Incorporation of non-noble metals (Ni, Cu, Co) into UiO-66(Zr) and NH_2-UiO-66(Zr)

The metal modified UiO-66(Zr) and NH_2-UiO-66(Zr) were prepared analogously to pristine MOFs (as described in Subsections 5.2.4 and 5.2.5). After dissolution of the linker 1 mL of the DMF solution containing chosen metal precursor (that is 0.5 mol% of non-noble metal precursor in relation to zirconium precursor) was added to the synthesis environment. The rest of the synthesis procedure remained unchanged.

5.4.4. Photochemical deposition of different metals (Ni, Cu, Co) on UiO-66(Zr) and NH_2-UiO-66(Zr)

Activated UiO-66(Zr) or NH_2-UiO-66(Zr) (0.20 g) was dispersed in 30 mL of ethanol in a 50 mL glass reactor, equipped with quartz window. Then, ethanol solution containing 0.5 wt% of $Cu^{2+,}$ Co^{2+} or Ni^{2+} (in relation to mass of MOF used) was added to the suspension and held under N_2 flow for 30 minutes with magnetic stirring. The as-prepared dispersion was treated with UV-Vis light for 60 minutes using 1000 W Xe lamp (ORIEL Instruments). PM100D Optical Power Meter (ThorLabs) was used to measure the light flux – equal to 200 $mW \cdot cm^{-2}$ and 205 $mW \cdot cm^{-2}$ for Vis (at 420 nm) and UV-Vis (at 350 nm) respectively. The precipitates were further isolated by centrifugation and washed with ethanol. The powder was then vacuum dried for 24 hours at 85 °C.

*5.4.5. Synthesis of composite **1** (UiO-67(Zr)+IL→NH_2-MIL-125(Ti))*

UiO-67(Zr) was prepared analogously as described in Subsection 5.2.6 with an additional step directly before the thermal treatment. Namely, 94.2 mg of [EMIM][Cl] (giving molar ratio of substrates equal to n_{H2BPDC}:n_{ZrCl4}:$n_{[EMIM][Cl]}$ = 1:1:0.25) was added to the synthesis environment and dissolved by using ultrasounds. 500 mg of the obtained product was then dispersed in the synthesis environment of NH_2-MIL-125(Ti), which was performed according to procedure described in Subsection 5.2.7.

*5.4.6. Synthesis of composite **2** (UiO-67(Zr)→IL→NH_2-MIL-125(Ti))*

UiO-67(Zr) was prepared as described in Subsection 5.2.6, after which 500 mg of the obtained powder was dispersed in 15 mL of acetone containing 50 mg [EMIM][Cl] (10% in relation to the used mass of solid). The suspension was slowly stirred at 50 °C to evaporate the solvent and then added to the synthesis medium of NH_2-MIL-125(Ti), which was performed according to procedure described in Subsection 5.2.7.

*5.4.7. Synthesis of composite **3** (UiO-67(Zr)→NH_2-MIL-125(Ti)+IL)*

UiO-67(Zr) was prepared as described above (Subsection 5.2.6), after which 500 mg of the obtained powder along with 293.2 mg of [EMIM][Cl] (giving molar ratio of the substrates equal to $n_{NH2\text{-}BPD}$:n_{TTIP}:$n_{[EMIM][Cl]}$ = 1.5:1:0.25) were directly added to the synthesis medium of NH_2-MIL-125(Ti) (procedure described in Subsection 5.2.7).

*5.4.8. Synthesis of composite **4** (UiO-67(Zr)→NH_2-MIL-125(Ti))*

UiO-67(Zr) was prepared as described above (Subsection 5.2.6), after which 500 mg of the obtained powder was added to the synthesis medium of NH_2-MIL-125(Ti) (procedure described in Subsection 5.2.7).

*5.4.9. Synthesis of composite **5** (UiO-67(Zr)→NH_2-MIL-125(Ti)→IL)*

Composite 5 was synthesized in the same manner as composite 4 (Subsection 5.4.8). After the synthesis, 1.5 g of as-prepared powder was dispersed in 20 mL of acetone containing 150 mg of [EMIM][Cl] (10% in relation to the used mass of solid). The suspension was slowly stirred at 50 °C to evaporate the solvent.

5.5. Activation of MOFs

Prior to the measurements, the as-synthesized samples were dispersed in 20 mL of methanol. For the next five days solvent was replaced with fresh portion. The exchange was performed five times a day at two-hour intervals. After that time, solvent was decanted, and the samples were dried in the oven at 150 °C under vacuum for 24 hours. Samples after post-synthetical impregnation with AAILs (Chapter 7) were only treated with the temperature and decreased pressure, without repeating solvent-exchange procedure.

5.6. Characterization of the samples

All methods utilized to characterize the prepared samples are listed below. If different equipment was used for a given method or other experimental conditions were used, this information is included in the description.

5.6.1. Powder X-ray diffraction (XRD)

Powder X-ray diffraction (XRD) measurements were carried out on a Rigaku MiniFlex 600 diffractometer equipped with Cu K_α irradiation source. The 2θ measurement range was from 2° up to 40° (Chapter 9), 60° (Chapter 8) or 70° (Chapter 6 and 7).

The amount of missing-linker defects, described in Chapter 8, was evaluated using following equation:

$$Rel(I)_{B.P.} = \frac{I(Broad\ peak)}{\left(\frac{I(111)+I(200)+I(600)}{3}\right)} \qquad \text{Eq. 1}$$

where I(Broad peak) stands for the intensity of the peak corresponding to the **reo** nanoregions, I(111), I(200) and I(600) correspond with the intensities of (111), (200) and (600) reflexes respectively.

5.6.2. N_2 adsorption isotherm at -196 °C

The specific surface area (S_{BET}) of the obtained materials was designated by using the Brunauer-Emmett-Teller (BET) nitrogen adsorption isotherms measured at -196 °C.

The BET isotherms of materials described in Chapters 7 and 8 were measured with Gemini V model 2365 (Micromeritics) within the relative pressure (P/P_0) range of 0.1–0.25 and 0.1–0.3, respectively. The surface area was determined by the multipoint BET method using the collected adsorption data. All samples were degassed under vacuum at 150 °C prior to the nitrogen adsorption measurements.

The BET isotherms of materials described in Chapters 6 and 9 were measured using BSD-660 analyzer (BeiShiDe Instrument Technology). The measurement procedure included *in situ* four-stage degassing at 150 °C directly before the gas adsorption. The surface area was determined by the multipoint BET method using the adsorption data in the relative pressure (P/P_0) range of 0.001–0.1, ensuring linear characteristic of chosen isotherm fragment. All S_{BET} values were designated taking into consideration at least five data points and that the C coefficient of the obtained BET equation was positive. The values of micropore surface area, total pore volume and pore size distribution were designated by using the apparatus software.

5.6.3. Thermogravimetric analysis (TGA)

Thermogravimetric analysis (TGA) was conducted using TGA2 SF/1100 (Mettler Toledo) apparatus. Alumina crucibles of 70 µl volume were loaded with few milligrams of powder samples. Analysis was carried out under a flow of chosen gas (50 $mL \cdot min^{-1}$), at a heating rate of 10 $°C \cdot min^{-1}$. The measurements described in Chapters 6 and 7 were carried out under N_2 atmosphere (50-800 °C), while in Chapters 8 and 9 under air atmosphere (25-800 °C). In the case of ILs studied in Chapter 7, to get rid of the easily absorbed moisture, additional 2-hours long isothermal segment at 100 °C was added before the dynamic segment (up to 1000 °C).

5.6.4. Diffuse reflectance spectroscopy (DRS)

In Chapter 8, the diffuse reflectance spectroscopy (DRS) was performed using a UV-vis spectrophotometer UV-2600 (Shimadzu) in the wavelength range of 250–600 nm. In Chapter 9, the measurement was carried out using a UV-Vis Evolution 220 spectrophotometer (Thermo Fisher Scientific) in the wavelength range of 200–800 nm.

5.6.5. Photoluminescence (PL)

The photoluminescence (PL) spectra of materials described in Chapters 8 and 9 were registered with a LS-50B (PerkinElmer) luminescence spectrometer with a xenon discharge lamp in the wavelength range from 300 to 700 nm at an excitation wavelength of 330 nm.

Luminescence decay curves presented in Chapters 8 were collected using a grating spectrograph Acton 2500i (Princeton Instr.) equipped with CCD streak camera C5680 (Hamamatsu) operating in the spectral range of 200–1100 nm with a temporal resolution of 50 ps.

A femtosecond laser Libra-S (Coherent) coupled to an optical parametric amplifier OPerASolo (Light Conversion) was used as an excitation source.

5.6.6. Volumetric CO_2 adsorption

The volumetric CO_2 adsorption-desorption isotherms were collected for all materials described in this work.

The measurements at -50 and 25 °C were carried out using Micro 200C analyzer (3P Instrument) for samples described in Chapters 7 (only at 25 °C) and 8 (both temperatures). All samples were degassed under vacuum at 150 °C directly prior to the CO_2 adsorption measurements. The volumetric CO_2 sorption capacity at 0 °C and 25 °C for materials described in Chapters 6 and 9 were measured using BSD-660 analyzer (BeiShiDe Instrument Technology). The measurement procedure included *in situ* four-stage degassing at 150 °C directly before the gas adsorption.

5.6.7. Optical microscopy

Delta Optical MET-1000-TRF optical microscope equipped with ToupTek Photonics MTR3CMOS20000KPA digital camera and a ToupView program were used to obtain images in reflectance mode (Chapter 6).

5.6.8. Scanning electron microscopy (SEM) and transmission electron microscopy (TEM)

High resolution scanning electron microscopy (HRSEM) in a high vacuum mode was performed using JSM-7610F unit (JEOL) to establish the particles' size and morphology.

The additional imaging presented in Chapters 8 and 9 was performed by scanning-transmission electron microscopy (STEM) coupled with energy-dispersive X-ray spectroscopy (EDS) by using Titan G2 60‑300 (FEI) to analyze the morphology and elemental distribution.

In Chapter 7, the elemental analysis and mapping were carried out using SEM 1430 VP (LEO Electron Microscopy Ltd) equipped with energy dispersive X-ray spectrometer Quantax 200 with XFlash 4010 detector (Bruker).

5.6.9. Fourier Transform Infrared Spectroscopy (FTIR)

Fourier Transform Infrared Spectroscopy (FTIR) was performed by using three different sampling methods: attenuated total reflectance (ATR-FTIR), transmission and *In situ* diffuse reflectance infrared Fourier transform spectroscopy (DRIFTs). All of them used the basic Nicolet iS10 (Thermo Fisher Scientific) unit equipped with a radiation source (HeNe laser). Additional unit, Nicolet iZ10 (Thermo Fisher Scientific) with liquid nitrogen cooled HgCdTe detector (MCT), was used for DRIFTs.

ATR accessory was equipped with diamond window. The spectra were recorded in the wavenumber range of 400-4000 cm^{-1} with a resolution of 4 cm^{-1}, 16 scans. This sampling method was used for analysis of ionic liquids (Chapter 7 and 9).

The use of Smart OMNI-Transmission™ accessory for transmission sampling method required preparation of powder samples in a form of pressed tablets. Pellets were prepared with mass ratio of 1:100 of MOF to KBr by grinding and further pressing with Mini-Pellet Press (Specac) into dedicated cells. The measurements were conducted at room temperature and ranged from 400 cm^{-1} to 4000 cm^{-1} with the resolution of 4 cm^{-1}. Prior to the measurement, the background spectrum was taken by using pellet consisting only of KBr. Method was used for MOF samples described in Chapters 6 and 7 with number of sample scans of 64 and 16 respectively.

The measuring system for *In situ* DRIFTs was equipped with Praying Mantis Diffuse Reflection Accessory (Harrick Scientific Products) placed in the Nicolet iZ10 unit. Samples were placed in the dedicated sample cup in High temperature reaction chamber (HVC) with ZnSe windows and Temperature Controller (Harrick Scientific Products). A steel mesh was placed on the bottom of the cup and filled with sample grinded with KBr with mass ratio of 1:100. The measurement was conducted at 150 °C under a nitrogen flow (30 $mL \cdot min^{-1}$) with previous conditioning in these conditions for one hour. Prior to that, the background spectrum was taken under identical conditions in the presence of KBr alone. All spectra were obtained with 32 scans at a resolution of 4 cm^{-1} in range 650-4000 cm^{-1}. Method was used to characterize chosen materials described in all Chapters.

5.6.10. X-ray Photoelectron Spectroscopy (XPS)

XPS measurements described in Chapter 8 were conducted using multi-chamber UHV analytical system (Prevac). The system was equipped with VG Scienta SAX 100 X-ray lamp with an aluminum anode as the source of photoelectron excitation (Al K_α radiation source), with a VG Scienta XM 780 monochromator.

5.6.11. Inductively coupled plasma - optical emission spectrometry (ICP-OES)

Amount of the introduced Cu, Co and Ni to samples described in Chapter 8 was analyzed by 5100 ICP-OES (Agilent Technologies) apparatus in accordance with PN EN ISO 11885:2009.

5.6.12. Elemental analysis

CHNS-O Flash 2000 (Thermo Scientific) was utilized to determine elemental composition of the samples in Chapter 7. The powder sample was closed tightly in a dedicated tin foil containers (5 x 8 mm).

5.6.13. Nuclear magnetic resonance spectroscopy (NMR)

Nuclear magnetic resonance spectroscopy (NMR) was performed using Bruker Avance III HD 400 MHz with three-channel TXI probe. Prior the measurement samples were placed in dedicated quartz tubes and dissolved in suitable deuterated solvent.

5.6.14. Gravimetric CO_2 sorption

The CO_2, CH_4 and N_2 sorption-desorption equilibrium isotherms were measured with gravimetric approach for samples described in Chapter 7. Measurements were performed at 25 °C

and in the range of 0-10 bar using apparatus with a high-accuracy ISOSORP 2000 magnetic-suspension balance (Rubotherm GmbH) coupled with double measuring cell providing possibility of simultaneous analysis of two samples [322].

The measuring system consisted of the gravimetric apparatus is a high-accuracy ISOSORP 2000 magnetic-suspension balance (Rubotherm GmbH) coupled with double measuring cell providing possibility of simultaneous analysis of two samples. Temperature inside the unit was controlled with F32-HL circulation thermostat (Julabo GmbH). Three separate pressure transducers dedicated for different pressure ranges were used *i.e.* for 0−1 bar – Baratron model 627D (MKS Instruments GmbH), for 0−10 bar – PX01C1-150A5T (Omegadyne Inc.), and for 0-30 bar – PX01C1-500A5T (Omegadyne Inc.). The pressure indication was supervised and documented by an in-house Labview-developed software.

After placing the pre-activated samples in the dedicated cell inside of the apparatus chamber and after checking the lack of gas leak in the assembled system, the circuit was degassed at 90 °C under vacuum for 4 h to get rid of eventual humidity and impurities still adsorbed into MOF pores during preparation procedure. After that, helium pycnometry at 40 °C was performed (procedure presented in details by Esteves *et al* [323]) to determine the solid matrix density of the samples. The main procedure of gas sorption-desorption equilibrium measurements at 25 °C was identical for N_2, CH_4 and CO_2. Complete regeneration of the samples upon sorption-desorption isotherms allowed that the measurements of the listed ordered gases were performed immediately after each other without removing the samples from the apparatus chamber. Once the temperature stabilized, the sorption equilibrium isotherm started at vacuum. The chosen gas was dosed slowly to reach desired pressure-steps. For sorption isotherm following measuring points were chosen: 0.15, 0.3, 0.7, 0.85, 1.0, 2.0, 4.0, 7.0 and 10 bar. After stabilization of the pressure, temperature and the mass shown by the ISOSORP 2000 balance, the sorption equilibrium data point was noted, and the portion of gas was dosed to reach next measurement point. Once the last adsorption point was reached and stabilized, desorption procedure started through depressurization steps to obtain the desorption equilibrium isotherm. For desorption equilibrium isotherm the following measuring points were chosen: 8.5, 5.5, 3.0, 1.5 and 0.6 bar.

The adsorbed gas amount can be reported in net (q_{net}), excess (q_{exc}) or total adsorption (q_t) quantities. Herein, the net adsorption quantity was considered, and it refers to the difference between the amount of sorbate found in a measurement cell with and without the presence of the sorbent [324]. The specific net amount sorbed (q_{net}) (expressed in unit of mol of gas per mass of sorbent) is expressed by the following equation

$$q_{net} = \frac{m - m_s - m_h + V_h \rho_g}{m_s M_W} \qquad \text{Eq. 2}$$

where

m – apparent weight indicated by the balance,

m_s – mass of degassed sorbent inside the sample holder,

m_h – mass of measuring sample holder contributing to buoyancy effects,

V_h – volume of measuring sample holder contributing to buoyancy effects,

ρ_g – gas density assessed from NIST Chemistry WebBook at equilibrium pressure and temperature conditions (in respect to the measured equilibrium data points), and

M_w – is the molecular weight of the sorbed gas.

The use of net quantity avoids uncertainty related to the used of probe molecules (e.g., He, N_2) for the determination of the required reference state. However, adsorption-desorption data in the literature is still largely reported in excess (q_{exc}) or total (q_t) quantities. The excess value is the amount of adsorbed gas in excess of the amount that would be present in the same solid-gas system if the adsorbate was at the equilibrium density of the bulk gas. Expressed in moles of adsorbed gas per unit mass of sorbent, net and excess (q_{exc}) quantity are related to following dependence:

$$q_{exc} = q_{net} + V_s \rho_g \qquad \text{Eq. 3}$$

where $V_s = 1/\rho_s$ is the specific solid volume of the sorbent that is impenetrable to the sorbate, value of which can be determined by He pycnometry.

The obtained data was analyzed with Sips and Toth adsorption equilibrium isotherm models by fitting it to the following equations:

Sips (Langmuir-Freundlich) equation:

$$q(P) = \frac{q_s (bP)^{1/n}}{1 + (bP)^{1/n}} \qquad \text{Eq. 4}$$

where q_s – saturation concentration, b – isotherm constant, n – heterogeneity factor;

Toth equation:

$$q(P) = q_s \frac{(bP)}{[1 + (bP)^t]^{1/t}} \qquad \text{Eq. 5}$$

where q_s – saturation concentration, b – isotherm constant, t – heterogeneity factor.

The excess amounts adsorbed are expressed in moles of adsorbed gas per unit mass of sorbent *i.e.* $mmol \cdot g^{-1}$.

Ideal selectivities of binary gas mixtures were calculated according to Ideal Adsorbed Solution Theory (IAST) using equation:

$$S_{\frac{CO_2}{X}} = \frac{q_{s\ CO_2}/q_{s\ X}}{p_{CO_2}/p_X} \qquad \text{Eq. 6}$$

where p_i stands for the partial pressure of *i* gas component, and X – CH_4 or N_2

5.6.15. Photoelectrochemical measurement procedure

The photoelectrochemical measurements were carried out for samples described in Chapter 9.

To obtain the working electrode MOF samples were deposited on fluorine-doped tin oxide (FTO). The FTO glass substrates (2.5 cm x 1.0 cm x 2.2 mm) were cleaned by submerging in pure ethanol and treatment with ultrasounds for about 5 minutes. After that time, glass was dried with stream of hot air. The area of the conductive side of the substrate that was to remain uncoated (area of 1.0 cm x 1.0 cm) was covered with protective tape during deposition. In an Eppendorf tube, 3 mg of the sample was dispersed in 150 µL of ethanol by using ultrasounds. After obtaining smooth dispersion, 3 µL of 5% Nafion solution was added and dispersed for another 5 minutes. The as-prepared suspension was transferred with a pipette and applied dropwise on the glass, which was pre-heated to on a hot plate set at 65 °C. After evaporation of ethanol, electrodes were heated for additional five minutes and then gently removed from the hot surface. After cooling down, the protective tape was removed. To provide sufficient contact with the measuring system, a stripe of copper tape with conductive glue was attached to the uncoated surface of working electrode.

Photoelectrochemical (photocurrent) measurements were conducted using potentiostat/galvanostat PGSTAT 302N (Metrohm-Autolab). The measuring system consisted of working electrode, saturated Ag/AgCl electrode and Pt counter electrode. The electrolyte (0.5 M aqueous solution of Na_2SO_4) was purged with pure argon for one hour before the measurements and for additional 10 minutes when the electrode system set in the glass cell. Prior the photocurrent measurement, linear sweep voltammetry (LSV) in darkness and under light illumination was recorded in the range of –0.2 V – +0.8 V with the scan rate of 10 $mV \cdot s^{-1}$. The 150 W Xe lamp (Hamamatsu Photonics) with the light flux of 22 $mW \cdot cm^{-2}$ (measured with C9536-01 Hamamatsu radiometer working in the spectral response range of 310-380 nm), was used as the source of UV-Vis light without any optical filter in combination with in-house manual shutter. Bias voltage of +0.3 V (designated by LSV of pristine MOFs) was used during photocurrent measurements. The shutter was switched by hand every 20 seconds during duration of the experiment (340 seconds).

5.7. CO_2 photoreduction experiments

5.7.1. Procedure of photoconversion in solid-liquid environment

The photoreduction procedure was preceded with cleansing photopurification under UV-Vis light irradiation to eliminate influence of any residual organic compounds [325]. For this purpose, a portion of MOF (50 mg for samples described in Chapter 8, 20 mg – in Chapter 9) was dispersed in 20 mL of 1:9 mixture of TEOA and MeCN (by volume). The photopurification was conducted

using 30 mL glass reactor equipped with quartz front window, under continuous N_2 flow for 120 min 10 °C. The 1000 W Xe lamp (ORIEL Instruments) was used as the light source with the flux of 205 mW·cm^{-2} (at 420 nm, measured by PM100D Optical Power Meter, ThorLabs). The sample was then three times washed with fresh portion of TEOA/MeCN mixture and centrifuged. The dispersion was exposed for 120 min of UV-Vis light irradiation again, preceded with filling the head space of the reactor with nitrogen. The washing procedure was then repeated. After dispersing the photocatalyst afresh, CO_2 was passed through the suspension for 30 min (0.4 NL·min^{-1}). The light driven reduction of CO_2 was performed at 10 °C in a 30 mL glass reactor of identical construction as for photopurification, but equipped with GG420 window (to cut UV irradiation). The experiments conducted under UV-Vis light irradiation (Chapter 8) were carried out in the same glass reactor with quartz front window, like in the case of cleaning procedure. The process lasted 4 hours, with a 1 mL portion of the suspension being taken for analysis every hour.

For processes described in Chapter 8, formic acid – the photoconversion product – was detected by the ion chromatograph 940 Professional IC Vario (Metrohm AG). Apparatus was equipped with conductivity detector and Metrosep A Supp-10 100x4.0 column, using 3.2 mM Na_2CO_3 and 1.0 mM $NaHCO_3$ as a mobile phase with a flow rate of 0.8 mL·min^{-1}. In the case of experiments included in Chapter 9, HCOOH was detected by the ion chromatograph Dionex ICS-1100 (Thermo Scientific) equipped with AS9-HC RFIC (4x250mm) column and ADRS 600 4 mm suppressor, using 9.0 mM Na_2CO_3 as a mobile phase with a flow rate of 1 mL·min^{-1}.

In Chapter 8 the statistical analysis of the photoconversion results – one- and three-way ANOVA together with post-hoc Tukey test – was performed using OriginPro 2018 software (OriginLab Corporation).

5.7.2. AQE for HCOOH production at selected wavelengths

The photoreduction of CO_2 using monochromatic light (bandpass filters at 300, 330, 360, 390, 420, 450 nm) was performed to calculate Apparent Quantum Efficiency (AQE) of the most efficient material described in Chapter 8. For this purpose, 3 mL of sample suspension in 1:9 mixture of TEOA and MeCN (by volume), preceded with photopurification, was transferred to a 7 mL quartz reactor. The process temperature was maintained at 18 °C, and the reaction mixture was continuously stirred for three hours. The power intensity of the monochromatic light was measured using an optical power meter PM100D (ThorLabs). The method of formic acid detection was the same as for regular photoconversion process (described in Subsection 5.7.1). AQE was calculated as a function of wavelength basing on the ratio of the rate of electron consumption to the flux of incident photons by speculating that two photons were required according to the reaction stoichiometry. AQE was calculated as follows:

$$AQE = \frac{2 \cdot n_{HCOOH} \cdot h \cdot c \cdot N_A}{t \cdot \lambda \cdot I} \cdot 100\% \qquad \text{Eq. 7}$$

where n_{HCOOH} is the amount of the produced HCOOH molecules (in mol), h is the Planck constant ($6.626 \cdot 10^{-34}$ J·s), c is the speed of light in free space ($3.0 \cdot 10^8$ m·s^{-1}), N_A is the Avogadro constant

($6.022 \cdot 10^{23}$ $1 \cdot mol^{-1}$), t is the illumination time (s), λ is wavelength of monochromatic light (m), and I is the light intensity (W).

5.7.3. Procedure of photoconversion in solid-gas environment (In-situ DRIFTS)

The detailed description of the apparatus and sample preparation for the measurement are available in Subsection 5.6.9. Before the photocatalytic measurements, the chamber was loaded with MOF grinded with KBr (about 0.5 wt% of MOF) and activated at 150 °C for 1 h under a N_2 flow at a rate of 30 $mL \cdot min^{-1}$. Then the background spectra (KBr with MOF) were collected at 25 °C with 32 scans and at a resolution of 4 cm^{-1} under the flow of 10 $mL \cdot min^{-1}$ N_2. The spectra were collected automatically as a series of measurements for 1 hour under a flow of 0.1 $mL \cdot min^{-1}$ CO_2 mixed with 10 $mL \cdot min^{-1}$ 10%H_2/N_2. OmniCure S2000 UV Curing System (Excelitas Technologies) equipped with High Pressure 200 W Mercury Vapor Short Arc lamp, optical fiber and filter (320-390 nm) was used as a light source.

6. The influence of the synthesis conditions on properties and performance of Cu-TDPAT MOF

Different combinations of synthesis conditions and metal precursors were investigated in order to validate their influence on the obtained product. Basing on the literature review [11], seven substantial synthesis parameters were identified and varied in the Cu-TDPAT synthesis procedure: solvent, vessel, modulator, time, temperature, n_{Cu}:n_{linker} ratio and Cu precursor. As for solvents, DMF and four solvent mixtures were used *i.e.* DMA/DMSO (1:1 by volume, abbreviated DD), DMF/DMSO (1:1 by volume), DMF/EtOH/water (1:1:1 by volume, abbreviated DWE), DMF/water (1:1 by volume, abbreviated DW). DMF and DMA/DMSO mixture were primarily used by Luebke [94] and Li [66], respectively, in their works concerning Cu-TDPAT. Basing on these works, to limit the use of DMF, its mixture with DMSO, water and ethanol as the synthesis environment was proposed herein. The DMF/EtOH/water mixture was proposed as it was successfully applied in the case of obtainment of highly crystalline another Cu-based MOF, namely HKUST-1 [75]. In the case of using DMF, DMA/DMSO or DMF/DMSO, small amount of water was also introduced (2.5 vol% in relation to the solvent mixture), as reported in the original study [66]. The most commonly used reaction vessels for solvothermal MOF synthesis were used: glass Schott bottle and stainless-steel autoclave with Teflon liner. The influence of modulator was investigated using nitric [94] and tetrafluoroboric acid [66] and compared to non-modulated products. To determine crystallization window, synthesis temperature was tested in the range of 65-95 °C with the increment of 10 °C. Additionally, in the case of synthesis in DD, the prolonged reaction time (120 h instead of 72 h) was used in order to verify the possibility to compensate the lowered temperature of synthesis. Due to the observed by-product formation in the case of DMF used as solvent, the influence of lowered n_{Cu}:n_{linker} molar ratio (from the original 13.9:1 to 3:1 and 1:1) was also investigated. At the end, the three different copper hydrates were used as metal precursors (nitrate, tetrafluoroborate and acetate) to verify how different anions of metal precursor affect the forming structure. While first two copper salts were chosen in reference to the previous reports regarding Cu-TDPAT [66,94], the last salt was chosen as a comparison based on the synthesis of other copper-based MOF [106].

Table 5.1 shows the summary of conducted syntheses under different conditions and their assigned symbols. Due to the large number of samples, the following naming system was adopted to facilitate their identification. Processes carried out in the conditions corresponding to the primary procedure described by Li *et al.* [66] – 72 h, 85 °C, glass vessel, $Cu(NO_3)_2$•$3H_2O$, n_{Cu}:n_{linker} = 13.9:1, HBF_4 – were named as Cu-TDPAT followed by solvent mixture name in brackets. Each sample, for which a change in parameters has been introduced, was named by combining the name of the used solvent mixture (skipping the MOF name) and then adding all the value of the changing parameter after separating hyphens. For example, DMF-AcO-3/1 designates the sample synthesized in DMF, utilizing copper(II) acetate hydrate as the precursor, with a 3:1 molar ratio of precursor to linker, and other parameters as in the primary procedure (72 h, 85 °C, Schott bottle, volume of added HBF_4). Yield of all reactions was shown in Table 6.1 along with gas sorption properties-related properties

Table 6.1 Yield and visual product assessment of prepared Cu-TDPAT samples and their BET surface area, porosity characterization and CO_2 sorption capacity of the obtained materials.

Entry	Yield (%) [a]	Product description	S_{BET} ($m^2 \cdot g^{-1}$)	Total pore volume ($cm^3 \cdot g^{-1}$) [c]	Micropore volume ($cm^3 \cdot g^{-1}$) T-Plot	Micropore Surface Area ($m^2 \cdot g^{-1}$) T-Plot	H-K (S-F) average pore size (nm)	CO_2 sorption capacity ($mmol \cdot g^{-1}$)	
								At 0 °C	At 25 °C
DD-65C	-	No solid product was formed	-	-	-	-	-	-	-
DD-65C-120h	-	No solid product was formed	-	-	-	-	-	-	-
DD-65C-120h-3/1	-	No solid product was formed	-	-	-	-	-	-	-
DD-75C	-	No solid product was formed	-	-	-	-	-	-	-
Cu-TDPAT(DD)	62.7	Turquoise crystalline powder	1976	0.81	0.66	1713	1.06	6.56	3.95
DD-R	35.4	Turquoise crystalline powder	1474	0.65	0.54	1337	1.05	5.14	3.26
DD-3/1	33.7	Turquoise crystalline powder	2010	0.84	0.77	1953	1.05	6.98	4.30
DD-1/1	-	No solid product was formed	-	-	-	-	-	-	-
DD-AcO	58.0	Greenish-turquoise crystalline powder	1690	0.70	0.56	1459	1.03	5.86	3.70
DD-AcO-R	54.3	Greenish-turquoise crystalline powder	986	0.45	0.30	750	1.05	3.60	2.07
DD-AcO-3/1	22.5	Greenish-turquoise crystalline powder	736	0.46	0.09	227	1.12	2.30	1.39
DD-BF4	46.6	Turquoise crystalline powder	1876	0.79	0.59	1529	1.05	6.09	3.78
DD-BF4-HNO3	-	No solid product was formed	-	-	-	-	-	-	-
DD-95C	56.9	Turquoise crystalline powder	2222	0.88	0.83	2162	1.06	7.65	4.73
DD-95C-AcO	65.1	Greenish-turquoise crystalline powder	1184	0.61	0.26	648	1.08	3.50	2.10
DMF-65C	223.8 [b]	Turquoise powder with dark particles	105 [d]	-	-	-	-	-	-
DMF-75C	189.0 [b]	Turquoise powder with dark particles	8.5 [d]	-	-	-	-	-	-
Cu-TDPAT(DMF)	133.0 [b]	Turquoise powder with dark particles	645	0.28	0.24	600	1.05	2.26	1.38
DMF-R	121.5 [b]	Turquoise powder with dark particles	311	0.16	0.12	280	1.08	1.08	0.67
DMF-0A	147.9 [b]	Greyish light blue powder (cyan)	1145	0.50	0.44	1098	1.06	3.82	2.33
DMF-0.5A	115.1 [b]	Greyish light blue powder (cyan)	305	0.19	0.10	256	1.06	1.21	0.77
DMF-3/1	68.8 [b]	Greyish light blue powder (cyan)	1000	0.48	0.41	931	1.09	3.09	1.92
DMF-AcO	129.4 [b]	Turquoise powder with dark particles	728	0.31	0.28	708	1.05	2.49	1.54
DMF-AcO-3/1	50.7	Turquoise crystalline powder	2144	0.87	0.82	2078	1.04	7.73	4.74
DMF-3/1-HNO3	37.7 [b]	Greyish blue powder	17.9 [d]	-	-	-	-	-	-
DMF-95C	113.1 [b]	Turquoise powder with dark particles	135 [d]	-	-	-	-	-	-
Cu-TDPAT(DMF/DMSO)	54.8 [b]	Olive-brown powder	12.6 [d]	-	-	-	-	-	-
DMF/DMSO-0A	80.8	Light blue powder	1189	0.55	0.40	1016	1.04	4.47	2.85
Cu-TDPAT(DWE)	66.2	Light blue precipitate	583	0.65	0.16	386	1.08	2.12	1.32
Cu-TDPAT(DW)	30.4	Light blue precipitate	2.0 [d]	-	-	-	-	-	-

[a] compared to the theoretical Cu-TDPAT yield based on linker amount; [b] occurrence of by-product(s) was detected, not included in the calculations [c] designated at p/p_0=0.990, pore size diameter <195.6 nm; [d] Preliminary value of S_{BET} designated from N_2 adsorption isotherm measured with Micromeritics Gemini V apparatus, in the range of relative pressure p/p_0 = 0.1-0.3, if the value was lower than 150 $m^2 \cdot g^{-1}$, the more advanced analysis was not carried out;

6.1. Synthesis in primary conditions

Cu-TDPAT(DD), the sample obtained *via* approach described by Li and co-workers [66], had a form of fine turquoise crystalline powder (Figure 6.1a). The designated yield reached 62.7% compared to the theoretical yield value (Table 6.1). After the process of activation (*i.e.* soaking in methanol for several consecutive days and vacuum drying at 150 °C), the powder becomes navy blue (Figure 6.1b). The dark color lasts as long as Cu-TDPAT have no access to air atmosphere, as adsorption of moisture makes MOF to return quickly to its original turquoise color (Figure 6.1c). The repeated thermal treatment under reduced pressure activates the structure again.

Among different mixtures of the solvents, the primary DMA/DMSO mixture was the one that facilitated the highest crystallinity of the product. All the reflexes visible on the PXRD spectrum of Cu-TDPAT(DD) were sharp and narrow (Figure 6.2a). The presence of the particular reflexes at 4.0°, 4.7°, 6.6°, 7.8°, 8.1°, 9.4°, 10.2°, 11.5°, 12.1°, 14.0°, 15.4° is consistent with the literature data [94] and indicate the presence of the (011), (110), (112), (121), (022), (220), (123), (312), (033), (134), (413) planes, respectively. Lack of additional peaks confirms that no by-products were created during the synthesis. Cu-TDPAT(DD) N_2 adsorption isotherm at -196 °C was classified as type I isotherm according to IUPAC (Figure 6.3). High degree of crystallinity was confirmed by the surface area value (S_{BET}) reaching almost 2000 $m^2 \cdot g^{-1}$ (Table 6.1). The material reached notable level of CO_2 uptake reaching 6.56 $mmol \cdot g^{-1}$ and 3.95 $mmol \cdot g^{-1}$ measured at respectively 0 °C (Figure 6.4) and 25 °C (Figure 6.5). The SEM imaging revealed an octahedral shape of resulting crystals with smooth walls and of width of approximately 20-25 μm (Figure 6.1d). In the case of several single crystals, the smaller octahedra (not exceeding 15 μm in size) present on the surface of larger octahedra, were observed.

The shape of the obtained TGA curve of Cu-TDPAT(DD) (Figure 6.6a) does not differ from the data available in the literature [326–328]. Three main mass losses can be distinguished. The first one begins at the start of the analysis at 50 °C and lasts until about 130 °C. It can be related to the evaporation of moisture adsorbed in the pores of MOF as a result of contact with air. As a confirmation *in situ* DRIFTs analysis was carried out at RT (under air atmosphere) and at 150 °C (under inert atmosphere of pure nitrogen) (Figure 6.7). The recorded spectra clearly indicate that the thermal treatment removes the adsorbed water, as the wide band assigned to stretching O-H vibrations between 3750 and 2650 cm^{-1} disappeared. The second mass loss, initiated at about 220 °C, and the one directly following it at about 380 °C (without clear plateau between these stages), may be related with the decomposition of linker leading to definite structural damage. After the thermal treatment the amount of solid remaining in the crucible drops to 32.37%.

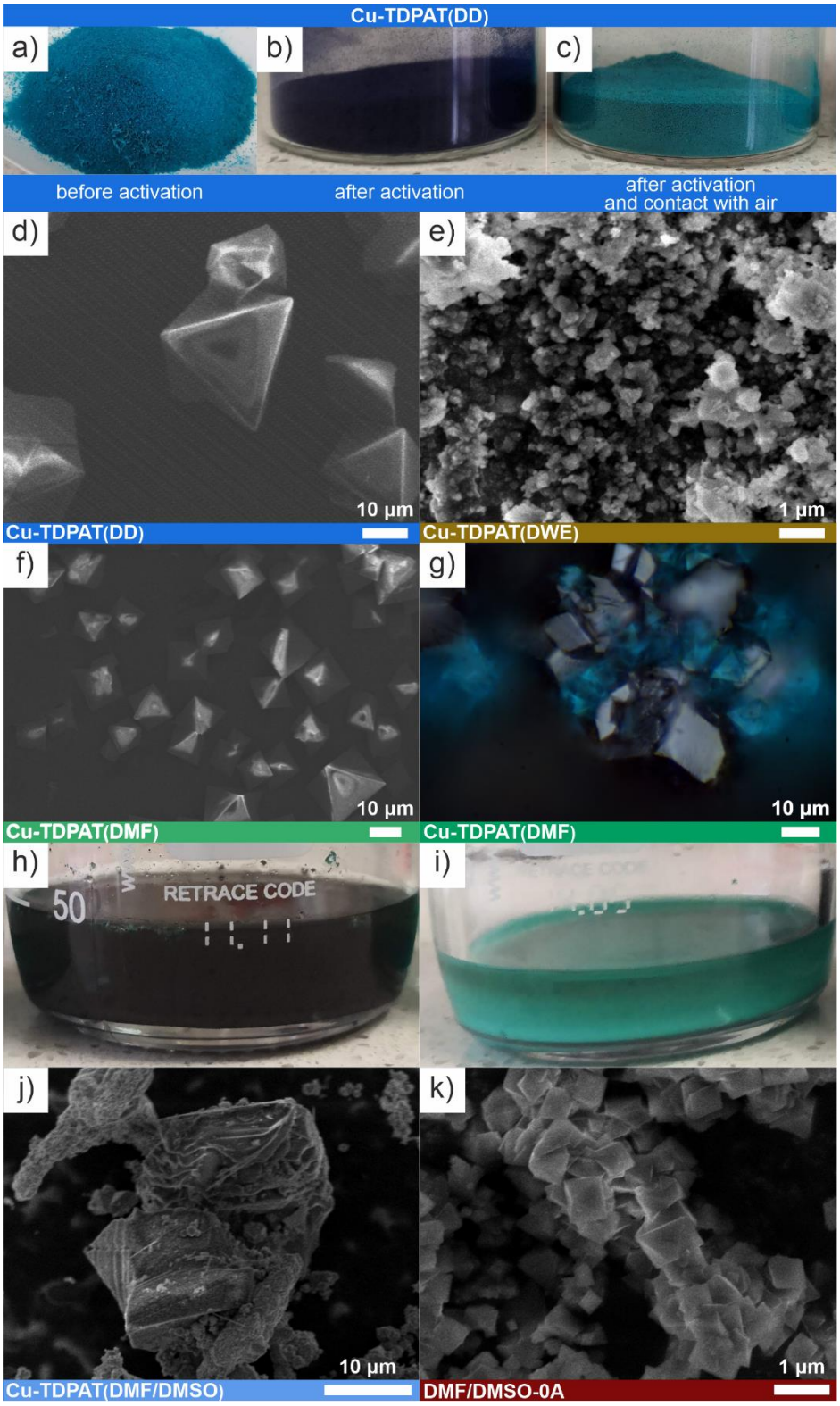


Figure 6.1 Photographs of Cu-TDPAT(DD) a) before activation, b) after activation, c) after activation and contact with air; SEM images of: d) Cu-TDPAT(DD), e) Cu-TDPAT(DWE); f) Cu-TDPAT(DMF) g) optical micrograph of Cu-TDPAT(DMF); Photographs of reaction solutions of: h) Cu-TDPAT(DMF/DMSO), i) DMF/DMSO-0A; SEM images of j) Cu-TDPAT(DMF/DMSO), k) DMF/DMSO-0A

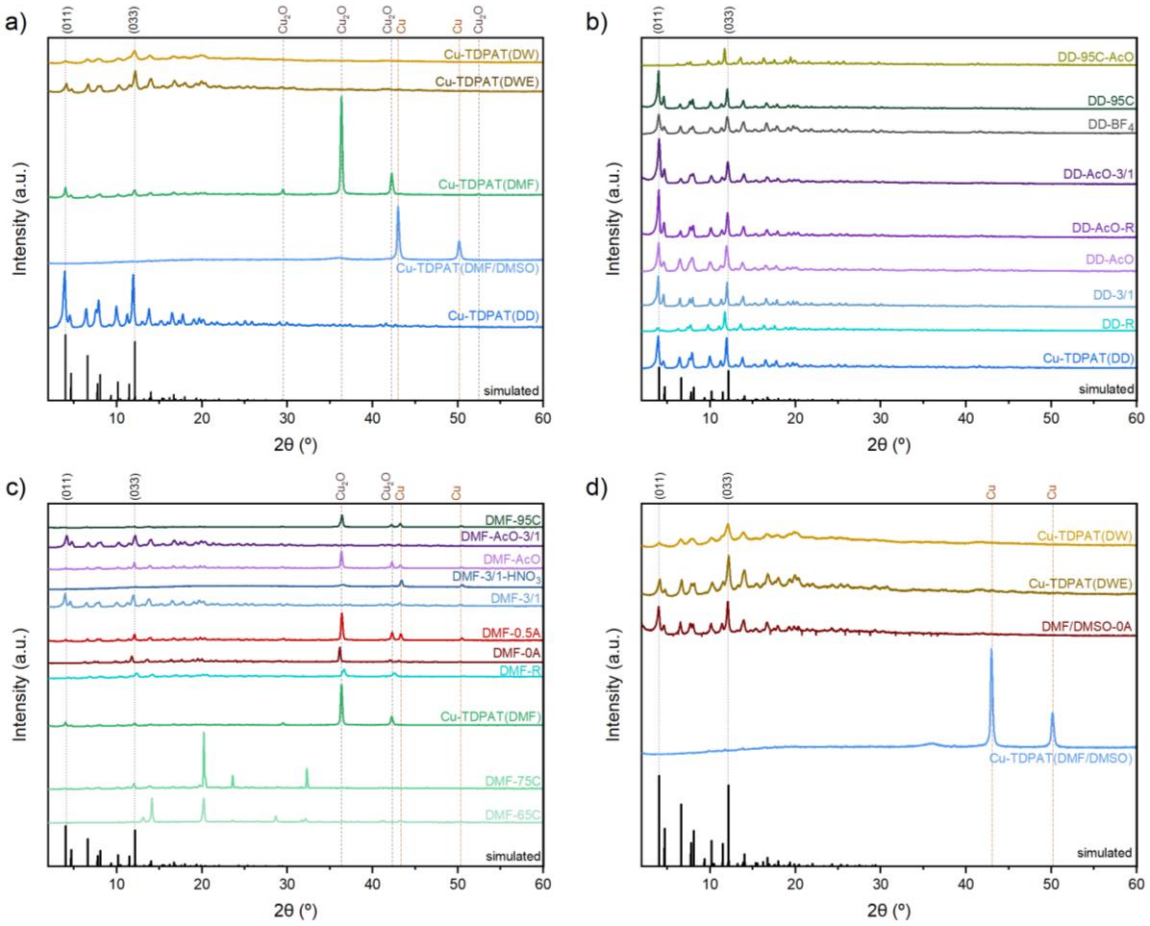


Figure 6.2 Comparison of PXRD patterns of the Cu-TDPAT samples synthesized: a) in the primary conditions in different solvents; b) in DMA/DMSO; c) in DMF; d) in other solvent mixtures.

The successful creation of MOF in Cu-TDPAT(DD) was also confirmed on the recorded FTIR spectra (Figure 6.8a). The presence of the most characteristic bands for Cu-TDPAT were observed in the range of 3750-2650, as well as at about 1709, 1619, 1561, 1517, 1369 and 617 cm^{-1} [329–331]. In the 3750-2650 cm^{-1} range, the deflection points at around 3300 and 3100 cm^{-1} can be assigned to N-H stretching vibrations in secondary amine and C-H stretching vibrations in the aromatic ring, respectively. Both signals are covered with broad signal corresponding to the O-H stretching vibrations of the adsorbed water, confirmed by its disappearance during DRIFTs measurement at 150 °C under inert atmosphere. Near to 1709 cm^{-1} an outline of a band characteristic for stretching vibrations of the C-O group in carboxylic functionality of the linker can be distinguished, merged with bending N-H vibrations at about 1619 and 1561 cm^{-1}. Additionally stretching C-N vibration of amine can be distinguished near to 1147 cm^{-1}. At around 1517 and 1370 cm^{-1} strong bands related to the vibrations in the core heterocyclic unit of the linker were observed. In the fingerprint region, the band at approximately 617 cm^{-1} confirmed the existence of Cu-O stretching vibrations in the obtained Cu-TDPAT(DD). Apart from that, other signals under 1000 cm^{-1} can be observed which can be interpreted as vibrations in aromatic ring characteristic for TDPAT linker.

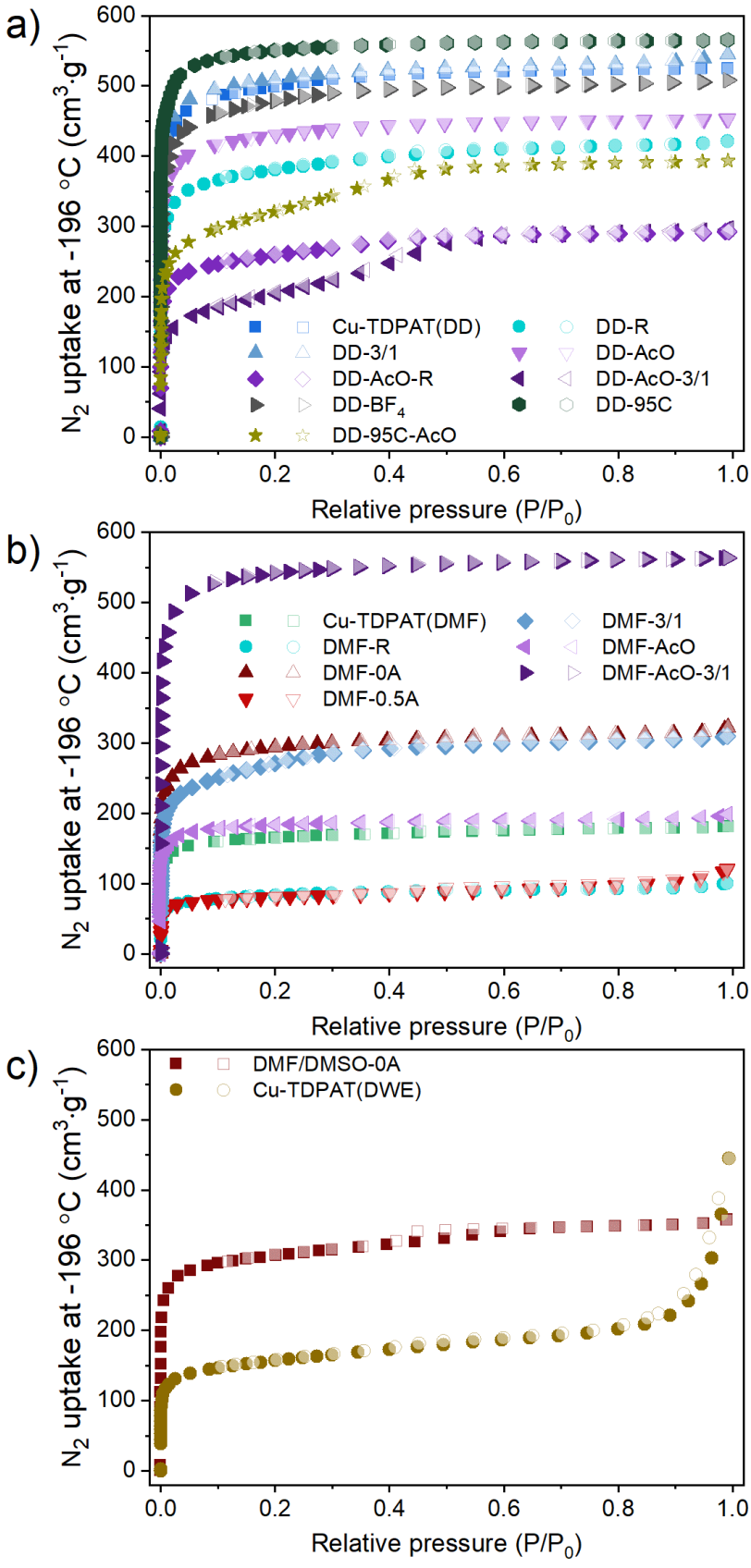


Figure 6.3 Comparison of N_2 adsorption-desorption curves at -196 °C; b) CO_2 at 0 °C c) CO_2 at 25 °C of the Cu-TDPAT samples

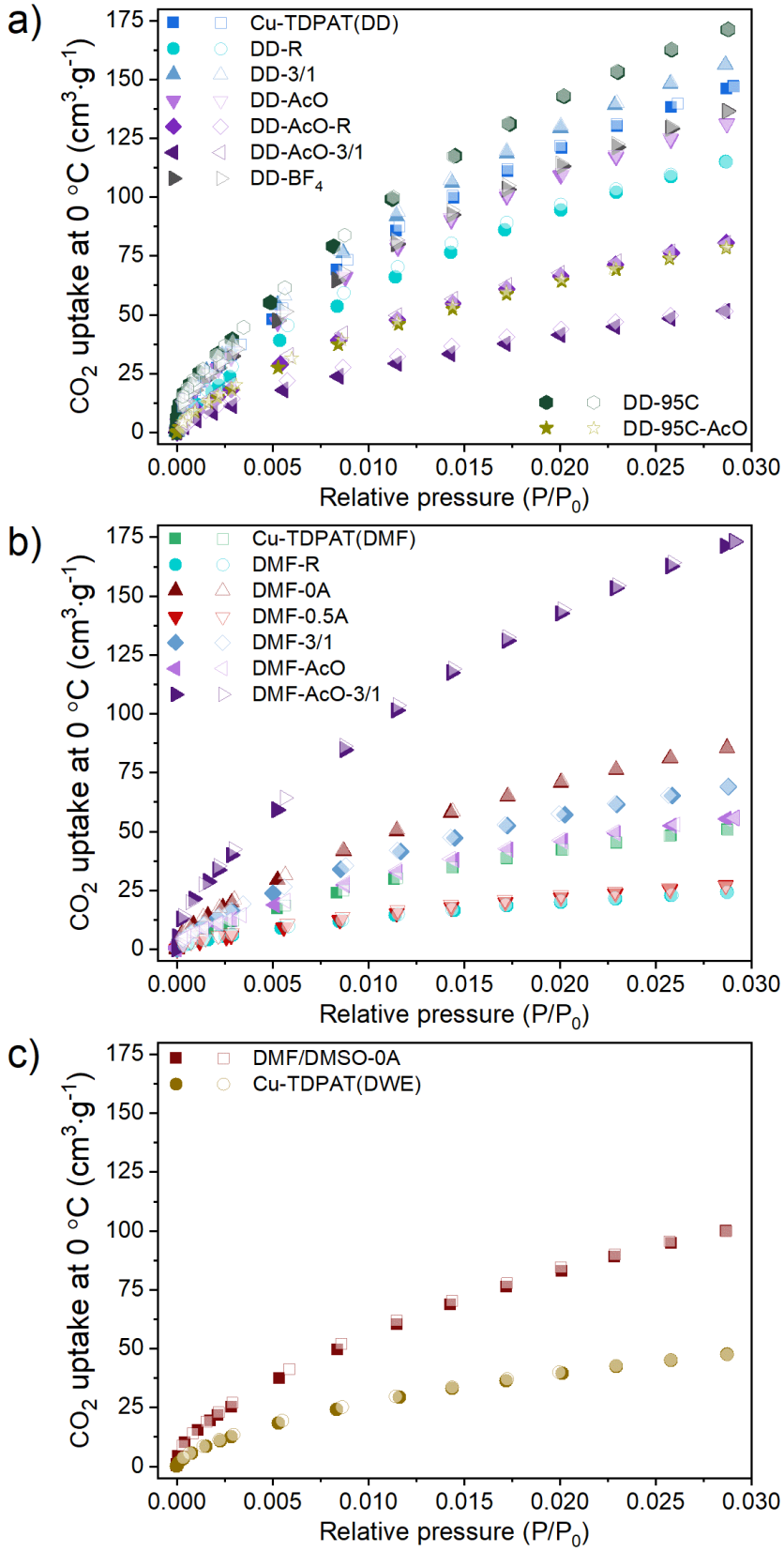


Figure 6.4 Comparison of CO_2 adsorption-desorption curves of the Cu-TDPAT samples measured at 0 °C

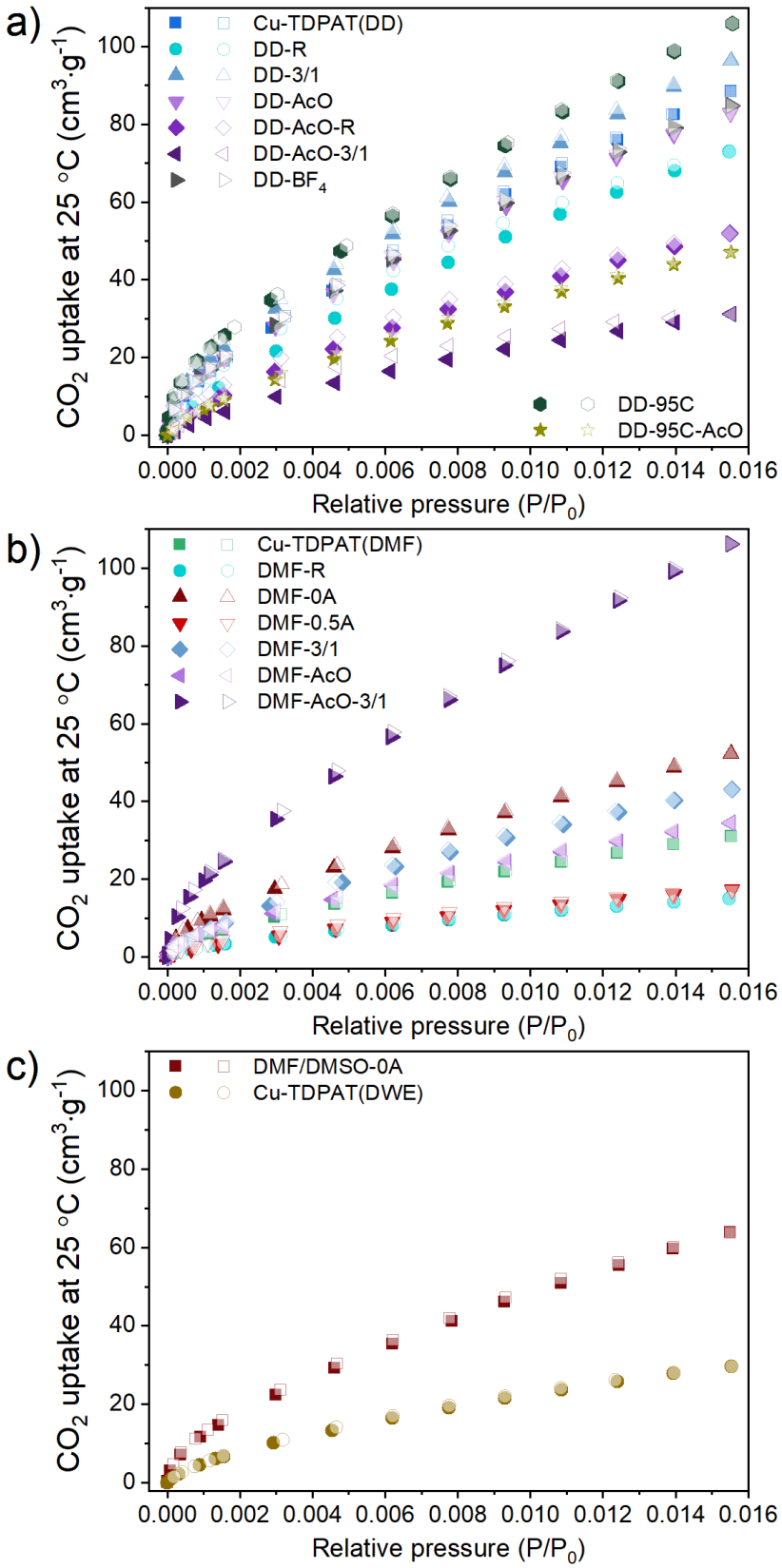


Figure 6.5 Comparison of CO_2 adsorption-desorption curves of the Cu-TDPAT samples measured at 25 °C

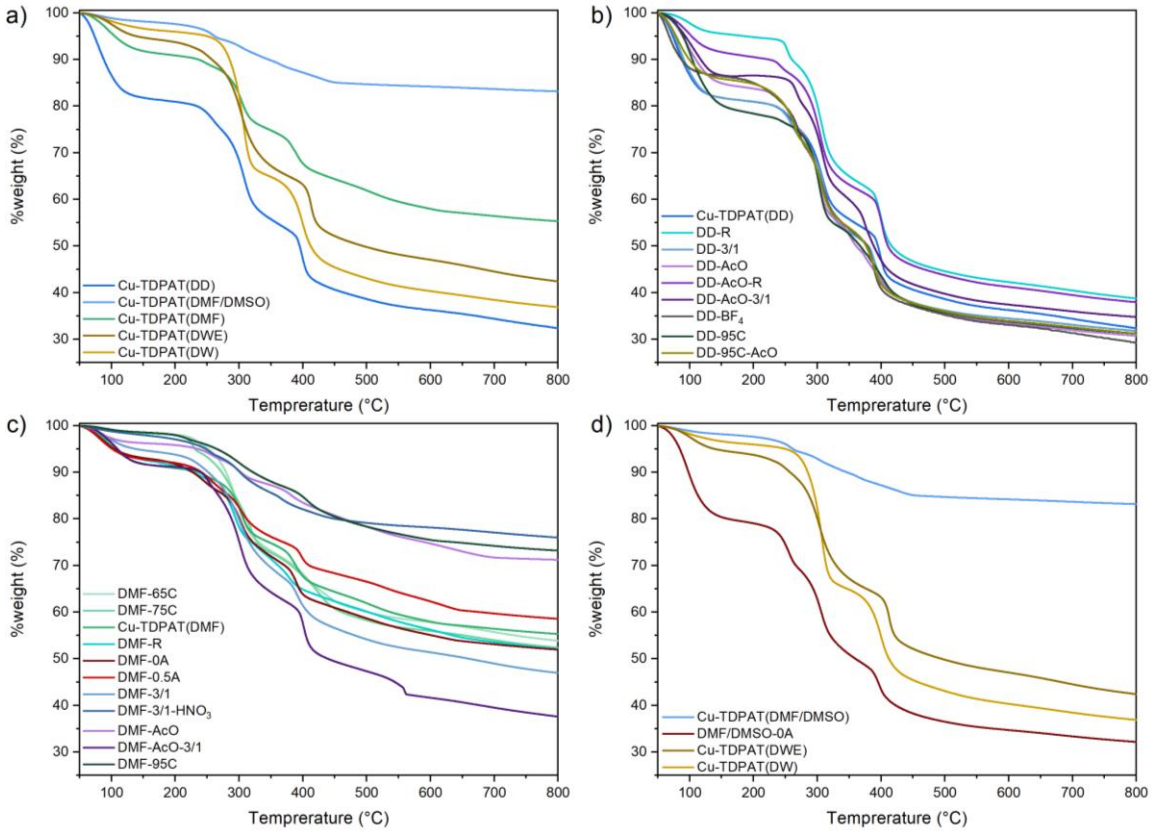


Figure 6.6 Comparison of TGA curves of the Cu-TDPAT samples synthesized: a) in the primary conditions in different solvents; b) in DMA/DMSO; c) in DMF; d) in other solvent mixtures.

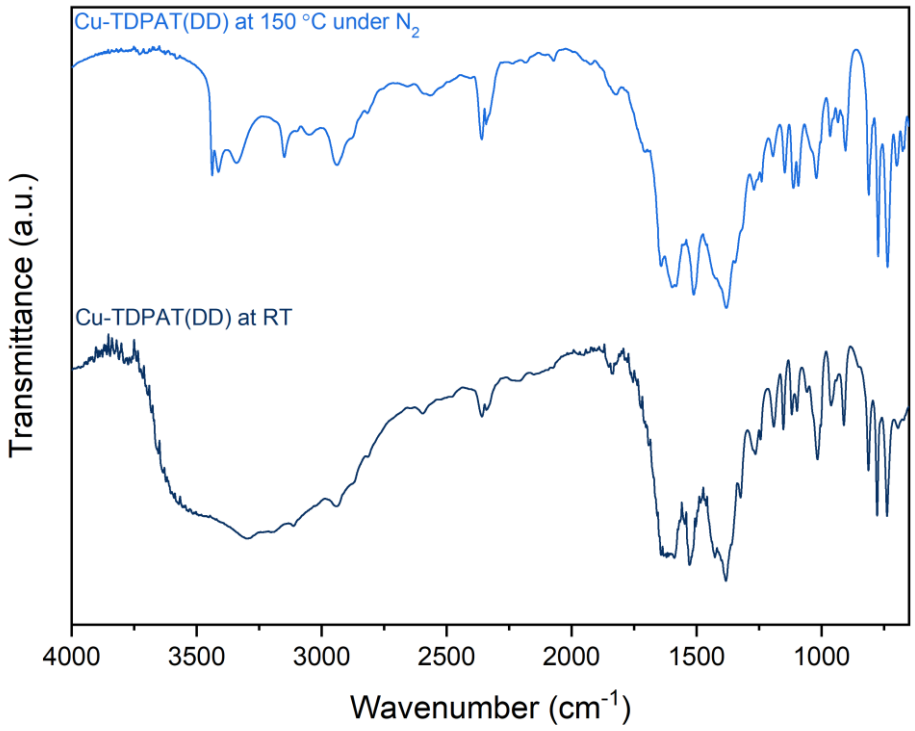


Figure 6.7 Comparison DRIFTs spectra of Cu-TDPAT(DD) recorded at RT in air atmosphere and at 150 °C under N_2 flow

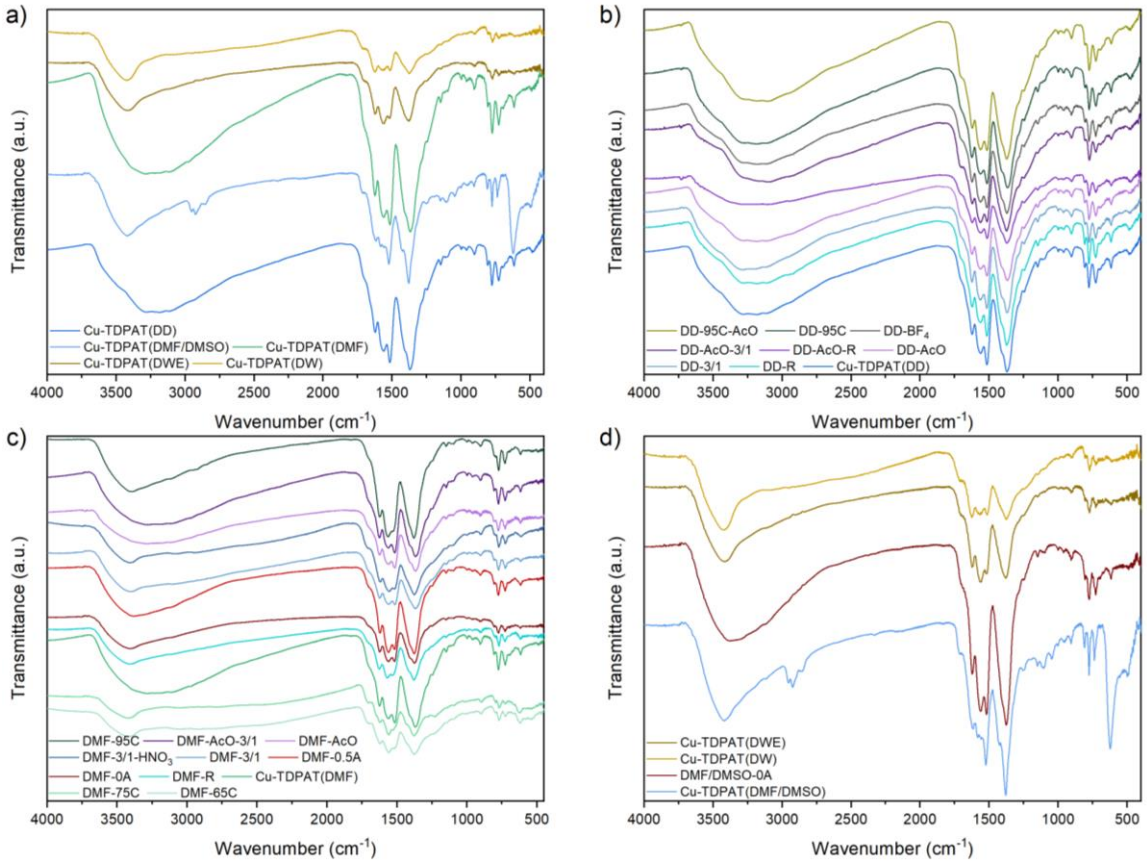


Figure 6.8. Comparison of FTIR spectra of the Cu-TDPAT samples synthesized: a) in the primary conditions in different solvents; b) in DMA/DMSO; c) in DMF; d) in other solvent mixtures

6.2. Synthesis in different solvents

Pure Cu-TDPAT MOF phase was also identified in the samples obtained in the DMF-ethanol-water and DMF-water mixtures. Even though the product yield for Cu-TDPAT(DWE) was similar to Cu-TDPAT(DD), the intensity of the reflexes observed on the PXRD pattern was noticeably lower and wider than for the primary sample. Additionally, N_2 isotherm measured for this sample was classified as II type according to IUPAC, as the only one among all tested MOFs. In the case of mixtures with water, the crystallinity of the obtained samples was even lower, indicating that the selected environments are not favorable to the formation of a Cu-TDPAT MOF with high crystallinity, further confirmed by the gas adsorption studies. The calculated S_{BET} value for Cu-TDPAT(DWE) did not exceed 600 $m^2 \cdot g^{-1}$ (decrease by about 70% compared to Cu-TDPAT(DD)), while in the case of Cu-TDPAT(DW) the preliminary measurement has shown only 2 $m^2 \cdot g^{-1}$. Similarly to nitrogen adsorption study, CO_2 adsorption study using Cu-TDPAT(DWE) have shown 67% uptake decrease at both temperatures. Environment with water also resulted in obtainment of particles of indefinite shape instead of the regular octahedral shape (Figure 6.1e). Cu-TDPAT(DWE) was characterized with the size of particles mainly not exceeding 0.1-0.2 μm, with the presence of few particles in the range of 0.5-0.6 μm was also observed (decrease by over 50 times in comparison with Cu-TDPAT(DD)). Although the overall course of the TGA curve remained unchanged, maintaining a similar structure breakdown temperature of about 220 °C, the relative

value of the first step of mass loss (associated with the evaporation of water from the pores) was reaching only about 4 and 6% for Cu-TDPAT(DW) and Cu-TDPAT(DWE), respectively. It is probably caused by the reduced porosity of both structures, resulting in lower adsorption of moisture. The FTIR spectra (Figure 6.8a) did not reveal substantial changes comparing to the primary sample. The only difference regarded diminishing of the very broad band related to O-H stretching vibrations at 3750-2650 cm^{-1} revealing narrower band centered at 3400 cm^{-1} corresponding to N-H stretching vibrations of the extending units in linker.

Formation of MOF was also confirmed for Cu-TDPAT(DMF), however, it was accompanied by the presence of a by-product in a form of reddish powder next to the turquoise solid being the MOF. Interestingly, the yield of the obtained precipitate was over two times higher than in the case of Cu-TDPAT(DD). Octahedrons of diverse size (width varying mainly between 8 and 15 μm, with few bigger ones, reaching 20 μm) were depicted with SEM (Figure 6.1f). Since no particles could be undoubtedly recognized as a by-product, optical imaging was performed. Next to the blue micrometrical bipyramidal crystals, optical microscopy revealed existence of dark cubic-shaped crystals (Figure 6.1g). In the PXRD pattern the presence of peculiar sharp reflexes confirmed the identity of the additional structures to be copper (I) oxide. The characteristic signals of Cu_2O were observed at 36.4°and 42.3° (corresponding to (111) and (020) planes, respectively) along with two accompanying minor reflexes at 29.6° and 52.4° (respectively assigned to (011) and (121)). Formation of Cu_2O can be explained as an effect of a side reaction of DMF with copper ions, which, under solvothermal conditions, can act as a reducing agent, leading to the formation of Cu_2O [332]. It is caused by the elevated temperature and the presence of water, leading to the partial decomposition of DMF into dimethylamine and formic acid, further reducing Cu^{2+} to Cu^{+}. Thus, it was deducted that in order to lower the probability of this side reaction occurrence, the stochiometric excess of copper should be limited. The presence of non-porous oxide was also confirmed on TGA, as almost 13% less product was decomposed during the thermal treatment of Cu-TDPAT(DMF) comparing to Cu-TDPAT(DD) without evident changes of the decomposition temperature. Despite the Cu_2O formation, Cu-TDPAT(DMF) was characterized with S_{BET} and CO_2 uptake values similar to Cu-TDPAT(DWE), which was characterized by pure MOF phase, but low crystallinity at the same time. Cu-TDPAT(DMF) reached the S_{BET} of 645 $m^2 \cdot g^{-1}$ and the CO_2 sorption capacity of 2.26 and 1.38 $mmol \cdot g^{-1}$ at 0 and 25 °C, respectively, giving about 10.5%, 6.5% and 4.5% increase in comparison with Cu-TDPAT(DWE). The particular sorption properties compared to Cu-TDPAT(DWE), as well as the unchanged IR spectrum in comparison with Cu-TDPAT(DD) (Figure 6.8a), may suggest that the formed MOF itself was characterized by relatively high crystallinity.

As a result of the Cu-TDPAT synthesis attempt in DMF/DMSO, brown-olive precipitate was formed (Figure 6.1h). PXRD analysis indicated presence of reflexes at 43.3° and 50.5° corresponding to the (111) and (200) planes, respectively, which are characteristic for pure copper. Additionally, a flat and broad rounding observed at $2\theta = 36.4°$ may also indicate the presence of trace copper(I) oxide, as a transitional compound of the progressive reduction of Cu^{2+} to Cu^{0}. Magnification of the diffractogram revealed very weak reflexes that were assigned to residual

contest of Cu-TDPAT (Figure 6.9). Instead of Cu-TDPAT octahedrons, a kind of layered chunks accompanied by agglomerates created by smaller than micrometric particles were observed by the SEM imaging (Figure 6.1j). Although the FTIR analysis confirmed presence of bands characteristic for Cu-TDPAT (Figure 6.8a), additional bands related to the asymmetric and symmetric stretching vibrations of the methyl group present in DMF were clearly outlined (3000-2800 cm^{-1}). In turn, the band at 626 cm^{-1} was assigned to the stretching vibration of Cu_2O [333] (Figure 6.10). The negligible content of MOF was also confirmed by the TGA (Figure 6.6a). In comparison with highly-crystalline Cu-TDPAT(DD), the overall mass loss observed for Cu-TDPAT(DMF/DMSO) was 34% lower (excluding the mass loss attributed to moisture evaporation), suggesting very small content of organic species, which were able to decompose during thermal treatment of the material. This stands in line with the value of S_{BET}, which only reached 12.6 $m^2 \cdot g^{-1}$. For the primary sample the presence of two distinct steps of mass loss in the range of 220-380 °C is characteristic, while for Cu-TDPAT(DMF/DMSO) in the same temperature range one smooth mass loss was observed. This may indicate that normally MOF disintegrates in the sequence first from the Cu-O-C bonds followed by the organic linker decomposition.

The presented data clearly indicates that among tested solvents, the originally used DMA/DMSO mixture is the most beneficial environment for the crystalline Cu-TDPAT synthesis. This MOF can be successfully obtained in the DMF-based environments as well, however, it's crystallinity (especially for DMF/EtOH/water and DMF/water mixtures) and phase purity (pure DMF) could be amended by adjustment of the other synthesis conditions.

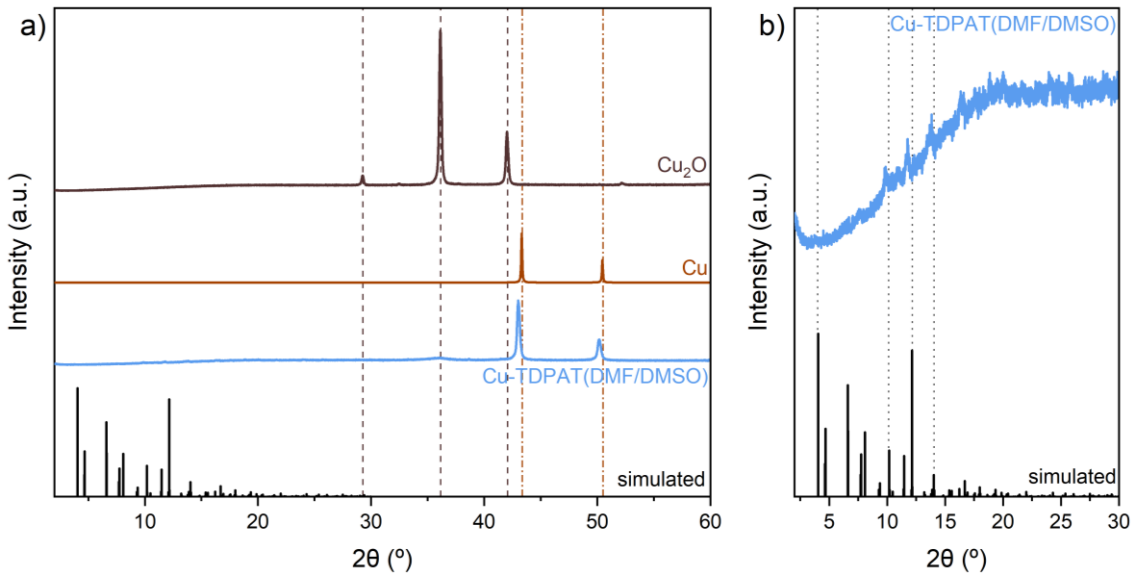


Figure 6.9 Comparison of PXRD patterns of: a) Cu-TDPAT(DMF/DMSO), Cu and Cu_2O; b) Cu-TDPAT(DMF/DMSO) with simulated Cu-TDPAT data in 2-30° range

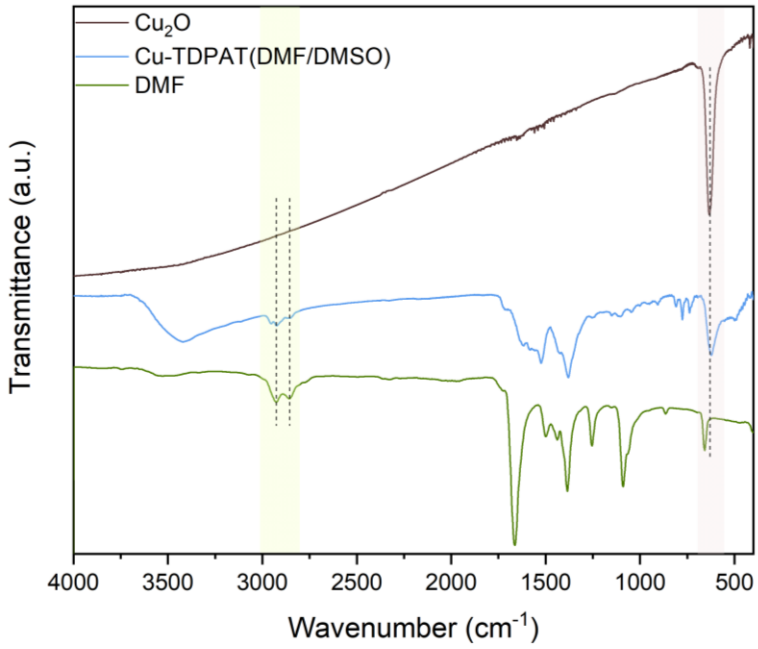


Figure 6.10 FTIR spectrum comparison of Cu-TDPAT(DMF/DMSO), Cu_2O and DMF

6.3. The influence of the reaction vessel

In the case of Cu-TDPAT, the vast majority of reports utilizes glass vials as synthesis vessels. Only He and co-workers [331] declared the use of stainless steel autoclave with Teflon liner, however, the work focuses on the modification of MOF rather than the characterization of the pristine product. Therefore, to compare the influence of the reaction vessel on the forming product, the synthesis using autoclave was conducted for DMF and DMA/DMSO acting as reaction environments. The resulting samples were named respectively DMF-R and DD-R. After activation, both obtained powders did not differ visibly from analogous samples obtained under the primary conditions proving that the usage of the autoclave also did not affect the by-product formation. In the case of DD-R, almost 10% decrease in the yield Cu-TDPAT in comparison to Cu-TDPAT(DD) was observed. At the same time, in the case of DMF-R, similarly to Cu-TDPAT(DMF), the yield exceeded 100%, suggesting formation of unwanted products. PXRD analysis confirmed that in DD-R no by-products were detected, whereas in DMF-R, Cu_2O was detected (respectively Figure 6.2b,c and Figure 6.8b,c). However, the relative intensity of the reflexes assigned to the Cu_2O by-product was comparable to the intensity of the highest reflexes assigned to the MOF, suggesting higher relative amount of crystalline MOF in this sample. Additionally, vanishing of two first reflexes at 4.0° and 4.7° was observed for either DMF-R and DD-R. The shape of the TGA curves for both samples remained practically unchanged in respect to the corresponding primary samples. However, the calculated content of decomposed solid was 16.6% higher for DD-R than for DMF-R. Both samples synthesized in the autoclaves were characterized by lower S_{BET} and CO_2 sorption capacity (at both 0 and 25 °C), than the respective samples obtained in the glass flasks (Table 6.1). In the case of DD-R the values were reduced by 17-25% in comparison with Cu-TDPAT(DD) At the same time, for DMF-R these values were diminished by even 52% in respect to Cu-TDPAT(DMF) and by 84%

compared to Cu-TDPAT(DD). This stands in line with the observed FTIR spectrum (Figure 6.8c), in which band centered at 3400 cm^{-1} corresponding to N-H stretching vibrations was visible instead of the band characteristic for water.

For DD-R and DMF-R, the general octahedral morphology of MOF captured by SEM (Figure 6.11) remained unchanged in comparison with the reference samples. Similarly to Cu-TDPAT(DMF), the size of the DMF-R particles was within the range of 10-18 μm but with noticeable rounding of structure's corners, which may be related to low crystallinity of MOF. In turn, in the case of synthesis carried out in DMA/DMSO solvent mixture, the use of an autoclave led to creation of particles of smaller size compared to the synthesis carried out in glass bottle, reaching the crystals width of 11-15 μm (Figure 6.11a). Even though, the surface of octahedra seemed to be smooth, visible cracks in their structure were observed.

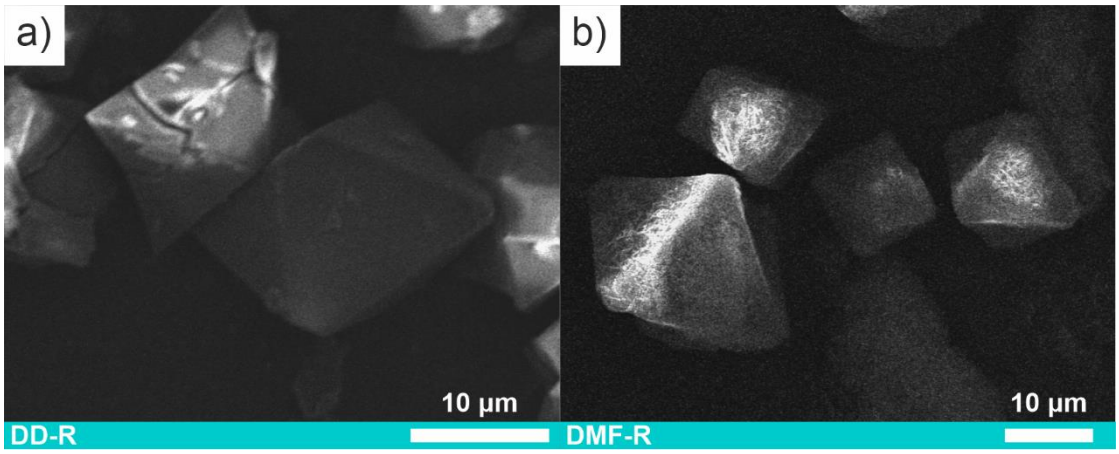


Figure 6.11 SEM images of a) DD-R and b) DMF-R

Taking into account the above observations, the use of autoclave was found not beneficial regarding the synthesis of Cu-TDPAT. It concerns both – the reaction yield (especially in the case of DMA/DMSO synthesis) as well as the crystallinity of the final product, making the use of glass Schott bottles a more advantageous approach.

6.4. Influence of the modulator presence and its type

As the first attempt to prevent the formation of by-products in the DMF-based synthesis environment, the acid content was adjusted to 50% (DMF-0.5A) and 0% (DMF-0A) of the original amount. In both cases, the fine greyish turquoise powder was obtained. The yield of MOF creation exceeded 100%, clearly indicating obtainment of by-products accompanying the Cu-TDPAT. The acquired PXRD patterns confirmed the formation of both MOF and Cu_2O (Figure 6.2, Figure 6.12a). Additionally, presence of pure copper was indicated (signals at 43.4° and 50.4° corresponding to (111) and (200) planes), suggesting no beneficial effect in preventing by-product formation. The magnification at the range of 2θ between 2° and 30° confirmed successful MOF creation (Figure 6.12b), however, characterized by relatively low crystallinity. As a confirmation of the limited MOF content in as-obtained samples, a reduced amount of decomposed solid (33.6% for DMF-0.5A and 40.2% for DMF-0A) in comparison with Cu-TDPAT(DD) (49%) was calculated from the TGA curves

(Figure 6.6c). Despite that, the trend off the curves remained unchanged. Interestingly, in the case of DMF-0A, the determined value of S_{BET} reached 1145 $m^2 \cdot g^{-1}$, giving 78% improvement in comparison with Cu-TDPAT(DMF). At the same time, for DMF-0.5A, the S_{BET} was decreased by 53% in relation to Cu-TDPAT(DMF). Similar relative changes in the measured CO_2 uptake were also observed.

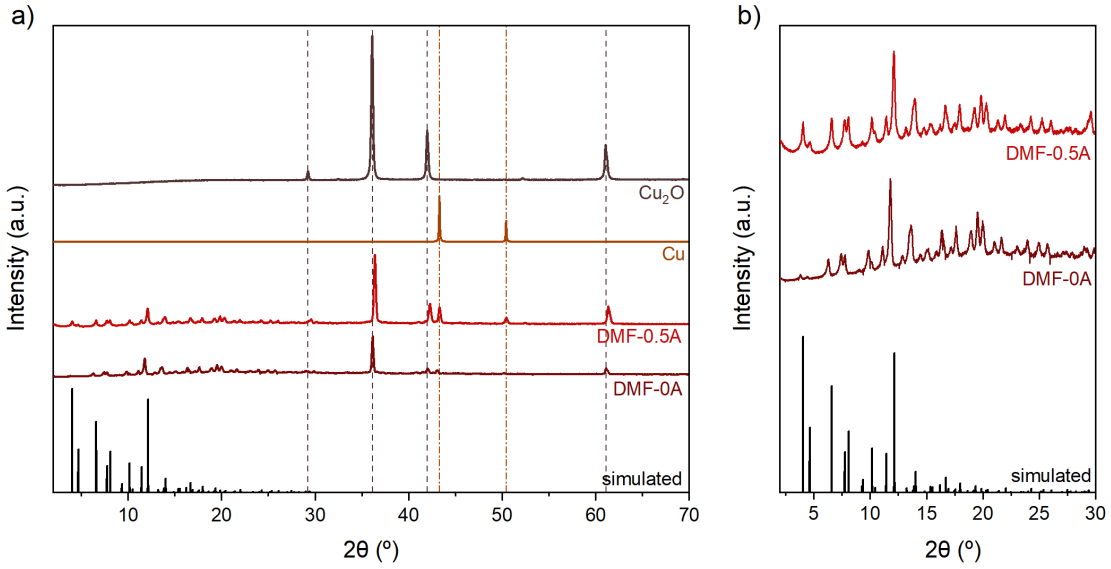


Figure 6.12 Comparison of PXRD patterns of: a) DMF-0.5A, DMF-0A, Cu and Cu_2O; b) DMF-0.5A and DMF-0A with simulated Cu-TDPAT data in 2-30° range.

The SEM images (Figure 6.13) revealed a presence of dominating content of fully developed octahedral crystals for both samples, accompanied by particles of irregular, fractured surface. The formed structures were of width about 1.5-3 μm and 3-5 μm in the case of DMF-0A and DMF-0.5A, respectively. Presence of smaller shapeless particles (smaller than 1 μm) was also detected for both samples. As expected, the modulating effect of HBF_4 is clearly visible as its growing content in the synthesis environment is accompanied by the growing size of forming particles. According to literature, HBF_4, being a strong Brønsted acid, can act as the nucleation inhibitor as a result of competitive interactions with the linker [334], which was herein observed. Interestingly, in the case of DMF-0A, intergrown interpenetrating octahedrons can be spotted. In crystallography, such a phenomenon is called a penetration twin and can be caused by misplacement of atomic structure during the nucleation step. This leads to creation of a plane of symmetry common for two growing crystals which will be growing at once interpenetrating [335,336].Thus, addition of modulator prevents the unwanted crystal defects, in this case twinning effect.

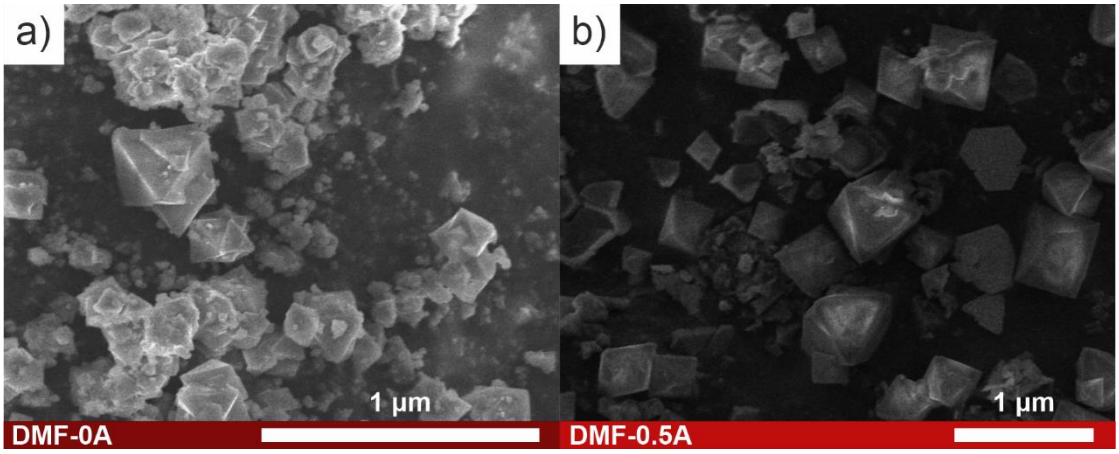


Figure 6.13 SEM images of a) DMF-0A and b) DMF-0.5A

The synthesis without modulator was also conducted in the DMF/DMSO solvent mixture (DMF/DMSO-0A). In this case the absence of the HBF_4 in synthesis environment resulted in creation of light turquoise powder (Figure 6.1i) with the yield reaching 80.8% - the highest among pure phase samples. In contrast to the Cu-TDPAT(DMF/DMSO), the acquired diffraction pattern for DMF/DMSO-0A (Figure 6.2d) confirms obtainment of pure Cu-TDPAT MOF without Cu_2O by-product. The S_{BET} of as-obtained sample was lower than for Cu-TDPAT(DD) by 40%, reaching just below 1200 $m^2 \cdot g^{-1}$. The sorption capacity for CO_2 was decreased by about 30%, reaching the level of 4.47 and 2.85 $mmol \cdot g^{-1}$ at 0 and 25 °C, respectively. The obtained TGA curve (Figure 6.6d) indicated that the sample is susceptible to water adsorption, as the mass loss attributed to its evaporation reached a value of 20.4% making it similar to Cu-TDPAT(DD). Analogously, also the content of pure MOF was calculated to be about 47.5%, which is similar to the primary sample. Similarly to DMF-0A, SEM imaging revealed creation of intergrown interpenetrating octahedrons for DMF/DMSO-0A (Figure 6.1k). Although, in this case the twinning particles formed larger clusters than in the case of DMF-0A, the width of the individual particles in the agglomerates did not exceed 1 µm and was within the range of 0.5-0.8 µm.

These observations clearly indicate the essential role of modulator in Cu-TDPAT synthesis on the reaction pathway and the size of crystals. In the case of pure DMF, HBF_4 was playing the role of capping and size controlling agent at once leading to formation of well-defined crystals without twinning defects. Interestingly, in the DMF/DMSO solvent mixture, apart from the MOF crystal modulation, the presence of this specific acid turns out to facilitate creation of side products rather than well-defined crystals of MOF, whereas in pure DMF by-product was formed regardless of the acid presence. There can be two coexisting possible explanations that are responsible for this phenomenon. One of them is the too high excess of the copper precursor in relation to amount of linker, which causes the excess amount of copper to undergo a competitive redox reaction. Investigation over the influence of the molar ratio of precursors will be discussed in details in following subsection. The second explanation may refer to the acid itself. As strong Brønsted acid, HBF_4 inhibits the deprotonation of carboxyl functionalities in linker, which leads to inhibition of nucleation and consequently the crystal growth. It is possible that taking into consideration such high concentration of copper in comparison with linker (almost 14 times more) and the strength of

the introduced acid, the pathway in which Cu^{2+} undergoes reduction to Cu^{1+} and Cu^{0} is more favorable, while as a consequence the nucleation of MOF is slowed down practically to zero, resulting in limited formation of its structure. The combination of these two factors is visible especially for DMF-based syntheses – no addition of acid elevated the S_{BET} to 1000 $m^2 \cdot g^{-1}$, making it one of the highest among samples obtained in DMF, even despite the fact that formation of by-products was confirmed for this sample. This may also indicate that in the case of synthesis in DMF-based environments, the thermal decomposition of amide and thus the release of formic acid, makes the acidic modulator content too high in the system. Therefore, the amount of acid added in this case should probably be strictly limited.

6.5. Influence of the time and temperature of the reaction

Another tested factors that influence the Cu-TDPAT forming were time and temperature. At first, the lower temperatures than the used in the original synthesis in the DMA/DMSO mixture were used, *i.e.* 65 and 75 °C. It was found out that the decrease of temperature led to inhibition of the crystallization process, as no solid product was formed after 72 hours (DD-65C and DD-75C). To compensate the effect of decreased temperature, the reaction time was prolonged, however without success, as no product was obtained (DD-65C-120h). It can indicate that activation energy was too high to be overcome in the applied synthesis conditions.

In contrast to DD-65C and DD-75C, synthesis in DMF at 65 °C and 75 °C led to the formation of a solid product. Freshly synthesized, the DMF-65C and DMF-75C had the form of turquoise powder. Formation of macroscopic pale turquoise agglomerates, resembling sea urchins, was observed when the reaction vessel has cooled down to the RT (Figure 6.15a,b). The urchin structures were very brittle, and the standard cleaning procedure have led to their collapse. The designated yield significantly exceeded 100% (Table 6.1), suggesting that the product was not a pure MOF. The PXRD analysis revealed that apart from very weak reflexes which were assigned to Cu-TDPAT, unknown intensive reflexes were also observed at 14.2°, 20.2°, 23.6°, 28.7°, 31.8°, 32.2° and 38.5° (Figure 6.2c). The needle-like crystals were recognized as $[(CH_3)_2NH_2][Cu(HCOO)_3]$ – a perovskite-like 1-D MOF – dimethylammonium copper formate (DMACuF) [337,338], basing on the simulated PXRD pattern obtained basing on the .cif file from the work of Collings and co-authors [339]. The fact that on the diffraction patterns of DMF-65C and DMF-75C, the different reflexes assigned to DMACuF were of varying relative intensity, can be explained by the one-dimensionality of the material and diverse orientation of the crystallites with the respect to the X-ray beam [340]. The presence of DMACuF crystals was confirmed both before and after the standard activation process (Figure 6.14a). According to the literature, DMACuF is highly water soluble, thus, to further confirm the presence of recognized structure, obtained powder was rinsed with water. In result, nearly full dissolution of the 1D MOF was observed, confirming the presence of this crystal structure. However, no improvement in the MOFs crystallinity (presence of weak reflexes in the range of 2-12° in Figure 6.14b) was observed after the by-product water washing procedure. Organic character of the by-product was also confirmed by the TGA analysis

(Figure 6.6c) – a larger mass of the sample was decomposed during the measurement of DMF-65C and DMF-75C in comparison with Cu-TDPAT(DMF), in the case of which inorganic Cu_2O was created as a by-product.

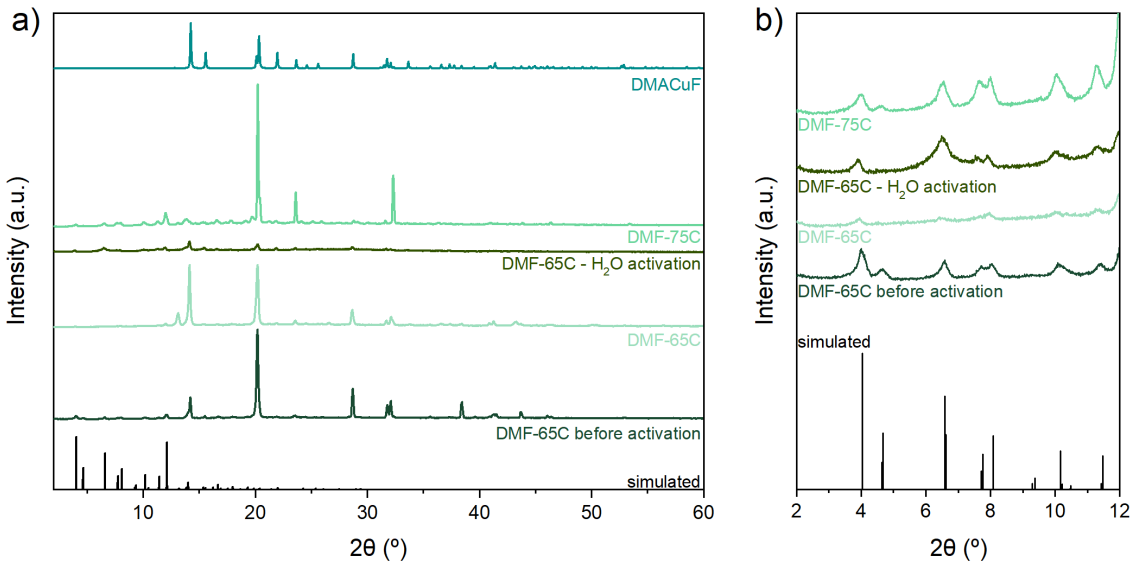


Figure 6.14 Comparison of PXRD patterns of: a) DMF-65C (before and after activation with MeOH and water), DMF-75C and DMACuF; b) DMF-65C and DMF-75C with simulated Cu-TDPAT data in 2-12° range.

The SEM images of DMF-65C and DMF-75C presented in Figure 6.15c and d, show the presence of MOF octahedrons with distorted vertices, being about 15-20 and 13-15 µm wide, respectively. Apart from that, plenty of diverse irregular particles of smaller size than the octahedrons were also observed. Probably these were the fragments of the fragile DMACuF or low-crystalline Cu-TDPAT. Both the results of TGA (Figure 6.6c) and the FTIR (Figure 6.8c) analyses confirmed that in comparison with Cu-TDPAT(DMF), both DMF-65C and DMF-75C were characterized with low porosity. This was evidenced by both the reduced amount of water released during thermal treatment (less than 2% of mass loss) and width of the band corresponding to the O-H stretching vibrations observed normally in the range of 3750-2650 cm^{-1}. Additionally, the S_{BET} values obtained from nitrogen adsorption at -196 °C, reached only the values of about 10 $m^2 \cdot g^{-1}$ and 100 $m^2 \cdot g^{-1}$ for DMF-75C and DMF-65C, respectively

Next, the effect of a higher temperature – 95 °C - was tested. In contrast to the processes caried out in lower temperatures, the synthesis performed at 95 °C in DMA/DMSO (DD-95) have led to successful precipitation of the product with the yield of reaction about 6% lower than for Cu-TDPAT(DD). Macroscopic observations did not reveal significant differences in appearance compared to the primary sample, as a turquoise crystalline powder was obtained. However, the SEM analysis revealed the less-defined morphology of the sample compared to the original Cu-TDPAT(DD) (Figure 6.15e). The vast majority of solids had a form of shapeless chunks of size between 10 and 50 µm. Among them, several well-defined octahedrons of width 13-18 µm were observed as well. The PXRD analysis confirmed formation of highly crystalline Cu-TDPAT without any by-products (Figure 6.2b) and, based on the TGA curve from Figure 6.6b, the mass loss assigned to degrading solid (47.6%) was similar to the Cu-TDPAT(DD) (48.9%). Despite the most

disturbed morphology, DD-95C exhibited one of the most developed surface areas (2222 $m^2 \cdot g^{-1}$) and the highest CO_2 uptakes (4.73 and 7.65 $mmol \cdot g^{-1}$ at 25 and 0 °C, respectively) among all obtained samples, giving 12 and 20% boost in comparison with Cu-TDAPT(DD).

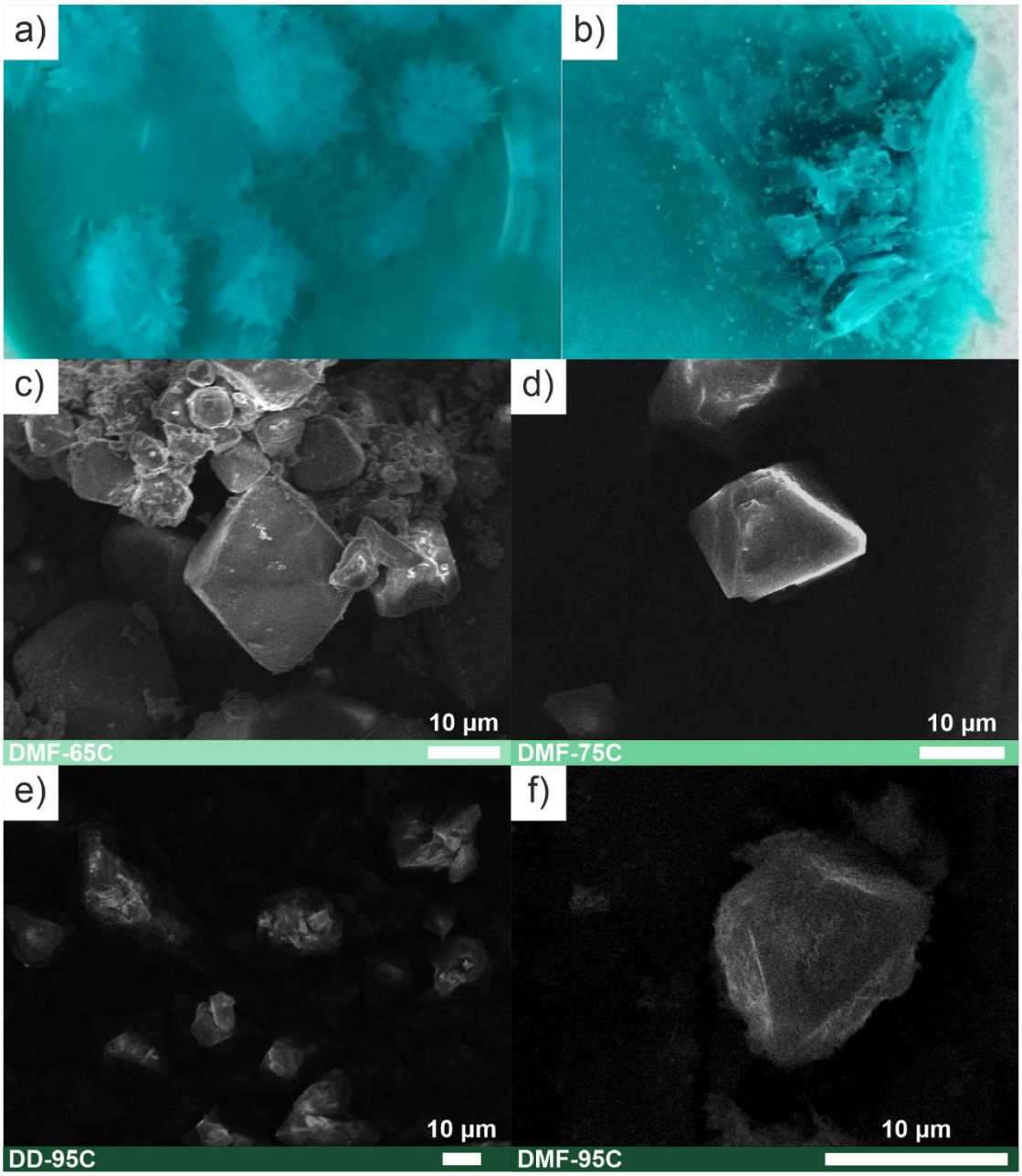


Figure 6.15 Digital images of a) DMF-65C and b) DMF-75C; SEM images of c) DMF-65C, d) DMF-75C, e) DD-95C and f) DMF-95C

The same increased temperature was also used in the DMF synthesis environment (DMF-95C). Similarly to other DMF syntheses, the presence of copper and copper(I) oxide was undoubtedly confirmed by the PXRD analysis (Figure 6.16a), explaining the determined reaction yields greater than the theoretical one. Vaguely outlined reflexes of Cu-TDPAT on the PXRD pattern were revealed when magnifying intensity in the range of 2-30° of 2θ (Figure 6.16b). As the value of S_{BET} was lower than 150 $m^2 \cdot g^{-1}$ the full N_2 adsorption-desorption isotherm at -196 °C as well as isotherm of CO_2 adsorption-desorption at both temperatures (0 and 25 °C) were not collected.

Similarly to the TGA curve measured for DMF/DMSO, the two distinct steps of mass loss characteristic for pure Cu-TDPAT in the range of 220-380 °C were almost indistinguishable (Figure 6.6c). Only single defective micrometric octahedrons with unevenly truncated vertices were tracked by SEM among aggregates of irregular nanoparticles (Figure 6.15f). The results of DMF-95C synthesis stand in agreement with the observations from the previous sections describing other DMF-based syntheses. In this case, the elevated temperature in the presence of significant copper precursor excess and of HBF_4 presence, seem to even more shift the equilibrium state towards the by-products formation.

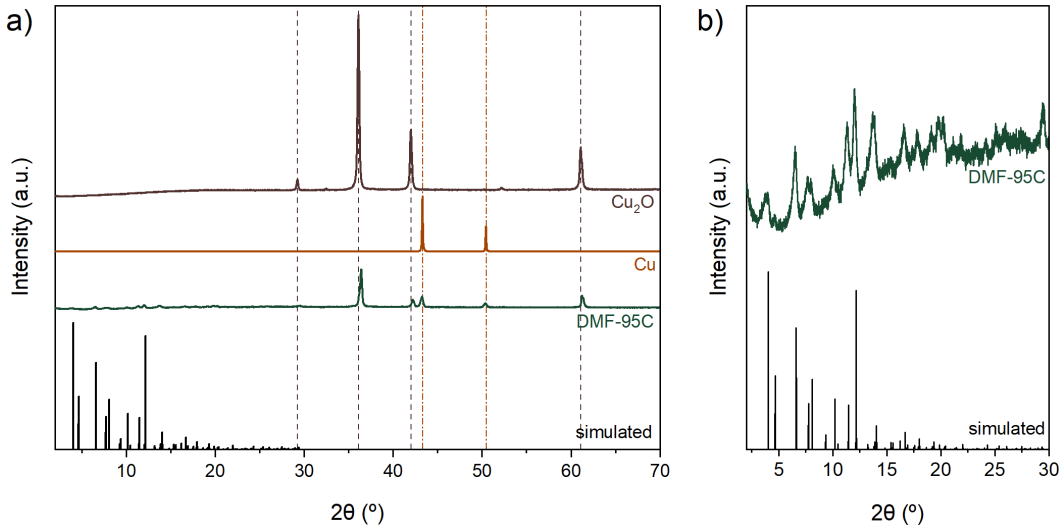


Figure 6.16 Comparison of PXRD patterns of: a) DMF-95C and by-products (Cu and Cu_2O) general overview; b) DMF-95C and simulated Cu-TDPAT data in 2-30° range

The temperature variations had a significant effect on the MOF crystals growth, however, the exact impact depends on the type of the liquid environments. In DMA/DMSO, lower temperatures disrupted the crystal growth process leading to no product formation. Below 85 °C, the insufficient thermal energy of the system suppresses standard framework nucleation by failing to overcome the activation energy barrier for organic linker deprotonation. At higher temperature the crystallinity of the product increased at the expense of the decreased yield and disturbed morphology. On the other hand, in DMF environment, the lowered temperature contributed limited growth of low-crystalline Cu-TDPAT and led unexpectedly to formation of 1-D MOF – dimethylammonium copper formate (DMACuF). The elevated temperature also disturbed the desired MOF crystal growth, probably due to slowed nucleation and the formation of copper and copper(I) oxide.

6.6. Influence of precursors molar ratio

In the next step, another factor – the molar ratio of precursors – was alternated. In order to prevent Cu_2O formation, the amount of copper precursor was decreased from 13.9 moles per one mole of the linker to its stoichiometric value – three moles of copper salt per each H_6TDPAT mole. In the DMA/DMSO solvent mixture (DD-3/1), the yield was lower by 29% in comparison with the original Cu-TDPAT(DD). No major changes were observed in terms of crystal structure, phase

purity (Figure 6.2b) and thermal stability (Figure 6.6b) of the product, as well as regarding the sorption properties comparing to Cu-TDPAT(DD). The S_{BET} increased by only 2%, while the CO_2 adsorption capacity raised by 6% at 0 °C and by 9% at 25 °C. No significant changes were also observed in the case of morphology (Figure 6.17a), as the created octahedrons were about 17-23 μm wide, what stands in agreement with the relatively modest increase of the S_{BET}, as the Cu-TDPAT(DD) octahedrons had the width of 20-25 μm. Additionally, the lowered molar ratio was also tested with lowered temperature (65 °C) and elongated time (120 h) (DD-65C-120h-3/1) of the reaction, but the product was not formed, further supporting the importance of temperature-induced nucleation and crystal growth in case of this solvent mixture. As expected, no reaction occurred when the ratio of metal precursor to the linker was intentionally changed from 13.9:1 to 1:1 (DD-1/1).

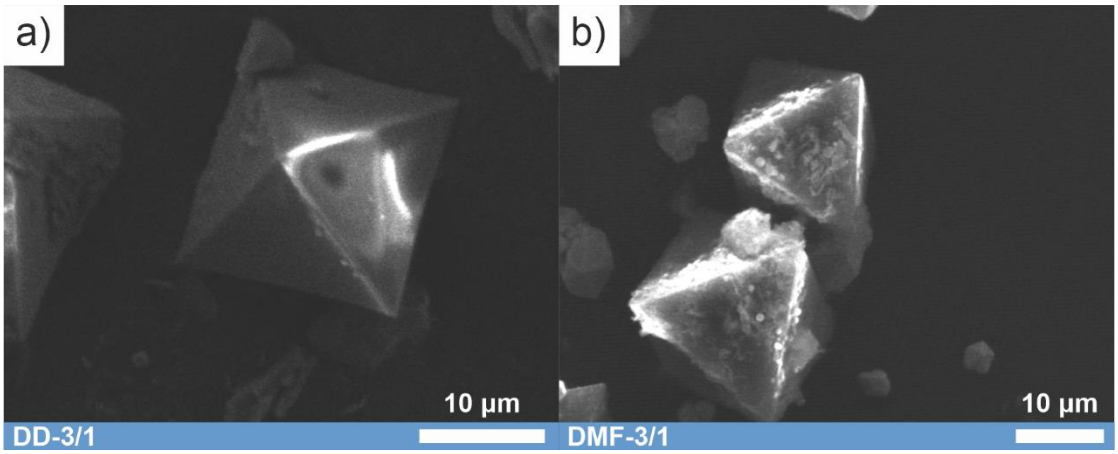


Figure 6.17 SEM images of a) DMF-3/1 and b) DD-3/1

The more pronounced effect of the reagents stoichiometry change was observed in pure DMF acting as the reaction environment. The obtained DMF-3/1 had a form of greyish turquoise product and the calculated yield was 68.8%. The successful formation of Cu-TDPAT MOF was confirmed by PXRD (Figure 6.2c) and FTIR (Figure 6.8c) analyses. The lowered amount of the copper precursor had beneficial effect on preventing the by-product formation, as only slight presence of low-intensity reflexes at 43.3° and 50.5° (Figure 6.18a), corresponding to the Cu planes ((111) and (200), respectively) was spotted in comparison to other DMF-based syntheses. Even though the by-product still formed, the sample surface area increased by 55% reaching 1000 $m^2 \cdot g^{-1}$, while CO_2 uptake elevated by almost 40% compared to pristine Cu-TDPAT(DMF), regardless of the temperature of analysis. The TGA analysis (Figure 6.6c) confirmed comparable to Cu-TDPAT(DD) content of solid has decomposed during the thermal treatment *i.e.* about 47.1%, that is only 1.8% less than for the primary sample, confirming low quantity of the by-product. At the same time, the decrease assigned to moisture evaporation reached only about 6% of mass loss, which stands in line with the S_{BET} value. The morphology recorded by SEM (Figure 6.17b) was not alternated significantly compared to Cu-TDPAT(DD) – bigger octahedrons of 18-22 μm and smaller particles, with an imperfect octahedral outline, being about 5-7 μm in size were observed. Based on the literature [94], to further investigate the most efficient approach to reduce the amount of by-

products when DMF is used as synthesis environment, HBF_4 was exchanged to HNO_3 to act as modulator (DMF-3/1-HNO_3). The PXRD measurement revealed mainly the presence of Cu_2O and Cu crystal structures. Only traces of very poor crystallinity Cu-TDPAT were revealed (Figure 6.18a and b), formation of which was confirmed by the FTIR spectroscopy (Figure 6.8). Additionally, the obtained DMF-3/1-HNO_3 was characterized by very low S_{BET} equal to only about 18 $m^2 \cdot g^{-1}$ and low amount of solid that degraded during thermal treatment (about 21.4%), confirming the findings of PXRD analysis. The SEM imaging revealed presence of particle chunks without any specific shape in the varying size between 5 and 40 µm (Figure 6.18c). Similarly, as it was mentioned in Section 6.4 on the influence on the modulator content, such outcome was probably caused by too high content the acid, leading to disturbance of the Cu-TDPAT formation in favor of by-products creation.

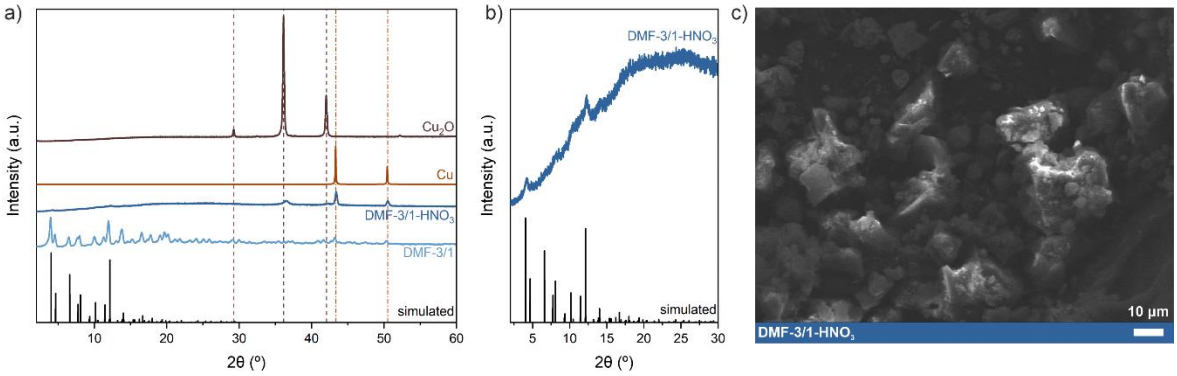


Figure 6.18 Comparison of PXRD patterns of DMF-3/1, DMF-3/1-HNO_3 and by-products (Cu and Cu_2O): a) general overview, b) DMF-3/1-HNO_3 and simulated Cu-TDPAT data in 2-30° range; c) SEM image of DMF-3/1-HNO_3

By the proper adjustment of molar ratio of the MOF precursors, it is possible to significantly limit the side reactions occurrence in DMF-based synthesis environment. Such change did not significantly alter the properties of product obtained in DMA/DMSO, but led to moderately decreased yield with simultaneous slight development of the surface area.

6.7. *Influence of the copper precursor*

At last, the influence of the counter anion in the copper salt type was investigated. The copper(II) nitrate trihydrate was exchanged to copper(II) acetate hydrate and copper(II) tetrafluoroborate hydrate in an attempt to improve the product crystallinity.

In comparison with the sample obtained using copper trihydrate in DMA/DMSO, the yield was decreased from 62.7% to 58% and 46.6% when acetate and tetrafluoroborate hydrates were used, respectively. The diffraction patterns and IR spectra of both samples, DD-AcO and DD-BF_4, indicated that pure Cu-TDPAT was formed (Figure 6.2b, Figure 6.8b). The intensity of peaks in low 2θ region was lower than for Cu-TDPAT(DD), which may suggest slightly lowered crystallinity of the samples obtained with alternative precursors. For DD-AcO the S_{BET} was equal to 1690 $m^2 \cdot g^{-1}$, giving about 14.5% decrease in comparison with Cu-TDPAT(DD), while the surface area measured for DD-BF_4 was reduced by only 6% (reaching 1876 $m^2 \cdot g^{-1}$). Respectively, similar changes compared to the primary sample were observed in the case of CO_2 uptake values at 0 °C (decrease

by 7 and 10.5% for DD-BF_4 and DD-AcO, respectively) and 25 °C (analogously, decrease by 4.5 and 6.5%). Similarly to Cu-TDPAT(DD), octahedral particles were observed by SEM for both DD-obtained samples with the alternated metal precursors (Figure 6.19a and b). Apart from bipyramids of 20-22 μm width noticeable for DD-BF_4, presence of lumps of similar size, but without a clearly defined shape were found. In turn, particles of more uniform outline in the size range of 7-17 μm were formed in the case of DD-AcO, however, some geometry imperfections were still detectable. Considering the thermal stability, the exchange of the copper source to tetrafluoroborate hydrate shifted the starting point of thermal decomposition towards lower values by about 30 °C to begin at about 190 °C, while for sample obtained by using acetate hydrate, this value was almost unchanged compared to Cu-TDPAT(DD) – *i.e.* slightly below 220 °C (Figure 6.6c).

Two additional variants of synthesis in the DMA/DMSO mixture using $Cu(AcO)_2{\cdot}H_2O$ as the metal source were also investigated, namely with lowered molar ratio of the precursors (DD-AcO-3/1) and with using autoclave as a reaction vessel (DD-AcO-R). The usage of the molar ratio equal to 3:1 (copper precursor to linker) led to obtainment of the sample with worsened characteristics compared to Cu-TDPAT(DD). Analogously to DD-3/1, the yield of DD-AcO-3/1 was lower than for the primary sample, reaching only 22.5% of the theoretical value. As for other samples obtained herein in the DMA/DMSO solvent mixture, the reflexes observed on PXRD pattern were sharp and intensive, with no sign of by-products (Figure 6.2b). The SEM imaging has shown that among all reported samples relatively the most ideal octahedrons of similar width between 12 and 15 μm were obtained in these conditions (Figure 6.19c). The result of the undisturbed octahedral shape of the formed particles was probably increased thermal properties, as the starting point of the decomposition was shifted up to 250 °C. However, the S_{BET} and the CO_2 sorption capacities of DD-AcO-3/1 at both temperatures were decreased by 63-65% in comparison with Cu-TDPAT(DD). Similarly, these values were significantly reduced also for DD-AcO-R – by about half compared to Cu-TDPAT(DD) – while the PXRD pattern presented clear and sharp reflexes (Figure 6.2b). In contrast to DD-R, the reflexes at 2θ at 4.0° and 4.7° (corresponding to (011) and (110) planes, respectively) were clearly outlined for DD-AcO-R and the yield was higher by about 20%, reaching 54.5%. On the other hand, the similarity to DD-R was also spotted and concerned the specific morphology of octahedral crystals with visible surface cracks, but also particles clearly torn apart into smaller shreds (Figure 6.19d). Apart from the fragments of an unspecified shape, the whole unharmed octahedra with a size of about 15-25 μm were recognized, as well as larger ones with the size exceeding 30 μm, which were clearly cracked. Comparing to the primary sample the thermal stability of DD-AcO-R remained unchanged.

To verify if the observed changes in the MOF formation were the effect of anion source change, the synthesis with the reversed source of anions was conducted, where nitrates from modulator and tetrafluoroborates from copper salt were supplied (DD-BF_4-HNO_3). However, this approach was not efficient as no solids were formed for, suggesting that HNO_3 was too weak to efficiently play the role of a modulator.

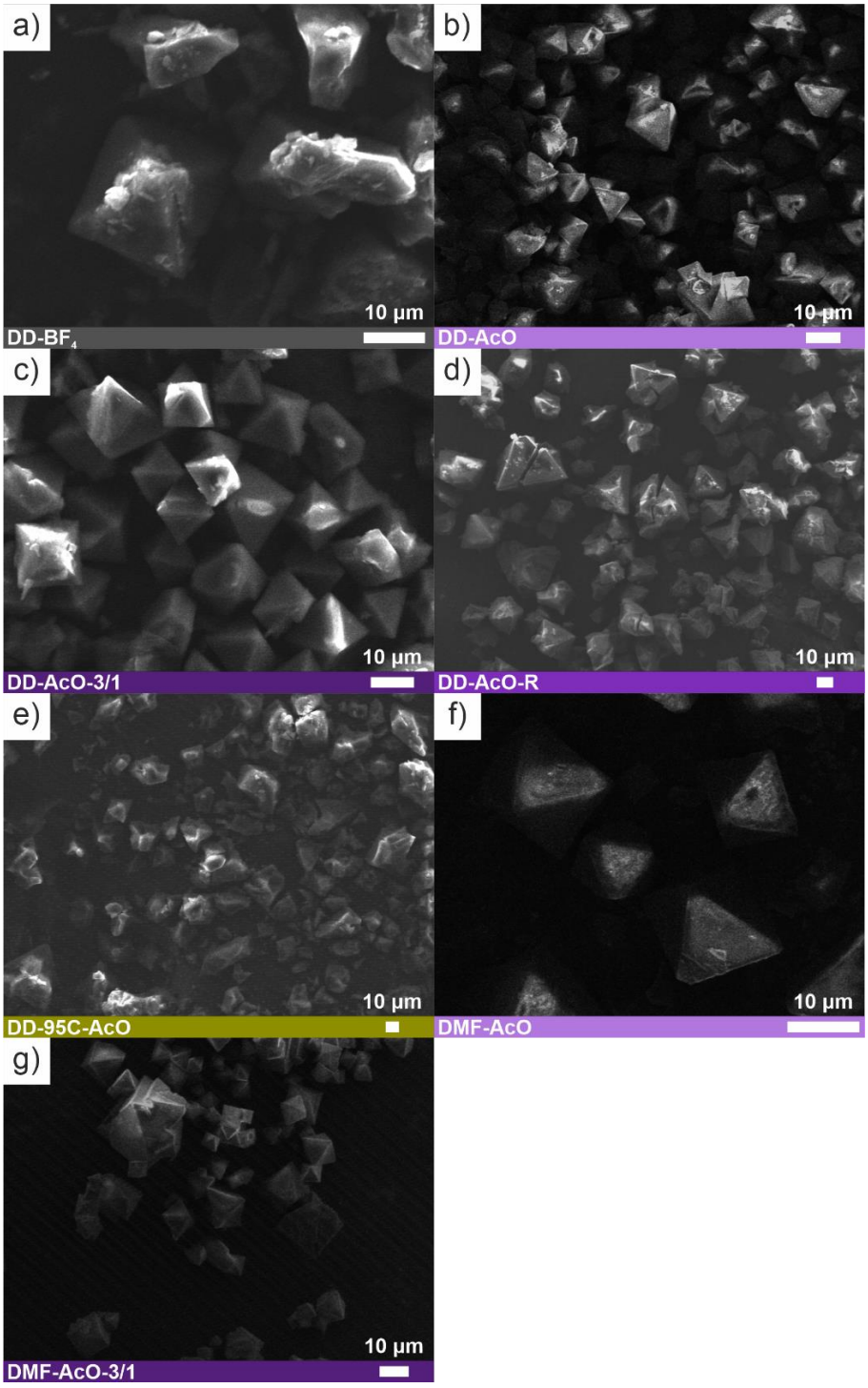


Figure 6.19 SEM images of a) DD-BF_4, b) DD-AcO, c) DD-AcO-3/1, d) DD-AcO-R, e) DD-95C-AcO, f) DMF-AcO, g) DMF-AcO-3/1

As the elevated temperature was found beneficial for the MOF formation in DD solvent mixture (DD-95C), similar approach was applied for copper(II) acetate hydrate precursor (DD-95C-AcO). The calculated yield for DD-95C-AcO in comparison with samples obtained using copper nitrate at 95 °C and 85 °C was higher by about 8% and 2.5% respectively. However, for this sample, disappearance of both reflexes corresponding to the (011) and (110) planes located at 2θ equal to 4.0° and 4.7° occurred (Figure 6.2b), accompanied by the decrease of the specific surface area, diminished to the level of 1184 $m^2 \cdot g^{-1}$. The material's ability to adsorb CO_2 was also diminished by

about 46% at both tested temperatures, compared to the primary sample. The described characteristics stand in accordance with the observed unspecified morphology of the sample, resembling disturbed octahedra, cracked into several pieces (Figure 6.19e). Both smaller solids of about 10-15 μm wide and 2-3 times larger pieces were noticed. This confirms, that higher temperature of the synthesis (95 °C) may be beneficial for the crystallization process of Cu-TDPAT. However, at the same time, the resulting large structures (even up to 50-60 μm taking into consideration the size of the biggest visible particles), may cause high stress in the crystal structure. This may lead to their final breakage, e.g. during drying in a high vacuum and at high temperature (as a result of capillary forces [341]) or under the influence of mechanical damage for example during sample transfer. It was also noted that the thermal stability was reduced by about 20 °C compared to Cu-TDPAT(DD) (Figure 6.6b).

For the DMF synthesis environment only copper(II) acetate hydrate was applied instead of copper(II) nitrate trihydrate. The exchange of the precursor itself did not affect the by-product formation, what was already indicated by the yield of DMF-AcO exceeding the theoretical value (reaching almost 130%). As a confirmation, the PXRD analysis of DMF-AcO (Figure 6.20) revealed presence of pure copper (reflexes at 43.3° and 50.5°) and copper(I) oxide (reflexes at 29.6°, 36.4°, 42.3° and 52.4°) in the sample. Similarly, as in the case of DMF-95C and DMF-3/1-HNO_3, the shape of TGA curve (Figure 6.6c) is more flattened, compared to other DMF-obtained samples, and the calculated content of solid that decomposed during the thermal treatment was equal to 24.8%, which is half as much as in the samples characterized as pure MOF. According to the nitrogen adsorption study at -196 °C, the sample was characterized by relatively low surface area as for Cu-TDPAT – about 728 $m^2 \cdot g^{-1}$ – which nevertheless represents a 13% increase compared to Cu-TDPAT(DMF). Similar improvement (about 10%) of DMF-AcO over Cu-TDPAT(DMF) was also observed regarding the measured CO_2 uptake. Additionally, the sample morphology recorded with SEM (Figure 6.19f) was comparable with the primary sample obtained in DMF – 10-15 μm wide octahedrons with rough surface were recognized.

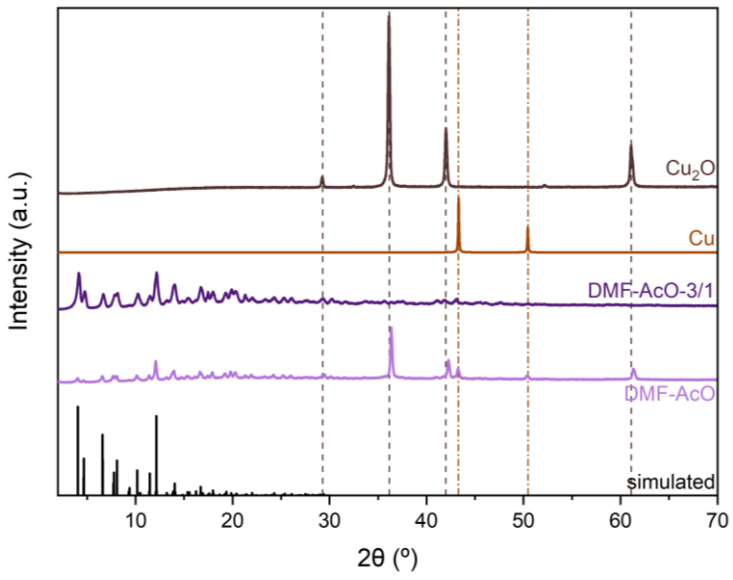


Figure 6.20 Comparison of PXRD patterns of DMF-AcO, DMF-AcO-3/1 and by-products (Cu and Cu_2O)

As the molar ratio change was found beneficial in the previous synthesis attempts for by-product limitation (*i.e.* DMF-3/1), this approach was also implemented utilizing acetate salt instead of a nitrate salt. In contrast to DMF-AcO, but similarly to DMF-3/1, the calculated yield for DMF-AcO-3/1 was in a range that does not suggest the formation of by-products. No signals corresponding to pure copper or its oxides were observed (Figure 6.20) confirming the fact of pure Cu-TDPAT formation. Another aspect confirming purity of the material was determined by the content of decomposed solids from the TGA curve (Figure 6.6c), value of which was similar to the value obtained for the primary sample. The sample DMF-AcO-3/1 was also characterized with the superior S_{BET} and CO_2 uptake, almost equal to DD-95C, reaching respectively 2144 $m^2 \cdot g^{-1}$ and uptake of 7.73 $mmol \cdot g^{-1}$ (at 0 °C) and 4.74 $mmol \cdot g^{-1}$ (at 25 °C). This result makes DMF-AcO-3/1 the sample of the best sorption performance among those obtained using DMF as a reaction medium practically doubling the results of the second-best DMF-obtained sample (DMF-0A) and represents almost 3.5-fold increase compared to Cu-TDPAT(DMF). The SEM imaging revealed formation of octahedra with distinct sharp edges with the width oscillating around 5-12 μm (Figure 6.19g). Interestingly, among the observed crystals, several of the biggest in size octahedrons have undergone a process of twinning during the synthesis.

The additional synthesis in the DMA/DMSO mixture at 95 °C proved that the elevated temperature can lead to overgrow of the crystals and by that to their breakage. Similar outcome was observed when the extra synthesis using the stainless-steel autoclave with Teflon liner was carried out. Probably, comparing to the Schott bottle, the pressure inside the autoclave is higher, what causes both structural damages as well as lowers the yield. In turn, the combination of proper molar ratio of reagents as well as the type of metal precursor, was found crucial in terms of the synthesis carried out in specific solvent or solvent mixture.

6.8. Analysis of synthesis conditions influence on Cu-TDPAT

The influence of changes introduced to the reaction conditions sets and the resulting influence on the forming product properties was summarized in Figure 6.21. Among thirty performed experiments, six of them did not let to obtain any solid product *i.e.:* DD-65C, DD-65C-120h, DD-65C-120h-3/1, DD-75C, DD-1/1 and DD-BF_4-HNO_3. Obviously, these synthesis conditions were concerning the same solvent mixture – DMA/DMSO – and confirm the minimal values of the reaction time and temperature, as well as the molar ratio of the precursors exist and must be reached to establish the thermo-kinetic equilibrium for the MOF formation to occur. Based on that the temperature appears to be the most critical aspect – too low temperature is very difficult to compensate even with extending the time of the reaction.

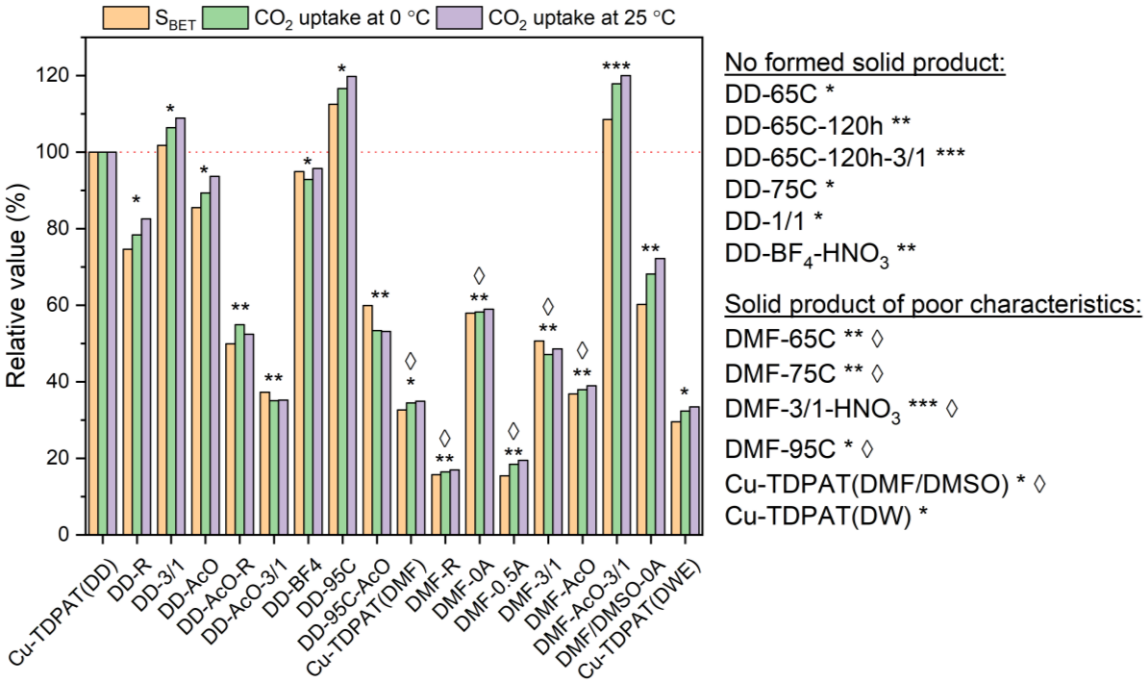


Figure 6.21 Relative changes observed for the fully analyzed Cu-TDPAT samples and summary of others. Each asterisk symbol stands for the factor that was changed for the actual synthesis compared to the reference sample (- one factor changed, ** - two factors changed, *** - three factors changed). Diamond (◊) symbolizes formation of by-products.*

Another six performed experiments led to formation of products characterized by low yield, low crystallinity of the product, obtainment of by-products, or combination of these. These samples were respectively: DMF-65C, DMF-75C, DMF-95C, DMF-3/1-HNO_3, Cu-TDPAT(DMF/DMSO) and Cu-TDPAT(DW). For all of them, DMF was the autonomous solvent or the component of the liquid environment. This underlines the fact that changing the solvent may demand significant alternation of other synthesis factors and narrows down the possibilities for efficient synthesis of highly crystalline, pure-phase product. Interestingly, changing of the temperature influenced only the type of forming by-products, while not significantly affecting other analyzed properties. Thus, other parameters should be adjusted rather than the temperature. Additionally, the growing concentration of water in the synthesis environment was found to successfully prevent the formation of side products. Even though, the characteristics of the product were poor and the other factors should have to be adapted as well, in order to improve the form of the growing Cu-TDPAT.

In the case of all nine DMA/DMSO obtained samples (the reference one, as well as the following DD-R, DD-3/1, DD-AcO, DD-AcO-R, DD-AcO-3/1, DD-BF_4, DD-95C and DD-95C-AcO), no unwanted products were found. Five of the samples were characterized with at least 75% of the value of Cu-TDPAT(DD) considering both – specific surface area (that is at least 1475 $m^2 \cdot g^{-1}$) and the CO_2 uptake (over 3 and 5 $mmol \cdot g^{-1}$ adsorbed at 25 and 0 °C, respectively). Two of them even exceeded the values of the reference sample, when molar ratio was decreased (DD-3/1) and when the temperature was increased (DD-95C - sample with the highest S_{BET} value). The visibly deteriorated characteristics were reported when the copper(II) acetate hydrate was used instead of the nitrate, but only when an additional factor was altered *i.e.* the reaction vessel, the molar ratio of

the precursors as well as the temperature. When only the salt was replaced (regardless if for tetrafluoroborate or acetate), both the S_{BET} and CO_2 uptake were decreased by 14.5% in the case of the most pronounced decrease when compared to Cu-TDPAT(DD), while preserving the satisfactory crystal structure of the MOF.

In contrast, among seven DMF-derived samples, only one had characteristics similar to the reference material, or even better than it. DMF-AcO-3/1 reached the second highest S_{BET} and the highest CO_2 sorption capacity regardless of the temperature of the measurement (comparable with DD-95C, but still slightly higher). At the same time, it was the only sample obtained by using only DMF, in the case of which no side products were detected. Compared to the reference sample, obtainment of such characteristic demanded exchange of three factors – two apart from the solvent, *i.e.* source of copper and molar ratio of precursors. This was confirmed by the properties of Cu-TDPAT(DMF) and the other five samples – DMF-R, DMF-0.5A, DMF-0A, DMF-3/1 and DMF-AcO – for which the alternation of one additional factor was not enough to result in formation of pure Cu-TDPAT. When DMF was used in mixture with water and ethanol (Cu-TDPAT(DWE)), pure MOF was obtained, however, its crystallinity and specific surface area did not reach satisfactory level. On the other hand, when DMF was mixed with DMSO, promising improvement, compared to pure DMF, was observed, but only when no acid was utilized for the synthesis (DMF/DMSO-0A). However, the combination of the accompanying synthesis conditions requires further adjustments.

Figure 6.22 shows the relationship between three determinants being the S_{BET}, CO_2 uptake at 0 °C and the type of factor that was alternated for each material. Due to the fact that the sorption capacity at both temperatures changed in a similar way, these dependencies were illustrated only on the example of one of them (0 °C). Results indicate that molar ratio was the most significant considering the improvement of the Cu-TDPAT characteristics, regardless of the used solvent. However, its change could also lead to a significant deterioration of selected material properties, which means it interacts strongly with other factors. The change of solvent was found the second most critical factor, requiring the adjustment of more than one additional factor to achieve satisfactory results. After changing the solvent, one of the key modifications included reduction the amount of acid (acting as modulator) or eliminating it entirely. Nevertheless, even with the adjustments, synthesis with changed solvent did not allow to reach the level of the samples exhibiting the most desirable properties *i.e.* high CO_2 uptake and extensive surface area. For all samples synthesized in the autoclave, the deteriorated characteristics were observed. Similarly as for changing the molar ratio of the precursors, the effect of temperature is also ambiguous. On one hand it led to obtaining the best material, while in other cases either the characteristics were deteriorated, or, alternatively, the MOF was not formed or was dominated by the formation of side products.

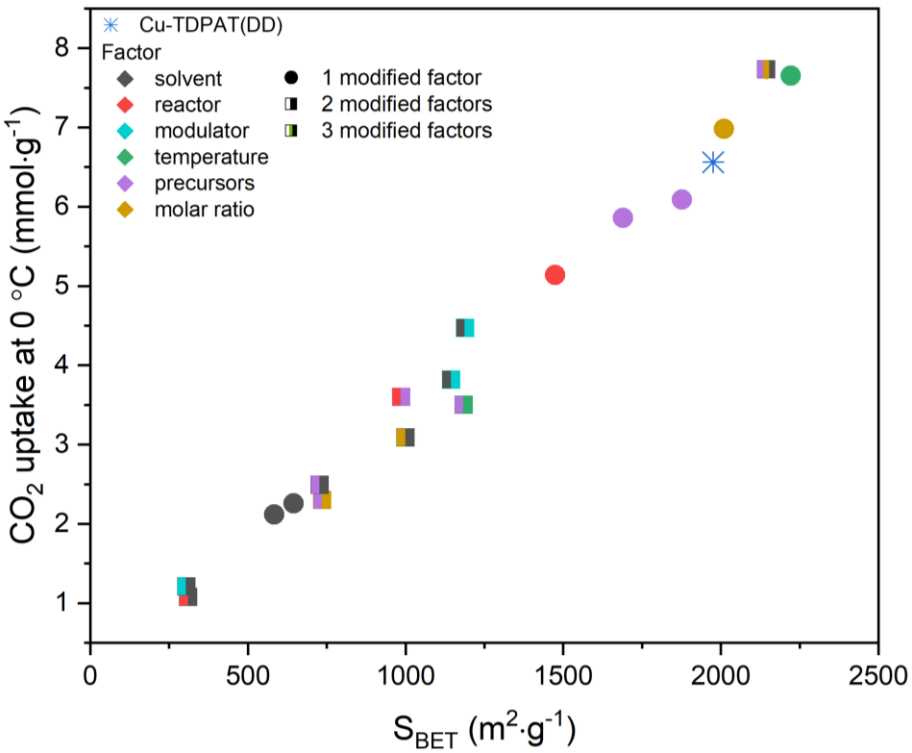


Figure 6.22 Relationship graph between S_{BET} and CO_2 uptake (at 0 °C). Colors and shapes were assigned to type of changed factor and number of changed factors for the specific sample. Asterisk symbol was assigned to the reference sample for clarity.

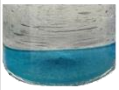
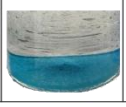
6.9. Stability of Cu-TDPAT in liquid environment of CO_2 photoconversion

Basing on the literature, eight different solvent combinations were chosen to act as the liquid environment of the CO_2 photoconversion in solid-liquid system. Apart from pure water [202], aqueous solutions of sodium carbonate (0.01 mol·dm^{-3}) [342], sodium sulfite (0.1 mol·dm^{-3}) and sodium hydroxide (0.1 mol·dm^{-3}) [343], as well as of TEOA (TEOA/H_2O 1:9 by volume) [211] were chosen. Similarly to the last mentioned solution, analogous mixture of TEOA in MeCN was also used (1:9 by volume) [110]. Among other selected organic solutions were DMF/TEOA/H_2O (respectively with volume ratio of 40:5:3) [209], MeCN/MeOH/TEOA (respectively with volume ratio of 4:1:1) [344] and additionally solution of trimethylamine (TMA) in MeCN (respectively 1:5 by volume) was proposed.

The appearance of MOF was assessed after each of the following steps – after dispersion in the liquid phase, after CO_2 injection to the photocatalytic environment and after irradiation of the system with UV-Vis light (Table 6.2). Cu-TDPAT was found not stable already after the contact with two aqueous solutions *i.e.* of Na_2SO_3+NaOH and of TEOA. In the first case, the turquoise powder turned black, while in the second case it fully dissolved to give clear blue solution. The obtained PXRD pattern confirmed destruction of MOFs structure in the case of treatment with Na_2SO_3+NaOH aqueous solution (Figure 6.23a). Saturation of the other six dispersions, led to disappearance of the solid photocatalyst in the case of TMA/MeCN solution, giving two distinguishable phases – top colorless solution and blue bottom solution. The treatment with light caused damage of the crystal structure of MOF, which was evidenced by PXRD analysis (Figure 6.23a). After the procedure, the

three visibly unchanged samples (*i.e.* treated with MeCN/MeOH/TEOA, TEOA/MeCN and DMF/TEOA/H_2O mixtures) were additionally left in the liquids overnight to verify their stability in the elongated time. The color of the liquid phase in the case of Cu-TDPAT left in MeCN/MeOH/TEOA and DMF/TEOA/H_2O changed the color to similar blue tone as in the case of TEOA/H_2O test, suggesting progressive dissolving of MOF. The remaining solid treated with DMF/TEOA/H_2O was analyzed with PXRD (Figure 6.23a), revealing disappearance of the main peaks at 4.0° and 4.7°, which stands in agreement with the partial structure collapse. Basing on the above, the water content in the liquid environment of CO_2 photoconversion in the case of Cu-TDPAT MOF has a critical for the stability of the structure and excludes the use of such solvent mixture. Only for MeCN/TEOA-treated sample no visible changes were observed, therefore the proper procedure of CO_2 photoconversion under UV-Vis light irradiation was performed. However, taking into consideration the behavior of the crystalline powder during photoconversion – sticking into bigger chunks or settling above the level of the liquid – it was concluded that this MOF is not suitable for this application. The use of Cu-TDPAT in powdered form significantly hinders not only the photocatalytic efficiency of the process, but also the question of photocatalyst regeneration after the process.

Table 6.2 Comparison of Cu-TDPAT sample presence after the next steps of CO_2 photoconversion procedure

Stage	Liquid environment							
	$Na_2CO_{3(aq)}$	$Na_2SO_{3(aq)}$ + $NaOH_{(aq)}$	H_2O	TEOA/H_2O	TEOA/MeCN	MeCN/MeOH /TEOA	DMF/TEOA /H_2O	TMA/MeCN
Dispersion of photocatalyst in liquid environment	+ 	Change of colour to black 	+ 	Dissolved 	+ 	+ 	+ 	+ 
Saturation with CO_2	+ 	-	+ 	-	+ 	+ 	+ 	Dissolved 
Light treatment	Change of colour to pale blue 	-	Change of colour to pale blue 	-	+ 	+ 	+ 	-

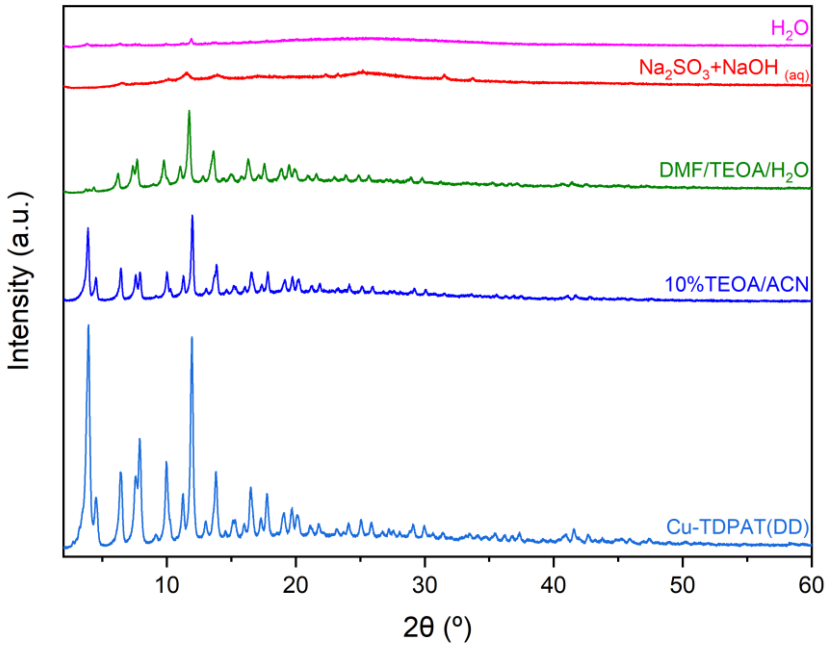


Figure 6.23 PXRD patterns of Cu-TDPAT after treatment with different liquid environments

6.10. Summary

The main aim of this Chapter was to verify the influence of different sets of synthesis conditions on the formation, morphology and properties of Cu-TDPAT. Seven different factors – type of solvent, temperature and time of the reaction, presence of modulator, molar ratio of precursors, the type of metal precursor and reaction vessel – were altered, resulting in total number of 30 different syntheses. It was found that the most determining factor among all was the type of solvent, which further determined the influenced the influence of other factors in Cu-TDPAT synthesis. A crystalline product with surface area exceeding 2000 $m^2 \cdot g^{-1}$ and ability to adsorb over 7.0 and 4.0 $mmol \cdot g^{-1}$ of CO_2, respectively at 0 and 25 °C, was obtained both in DMA/DMSO mixture and in pure DMF at 85 °C. In both cases such results were enabled by changing different variables, compared to the standard procedure. In comparison with DMF, the DMA/DMSO mixture was found out to be more favorable as the most of condition sets led to obtainment of highly crystalline product characterized by developed surface area evidenced by S_{BET} exceeding 1600 $m^2 \cdot g^{-1}$. At the same time, among samples obtained by using DMF-based environments, there was only one specific set of conditions providing both the crystalline phase purity and developed surface area, namely DMF-3/1-AcO. For these environments, the investigated conditions usually resulted in obtainment of poor-crystallinity Cu-TDPAT contaminated with copper-based by-products. Interestingly, it was found that the significant excess of copper source was the main cause of side reactions occurrence in DMF-based syntheses.

The impact of changing the copper source was also found more profound for DMF-based synthesis medium, as for DMA/DMSO only neglectable changes were observed. The choice of acetate hydrate was more beneficial in terms of morphology and the development of the surface

area. It was additionally proved that the used modulator played the role of capping and size controlling agent, regardless of the synthesis environment. However, the second face of the used HBF_4 was evidenced in the DMF-based environments, as it was found to be partially responsible for the formation of by-products, highlighting the necessity of the HBF_4 content optimalization. In opposition to these parameters, the influence of temperature, time and type of reaction vessel was found not solvent dependent. It was revealed that there is a certain temperature threshold below which the Cu-TDPAT MOF formation in the evaluated solvothermal reaction was not possible, probably due to thermo-kinetical reasons. On the other hand, exceeding the original synthesis temperature resulted in significant increase of the size of growing crystals, with simultaneous disruption of the octahedral morphology, probably as a result of stress in the crystal framework.

Taking all of that into consideration, this MOF's sensitivity is a double-edged sword – both considering both the synthesis conditions changes, as well as for the conditions of application. On the one hand, the synthesis conditions can be adjusted accordingly, however it is limited only to those already known ones. Thanks to this sensitivity, it is possible to precisely tune the properties of the resulting MOF by changing specific aspect of the set conditions. This characteristic can be beneficial in the design of material tailored for the selected applications. On the other hand, when introducing a new factor, the process can be significantly complicated and the desired satisfactory yield level of the synthesis or the appropriate product characteristics may not be achieved. In turn, the water sensitivity determines the use of Cu-TDPAT in the case of CO_2 photoconversion, limiting the possible liquid environments that can be used to anhydrous ones. On the other hand, in the case of powder material, even the use of an anhydrous reaction medium does not guarantee as good a result as it could if the material was placed stably for example grown on a substrate.

Considering the long synthesis time of Cu-TDPAT and its high sensitivity to changes in the synthesis environment, it was decided that another copper-based MOF would be modified using ionic liquids. Investigation over ILs influence on the sorption capacity of the chosen MOF – HKUST-1 – was decided to be performed without further testing the photocatalytic properties due to highly probable poor stability in solid-liquid environment of CO_2 photoreduction.

7. HKUST-1 modified with heterocyclic amino acid ionic liquids for selective CO_2 adsorption

HKUST-1 MOF was successfully modified using four different AAILs and one referential commercial IL (structures shown in Figure 7.1) *via* two different pathways: by addition of IL to the synthesis environment of MOF or post-synthetically by impregnation. Schematical representation of modification pathways in comparison with the standard HKUST-1 synthesis were shown in Figure 7.2. In this work, particular attention was given to investigate the effect of L-histidine and L-proline (acting as anions of different ILs) on the resulting morphology and sorption properties of the obtained products. Additionally, to reduce the probability of pores clogging, cations with different lengths of the side chains (ethyl- [EMIM] and butyl- [BMIM]) were used. In the synthetical route two different molar ratios of the substrates were used – n_{Cu}:n_{linker}:n_{IL} = 1.6:1:0.1 and 1.6:1:0.25. For the post-synthetical impregnation, solutions containing 1 and 10 wt% in relation to MOF mass were used. The modifications with [BMIM]-based ILs were only conducted using higher contents of ILs. The summary of all samples is presented in Table 7.1. To abbreviate names of the modified samples, symbols consist of IL amount (referring to the modification method) and first letters corresponding to cation and anion given.

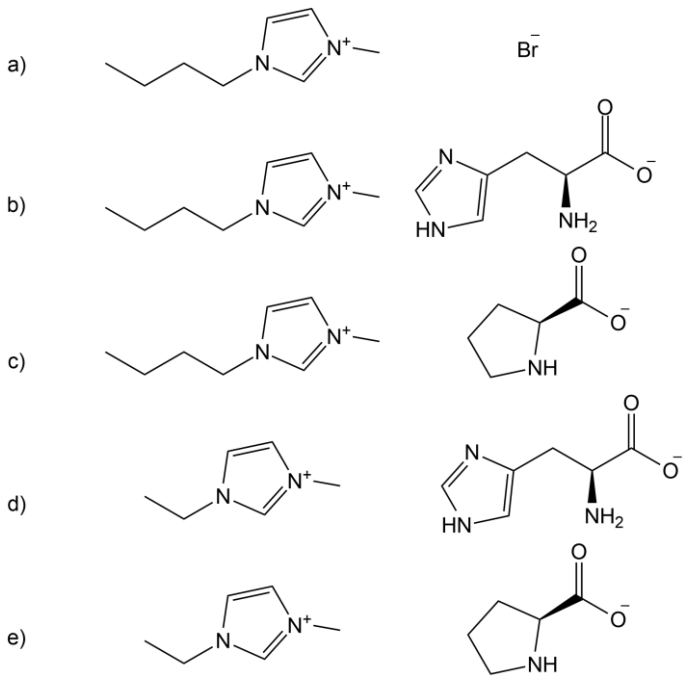


Figure 7.1 Chemical structures of: a) 1-Butyl-3-methylimidazolium bromide [BMIM][Br], b) 1-Butyl-3-methylimidazolium histidinate [BMIM][His], c) 1-Butyl-3-methylimidazolium prolinate [BMIM][Pro], d) 1-Ethyl-3-methylimidazolium histidinate [EMIM][His], e) 1-Ethyl-3-methylimidazolium prolinate [EMIM][Pro].

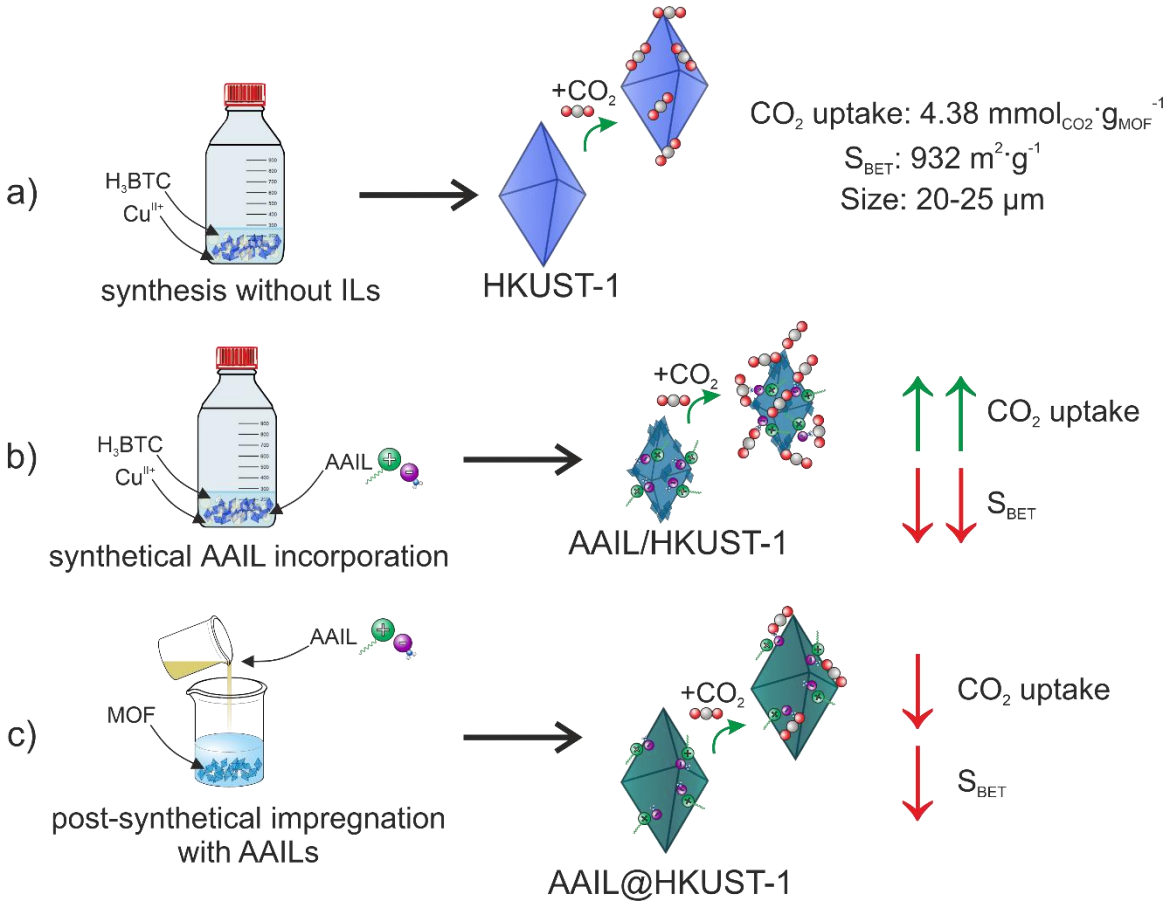


Figure 7.2 Schematical representation of: a) pristine HKUST-1 synthesis; b) synthetical AAIL introduction, c) post-synthetical AAIL impregnation.

Table 7.1 Sample labels, method of ILs introduction, amount and name of ILs, CO_2 sorption capacity (measured by volumetric method, at p~99 kPa) and BET surface area of HKUST-1 samples. Sample symbols consist of the IL amount introduced (0.1 and 0.25 for synthetical approach. 1% and 10% for post-synthetical approach), first letter of cation side chain (B – butyl, E – ethyl) and first letter of anion name (B – bromide, H – histidinate, P – prolinate).

Sample symbol	Method of IL introduction	Molar ratio of precursors $n_{Cu}:n_{linker}:n_{IL}$	Ionic Liquid	CO_2 uptake at 25 °C (mmol·g^{-1})	S_{BET} (m^2·g^{-1})
HKUST-1	-	-	-	4.38	931.6
0.1EP	in the synthesis environment	1.6:1:0.1	[EMIM][Pro]	5.26	1013.6
0.25EP	in the synthesis environment	1.6:1:0.25	[EMIM][Pro]	6.26	44.1
0.1EH	in the synthesis environment	1.6:1:0.1	[EMIM][His]	5.01	978.0
0.25EH	in the synthesis environment	1.6:1:0.25	[EMIM][His]	6.05	29.5
0.25BP	in the synthesis environment	1.6:1:0.25	[BMIM][Pro]	5.96	29.2
0.25BH	in the synthesis environment	1.6:1:0.25	[BMIM][His]	5.98	58.3
0.25BB	in the synthesis environment	1.6:1:0.25	[BMIM][Br]	6.04	664.2
Sample symbol	**Method of IL introduction**	**Amount of IL (% of used MOF mass)**	**Ionic Liquid**	**CO_2 uptake at 25 °C (mmol·g^{-1})**	**S_{BET} (m^2·g^{-1})**
1%EP	post-synthetical impregnation	1%	[EMIM][Pro]	4.11	962.9
10%EP	post-synthetical impregnation	10%	[EMIM][Pro]	3.92	696.0
1%EH	post-synthetical impregnation	1%	[EMIM][His]	4.41	924.2
10%EH	post-synthetical impregnation	10%	[EMIM][His]	3.81	569.2
10%BP	post-synthetical impregnation	10%	[BMIM][Pro]	2.08	315.6
10%BH	post-synthetical impregnation	10%	[BMIM][His]	1.95	176.1
10%BB	post-synthetical impregnation	10%	[BMIM][Br]	2.30	375.9

7.1. Characterization of materials

Structures of the obtained samples were confirmed by powder X-ray diffraction (PXRD) analysis. Diffractograms shown in Figure 7.3a and b. indicate presence of peaks characteristic for HKUST-1 at 6.8°, 9.6°, 11.7°, 13.4°, 14.7°, 16.5°,17.5°, 18.0° and 20.2°, which can be assigned to the respective planes: (200), (220), (222), (400), (331), (422), (333), (440), (442) [345]. In comparison with the reference sample, the reflexes observed for the samples modified by ILs introduced during the synthesis are characterized with lower intensity and wider signal base (Figure 7.3a and b). Even though the reflexes in the diffractograms of the impregnated materials are of soaring shape, nearly complete disappearance of reflexes corresponding to (200) plane is noticeable for most samples impregnated with 10% of ILs (Figure 7.3b). Remarkably, it can be still distinguished for samples 1%EH, 1%EP and 10%EH. Similar phenomenon, where the relative intensity of this reflex was significantly decreasing for HKUST-1 after post-synthetical impregnation with [EMIM][Tf_2N] was observed by Lin and co-workers [312]. The disappearance of this particular reflex was also observed by Sen *et al.* when methyl propiolate was loaded on MOF and further polymerized [346]. This indicates that the presence of guest molecules inside the MOF pores can disturb the diffraction of the X-ray on this particular plane, which results in its reduced intensity. Apart from typical signals characteristic for pristine HKUST-1, small reflex at 5.9° is visible for pristine sample and 1%EH, 1%EP and 10%EH. For the samples modified synthetically, the signal has blended with (200) plane reflex. As reported by Singh *et al.*, presence of this peak can be related to the structure hydration due to moisture adsorption [345]. It can be supported by the fact that the color of activated samples changes from dark blue to light blue after contact with air and the moisture contained therein. The color change is reversible and becomes darker after drying. Additionally, comparison of *in-situ* DRIFTs spectra recorded at RT and at 150 °C, shows visible diminishing intensity of the bands characteristic to moisture content, especially the wide peak ranging between 3750-2750 cm^{-1} which corresponds to stretching vibrations of O-H bonds as well as in the fingerprint region, *i.e.* below 1000 cm^{-1} (Figure 7.3c).

Figure 7.4a shows FTIR spectra in range of 4000-400 cm^{-1} of all obtained MOF samples confirming the presence of the same bands in all samples. Figure 7.4b-f show the magnified spectra of the samples grouped considering the type of introduced IL and the ILs themselves, in the wavenumber range limited to 2000-400 cm^{-1}. The band visible at about 490 cm^{-1} can be assigned to stretching vibrations of Cu-O [345]. Two adjacent peaks at 759 cm^{-1} and 729 cm^{-1} refer to the bending vibrations of C-H out-of-plane [347], while the in-plane vibrations are associated with the weak peak at about 1111 cm^{-1} [345]. Antisymmetric stretching vibrations of COO can be assigned to a pair of signals with maximums at 1641 cm^{-1} and 1449 cm^{-1} [345]. In turn, peak at 1374 cm^{-1} can be attributed to symmetrical stretching mode of COO [345]. The signal visible at 1585 cm^{-1} with tip clearly pointing towards left side refers to symmetric stretching mode of C-C bonds in aromatic ring of the linker [348]. In the case of spectra of the samples impregnated with 10 wt% IL, the tip is moved towards lower values *i.e.* about 1570 cm^{-1}. The shifted position of the peak's maximum is related to rocking vibrations of the bond between carbon atom of methyl side chain and the nitrogen

atom in the imidazolium cation [347], which confirms the presence of post-synthetically introduced ILs. Additional faint outlines of bands ascribed to IL at 1165 cm^{-1}, 650 cm^{-1} and 620 cm^{-1} suggesting respectively bending vibrations of the H-C-N bond in the imidazole ring, C-N bending oscillation and stretching vibrations of C-N of the longer side chain of the imidazole cation [347]. The signals at about 1463 cm^{-1} (asymmetric bending of C-H in the side chains) [349], 1380 cm^{-1} (wagging and twisting of N-C bonds at side chains) and 750 cm^{-1} (out of plane bending of C-H bonds in imidazole ring) [293] were undistinguishable in modified MOFs due to the presence of sharp bands related to the MOF structure of relatively high intensity.

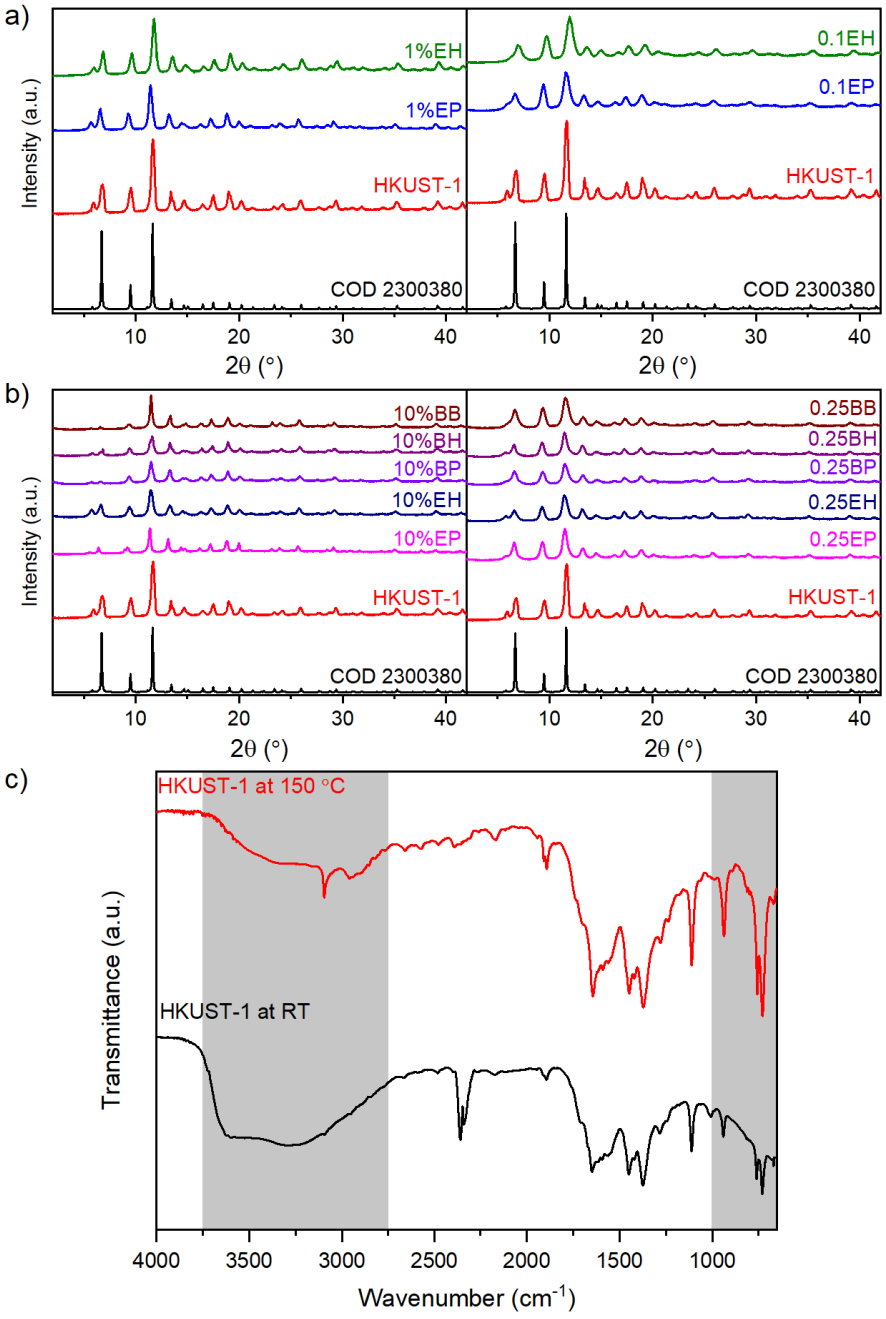


Figure 7.3 PXRD of the HKUST-1 samples: a) post-synthetically impregned with 1% of ILs or synthesized in presence of 0.1 mole equivalents of ILs, b) post-synthetically impregnated with 10 wt% of ILs or synthesized in presence of 0.25 mole equivalents of ILs; c) comparison of DRIFT spectra of HKUST-1 at RT and at 150 °C

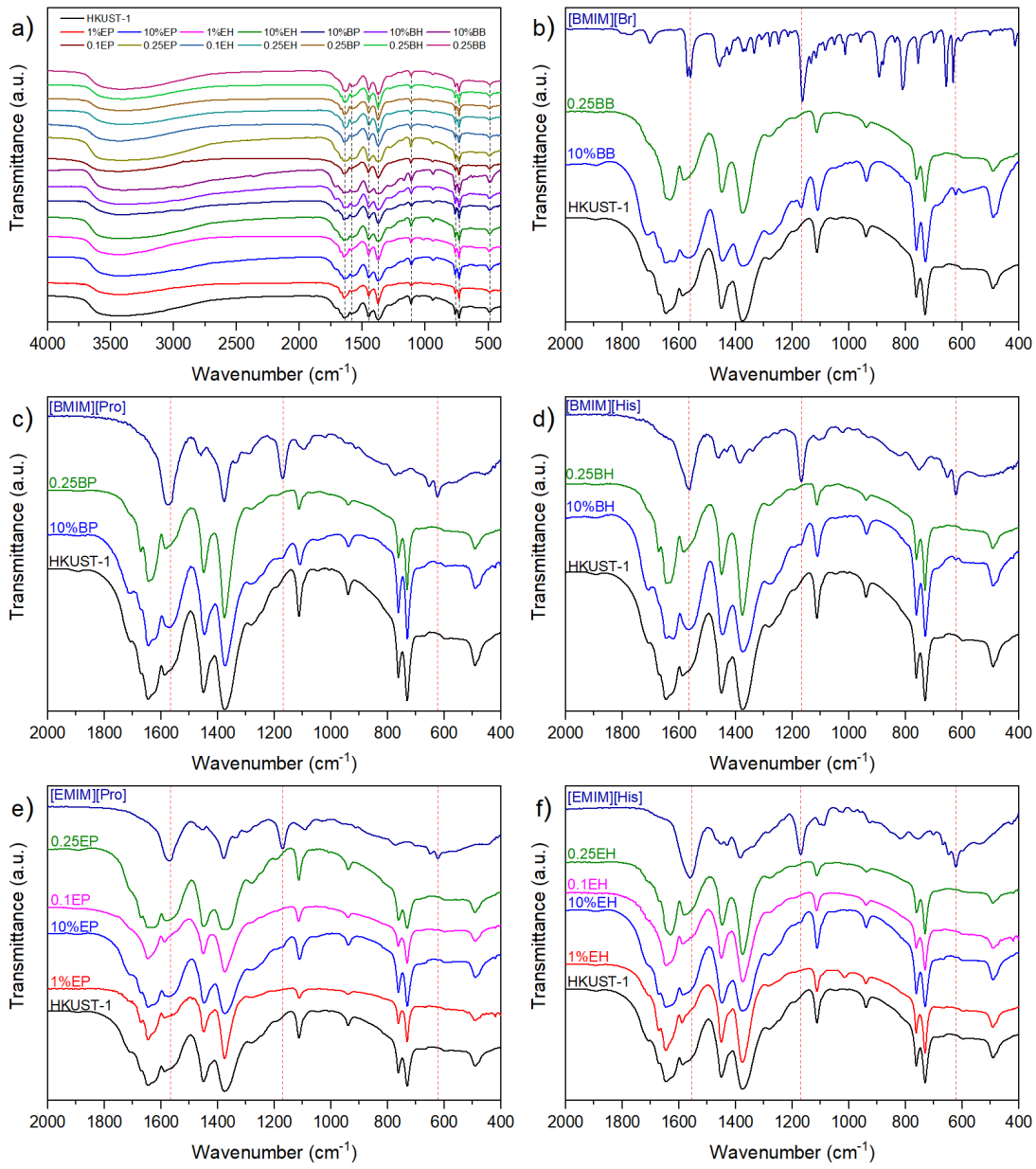


Figure 7.4 Comparison of FTIR spectra of :a) all MOF samples; samples modified with: b) [BMIM][Br], c) [BMIM][Pro], d) [BMIM][His], e) [EMIM][Pro], f) [EMIM][His]; the red dashed lines refer to the signals assigned to the ionic liquids

To further support the successful introduction of AAILs into the MOF and strengthen the evidence drawn from FTIR, content of elements was calculated using SEM-EDX (Table 7.2, Figure 7.5) and CHN elemental analysis (Table 7.3) for chosen samples modified by [EMIM][Pro] and [EMIM][His]. Both methods revealed increased level of nitrogen for samples modified by both – synthetical and post-synthetical approaches, what is consistent with expectations and observations of other researchers [300–302]. This also stands in agreement with the reduced content of oxygen atoms determined by SEM-EDX and simultaneous increase of the carbon content, which were determined by both methods. In the case of CHN elemental analysis, the discrepancies between theoretical C, H, N content values and the values designated by the measurement were also observed by Sezginel *et. al* [300]. The decreased carbon content and increased hydrogen content

may be related to the presence of water absorbed during sample preparation before the measurement. Additionally, presence of nitrogen may be associated with presence of DMF remaining in the MOF pores after synthesis. Higher content of nitrogen observed for 10%EH and 0.25EH by CHN by 1.6 and 2.0 wt%, respectively, in comparison with corresponding 10%EP and 0.25EP, can be explained by the number of nitrogen atoms present in specific amino acids (three nitrogen atoms in L-histidine *vs.* single nitrogen atom in L-proline). The very low amount of disclosed chlorine in 0.25EP, can be explained as residues of unreacted commercial [EMIM][Cl], used as starting material for obtaining both [EMIM]-based AAILs.

Table 7.2 Average elements content designated by SEM-EDX

Entry	Mass content (wt%)				
	C	N	O	Cu	Cl
HKUST-1	21.9±0.2	5.8±0.3	39.9±1.0	32.4±1.1	-
10%EP	21.5±0.2	6.9±0.2	38.4±1.2	33.1±1.1	-
0.25EP	22.7±0.9	6.5±0.5	37.8±0.5	32.8±0.7	0.24±0.02

Table 7.3 Elements concentration designated by CHN elemental analysis, normalized

Entry	Mass content (wt%)		
	C	N	H
HKUST-$1_{theoretical}$	97.3	0	2.7
HKUST-1	83.3	2.8	13.9
10%EP	84.3	5.0	10.7
10%EH	83.5	6.6	9.9
0.25EP	85.2	5.8	9.0
0.25EH	83.4	7.8	8.8

In comparison with pristine HKUST-1, no significant changes in the shape of the IL-modified MOF materials were indicated by SEM (Figure 7.6 and Figure 7.7). Similarly to the reference sample, presence of octahedral crystals was observed in all modified materials. The particle size for pristine MOF and samples impregnated with ILs was around 20-25 μm (considering width and side wall edge of the pyramids creating the octahedrons), regardless of the IL type. However, the size of the octahedral crystals obtained *via* synthetical modification route was smaller (10-15 μm), confirming the size controlling properties of the introduced ILs as a result of steric stabilization [11]. It is possible that ILs present in the synthesis environment have notable role in accelerating the nucleation step of the MOF crystals leading to growth limitation [350]. Additionally, existence of an octahedrons fraction of about 0.5-1 μm in size (close-up presented in Figure 7.6e and j, Figure 7.7e and i) was also discovered. The presence of two size fractions of HKUST-1 can be explained by occurrence of secondary nucleation process [351]. The role of ILs in MOF synthesis can be summarized in three aspects *i.e.* capping effect of ILs [352], affected density and viscosity of the synthesis medium [149], as well as modulating effect of AAILs (as they possess functional groups) [353,354]. In result AAILs molecules may interact with the growing MOF crystals blocking their outermost surfaces (capping effect) and preventing their further expansion. It is additionally intensified by the increased viscosity of the reaction solution. As the crystal growth is disrupted, new crystallites are formed in the less concentrated environment originating from the remaining unreacted precursors. Apart from that, the functionalized anion of the AAIL may play a role comparable to modulators like small monocarboxylic acids disrupting the balance between nucleation and growth rate. Interestingly, [EMIM]-based AAILs addition (considering molar ratio

n_{Cu}:n_{linker}:n_{IL} 1.6:1:0.25) resulted in the number of smaller particles sticking to the surface of the big octahedrons, covering it tightly, regardless of the anion type. On the other hand, both smaller and bigger fractions of crystals occur separately, not sticked to each other, when [BMIM]-based ILs were added to the synthesis. Such behavior can be explained by the difference of the length of the cation side chain. As the [EMIM][Pro] and [EMIM][His] possess shorter side chain, they create smaller steric hindrance compared with analogous [BMIM]-based ILs, thus they do not prevent the finer particles from settlement and agglomeration on the surface of big octahedrons (their capping abilities are relatively limited), as it happens for [BMIM]-based ILs.

Thermogravimetric analysis was used to determine the thermal stability of the obtained samples (Figure 7.8ab). Introduction of ILs to the synthesis environment of HKUST-1 does not influence the thermal stability of the obtained structures. In all samples, two declines separated by pronounced plateau can be observed. The first immediate mass loss at the beginning of the measurement – from 50 °C up to about 150 °C – refers to the evaporation of moisture and possibly methanol present in the pores of MOF. The initial moment of the synthetically modified MOF structure collapse remains at about 330 °C as for pristine sample (Figure 7.8). More diverse thermal performance can be observed for the samples modified post synthesis. The TGA curves of 10 wt% IL-impregnated powders, do not clearly outline shape of dual-stage decomposition. The plateau between the first and second mass loss turns into rather steady, slow weight loss. This can be probably caused by the decomposition of IL, which in contrast to synthetically modified samples, is not trapped inside pores, but is covering the surface of the samples. Interestingly, in the first step of decomposition, relatively lower decrease of samples mass can be observed comparing 10 wt% IL-impregnated materials (about 5%) to 1%-IL modified (about 10%) or reference sample (12%). This suggests that the samples containing higher IL amounts possess less accessible pores, thus less humidity can be adsorbed during the sample preparation. Additionally, impregnation of the samples visibly shifts the decomposition temperatures towards lower values, by even about 70 °C for 10%BP, what may indicate decomposition of unbound IL. It is consistent with the thermal stability of the chosen pure ILs, which start to decompose at temperature of about 190 °C (Figure 7.8c).

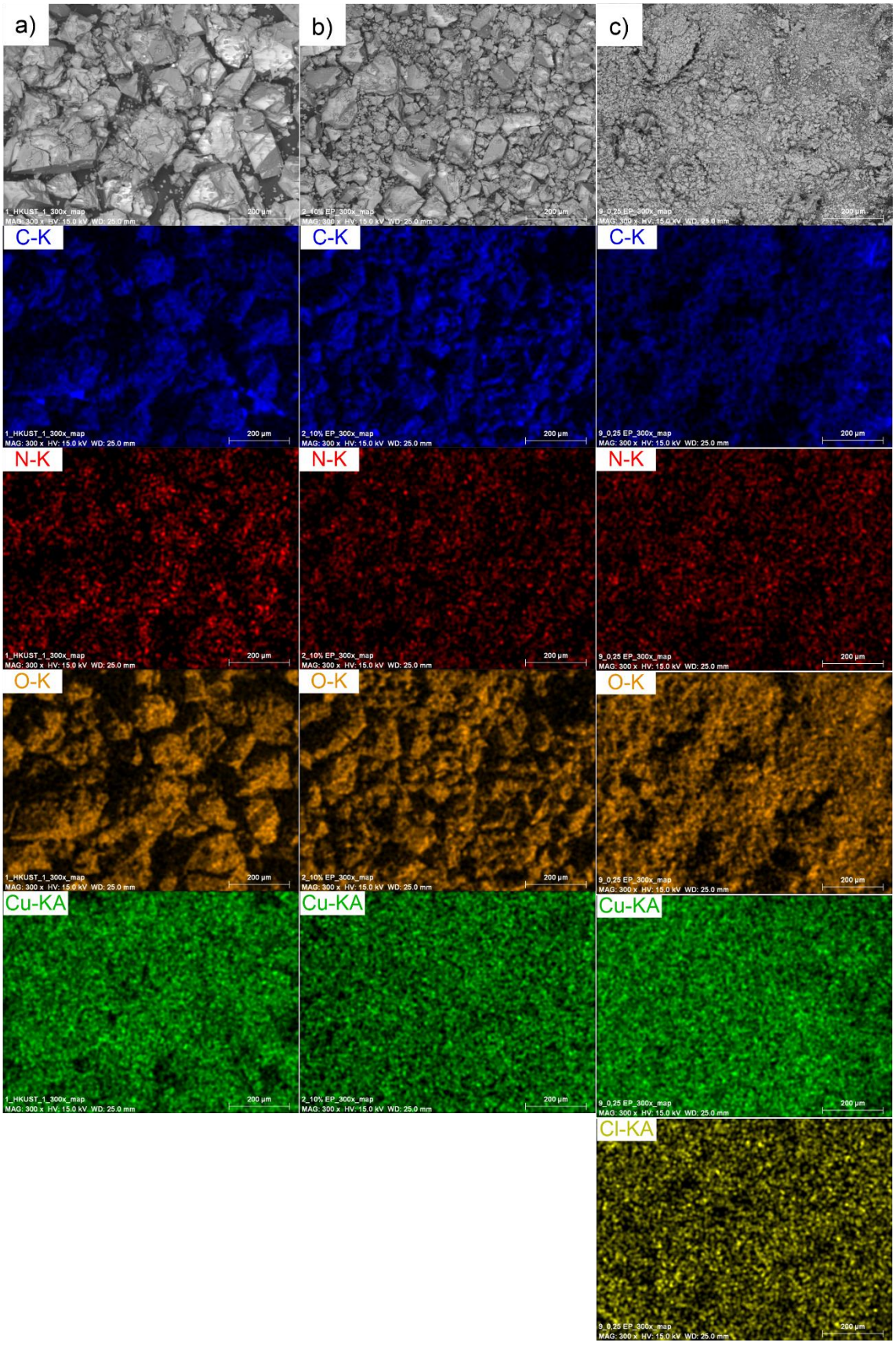


Figure 7.5 SEM images and EDX mapping of: a) HKUST-1, b) 10%EP, c) 0.25EP

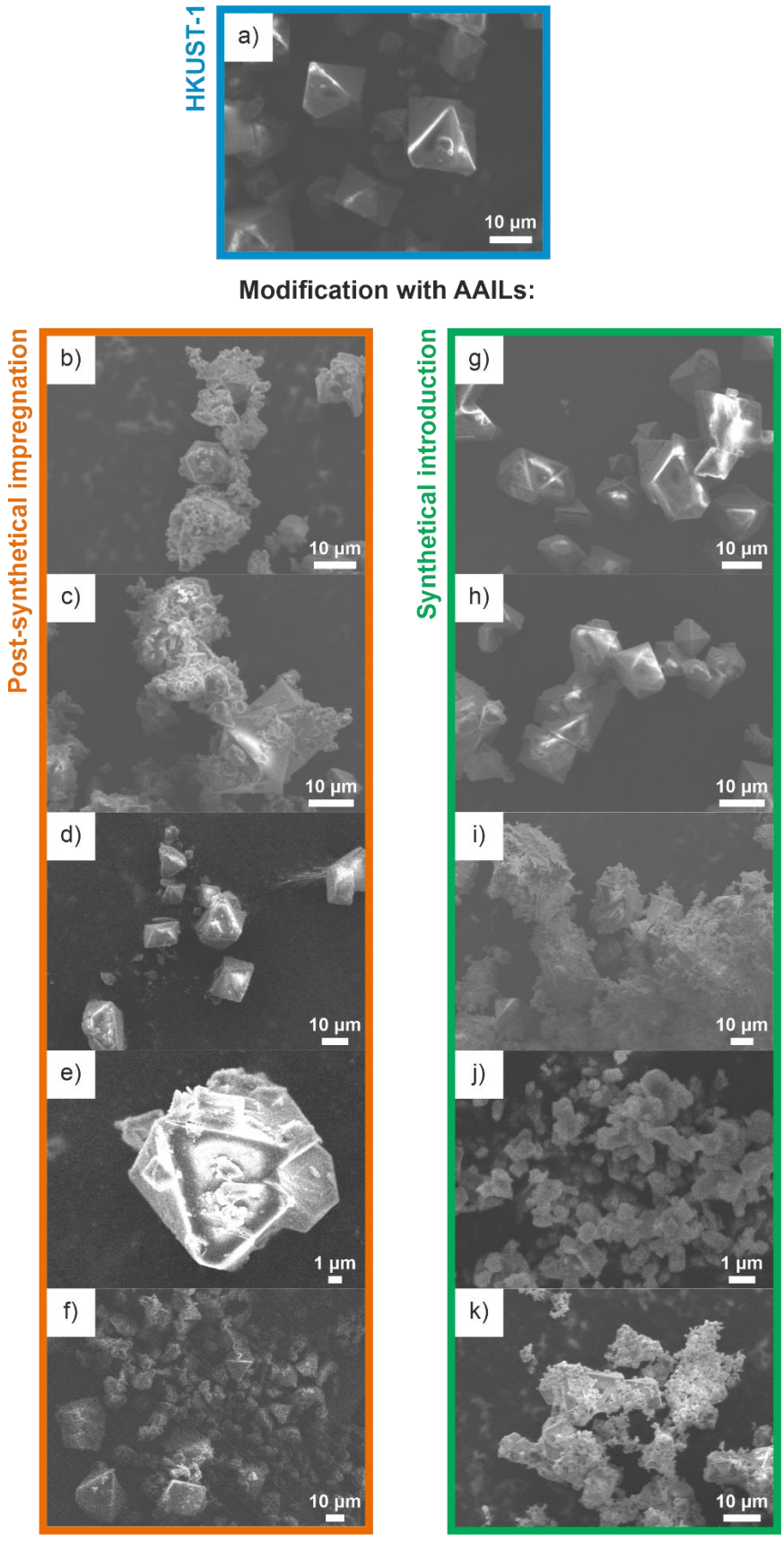


Figure 7.6 SEM images of: a) HKUST-1; samples modified post synthesis with [EMIM]-based ILs: b) 1%EP, c) 1%EH, d) 10%EP, e) 10%EP (magnification on finer fraction), f)10%EH, the samples modified with [EMIM]-based ILs during the synthesis: g) 0.1EP, h) 0.1EH, i) 0.25EP, j) 0.25EP (magnification on finer fraction), k) 0.25EH.

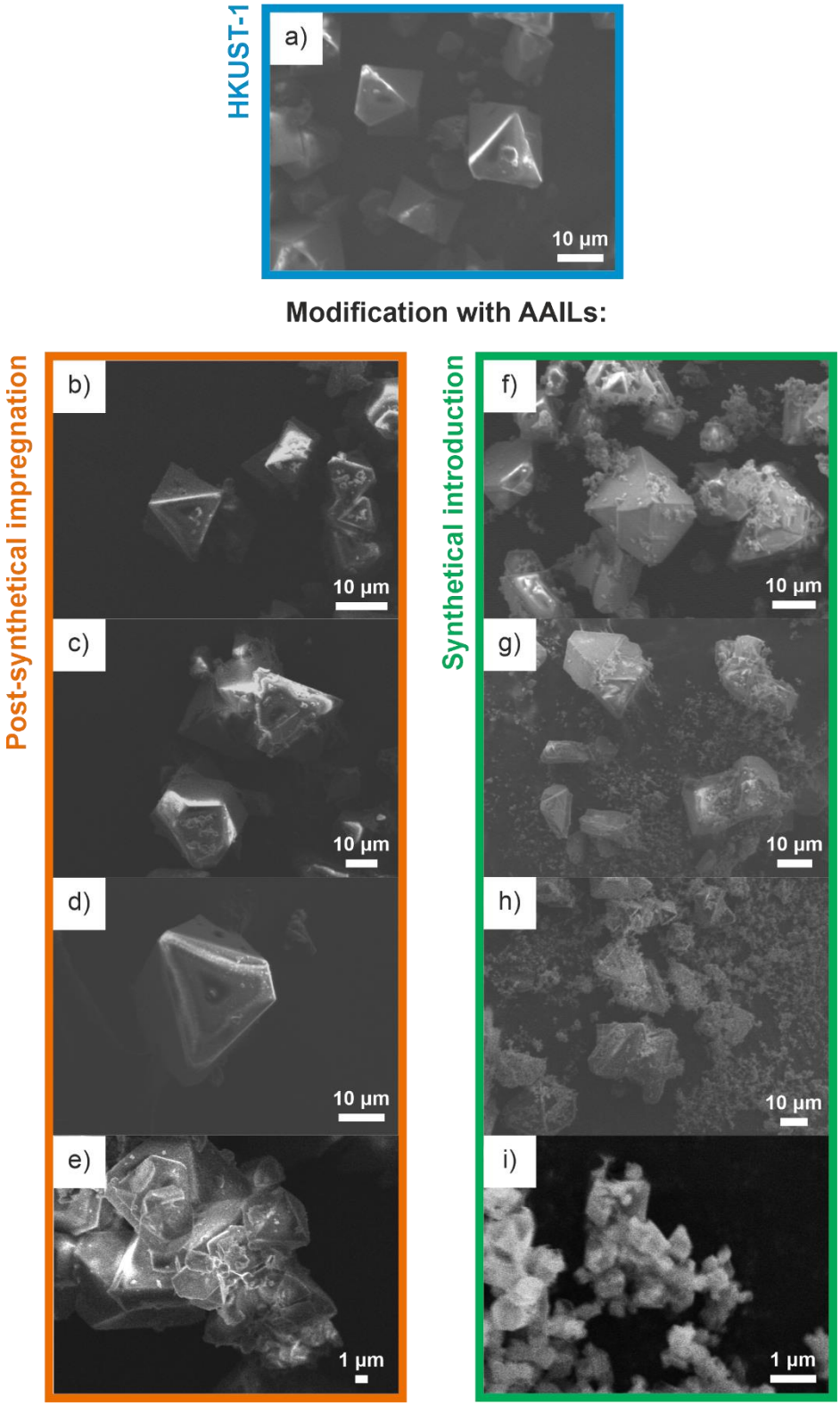


Figure 7.7 SEM images of: a) HKUST-1 samples modified post synthesis with [BMIM]-based ILs: b) 10%BB, c) 10%BP, d) 10%BH, e) 10%BH (magnification on finer fraction), the samples modified with [BMIM]-based ILs during the synthesis:, f) 0.25BB, g) 0.25BP, h) 0.25BH, i) 0.25BH (magnification on finer fraction).

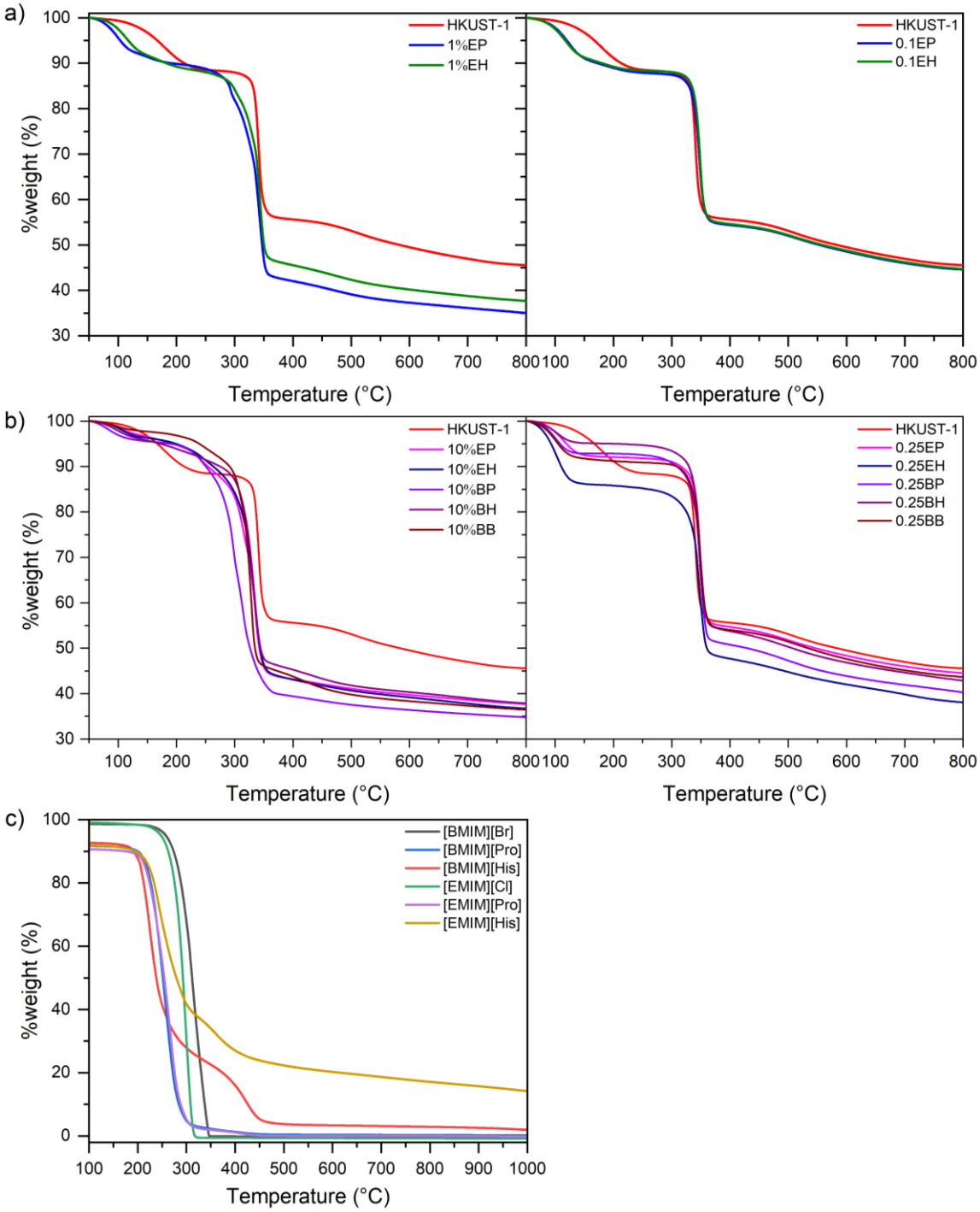


Figure 7.8 TGA curves of: a) HKUST-1 samples post-synthetically impregned with 1% of ILs or synthesized in presence of 0.1 mole equivalents of ILs, b) HKUST-1 samples post-synthetically impregnated with 10 wt% of ILs or synthesized in presence of 0.25 mole equivalents of ILs; c) ionic liquids.

7.2. Sorption properties

The effect of AAIL on the surface area and volumetric CO_2 sorption capacity of HKUST-1 is shown in Figure 7.9. In general, it can be clearly seen that the synthetical approach of IL introduction is more beneficial in terms of boosting CO_2 uptake of HKUST-1 compared to the post-synthetical impregnation. The highest CO_2 sorption capacity was measured for MOF modified

synthetically by IL containing ethyl substituent in the imidazolium cation, namely 0.25EP and 0.25EH, reaching 6.26 mmol·g^{-1} and 6.05 mmol·g^{-1}, respectively at 25 °C and pressure of about 1 bar. Introduction of the same amount of [BMIM]-based ILs to the synthesis environment resulted in slightly lower results, but still reaching almost 6 mmol·g^{-1} (increase by 36% in comparison with the non-modified sample). However, at the same time, these samples have reached the lowest S_{BET}, value of which was drastically decreased, by 94-97%, in comparison with the reference sample (Figure 7.9). The exception was the 0.25BB sample, which contained bromide anion instead of the amino acid – the S_{BET} value decreased by only about 29%. When lower amount of [EMIM][His] and [EMIM][Pro] was introduced to the synthesis, *i.e.* 0.1 molar equivalent of AAILs instead of 0.25 molar equivalent, the S_{BET} increased by about 5% and 9% and the CO_2 uptake was greater by 14.4% and 20.0% in comparison with the pristine sample, respectively. This clearly indicates that the larger amount of introduced IL to the synthesis environment of MOF leads to increased affinity of the material towards CO_2 adsorption despite lowered S_{BET}.

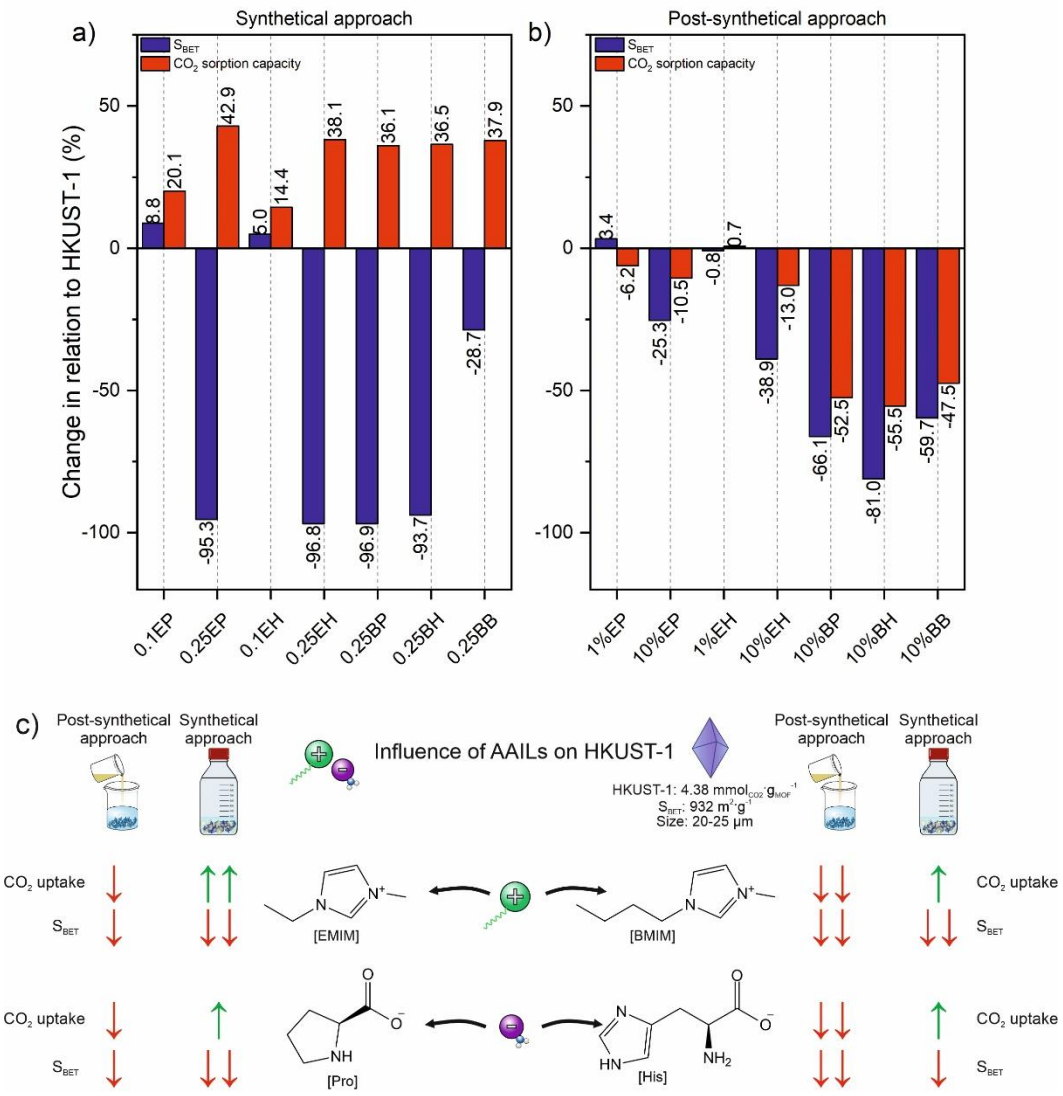


Figure 7.9 Relative change of S_{BET} and CO_2 sorption capacity at 25 °C of samples modified: a) during synthesis, b) post-synthetically (calculated basing on Table 7.1); c) schematical representation of anion and cation influence on S_{BET} and CO_2 uptake of modified HKUST-1 samples

The opposite influence of ILs on the CO_2 uptake was observed when MOFs were impregnated with ILs. Impregnation with 10 wt% of different ILs have led to reduction of both S_{BET} and CO_2 sorption capacity in the following order 10%EP>10%EH>10%BB>10%BP>10%BH. While the values of CO_2 sorption capacity of samples modified with [EMIM]-based ILs decreased by only 10-13%, impregnation with [BMIM]-based ILs resulted in a significantly greater reduction (48-56%) compared to the pristine sample. This effect is likely related to the size of the cation (*i.e.* longer side chain), which may have caused clogging of the MOF pores, as supported by the reduced S_{BET} values. In contrast, impregnation of HKUST-1 with 1 wt% of [EMIM][Pro] and [EMIM][His] led to only minor changes in surface area, with an increase of 3.4% and a decrease of 0.8%, respectively. Meanwhile, the CO_2 sorption capacity decreased by 6.2% and increased by 0.7%, respectively.

Utilization of commercial bromine-based IL yielded higher S_{BET} values than the corresponding AAIL-modified samples modified with the same amount of IL, which may be related to the smaller size of the anion of this particular IL. The CO_2 sorption capacity of 0.25BB and 10%BB remained comparable to that of equivalent samples modified with AAILs. The influence of the amino acid type, acting as the anion in [EMIM]-based AAILs, on the surface area and CO_2 sorption capacity of the modified MOFs is noticeable regardless of the IL introduction method. For ILs containing cation with the shorter side chain, the anion size appears to be the most affecting factor. The introduction of the smaller L-proline anion results in higher surface area and CO_2 sorption capacity than that of the relatively larger L-histidine anion. In the case of [BMIM]-based AAILs, this effect is less visible. Regardless of the amino acid type, modified MOFs exhibit similar CO_2 sorption capacity, while slightly differing in surface areas, depending also on the modification method. However, in both cases, the surface area was the highest when [BMIM][Br] was used.

Similar trend was observed by different researchers for HKUST-1 impregnated with classical ILs (Table 4.4). However, higher amounts of ILs are typically used to impregnate MOFs in comparison with reported herein. As another example, Xia *et al.* reported simultaneous decrease of S_{BET} (by 60-70%) and CO_2 uptake (by 40-50%) for HKUST-1 modified after the synthesis with 20 wt% (in terms of the mass of MOF used, as in reported herein methodology, this is 25 wt%) of [BMIM][PF_6] and [BMIM][BF_4] [302], which is in line with the decreases observed in this study for the samples modified with BMIM-based AAILs. Comparable changes were also observed by Nozari and co-workers for HKUST-1 modified with 30 wt% of [BMIM][PF_6] and [BMMIM][PF_6] [304] (43 wt% according to the mass of MOF used). Basing on the presented literature data, it can be suggested that there is some threshold limit of post-synthetical addition of certain ILs to HKUST-1 above which there is no noticeable changes in S_{BET} and CO_2 uptake values. However, increase of CO_2 sorption capacity at 40 °C with increasing IL loading (even up to 70 wt%). was reported in the literature for NH_2-UiO-66(Zr) and NH_2-MIL-125(Ti) modified with [BMIM]-based AAILs, with L-glycine and L-arginine acting as anions [308]. This indicates that, unlike ionic liquids without functional groups, the particular composition of AAILs, possessing pending amino groups, can provide significant improvement fo CO_2 uptake (even up to 317% in comparison with the bare MOF [308]). This proves

that by careful selection of AAIL composition, the excessive pore occupation by ILs (regardless of its introduced amount) leading to decrease of gas sorption uptake of the material can be omitted.

In the case of ILs introduced to the synthesis environment of MOFs, no direct comparison to the literature can be found according to the best of the authors knowledge. In one study, HKUST-1 was synthesized in reverse microemulsion system containig choline dioctylsulfosuccinate [Cho][AOT] [311] with ethanolammonium formate and R-limonene. The measured values of CO_2 adsorption (0.88 mmol·g^{-1} at 1 bar, temperature not specified) was more than five times lower than reported herein. In addition, the molar ratio of the precursors and IL added was significantly different – roughly 1.5:8.1:3.75 for n_{Cu}:n_{linker}:n_{IL}. It is another indication that not only the substrates, but also ratios between them can signifficantly impact the properties of the obtained material.

7.3. Gas Adsorption/Desorption Equilibrium Measurements

Single-component gravimetric adsorption-desorption equilibrium analyses of N_2, CH_4 and CO_2 at 25 °C in pressure range of 0.15-10 bar were carried out for the reference sample and five selected modified samples (equilibrium isotherms shown in Figure 7.10). Two samples with the highest volumetric CO_2 uptake, namely 0.25EH and 0.25EP, were chosen to evaluate the influence of the type of AAIL anion (L-Histidine *vs.* L-Proline) on the sorption properties. To compare influence of the amount (different molar ratios of precursors) and the method of AAIL introduction (synthetical *vs.* post-synthetical) on the properties of the resulting product, 0.1EP, 1%EP and 1%EH were examined.

According to the IUPAC categorization system, all isotherms were classified as Type I, indicating monolayer adsorption in typical microporous materials [355]. As expected, the obtained materials followed the assumed trend, *i.e.* increasing sorption capacity in the order of N_2<CH_4<CO_2. The adsorption capacities of HKUST-1 reached 0.29 mmol·g^{-1} (at 1 bar) and 2.31 mmol·g^{-1} (at 10 bar) for N_2, 0.91 mmol·g^{-1} (at 1 bar) and 5.44 mmol·g^{-1} (at 10 bar) for CH_4 and 4.60 mmol·g^{-1} (at 1 bar) and 12.7 mmol·g^{-1} (at 10 bar) for CO_2. Surprisingly, the measured values do not vary significantly regardless of the MOF modification method. In comparison with the reference sample, the samples modified post synthesis *i.e.* 1%EP and 1%EH exhibited higher sorption of N_2 and CH_4 at 1 bar by about 10% and 2%, respectively. However, with the increasing dosage of both mentioned gases, the trend has reversed – the sorption capacity was diminished by 4.5-6% for the modified materials when reaching 10 bar. Of the samples synthesized in the presence of AAILs, only 0.25EP showed increased sorption at all the collected points for all three gases, whereas 0.1EP and 0.25EH performed worse than the pristine sample.

In contrast to the volumetric measurements described in Section 7.2, only 0.25EP reached the gravimetric CO_2 sorption capacity higher than that of the reference sample. However, the increase was not significant at comparable pressure, *i.e.* excess adsorbed quantity (q_{exc}) at about 1 bar was 4.60 mmol·g^{-1} for HKUST-1 *vs.* 4.65 mmol·g^{-1} for 0.25EP, giving only 1% improvement in comparison to 43% boost observed during volumetric measurement. 0.1EP and 0.25EH were

characterized with lower values of sorption capacity, similar to samples impregnated with 1 wt% of these AAILs.

The IL-modified MOFs are less often characterized by the gravimetric method of CO_2 adsorption (Table 4.4). In one study of HKUST-1, da Silva *et al.* [301] had used 10 wt% (in relation to mass of used MOF) of [BMIM][PF_6], resulting in decrease of S_{BET} and CO_2 uptake (at 1 bar, 25 °C) by respectively about 80% and 70%. Philip and Henni modified ZIF-8 [191] and MOF-177 [305] with 10, 20 and 30 wt% of two AAILs, namely [EMIM][Gly] and [EMIM][Ala]. Although the CO_2 uptake at 1 bar and 30 °C nearly doubled for the 30 wt%-modified samples, the absolute values are lower than the ones reported herein. However, authors have used commercial MOFs without any further purification which may explain very low sorption values recorded for the pristine samples – 0.6 and 0.7 mmol·g^{-1} for ZIF-8 and MOF-177, respectively. In contrary to the described studies, Mohamedali *et al.*, who impregnated ZIF-8 with 1-butyl-3-methylimidazolium acetate [BMIM][Ac] and 1-ethyl-3-methylimidazolium acetate [EMIM][Ac], observed increase of CO_2 uptake at 1 bar and 30 °C from 0.6 to about 0.7 mmol·g^{-1} for 10 wt% modified samples, while at 10 bar the same samples have shown values lower by 1 and 2 mmol·g^{-1} compared to pristine ZIF-8 (uptake of about 6 mmol·g^{-1}), respectively [296]. Considering only the CO_2 adsorption capacity measured at 1 bar, values reported herein were at least two times higher compared to the materials modified with at least 10 wt% of IL reported elsewhere.

The data presented in Table 7.4 shows the parameters obtained from fitting the experimental sorption-desorption equilibrium data to the Sips and Toth models [356] according to Eq. 4 and Eq. 5 respectively, presented in Subsection 5.6.14. Interestingly, both models predict similar saturation concentration for CO_2 and CH_4 or even higher for CH_4 than for CO_2. This may indicate that the range in which the measurements were conducted was too narrow to fully provide the trend of the isotherms (especially of CH_4). In contrast to CO_2 isotherm, in the studied range of CH_4 and N_2 adsorption, there is no inflection point of the function indicating a plateau. The extrapolation of the experimental isotherm models suggests that the methane and nitrogen adsorption capacities would continue increasing with pressure, without the clear saturation behavior observed for CO_2. However, this behavior cannot be unequivocally confirmed from the experimental data due to the limited pressure range available. In this context, molecular simulations could provide a useful complementary approach to extend the accessible pressure range and to obtain molecular-level insight into the adsorption mechanisms of the different gases in the framework.

Basing on data received from the gravimetric adsorption-desorption study, the ideal selectivity (Figure 7.11) of the obtained materials towards CO_2 at 25 °C was designated using Eq. 6. Gas mixtures of partial pressure ratio of 50:50 were considered for both CO_2/N_2 and CO_2/CH_4. Additionally, the selectivity for model flue gas (CO_2/N_2) and model biogas (CO_2/CH_4) of 15:85 and 40:60 partial pressure ratios respectively, were also calculated. Regardless of the model used (Sips or Toth) to designate the full isotherms, in most cases the designated selectivity of the analyzed HKUST-1-based materials decreases with the growing pressure of gas mixture. The deviations from this trend were observed at the low pressure range, below 1 bar, especially for the gas mixtures

with other ratio than 50:50. After exceeding this pressure value, the selectivity generally starts to shift in the favor of N_2 or CH_4. Only in the case of model flue gas, the total changes of selectivity are minor, changing from about 3.5 (at 1 bar) to 3.0 (at 10 bar). In general, the trend of the selectivity designated for the modified samples remains similar to pristine HKUST-1 or slightly lower. In the case of the 50:50 CO_2/N_2 mixture, the selectivity at 10 bar of all samples lays in the 7.6-8.2 range. More pronounced differences were observed at 1 bar, where selectivity reached about 18 (according to data from Sips fitting) for HKUST-1. For the modified samples, these values were lower by 1 (0.25EP) to 2.5 (0.25EH). In the case of the second gas mixture *i.e.* CO_2/CH_4, in the range of pressure above the level of atmospheric pressure selectivity decreases gradually with the increasing pressure, regardless of the composition of the gas mixture. For biogas, the selectivity drops together with rising pressure by approximately 30%, while for equal mixture – by about 40%. In both cases, the reference sample remains the most efficient separator of CO_2 from both other gases.

Table 7.4 Sips and Toth model fitting parameters for N_2, CH_4, and CO_2 on HKUST-1 samples. For Sips equation: q_s – saturation concentration, b – isotherm constant, n – heterogeneity factor; for Toth equation: q_s – saturation concentration, b – isotherm constant, t – heterogeneity factor. For both models: ARE – absolute relative error.

Sample label	Parameter	SIPS			Parameter	TOTH		
		N_2	CH_4	CO_2		N_2	CH_4	CO_2
HKUST-1	q_s	8.730	15.089	15.152	q_s	8.889	20.480	14.312
	b	0.036	0.054	0.476	*b*	0.035	0.053	0.412
	n	0.998	1.067	0.949	*t*	0.997	0.713	1.246
	ARE (%)	1.32	0.62	1.18	*ARE (%)*	1.42	1.11	0.78
0.25EP	q_s	8.377	15.414	14.932	q_s	8.115	21.207	14.414
	b	0.040	0.054	0.512	*b*	0.039	0.053	0.409
	n	0.989	1.067	0.894	*t*	1.054	0.707	1.287
	ARE (%)	1.06	1.13	1.57	*ARE (%)*	1.04	0.69	0.79
0.1EP	q_s	7.421	14.104	12.740	q_s	7.923	23.273	12.311
	b	0.039	0.049	0.521	*b*	0.037	0.047	0.417
	n	1.000	1.105	0.895	*t*	0.964	0.600	1.282
	ARE (%)	2.90	0.55	1.70	*ARE (%)*	3.18	1.22	0.99
0.25EH	q_s	8.796	13.732	13.612	q_s	12.319	19.659	13.199
	b	0.032	0.057	0.511	*b*	0.027	0.057	0.417
	n	1.033	1.084	0.904	*t*	0.769	0.669	1.248
	ARE (%)	0.66	0.85	1.60	*ARE (%)*	0.98	0.50	0.96
1%EP	q_s	7.754	12.693	13.390	q_s	9.476	16.540	13.107
	b	0.039	0.067	0.513	*b*	0.035	0.069	0.457
	n	1.022	1.075	0.949	*t*	0.830	0.715	1.134
	ARE (%)	1.03	0.57	1.30	*ARE (%)*	0.89	0.92	1.06
1%EH	q_s	7.873	12.328	13.545	q_s	10.099	15.006	13.261
	b	0.038	0.072	0.512	*b*	0.033	0.074	0.456
	n	1.026	1.056	0.950	*t*	0.813	0.773	1.131
	ARE (%)	1.05	1.09	1.30	*ARE (%)*	0.85	0.73	1.08

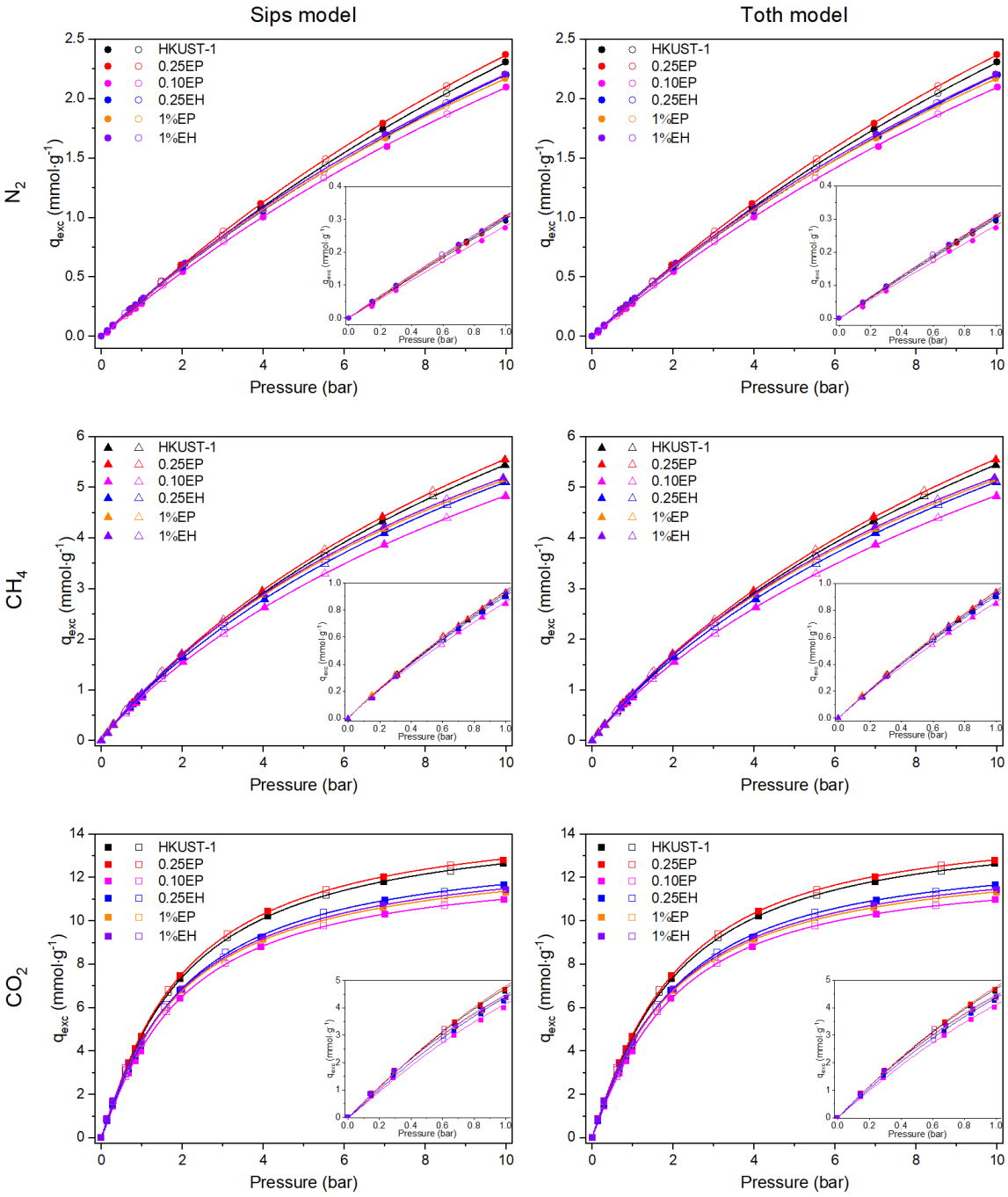


Figure 7.10 N_2, CH_4 and CO_2 adsorption/desorption equilibrium isotherms at 25 °C for HKUST-1 and AAILs-modified composites in full and low-pressure region (insets). Closed and open symbols denote the adsorption and desorption data, respectively. Lines represent the Sips (left) and Toth (right) adsorption isotherm model fitting

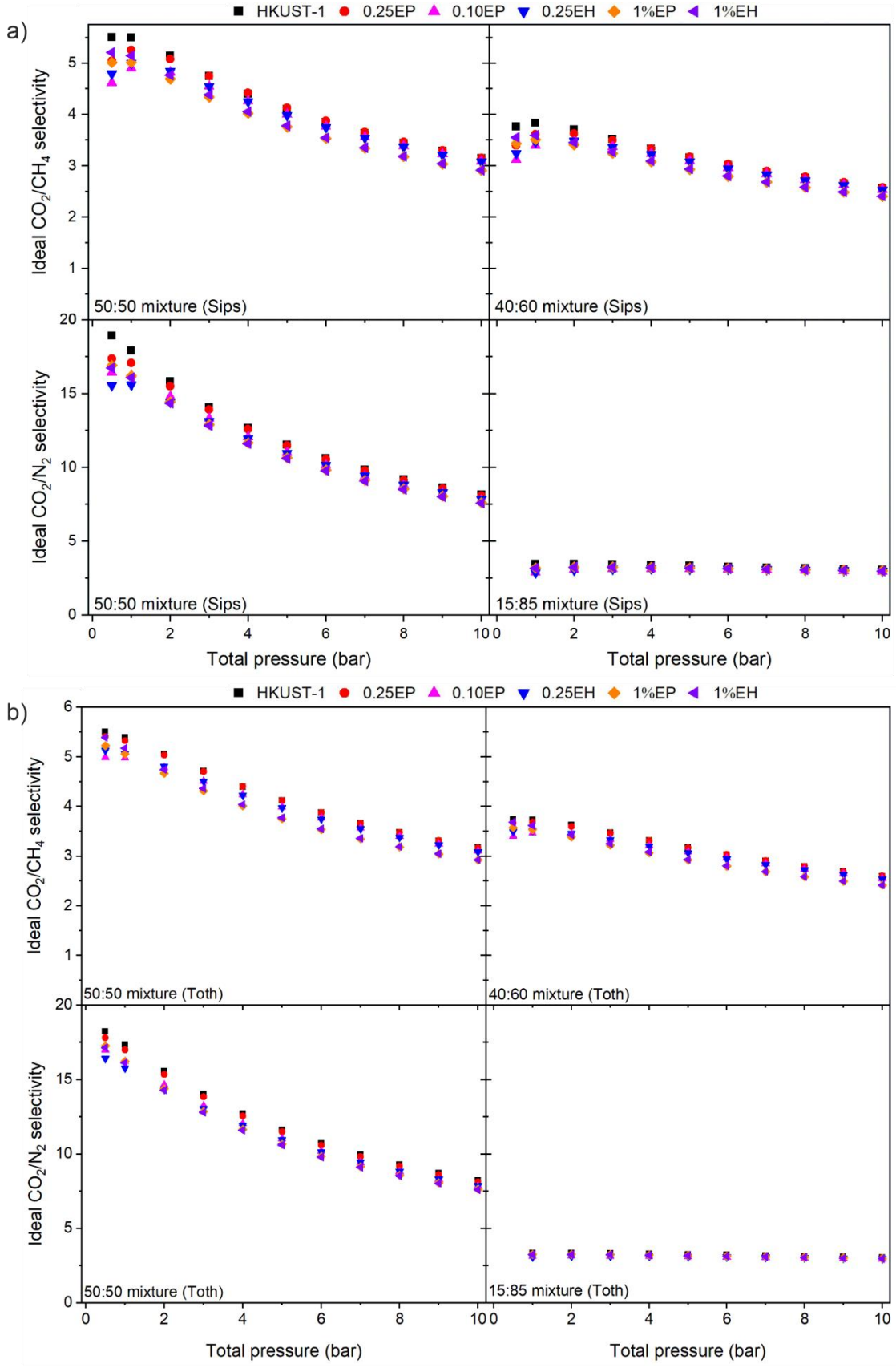


Figure 7.11 Ideal selectivity of HKUST-1 and AAIL-modified samples based on experimental data fitted with a) Sips and b) Toth models

Interestingly, both Sips and Toth models predict similar saturation concentration for CO_2 and CH_4 or even higher for CH_4 than for CO_2 (Table 7.4). This may indicate that the range in which the measurements were conducted was too narrow to fully provide the trend of the isotherms (especially of CH_4). In contrast to CO_2 isotherm, in the studied range of CH_4 and N_2 adsorption, there is no inflection point of the function indicating a plateau. The extrapolation of the experimental isotherm models suggests that the methane and nitrogen adsorption capacities would continue increasing with pressure, without the clear saturation behavior observed for CO_2. However, this behavior cannot be unequivocally confirmed from the experimental data due to the limited pressure range available. In this context, molecular simulations were performed by the team of Azahara Luna-Triguero and Jose Manuel Vicent-Luna from Eindhoven University of Technology and included in joint research paper, which is currently after first revision in Chemical Engineering Journal (as of 16.09.2026). The computational research provides a useful complementary approach to extend the accessible pressure range and to obtain molecular-level insight into the adsorption mechanisms of the different gases in the framework. Molecular simulations were performed to evaluate the capability of the selected models to reproduce the adsorption of CO_2, CH_4, and N_2 in pristine HKUST-1. The excellent agreement of the simulated data with the experimental data over the entire pressure range, demonstrates that the molecular models provide an accurate description of the adsorption behavior in the pristine material and allow to explore adsorption behavior beyond the experimentally accessible range (up to 100 bar) and to assess the trends predicted by the fitted isotherm models. Additionally, the combined analysis of molecular simulations, thermodynamic mixture predictions, and dynamic breakthrough calculations were performed to evaluate the separation performance of the investigated materials.

7.4. Summary

The presented research results clearly indicate that structure and sorption properties of HKUST-1 can be altered by the presence of different AAILs and method of their introduction. Although the MOF's specific crystal structure was not altered, post-synthetical impregnation brought overall worse properties of resulting materials – down to 20% of the S_{BET} and 45% of the volumetric CO_2 uptake comparing to the reference values. The addition of AAILs to the synthesis environment has changed the crystal formation process, leading to more heterogenous crystals' size distribution, affecting the resulting specific surface area by decrease up to 97%. Despite that, synthetically introduced AAILs promoted the volumetric CO_2 sorption capacity of modified HKUST-1 leading to its increase up to 43%. It was also observed that the IL structure, especially the length of the cation side-chain, has a determining role in altering the properties of HKUST-1. In general, butyl-substituent led to relatively impaired active area and CO_2 uptake in comparison with analogous AAILs with ethyl- side chain. Even for IL with the smallest anion, [BMIM][Br], the value of S_{BET} was lower than for HKUST-1 (decrease by about 30% and 60% for respectively synthetical and post-synthetical pathway), and the CO_2 uptake was similar to corresponding samples (increase up to about 6 $mmol \cdot g^{-1}$ for synthetical approach and decrease to about 2 $mmol \cdot g^{-1}$ for post-synthetical approach). As for anions, L-proline-based AAILs showed more beneficial effect (5-6% higher CO_2

uptake) in comparison with L-histidine-based ones. It further supports the determining role of IL's constituents size on the properties of resulting MOFs, as better results were observed for AAILs possessing less nitrogen atoms, showing different trend than known for standalone AAILs. Although the single component gravimetric adsorption-desorption isotherms did not reveal substantial changes of N_2, CH_4 or CO_2 adsorption capacity, as well as the selectivity of modified MOFs towards the model bio- and flue gases (CO_2/CH_4 and CO_2/N_2) remained almost unaffected. Overall, this sample, modified synthetically with the [EMIM][Pro] – AAIL consisting of cation with the shortest side-chain and smallest amino acid as anion – shows the highest potential of MOF modification towards application for selective CO_2 adsorption.

It would be necessary to consider, first, whether the synthesis is repeatable, and secondly, whether the modified MOF exhibits adequate gas storage stability, and if not, to what extent. The material's ability to operate in multiple cycles and its regeneration efficiency should also be assessed. Furthermore, tests should be conducted on actual gas mixtures, and the impact of additional gases/contaminants present in flue gases or biogas on the material's stability and effectiveness should also be considered.

Taking into consideration the Cu-based MOFs are characterized with poor stability – both in the liquid environments of CO_2 photocatalysis, but apparently also after the modification with AAILs, it was established that different MOFs must be chosen photoreduction studies. Basing on the literature zirconium- and titanium-based MOFs were found to be characterized by greater tolerance to relatively harsh conditions. Therefore, the two following chapters will focus on three MOFs from UiO family (UiO-66(Zr), NH_2-UiO-66(Zr) and UiO-67(Zr)) and NH_2-MIL-125(Ti).

8. The influence of defect induction by introduction of non-noble metals on the photocatalytic performance of UiO-66(Zr) and NH_2-UiO-66(Zr)

UiO-66(Zr) and NH_2-UiO-66(Zr) – two zirconium-based MOFs, were obtained by the solvothermal approach. Their structures were modified with two different methods by the use of three different non-noble metals – copper, nickel and cobalt. The first approach included addition of a modifying metal precursor to the reaction environment of the MOF, while the second method involved the use of UV-Vis light for facilitating deposition of these metals on the MOF surface. The sample codes and the synthesis conditions were presented in Table 8.1.

Table 8.1 Sample codes and synthesis conditions of the UiO-66(Zr) and NH_2-UiO-66(Zr) samples; inc – incorporation, dep – photodeposition, BDC – terephthalic acid, NH_2-BDC – 2-aminoterephthalic acid, mol_{Zr}% – amount of the modifying metal in relation to the number of moles of the zirconium precursor, wt_{MOF}% – amount of the modifying metal in relation to the mass of MOF to be modified

Sample label	Linker	Precursor of metal used during modification	Method of modification	Amount of the introduced metal
UiO-66	BDC	-	-	-
Cu_{inc}-UiO	BDC	$Cu(NO_3)_2{\cdot}3H_2O$	incorporation	0.5 mol_{Zr}%
Ni_{inc}-UiO	BDC	$Ni(NO_3)_2{\cdot}6H_2O$	incorporation	0.5 mol_{Zr}%
Co_{inc}-UiO	BDC	$CoCl_2$	incorporation	0.5 mol_{Zr}%
Cu_{dep}-UiO	BDC	$Cu(NO_3)_2{\cdot}3H_2O$	photodeposition	0.5 wt_{MOF}%
Ni_{dep}-UiO	BDC	$Ni(NO_3)_2{\cdot}6H_2O$	photodeposition	0.5 wt_{MOF}%
Co_{dep}-UiO	BDC	$CoCl_2$	photodeposition	0.5 wt_{MOF}%
NH_2-UiO-66	NH_2-BDC	-	-	-
Cu_{inc}-NUiO	NH_2-BDC	$Cu(NO_3)_2{\cdot}3H_2O$	incorporation	0.5 mol_{Zr}%
Ni_{inc}-NUiO	NH_2-BDC	$Ni(NO_3)_2{\cdot}6H_2O$	incorporation	0.5 mol_{Zr}%
Co_{inc}-NUiO	NH_2-BDC	$CoCl_2$	incorporation	0.5 mol_{Zr}%
Cu_{dep}-NUiO	NH_2-BDC	$Cu(NO_3)_2{\cdot}3H_2O$	photodeposition	0.5 wt_{MOF}%
Ni_{dep}-NUiO	NH_2-BDC	$Ni(NO_3)_2{\cdot}6H_2O$	photodeposition	0.5 wt_{MOF}%
Co_{dep}-NUiO	NH_2-BDC	$CoCl_2$	photodeposition	0.5 wt_{MOF}%

Octahedral morphology of the NH_2-UiO-66(Zr) samples and a rounded morphology of the UiO-66(Zr) samples was observed by either SEM and TEM methods (Figure 8.1 and Figure 8.2). Negligible size changes after photodeposition of non-noble metals on MOFs was observed. The photodeposition of nickel contributed to increased particle agglomeration regardless of the type of MOF modified (Figure 8.2). The EDS mapping confirmed even distribution of the metals introduced to the NH_2-UiO-66(Zr) samples *via* photodeposition approach. No visible nanoparticles of Co/Cu/Ni species were observed on the surface of obtained crystallites, suggesting presence of the elements inside the MOF pores Figure 8.1e-g. Minor differences in size and no evident shape changes due to incorporation of the metals were observed (Figure 8.2).

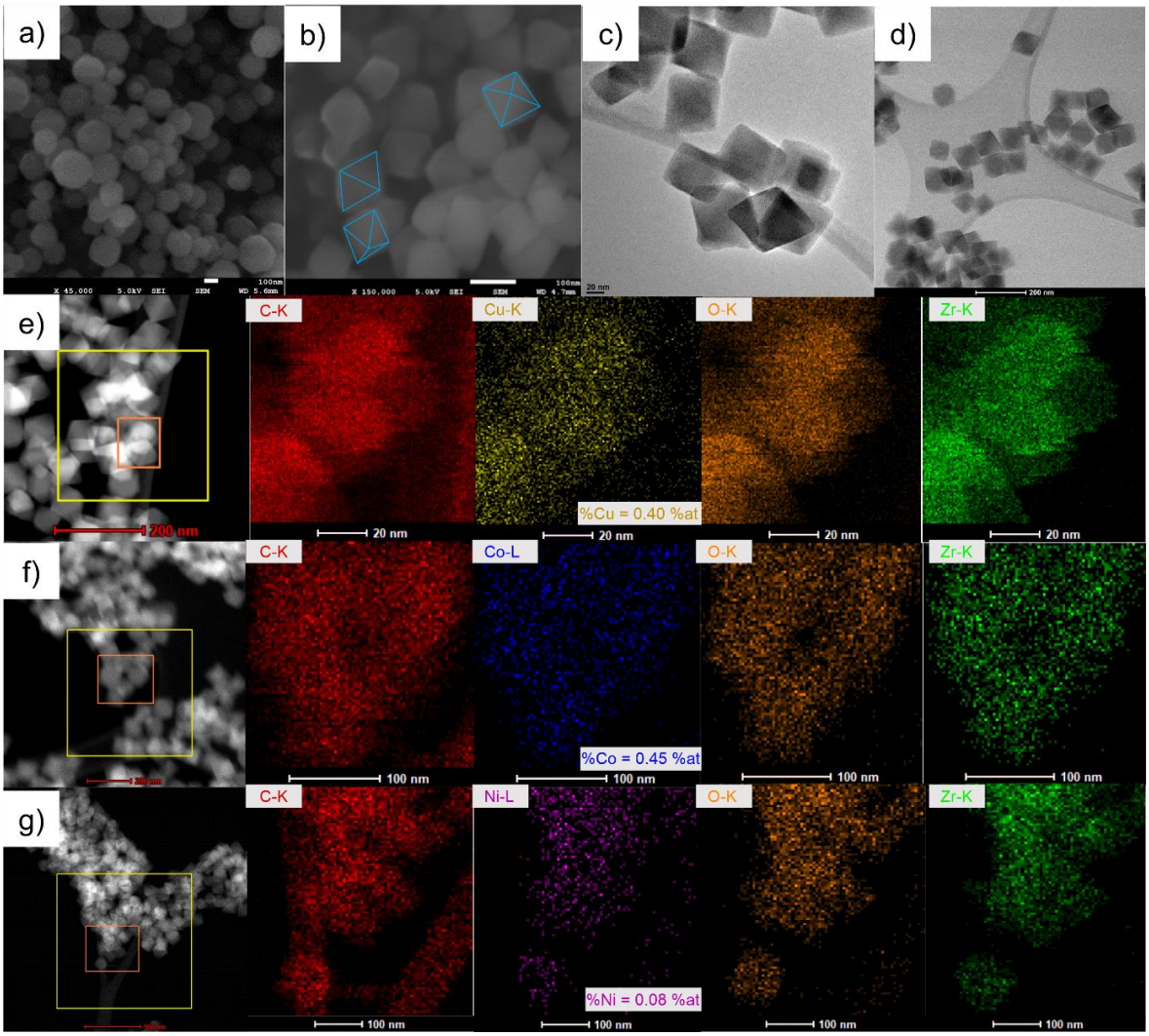


Figure 8.1. SEM images of: a) UiO-66, b) NH_2-UiO-66; TEM images of: c) Cu_{dep}-NUiO, d) Co_{dep}-NUiO; EDS mapping of: e) Cu_{dep}-NUiO, f) Co_{dep}-NUiO, g) Ni_{dep}-NUiO;

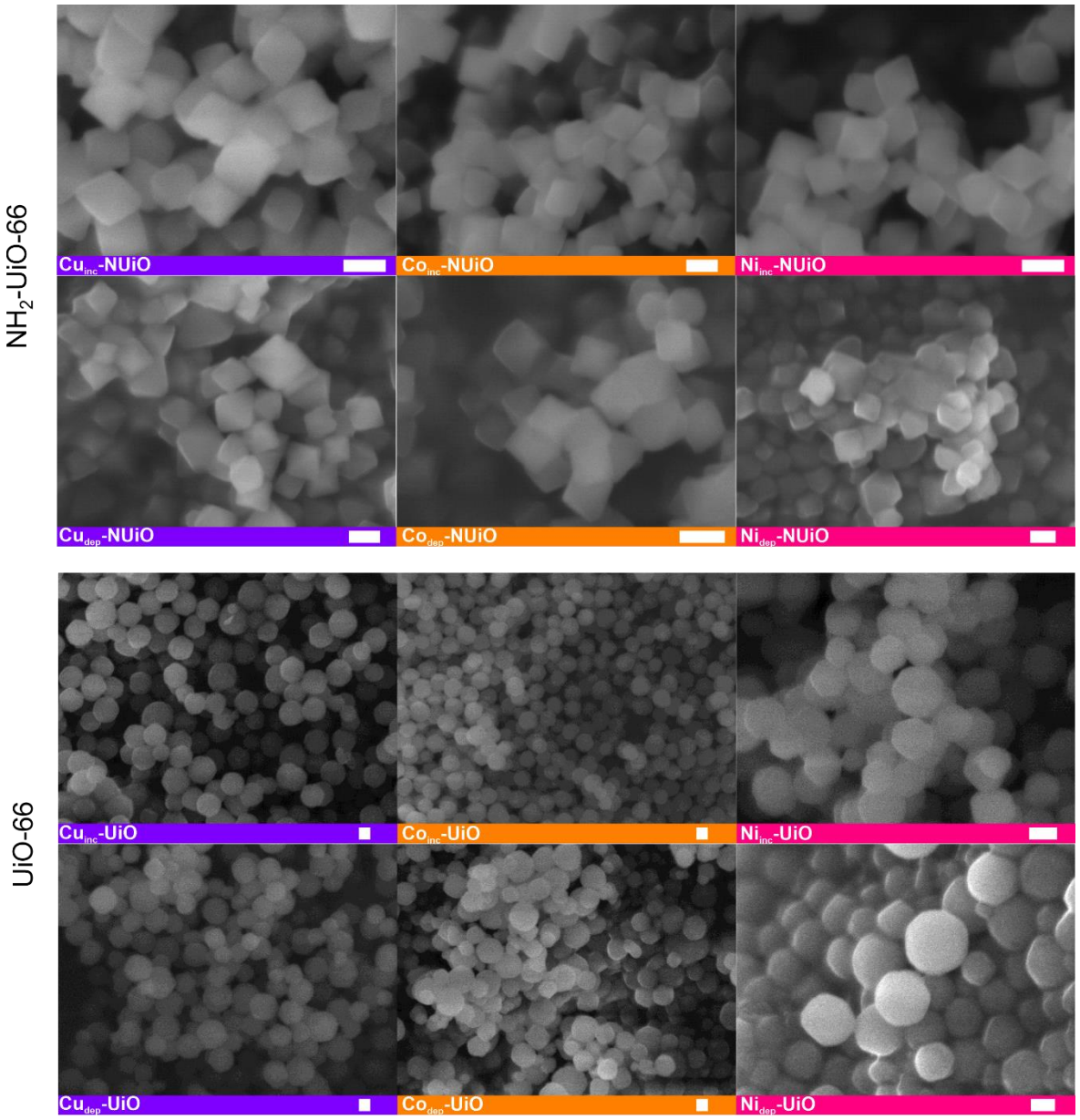


Figure 8.2 SEM images of metal-modified NH_2-UiO-66(Zr) and UiO-66(Zr) samples; scale bars represent 100 nm.

8.1. Structure of the pristine and modified MOFs

Formation of UiO-66(Zr) and NH_2-UiO-66(Zr) structures was identified by *in situ* DRIFTS at 150 °C under flow of N_2 (Figure 8.3). The symmetric and asymmetric stretching vibrations of OCO group in the linker and the stretching vibrations of C=C of its benzene rings were recognized as sharp peaks at the wavenumbers of about 1390 cm^{-1}, 1570 cm^{-1} and 1500 cm^{-1}, respectively [93,236,357]. The presence of the aromatic ring in the linker was also confirmed by the presence of vibration bands in the region of 900-650 cm^{-1}. In turn, the confirmation of bond existing between zirconium and oxygen was established on the basis of the signals at 682 cm^{-1} and 730 cm^{-1}. In the case of NH_2-UiO-66(Zr), the additional bands at 1255 cm^{-1} and 1337 cm^{-1} were ascribed to C–N stretching vibrations, while the N–H bending and swing vibration bands were observed at 1432 cm^{-1} and 765 cm^{-1} [236,358]. For both MOFs, the thermal treatment removed the adsorbed water from the pores and revealed presence of a band at

3670 cm^{-1}, which was assigned to the stretching vibration of the -OH bond in the SBU. Compared to UiO-66(Zr) the additional two bands at 3388 cm^{-1} and 3498 cm^{-1} were detected for NH_2-UiO-66, which were recognized as the N-H symmetric and asymmetric stretching vibrations in primary amine.

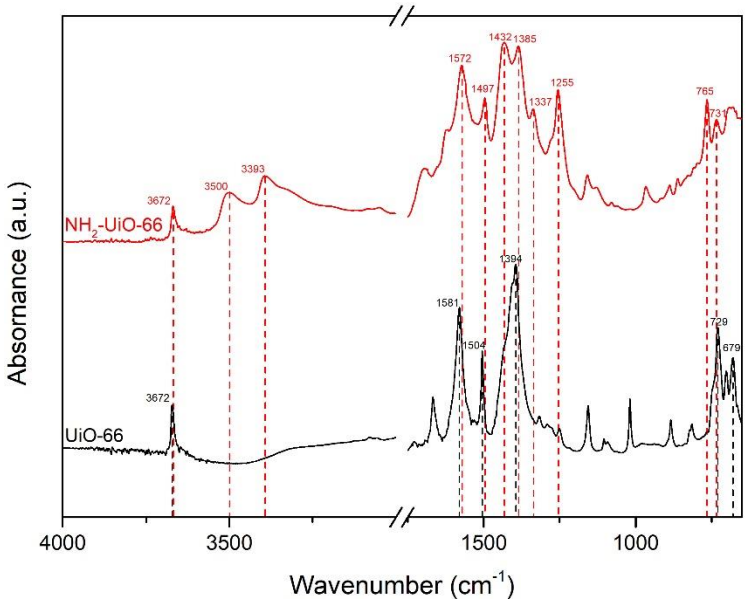


Figure 8.3 DRIFTs spectra of UiO-66(Zr) and NH_2-UiO-66(Zr) after activation at 150 °C under N_2 flow.

The crystal structure of the obtained MOFs was confirmed by XRD (Figure 8.4). The reflexes observed at about 7.4°, 8.6°, 12.1°, 14.2°, 14.8°, 17.1°, 18.6°, 19.1°, 21.0°, 22.3°, 24.3°, 25.4°, 25.7°, 28.2° and 29.8° can be assigned to the following respectively: (111), (020), (022), (131), (222), (040), (133), (042), (242), (151), (044), (153), (244), (353), (444). The obtained diffraction patterns stand in agreement with Information Card no. 4512075 from Crystallography Open Database referring to crystal structures of the UiO-66 MOFs family [359]. No visible signs of Cu, Co or Ni metals or their oxides, as well as of Co-BDC [360], Ni-BDC [361] or Cu-BDC [362] formation were observed apart from crystalline phase of MOF for either incorporation or photodeposition method. However, this does not exclude the introduction of small quantities of the non-noble metals into the MOF structure. Increased crystallinity of all metal-modified samples was observed as the intensity of the (111) diffraction peak higher than for the pristine MOFs. The photodeposition increased its intensity by 1.75-2 times for UiO-66(Zr), while by 1.25-1.40 times after synthetical incorporation. In the case of NH_2-UiO-66(Zr) the change was still positive, but not so high achieving growth of 1.05-1.40 times, regardless of the modification method.

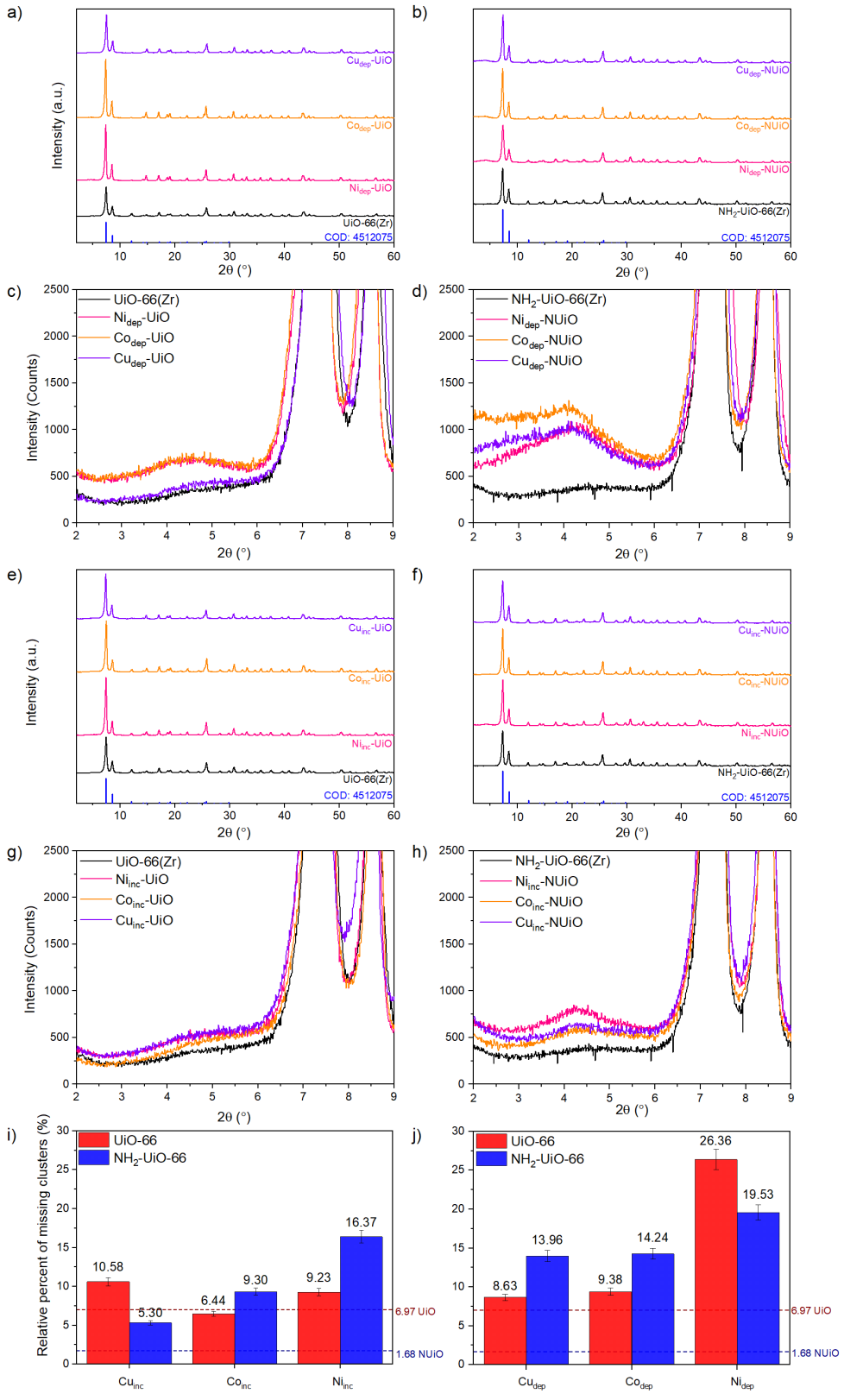


Figure 8.4.The XRD patterns of: a) UiO after photodeposition of Cu/Ni/Co, b) NH_2-UiO-66 after photodeposition of Cu/Ni/Co; low 2θ region of diffraction pattern of: c) UiO after photodeposition d) NH_2-UiO-66 after photodeposition; e) UiO after incorporation of Cu/Ni/Co, f) NH_2-UiO-66 after incorporation of Cu/Ni/Co; low 2θ region of diffraction pattern of: g) UiO after incorporation h) NH_2-UiO-66 after incorporation; comparison of MC defects in obtained UiO-66 and NH_2-UiO-66 samples after: i) incorporation, j) photodeposition

In the range of low 2θ values (3-7°) presence of broad signal of low intensity was observed (Figure 8.4c, d, g and h). According to Cliffe [92] and Shearer [93] existence of this reflex indicates the formation of missing clusters defects in the MOF's structure. The mentioned authors exhaustively discussed the phenomenon of **reo** nanoregions formation in UiO-66, it is the situation when the unit cell of formed UiO-66(Zr) lacks in one of four Zr_6 clusters. It is also accompanied by the lack of linkers that should regularly be connected to this cluster. Formation of such deficiency can be induced by introduction of monocarboxylic acids to the synthesis medium, thus creation of competing interactions between linker and the modulator, leading to connection of the latter molecule with the forming net. The increasing content of monocarboxylic acid increases the deficiency level, as more molecules can compete with the linkers [93]. Taking into consideration the fact that after modification with non-noble metals *via* both chosen approaches the intensity of the reflex at 2θ=3-7° (corresponding to the **reo** nanoregions presence), the deficiency of obtained materials is higher than in the case of pristine MOFs. The relative content of the missing clusters was calculated by using the Eq. 1 basing on the XRD data and compared and presented in the form of a bar chart (Figure 8.4i-j).

The introduction of an additional metal of a different valence than the original metal in the synthesis environment of MOF may disturb the equilibrium of its formation reaction. Therefore, creation of defects is induced as a result of competing interactions of zirconium and non-noble metals with linker. In turn, the formation of new clusters containing non-noble metals can be disrupted by possible interactions of these metals with modulator. Consequently, depending on the type of the introduced non-noble metal, the relationship between the occurrence of these phenomena may be different, which explains the different number of missing-cluster defects among samples containing different metals. The level of MC defects after metals photodeposition on NH_2-UiO-66(Zr) was higher than after the incorporation method (~14-19.5 vs ~5-16, respectively), suggesting different mechanism responsible for the creation of defects depending on the modification approach. In the case of the post-synthetical method of modification, it was UV light irradiation exposition to which was recognized as a factor facilitating the intentional defect engineering and structure alternation [363]. Despite this the overall integrity of the crystal structure maintained preserved.

Defectivity of the modified UiO-66(Zr) and NH_2-UiO-66(Zr) structures was also supported by the results of the thermogravimetric analysis (Figure 8.5 a-d). The measurement carried out in air atmosphere allows not only to obtain information on the thermal stability of the structure, but also to determines the content of missing-linker defects [67,93]. Three main mass losses can be distinguished for both structures. First of them starts already at about 50 °C and can be assigned to the escape of water molecules adsorbed by MOF's pores during contact with air during the preparation of sample for the measurement. After that, the next mass decrease is visible at 300 °C and 330 °C for the UiO-66(Zr) and NH_2-UiO-66(Zr) samples, respectively. It may be caused by two factors. First of them is the dehydroxylation of the MOF structure – *i.e.* detachment of -OH groups connected to SBU units [357]. The second possibility concerns the decomposition of unbound linker molecules remaining in the pores of MOF, which is confirmed by the TGA of the linkers – H_2BDC and NH_2- H_2BDC (Figure 8.5 e-f). The

final breakdown of MOF structure takes place at about 500 °C and 450 °C for UiO-66(Zr)- and NH_2-UiO-66(Zr)-based samples, respectively.

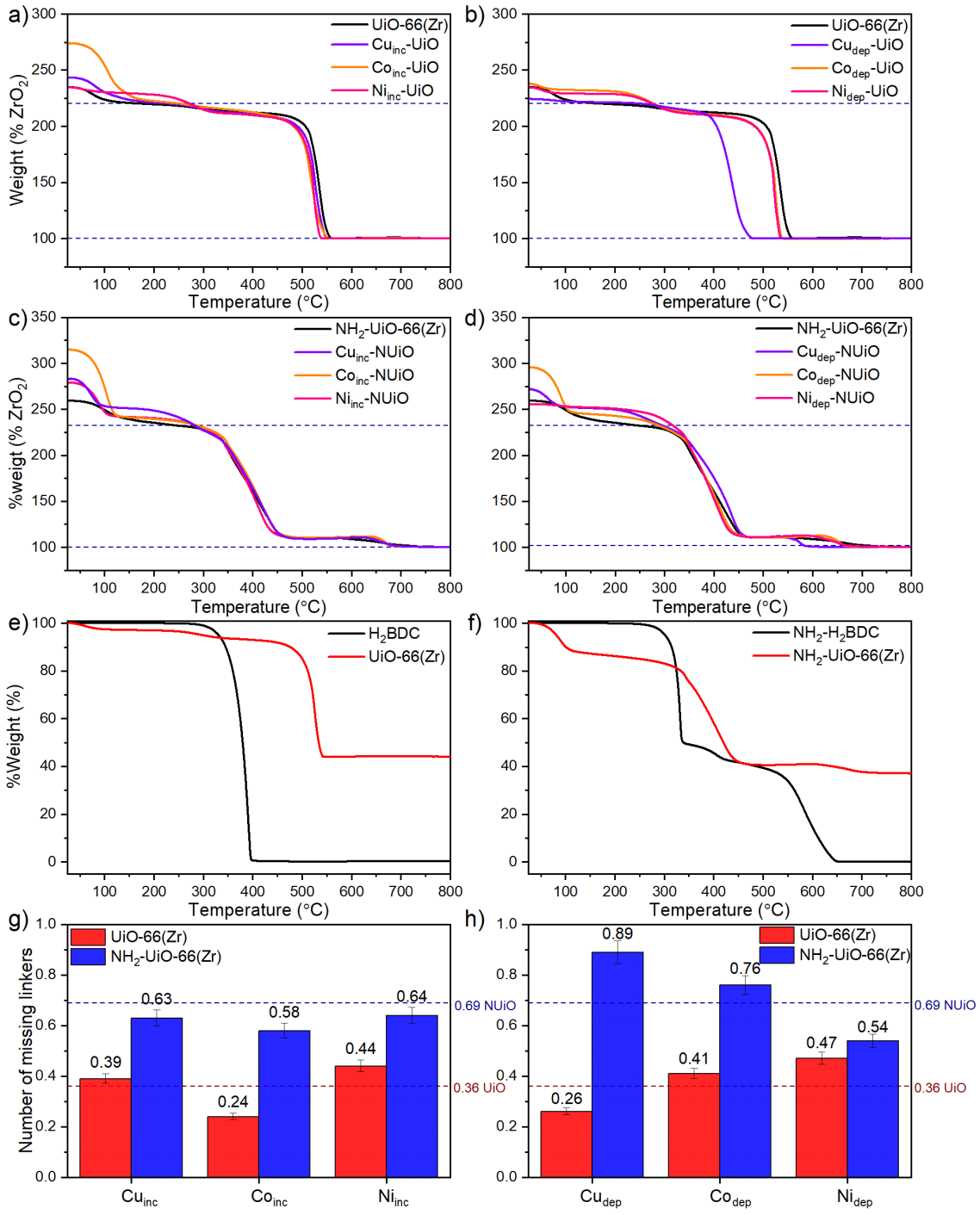


Figure 8.5 TGA curves of: a) UiO-66(Zr) after incorporation, b) UiO-66(Zr) after photodeposition, c) NH_2-UiO-66(Zr) after incorporation, d) NH_2-UiO-66(Zr) after photodeposition; comparison of the TGA curves of: e) H_2BDC and UiO-66(Zr), f) NH_2- H_2BDC and NH_2-UiO-66(Zr); Comparison of missing-linker defects in obtained UiO-66(Zr) and NH_2-UiO-66(Zr) samples after: g) incorporation, h) photodeposition

In the case of NH_2-UiO-66(Zr) samples, additional mass loss visible at about 650 °C, as in the case of the second step of mass loss, it can be attributed to linker degradation (Figure 8.5f). Assuming the full dehydroxylation of MOFs during the heating under air flow and that ZrO_2 is the only solid product remaining after the analysis, the amount of missing linkers was calculated [67,93]. The determined

number of MLs per structural units of UiO-66(Zr) and NH_2-UiO-66(Zr), that is respectively $Zr_6O_6(BDC)_6$ or $Zr_6O_6(NH_2\text{-}BDC)_6$, is presented in Figure 8.5g-h. In the case of pristine MOFs, NH_2-UiO-66(Zr) was found more defected than UiO-66(Zr), possessing 0.69 and 0.36 missing linker per structural unit, respectively, probably as a result of the functional group attached to the linker. As a steric hindrance, the pending functionality is more prone to disturb the formation of non-defected structure. A similar observation was made for the samples modified with the non-noble metals. Regardless of the MOF type, the more pronounced linker deficiency was determined for MOFs after photodepostion than for samples after incorporation. In the case of UiO-66(Zr), the number of ML after photodeposition was increased by number of 0.05-0.15 compared to pristine MOF, while for NH_2-UiO-66(Zr) the difference reached level of about 0.1-0.2 MLs per structural unit.

XPS measurements were performed to confirm the presence of introduced elements and determine their chemical identity (Table 8.2). Successful introduction of Co (by photodeposition) and Cu (both methods) into both MOFs was established (Figure 8.6). Taking into account the very low Ni content in both samples (close to the detection limit of the analyzing unit and additionally disturbed by Zr presence [271]) and its extensive distribution in the pores of the MOFs, its presence was confirmed only by TEM-EDS (Figure 8.1g). The chemical state of the modifying metals and the type of their interaction with the structure UiO-66(Zr) and NH_2-UiO-66(Zr) was analyzed in details.

Table 8.2 Atomic concentration of elements analyzed with XPS

Entry	at% conc.						
	C	Zr	O	N	Cu	Co	Ni
UiO-66(Zr)	61.6	7.9	30.6	-	-	-	-
Cu_{inc}-UiO	63.8	7.1	29.1	-	-	-	-
Cu_{dep}-UiO	62.0	7.5	30.1	-	0.4	-	-
Co_{dep}-UiO	61.6	7.4	30.4	-	-	0.6	-
Ni_{dep}-UiO	60.1	8.1	31.8	-	-	-	Below detection
NH_2-UiO-66(Zr)	55.7	7.9	31.6	4.8	-	-	-
Cu_{inc}-NUiO	57.6	7.4	29.4	5.7	-	-	-
Cu_{dep}-NUiO	56.5	7.5	30.0	5.7	0.3	-	-
Co_{dep}-NUiO	57.4	7.3	29.8	5.1	-	0.5	-
Ni_{dep}-NUiO	56.8	7.5	29.9	5.8	-	-	Below detection

In the case of samples modified with Cu *via* photodeposition approach, the deconvolution of peaks at 932.9 eV and 932.8 eV (respectively for bare MOF and aminated one) on the high-resolution spectra of Cu $2p_{3/2}$ (Figure 8.7) was assigned as Cu^0 and/or Cu^+ in oxide [364]. Such interpretation may indicate that nanoparticles were created and present in the pores of MOFs. Additionally, additional signal at 934.7 eV and its satellites was detected for Cu_{dep}-UiO and may be assigned to the Cu^{2+} species coordinated with the -OH groups of the SBUs in MOF [364,365]. The copper species of the same valence were attributed to the peak at 934.1 eV and the satellite at 941.1 eV in the case of Cu_{dep}-NUiO [366]. In this case, connection of copper species with MOF net could be attributed to either hydroxyl groups (as in the case of Cu_{dep}-UiO), but simultaneously coordination with amino group of the linkers was also possible. However, the low content of Cu hindered the detailed determination of the actual structure, as the shifts of the binding energy of Cu-O and Cu-N peaks were probably drowned in the larger peaks related to O and N (Figure 8.8). Compared to Cu^0/Cu^+, the content of Cu^{2+} is doubled considering the area of the peaks.

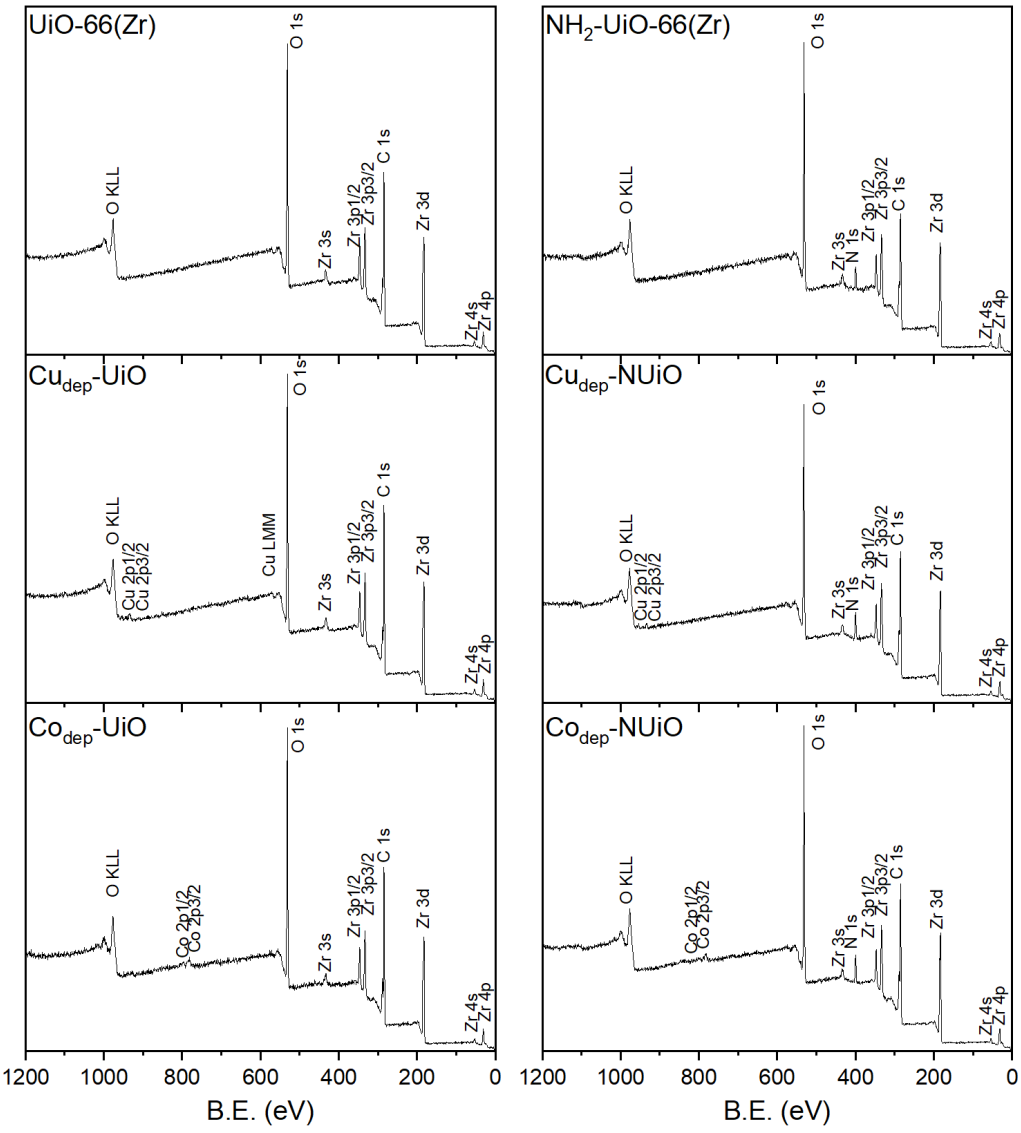


Figure 8.6 Survey spectra of UiO-66(Zr), NH_2-UiO-66(Zr) and samples after photodeposition of Co and Cu

Two main peaks at 781.5 eV and 781.3 eV (Figure 8.7) were identified as a result of Co $2p_{3/2}$ spectra deconvolution for Co_{dep}-UiO and Co_{dep}-NUiO, respectively. Their specific location does not correspond to standard positions of single Co species. For both samples after Co photodeposition four peaks were recognized *i.e.* two main and satellite peaks each (including the mentioned main peaks). Their location does not correspond well with BE values characteristic for either oxides or hydroxides of this specific element [367]. Similarly, compared to CoO and Co_3O_4, the distance between the peaks and satellites does not match the characteristic values, respectively 6 eV and 9-10 eV [367,368]. Such lack of a clear match may indicate presence of cobalt in mixed valence states *i.e.* Co^{2+} as well as Co^{3+}. Formation of the second one can be explained by partial photooxidation of Co^{2+} [369]. Cobalt may be bound to the through carboxylic groups [370,371], hydroxyl groups in zirconium clusters with missing-linker defects [372] or, in the case of NH_2-UiO-66(Zr), with amino groups [373]. Existence of cobalt

complexes connected with MOFs structures may be also supported by the TEM imaging (Figure 8.1d,f), which did not indicate the presence of NPs, while the uniform distribution of Co was confirmed.

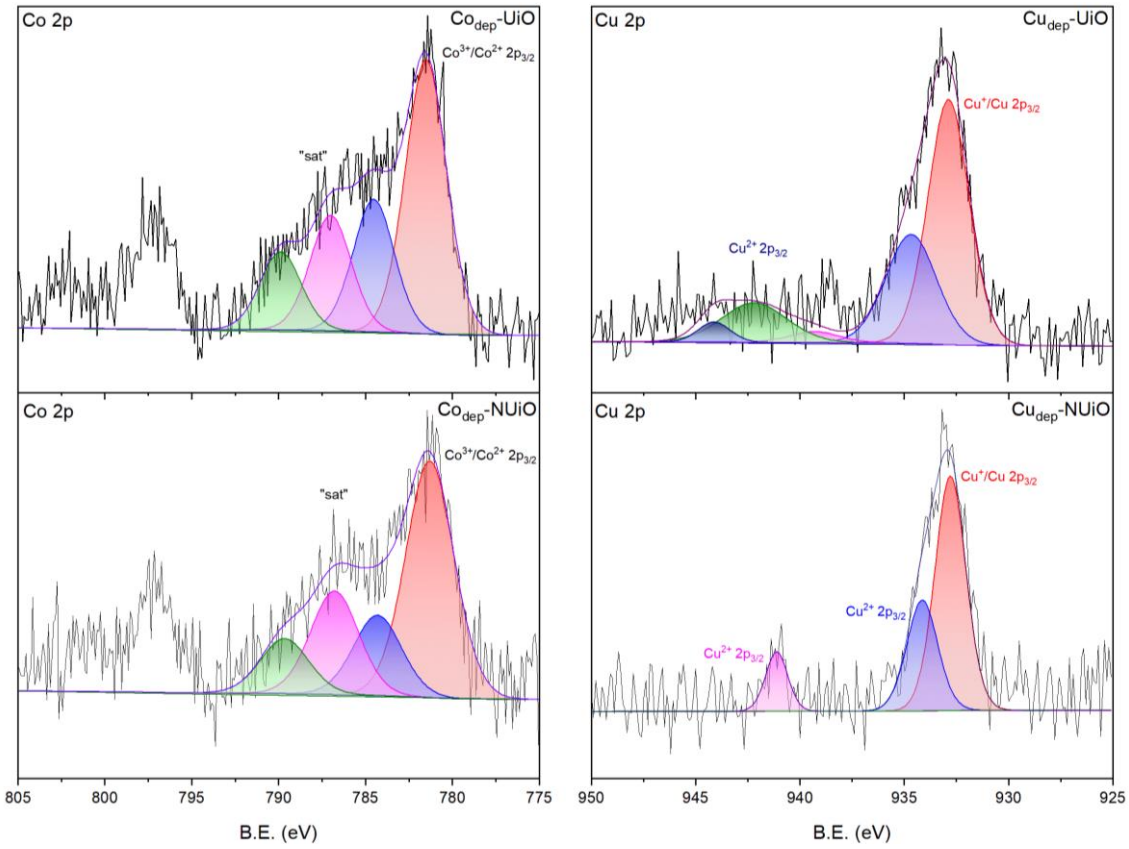


Figure 8.7 High-resolution spectra of Co 2p and Cu 2p of UiO-66(Zr) and NH_2-UiO-66(Zr) modified by photodeposition

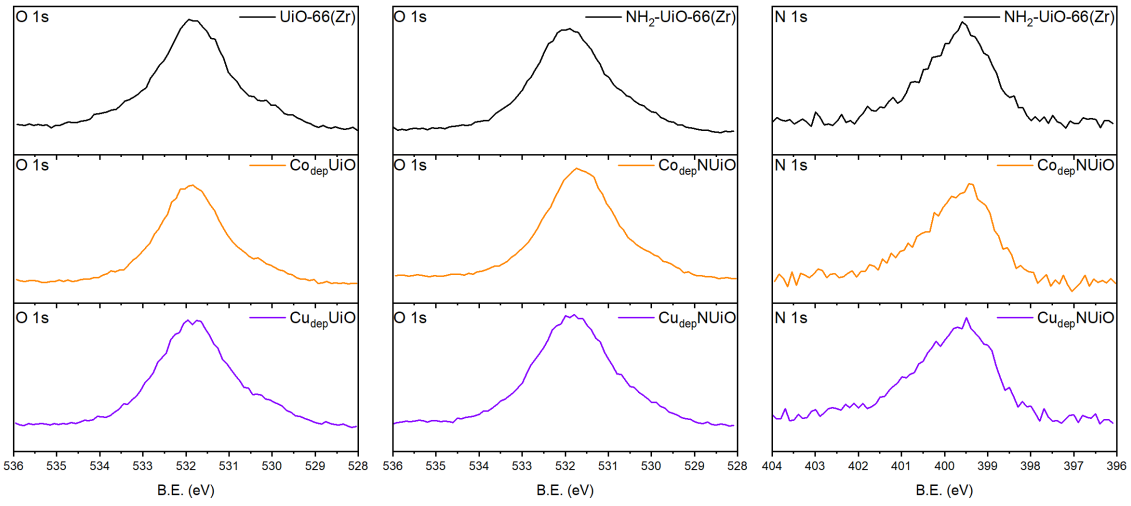


Figure 8.8 High resolution spectra of O 1s and N 1s (where applicable) of UiO-66(Zr), NH_2-UiO-66(Zr) and samples modified by photodeposition of Cu and Co

The values of optical gaps of the obtained for pristine materials and samples modified by incorporation were calculated basing on Tauc plots (Table 8.3). For this purpose, DRS spectra were recorded (Figure 8.9) and converted considering allowed direct transitions (n=2). For UiO-66(Zr) the

designated optical gap was equal to 4.05 eV, while for NH_2-UiO-66(Zr) – 2.91 eV. The introduction of non-noble metals only negligibly influenced the numbers. In the case of modified the first MOF the calculated values were slightly increased and were within the range of 4.07-4.09 eV, regardless of the metal type and the method of their introduction. Compared to the pristine aminated MOF, modification led to slight decrease of the values to the range of 2.81-2.86 eV. Such fluctuations can be explained by the varying content of the structural defects in the synthesized structures, which was previously proved and described in details by Wang *et al* [7]. In the case of samples after photodeposition, the use of this method of designating optical gap is not suitable, as the photodeposition of the non-noble metal-based moieties on MOF should be treated as creation of heterostructure, while the Tauc method is only reliable for a single material [374].

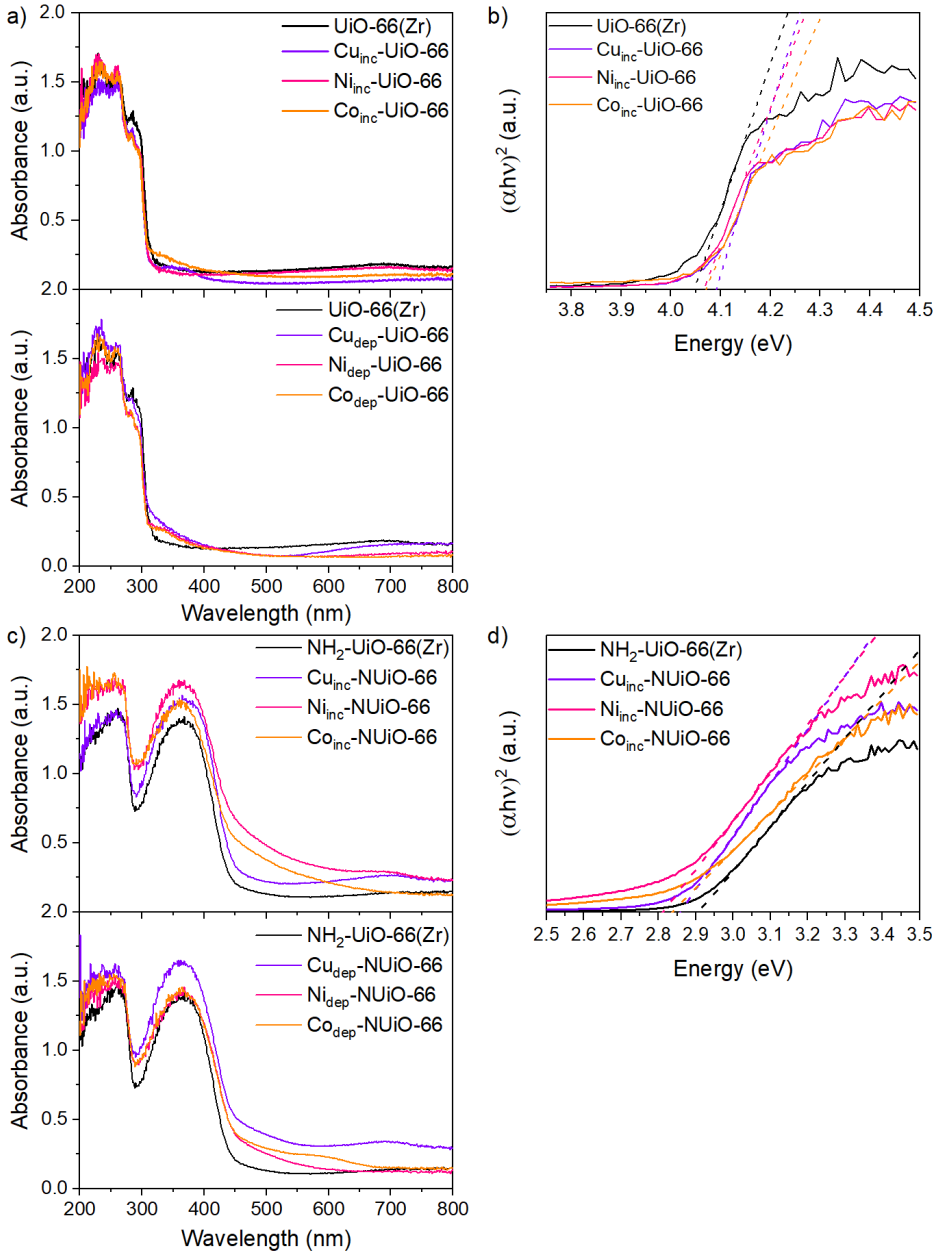


Figure 8.9 DRS spectra of a) UiO-66(Zr) after incorporation and photodeposition and c) NH_2-UiO-66(Zr) after incorporation and photodeposition; Tauc plots of b) UiO-66(Zr) after incorporation and d) NH_2-UiO-66(Zr) after incorporation

Basing on the described results, additional computational modelling study was conducted by Azahara Luna-Triguero and Jose Manuel Vicent-Luna and published in joint research paper [12]. The considerations on the influence of cobalt and defects on the electronic structure of the obtained material are described in the mentioned work in details.

8.2. Sorption properties

The influence of non-noble metals and of the method of their introduction to the MOFs on their gas sorption properties was investigated. The sorption of nitrogen at -196 °C and of carbon dioxide at -50 °C and 25 °C was measured, to designate the S_{BET} value and to evaluate how the affinity to CO_2 impacts the resulting photocatalytic abilities in the process of its reduction. Results of these analyses were presented in Table 8.3. The specific surface area of pristine MOFs – UiO-66(Zr) and NH_2-UiO-66(Zr) – reached the level of respectively 906.5 and 863.9 $m^2 \cdot g^{-1}$. The presence the amino functionality promoted the CO_2 uptake at both temperatures. At 25 °C, the sorption capacity of 2.25 $mmol \cdot g^{-1}$ and 2.66 $mmol \cdot g^{-1}$ were measured for UiO-66(Zr) and its aminated analogue, respectively, giving moderate increase of almost 20%. In turn, at -50 °C, the introduction of -NH_2 functionality was accompanied by 52% boost *i.e.* from 6.16 $mmol \cdot g^{-1}$ to 9.34 $mmol \cdot g^{-1}$. Generally, in the MOF structure, the CO_2 particles can be effectively stored as a result of formation of hydrogen bonds (for example with the hydroxyl groups in SBUs [235]) or by quadrupole-delocalized electrons interactions (between CO_2 and the charged benzene rings [236]). In the case of NH_2-UiO-66(Zr) the extra chemical interaction between CO_2 and amino- functionality (as amine carbamate can be created [237]) may be responsible for the improved performance. The light-assisted deposition of the chosen non-noble metals on UiO-66(Zr) and NH_2-UiO-66(Zr) decreased the S_{BET} by 5.4-5.9% (to ~850 $m^2 \cdot g^{-1}$) and 29.1-33.0% (to about 580-630 $m^2 \cdot g^{-1}$), respectively. In contrast to the pristine NH_2-UiO-66(Zr), the samples modified *via* photodeposition approach were characterized with CO_2 uptake with a value similar (Cu_{dep}) to or lower (Ni_{dep} and Co_{dep}) than the respective UiO-66(Zr) modified samples. As an example, Ni_{dep}-UiO showed the CO_2 sorption capacity of 6.19 $mmol \cdot g^{-1}$ at -50 °C, giving about 17% improvement compared to pristine UiO-66(Zr), while the value for Ni_{dep}-NUiO reached only 4.55 $mmol \cdot g^{-1}$, that is 51% decrease in respect to NH_2-UiO-66(Zr). The generally worsened gas sorption properties (decreased S_{BET} and CO_2uptake) of samples after photodeposition suggests clogging of the pores by the introduced non-noble metals and formed complexes with MOF structures. This results in limitation of the adsorption sites available for gas molecules, as the amino groups get occupied. No similar dependences were observed, especially in the case of UiO-66(Zr)-based samples after photodepostion of Cu, Co or Ni.

Concerning the samples after incorporation of non-noble metals, no universal dependence was concluded regarding the gas sorption properties of the obtained materials. Incorporation of Co to UiO-66(Zr) decreased the S_{BET} to the level of about 850 $m^2 \cdot g^{-1}$, while Ni led to increase – 1000 $m^2 \cdot g^{-1}$ was slightly exceeded. The synthetical introduction of copper had diverse influence on UiO-66(Zr) and NH_2-UiO-66(Zr). In the case of the first MOF – the value of S_{BET} was slightly risen (by 7.5%), while for the second this value dropped (by 16.5%). Only in the case of Co-incorporated sample, the value of CO_2 uptake for aminated sample is lower than for the elementary Zr-based MOF, regardless of the temperature of analysis. Both Cu_{inc}NUiO and Ni_{inc}NUiO were characterized with higher CO_2 sorption

capacities than respectively modified UiO-66(Zr) samples. At 25 °C, the incorporation of 0.5 % of Cu and Ni to NH_2-UiO-66(Zr) increased the sorption capacity by about 50-55 %. Interestingly, for analogous UiO-66(Zr)-based samples, compared to unmodified MOF for Cu-modified one – decrease of about 30% was noted, while for Ni-incorporated MOF even 73% increase, however, the reached value was still lower than for Ni_{inc}NUiO. Even though, both Ni-incorporated samples have shown the most developed surface areas and the highest affinity towards CO_2 adsorption at both temperatures. Taking into account the determined values of adsorption enthalpy (basing on the measured isotherms of CO_2 adsorption), possessing value between -10.8 and -26.9 kJ for NH_2-UiO-66(Zr) and -11.5 and -25.4 kJ for UiO-66(Zr), the physical mechanism of adsorption was indicated for all materials. The highest values were designated for pristine NH_2-UiO-66(Zr), as well as for Cu_{inc}-UiO and Cu_{dep}-NUiO, while the lowest values were calculated for Ni_{dep}UiO and Co_{inc}-UiO. It was assessed that these values had no direct impact on the photocatalytic ability of the materials.

Table 8.3 Actual content of the non-noble metals (ICP-OES), specific surface area, CO_2 sorption capacity, enthalpy of adsorption, band gap values and HCOOH formation efficiency of UiO-66(Zr)- and NH_2-UiO-66(Zr)-based samples

Entry	True value of modifying metal content (wt%)	S_{BET} ($m^2 \cdot g^{-1}$)	CO_2 uptake at 25 °C ($mmol \cdot g^{-1}$)	CO_2 uptake at-50 °C ($mmol \cdot g^{-1}$)	Enthalpy of adsorption ($kJ \cdot mol^{-1}$)	Optical gap (eV) (direct n=2)	HCOOH generation after 4h of UV-Vis irradiation ($\mu mol \cdot g^{-1}$)	HCOOH generation after 4h of Vis irradiation ($\mu mol \cdot g^{-1}$)
UiO-66(Zr)	-	906.5	2.25	6.19	-17.7	4.05	54.60	-
Cu_{inc}-UiO	<0.001	971.4	1.62	6.83	-25.4	4.09	49.71	-
Ni_{inc}-UiO	0.01	1008.6	3.89	10.5	-19.3	4.07	69.69	-
Co_{inc}-UiO	0.01	849.8	2.44	6.73	-18.0	4.07	28.81	-
Cu_{dep}-UiO	0.49	853.7	1.97	6.66	-18.8	-	50.82	-
Ni_{dep}-UiO	0.11	853.1	2.64	7.25	-11.5	-	35.05	-
Co_{dep}-UiO	0.37	857.2	1.81	6.05	-14.9	-	57.99	-
NH_2-UiO-66(Zr)	-	863.9	2.66	9.34	-26.9*	2.91	54.12	50.20
Cu_{inc}-NUiO	<0.001	755.3	4.00	8.96	-16.2	2.86	20.00	40.40
Ni_{inc}-NUiO	0.02	969.4	4.10	11.3	-20.4	2.81	54.18	47.42
Co_{inc}-NUiO	0.02	786.7	2.57	5.14	-10.8	2.84	44.72	42.93
Cu_{dep}-NUiO	0.49	612.3	1.86	6.78	-23.3	-	72.30	36.14
Ni_{dep}-NUiO	0.06	627.5	1.70	4.55	-14.0	-	13.60	62.85
Co_{dep}-NUiO	0.32	578.8	1.61	5.15	-17.5	-	73.33	37.94

* determined using isotherms of CO_2 adsorption at 15 °C and 25 °C

8.3. Photocatalytic performance

The influence of cobalt, copper and nickel, as well as the method of their introduction to MOFs and the induced defectivity on the overall photocatalytic ability to reduce CO_2 was investigated. The light-assisted processes of CO_2 conversion were performed liquid environment of acetonitrile and triethanolamine mixed with volume proportion of 9:1. TEOA was used as a hole scavenger to prevent recombination of electrons and holes and as a source of hydrogen. When only the liquid environment was used for the photoconversion procedure, no formic acid was detected. For all samples the photocatalytic reactions and the preceding purification procedure were carried out under UV-Vis light irradiation. The photopurification was necessary to ensure that the detected products were created actually consuming the dosed CO_2 and not the eventual remaining present in the pores of MOF, like for example DMF [325,375]. The procedure was performed immediately before the actual CO_2

photoconversion experiment and included UV-Vis irradiation of MOF suspended in the MeCN/TEOA mixture under nitrogen flow and exchange of the liquid phase for fresh portion. The effectiveness of the procedure was proven by analyzing the product content with ionic chromatography after carrying out a reference experiment using N_2 instead of CO_2. The results of processes employing the unmodified samples – UiO-66(Zr) and NH_2-UiO-66(Zr) – including detection of the product after every hour during the four-hour reaction was shown in Figure 8.10a. Respectively 54.60 μmol·g^{-1} and 54.12 μmol·g^{-1} of HCOOH was generated after 4 h by UiO-66(Zr) and NH_2-UiO-66(Zr), which is a comparable result (p=0.05). This confirms the negligible influence of the CO_2 sorption capacity of the materials on their photocatalytic performance, as the CO_2 uptake was higher for NH_2-UiO-66(Zr) compared to UiO-66(Zr) – respectively 2.66 mmol·g^{-1} and 2.25 mmol·g^{-1} at 25 °C.

The comparison of described herein materials can be found in Table 4.1. The data regarding the use of UiO-MOFs for CO_2 photoreduction is rather dominated by reports on other products than formic acid. Among several works indicating HCOOH as the main product of photoconversion, Bhattacharya *et al*. [203] reported the efficiency of pristine UiO-66(Zr) at level of 9.7 μmol·g^{-1}·h^{-1}, which is less compared to this work (13.65 μmol·g^{-1}·h^{-1}). In other work, the non-modified NH_2-UiO-66(Zr) achieved the photocatalytic efficiency exceeding 13.5 μmol·g^{-1}·h^{-1}of HCOOH, where the photocatalytic procedure was preceded by additional freeze–pump–thaw cycles [203]. In turn Zhao *et al.* [206] demonstrated that the chitosan-embedded NH_2-UiO-66(Zr) photocatalyst under visible light irradiation (400-760 nm) yielded mainly in CO (21.25 μmol·g^{-1}·h^{-1}), while only trace amount of HCOOH was detected in.

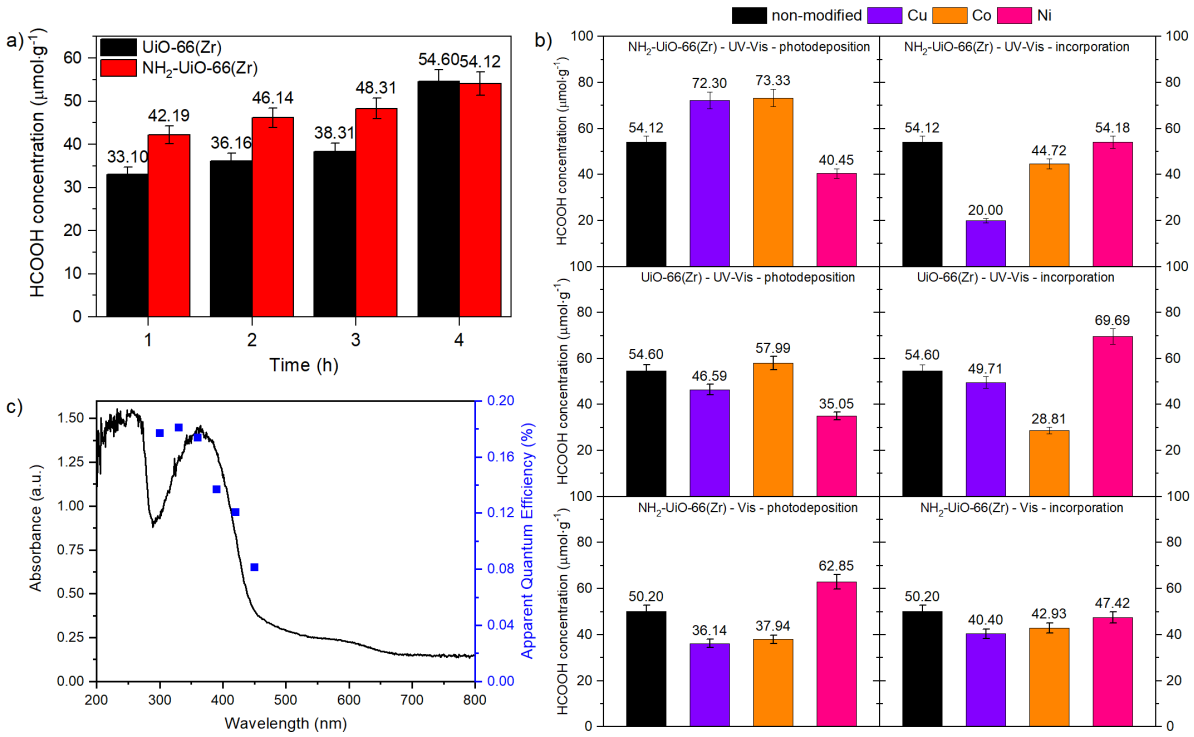


Figure 8.10 a) Concentration of generated HCOOH by UiO-66(Zr) and NH_2-UiO-66(Zr) under UV-Vis irradiation (Xe lamp; environment: 10%TEOA/MeCN); b) Concentration of generated HCOOH after 4 hours under UV-Vis irradiation for: NH_2-UiO-66(Zr) after photodeposition and incorporation, UiO-66(Zr) after photodeposition and incorporation, as well as under Vis irradiation for: NH_2-UiO-66(Zr) after photodeposition and incorporation, (Xe

lamp; environment: 10% TEOA/MeCN); c) Action spectra for HCOOH generation vs. absorption spectrum of Co_{dep}-NUiO

The photocatalytic efficiency of MOFs modified with the chosen non-noble metals was shown in Figure 8.10b. Increased concentration of HCOOH was designated for NH_2-UiO-66(Zr) after photodeposition of Co and Cu and showing improvement of 35.5% and 33.6%, respectively, compared to the pristine sample. Interestingly, it was achieved even though the CO_2 sorption capacity measured for these samples was lower than for NH_2-UiO-66(Zr). The recorded photoluminescence spectra (Figure 8.11) did not show change of the PL intensity, suggesting no substantial influence of the modification on the recombination of the reactive electron–hole pairs. In comparison with the pristine sample for both materials Cu_{dep}-NUiO and Co_{dep}-NUiO, raised amount of ML and MC defects was observed. For the other modified NH_2-UiO-66(Zr)-based samples, lowered reduced photocatalytic activity was accompanied by a smaller amount of ML defects, suggesting its potential significance regarding CO_2 photoreduction under UV-Vis irradiation. The corresponding Cu- and Co-modified by photodeposition UiO-66(Zr) samples did not show significant improvement of the photocatalytic abilities maintaining the level of HCOOH generation similar to the pristine sample thus confirming the key role of the amino functionality. Taking into account the content of non-noble metals designated by XPS (Table 8.2) and ICP-OES (Table 8.3), it was excluded that the presence of the amino functional group affects the amount of effectively introduced metal, as in the case of corresponding samples the differences were negligible. According to DSR spectra (Figure 8.9) the Ni-photodeposited samples were characterized by decreased absorbance compared to other samples modified with this method, which stands in line with the worsened results of CO_2 photoconverion ($p=0.05$). The use of Ni_{dep}-UiO reduced the amount of photogenerated HCOOH by 35.8% and by 25.3% in the case of the respective Ni_{dep}-NUiO. Even though the PL intensity measured for Cu_{inc}-NUiO and Co_{inc}-NUiO (Figure 8.11) suggested more beneficial, delayed recombination of $e^- – h^+$ pairs compared to the reference sample, the photocatalytic activity was lowered. In turn, in the case of Ni_{inc}-UiO the boosted photocatalytic activity stands in line with the slower recombination of photogenerated carriers (Figure 8.11) and additionally with the increased CO_2 sorption capacity (Table 8.3).

To get a deeper insight into the poor photocatalytic performance of Ni_{dep}-NUiO and confirm the cause of this problem, PL lifetime analysis was performed (Figure 8.12). The designated decay time for NH_2-UiO-66(Zr) was the shortest, indicating relatively fast recombination of photogenerated electron-hole pairs. Interestingly, the measured decay time for Ni_{dep}-NUiO was the longest which was not reflected in the photocatalytic performance. Considering that the best two samples (Cu_{dep}-NUiO and Co_{dep}-NUiO) have shown shorter decay time than Ni-modified sample, but at the same time – a better overall result of photocatalytic process – no simple relationship between activity and carrier lifetime can be concluded. Such phenomenon can be related to few factors. Among them presence of trap states and defects [376], low charge mobility [377], mismatched energy levels [378] or occurring radiative and non-radiative processes [379] can be distinguished.

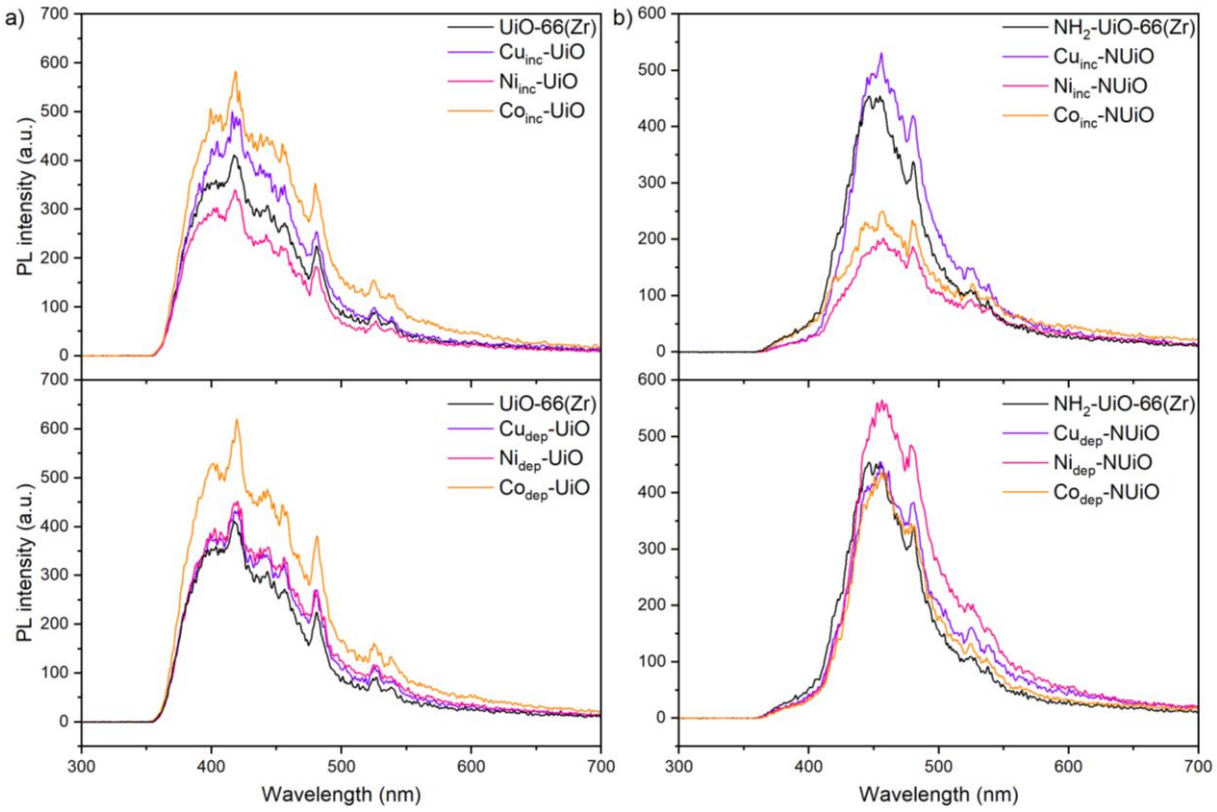


Figure 8.11 PL spectra of a) UiO-66(Zr) and b) NH_2-UiO-66(Zr) after Cu, Co or Ni incorporation and photodeposition

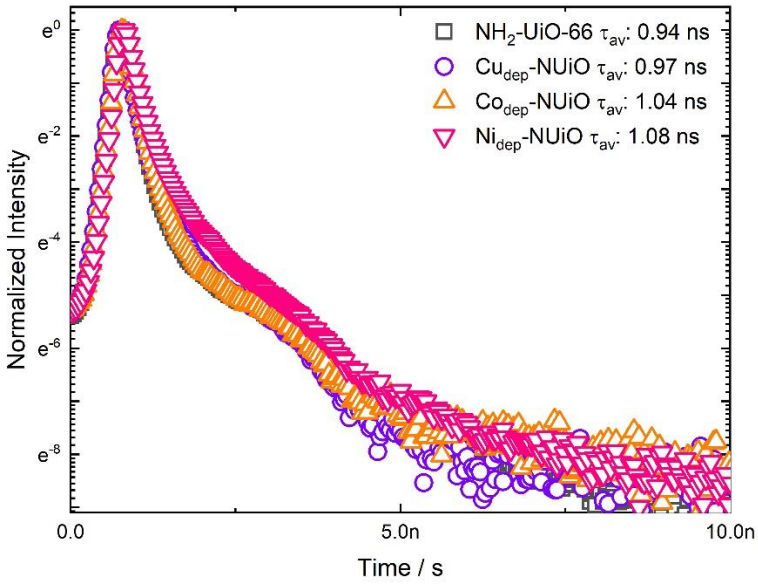


Figure 8.12 Time-resolved photoluminescence decay spectra of NH_2-UiO-66(Zr) and samples via photodeposition approach. Spectra were recorded under 330 nm excitation and monitored at the emission maximum wavelength.

To verify the photocatalytic properties of NH_2-UiO-66(Zr)-based samples under visible light irradiation, additional processes were carried out with exchange of the reactor front glass to optical filter (420 nm cut off filter). The performed DRS studies (Figure 8.9) indicated the shift of light absorption edge towards higher valuers of wavelengths compared to the primary UiO-66(Zr). No significant change ($p=0.05$) in visible light-driven HCOOH generation (50.20 $\mu mol \cdot g^{-1}$) was observed compared to the

results achieved under UV-Vis light (54.12 μmol·g^{-1}) (Figure 8.10b), confirming the possibility to excite NH_2-UiO-66(Zr) with solar irradiation. Despite that, regardless of the approach of non-noble metals introduction, the modified samples exhibited worsened photocatalytic performance (p=0.05). Regardless of the metal type, their incorporation contributed to decrease of detected HCOOH to the level of 40-47 μmol·g^{-1}, slightly below the result of pristine sample. In turn, in the case of photodeposition, Co_{dep}-NUiO and Cu_{dep}-NUiO shown 25-27% decrease compared to pristine MOF, while only Ni_{dep}-NUiO have shown improvement up to 62.85 μmol·g^{-1} (p=0.05). Examples of modifications executed on UiO-66(Zr) MOFs in order to improve their photocatalytic performance were listed in Table 4.1. Similar approach as described herein *i.e.* regarding the introduction of other metal than the original was described, but with the difference that the modifying metal was of the same valence as Zr. This enabled exchange of metal atoms in SBUs for Ti (*via* either post-synthetical and synthetical approaches) and resulted in increased photocatalytic HCOOH generation to the level of 1 mmol·g^{-1}·h^{-1} [171] and 180 μmol·g^{-1}·h^{-1} [121], respectively, in situation when Ti was introduced by PSE approach or added to synthesis. Interestingly, similar approach of modification on NH_2-UiO-66(Zr) described by Sun *et al.* [110] did not allow for obtaining spectacular improvement, as only 1 μmol·g^{-1}·h^{-1} of HCOOH was detected. Depending on the metal introduced, various authors also reported increased generation of other products of photocatalytic CO_2 reduction. For example, modification of NH_2-UiO-66(Zr) with Cu enabled generation of EtOH and MeOH in water environment [214], while decoration of MOIF surface with metallic coper and Cu_2O increased the production rate of CO by almost three and a half times and enabled generation of CH_4 [156]. Threefold improved photocatalytic CO production was also achieved by Su *et al.* when indium was incorporated to NH_2-UiO-66(Zr) [207].

The actual origin of HCOOH (the dosed carbon dioxide) was confirmed by performing the CO_2 photoconversion using its isotope *i.e.* $^{13}CO_2$. The photoreduction process was analogous to the elementary experiment with the difference that smaller reactor – of only 6 mL volume – was used. The quantities of the photocatalyst and the liquid environment used have also been adjusted *i.e.* 12.5 mg of Co_{dep}-NUiO was dispersed in 5 mL of 10%TEOA/d_3-MeCN (the regular acetonitrile was also replaced by the deuterated isotope). The photopurification procedure was performed as during regular procedure, after which feeding with $^{13}CO_2$ was carried out before irradiation with UV-Vis light. Formation of isotopic products of photoconversion was validated with ^{1}H NMR spectroscopy (Figure 8.13). Presence of two singlets at about 8.11 ppm and 8.48 ppm was found and assigned to the presence of isotopic $H^{13}COO^-$ confirming the $^{13}CO_2$ to be the source [380,381]. Analogous peaks were not found in the pure 10%TEOA/d_3-MeCN liquid phase, excluding the possibility of regular HCOOH formation from other source than the deuterated CO_2. Nature of the observed singlet at 8.04 ppm was not identified, but probably it was related to the liquid phase rather than ^{12}C formic acid.

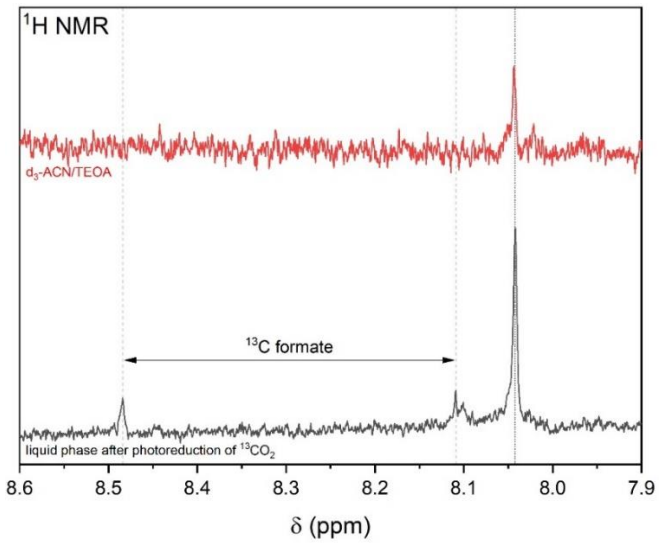


Figure 8.13 ^{1}H NMR spectra of pure 10%TEOA/d_3-MeCN and of the liquid phase after photoconversion under UV-Vis light using $^{13}CO_2$ and Co_{dep}-NUiO (24 hours, Xe lamp).

The one- and three-way ANOVA were employed (p=0.05) to evaluate the effect of non-noble metals introduction on the properties of obtained MOFs. In the vast majority of the samples, the one-way analysis indicated significant influence of introduced metals on the photocatalytic performance. For Ni_{inc}-NUiO (under both Vis and UV-Vis light), Co_{inc}-UiO and Co_{dep}UiO no significant changes in the yield of CO_2 photoreduction were observed in comparison with the respective reference samples. In turn, the type of defect that was created in MOF's structure and its content, were found dependent from the type of the non-noble metal. Photodeposition of Co (for both MOFs), incorporation of Cu (for both MOFs) or Ni (only in the case of UiO-66(Zr)) were found not significant in terms of ML defects formation (p=0.05), while in the case of MC defects only, for two UiO-66(Zr)-based samples *i.e.* Co_{inc}-UiO and Cu_{dep}-UiO, the changes were defined as insignificant.

The three-way ANOVA was used to evaluate the possible effects of MOF and non-noble metals type, as well as the method of metals introduction to MOF on the structural defectivity and photocatalytic performance under UV-Vis light. At a confidence level of p=0.05, it was established that all three factors and their interactions were significant in terms of the evaluated properties values. Significant impact on the amount of MC and HCOOH production under UV-Vis light irradiation was determined for all metal types, while only introduction of Co was recognized as significant in term of ML content.

In order to confirm the correlations between defect concentration and activity additional quantitative analysis was made. The designated relation between missing linker or missing cluster defects and the photocatalytic activity of the obtained materials was presented in Figure 8.14. Considering NH_2-UiO-66(Zr) and its derivatives, approximately 14% content of MC was found favorable in the case of UV-Vis light-driven CO_2 photoconversion. In the case of modified NUiO samples, any deviations from that value were found to cause contrary effect. In turn, for the same materials under the same light irradiation, the higher the content of ML defect is, the more beneficial influence on the photocatalytic activity is predicted. In order to assess whether there is a critical content of ML beyond

which this trend is disturbed, the number of samples should be increased. In turn, when using only visible light for the photocatalytic process, the inverse dependence was observed for MC content. In this case, the amount of 14% MC was the most unfavorable. Under the visible light irradiation, the decreasing photocatalytic yield of NH_2-UiO-66(Zr)-based materials was also observed for growing content of ML defects, unlike for UV-Vis light-driven photocatalysis. No straightforward dependence of MC content on UiO-66(Zr) performance was concluded, as both relatively high and low yields were designated for samples with low amount of MC designated. Only single point was found in the region of relatively high MC content. It suggests that increasing MC content is unfavorable in terms of CO_2 photoreduction, but cannot be undoubtedly confirmed. Similarly to NH_2-UiO-66(Zr) the quantitative analysis revealed that for UiO-66(Zr), the photocatalytic performance under UV-Vis light irradiation may be boosted by introduction of higher amount of missing linker defects.

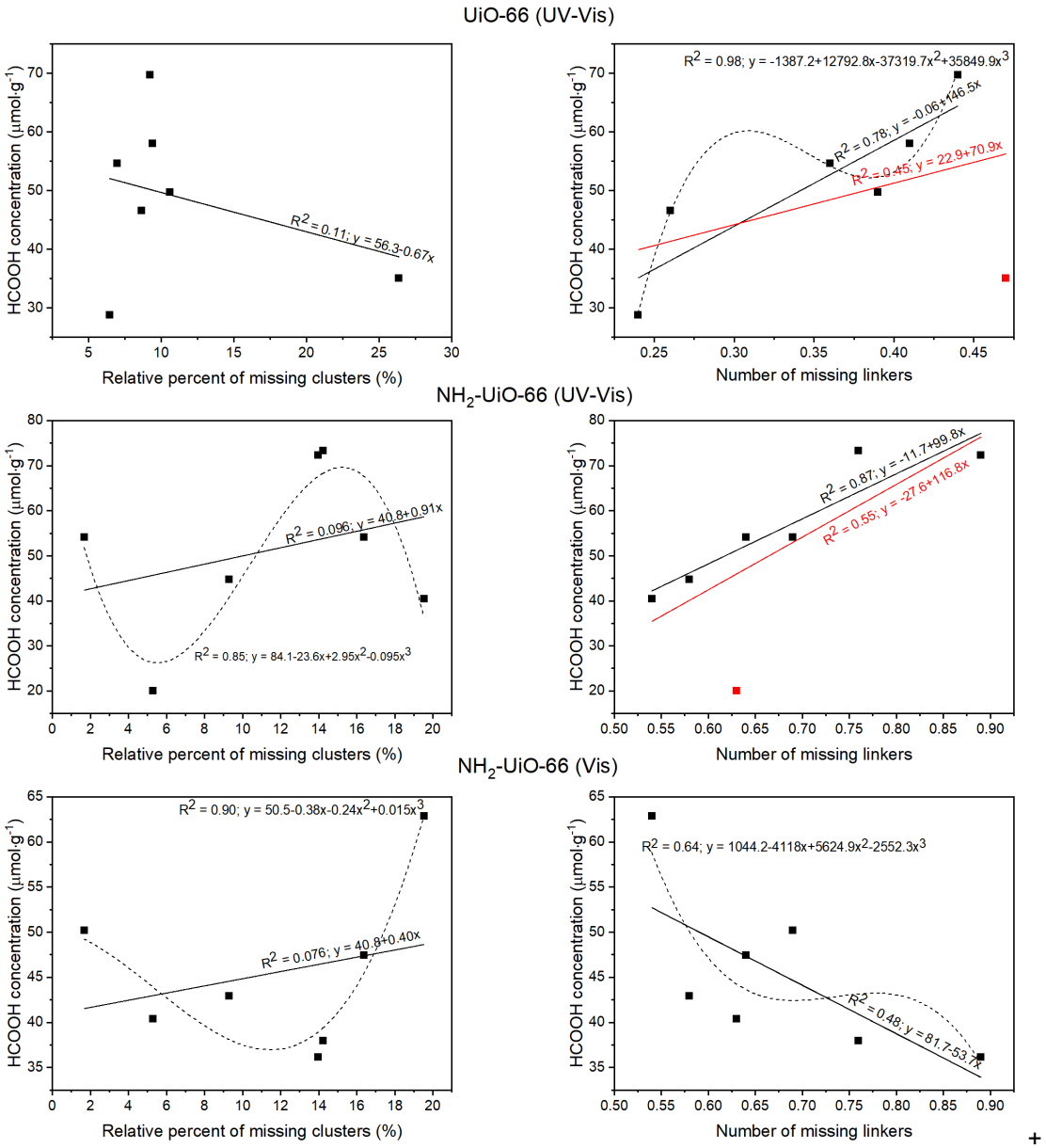


Figure 8.14 Quantitative analysis of ML or MC content influence on the photocatalytic activity of MOFs. The black fitted curves consider all data points, red curves – data sets after exclusion of outlying points (also marked with red). Polynomial fit was distinguished with dashed lines.

The Apparent Quantum Efficiency (Figure 8.10c) was designated for Co_{dep}-NUiO – the sample showing the best photocatalytic performance, regardless of the range of light used for the process. AQE determines the efficiency of the photocatalyst depending on the specific wavelength of light. The overall photocatalytic procedure was analogous to the regular experiment, but with slight modification regarding the source of light and the reaction vessel (details provided in Subsection 5.7.2.). Monochromatic light at wavelengths in the 300-450 nm range at every 30 nm was applied during separate processes. The highest values of AQE were obtained at the lowest analyzed wavelengths *i.e.* at 300, 330 and 360 nm, reaching the similar level of about 0.18%. As the wavelength of light was increased, the calculated value decreased, which is consistent with the DRS spectrum and what also explains the reduced efficiency of this material under the influence of visible light. In vast majority of reports concerning the use of MOFs for CO_2 photoreduction, the values of AQE are not designated (Table 4.1), especially when HCOOH is recognized as the main product. Among this limited data Hao *et al.* determined AQE value for HCOOH for ML-rich Ir-modified NH_2-UiO-66(Zr) [215]. The authors stated that in solid-liquid environment the photoreduction of CO_2 has reached AQE of 2.51% at λ=420 nm, that is about fourteen times more than herein, considering the best result obtained at both 300 and 330 nm, and even twenty times more when analyzed at the same wavelength. This example exhausts the possibility of direct comparison of the material reported herein. Comparing the AQE values with others can be misleading. Taking into account that not only he products of photoconversion are differing, the overall characteristics of the photocatalytic process are changing. This includes, for example, the type of reaction environment (solid-liquid or solid-gas), various radiation sources (different lamps of varying power) or the methods of product quantification. Therefore, subsequent comparisons will be more general. The order of magnitude of the reported herein AQE was the same or even higher than for pristine or modified UiO-based material reported in the literature [7,8,204,205,207]. AQE of respectively 0.14% and 0.05% at 350 nm and 420 nm were designated for NH_2-UiO-66(Zr) [205] and [204] concerning carbon monoxide generation instead of HCOOH. In the case of NH_2-UiO-66(Zr) with targeted ML deficiency, the AQE of CO generation of 0.9% was reported in [7]. The same work does not provide the information regarding AQE of non-defected structure. The indium-doped NH_2-UiO-66(Zr) obtained by Su *et al.* [207] reached AQE of CO light-driven production reaching 0.21% at λ=420 nm. However, the work misses a deeper insight into finding dependence of defect formation related to the introduction of In and resulting from this change in efficiency of CO_2 photoreduction. Basing on the abovementioned literature positions, it can be deduced that the intentional introduction of defects to MOFs structures is beneficial, especially in terms of boosting the photocatalytic activity towards CO_2 reduction. In general, the increased AQE value accompanies the increased photocatalytic activity and increased content of defects in the structure of MOF, regardless of the photoconversion product.

Co_{dep}-NUiO was also used in stability test, which included five consecutive cycles of CO_2 photoreduction carried out under UV-Vis light irradiation. Sample was washed between the following cycles with fresh portion of the TEOA/MeCN solution to remove any residual HCOOH trapped in the pores of MOF. Significant yield decline of about 53% was observed already after the second process

(Figure 8.15a). From the third cycle the efficiency has stabilized at the level between 22.3 and 24.9 μmol·g^{-1}, which is an even greater decrease compared to the first cycle (almost 70%). To verify the structural stability of photocatalyst XRD was performed (Figure 8.15b). Although no changes in the position of reflexes or the appearance of new ones (indicating the decomposition products of MOF) were observed, their reduced intensity suggests a gradual degradation of the crystal structure. Additionally, decreased S_{BET} value by 32% was also measured compared to the unused sample (Figure 8.15b). This stands in agreement with the probable structure degradation or may indicate the clogging of the pores. Basing on the photoactivity data, the major part of the structural collapse occurs after the first photocatalytic cycle, after that the structure stabilizes at certain level after the third cycle (Figure 8.15a). The TGA analysis showed no significant changes in the thermal stability of the material as the course of the degradation curve was preserved (Figure 8.15c). However, the ratios of the subsequent mass loss stages have changed. The first decrease stage, which was previously related with the moisture and solvents evaporation, was significantly limited. This is consistent with the observed reduced sample specific surface area after the performed series of photocatalysis. In order to determine the ML defects content, conversion of the data to a form dependent from the mass of ZrO_2 was applied as previously. Interestingly, the characteristic deflection point of plot, assigned before to the obtainment of dehydroxylated MOF form, was not visible, which made it impossible to determine ML content. This suggests that during the modification of MOF, the defects are formed close to the surface rather than in the deeper parts of crystal. Therefore, the outer defected segments easily break, probably due to chemical, mechanical or combined mechanism.

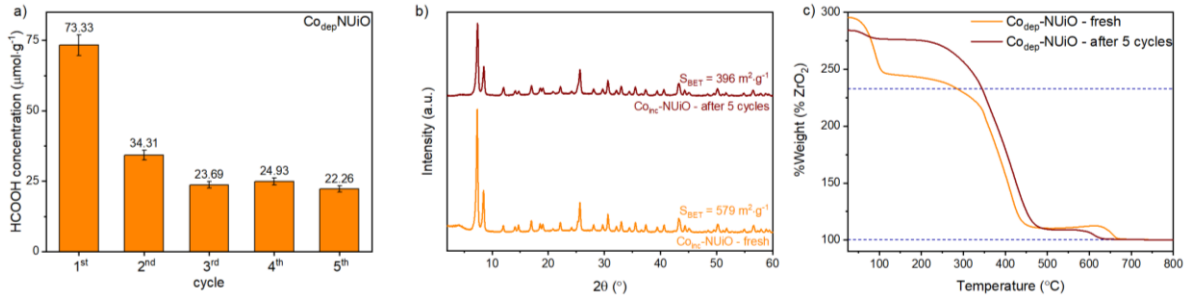


Figure 8.15 Stability test of Co$_{dep}$-NUiO photocatalyst: a) concentration of HCOOH after 4 hours irradiation under UV-Vis (Xe lamp; environment: 10%TEOA/MeCN); b) XRD patterns and S_{BET} values of Co$_{dep}$-NUiO before and after 5 cycles of photocatalytic CO_2 reduction; c) TGA curves of Co$_{dep}$-NUiO before and after 5 cycles of photocatalytic CO_2 reduction

Additional photocatalytic experiment using Cu$_{dep}$-NUiO was performed employing *in situ* DRIFTs for analysis in the gas-solid mode. Intense bands between 2385-2300 cm^{-1} and at 670 cm^{-1} were observed when the sample was purged with CO_2 mixed with N_2 and H_2. Respectively, the signals were recognized as anti-symmetric stretching and bending vibrations of C=O in CO_2 and confirming the adsorption of the gas on MOF. The maxima at 2359 and 2339 cm^{-1} were assigned to the R and P branch transitions originates from the rotational-vibrational coupling [382]. The first several records show rapid growth of bands' intensity when the gas flow was started, with gradual decrease coming after and the final stabilization of spectrum (Figure 8.16a). When the irradiation was applied, steady growth of a small band at about 2209.5 cm^{-1} was observed (Figure 8.16b), suggesting formation of a photoconversion product. Additionally, the signal was vanishing after the thermal treatment confirming its physisorption

on the photocatalyst surface rather than the formation of a strong chemical bond (Figure 8.16c). After resuming the CO_2 photoconversion process, the band appeared again. In order to identify the created product further experiment was carried out employing the use of CO flow through the photocatalyst. Two strong serrated bands at 2170.5 cm^{-1} and 2119.3 cm^{-1}, corresponding respectively to R and P branch transitions of CO [383], were observed immediately after its application (Figure 8.16d). Based on this observations it was concluded that the band appearing at 2209.5 cm^{-1} originated from CO adsorbed on Zr^{4+} sites [384]. The light-driven transformation of CO_2 to CO was also proved by the presence of different intermediates observed (Figure 8.17). In the region between 1700 and 1600 cm^{-1} bands related to the bending vibration of CO_2^- were identified, while in the range of 1600-1200 cm^{-1}, characteristic peaks *i.e.* formate ($HCOO^-$), monodentate carbonate (m-CO_3^{2-}), bidentate carbonate (b-CO_3^{2-}), and hydrocarboxylate (HCO_3^-) were observed [204,385–387].

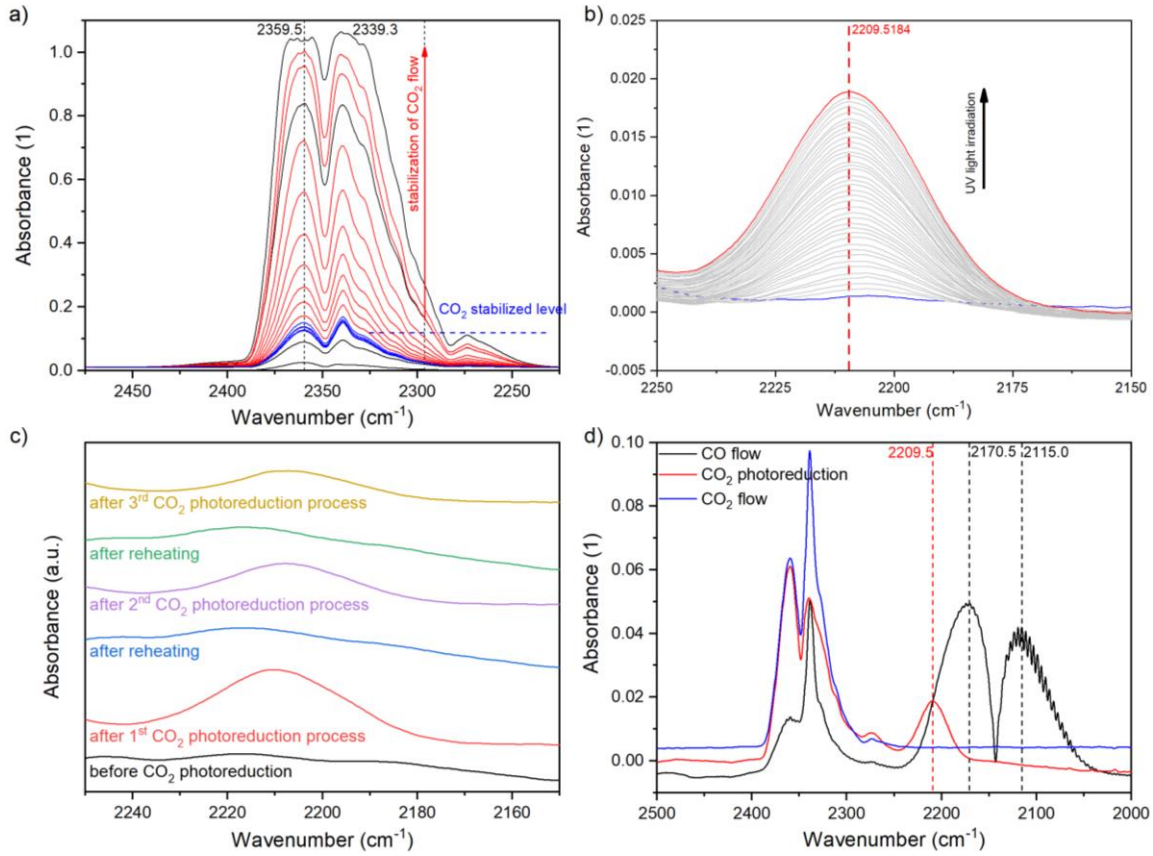


Figure 8.16 In situ DRIFTs spectra recorded for Cu_{dep}-NUiO: a) time-resolved difference spectra of MOF exposed to CO_2 flow; b) time-resolved difference spectra of MOF exposed to UV light and steady CO_2/H_2 flow; c) stability of CO generation during three cycles of photoreduction; d) comparison of spectra during CO flow, CO_2 flow and during CO_2 photoreduction

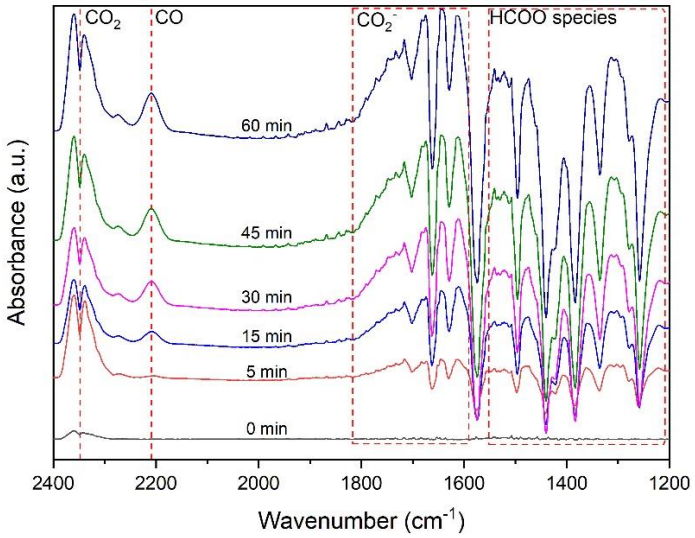


Figure 8.17 Time-resolved In situ DRIFTs spectra of Cu_{dep}-NUiO during gas-solid CO_2 photoconversion

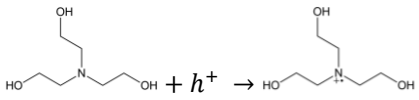
8.4. Mechanism of CO_2 photoreduction

The possible mechanism of the UV-Vis light-driven CO_2 photoconversion to HCOOH in solid-liquid system by NH_2-UiO-66(Zr) and its modified derivative – Co_{dep}-NUiO – was suggested on the basis of the experimental work presented herein as well as taking into consideration the computational part described in details in [12]. At first, the molecules of CO_2 are sorbed by MOF and TEOA. The irradiation with the light from UV-Vis range facilitates generation of the electron-hole pair (Eq. 8). In the non-defected NH_2-UiO-66(Zr), an electron from HOCO located at linker (2.472 V, designated with density functional theory (DFT) [12]) is excited and transferred to LUCO spread mainly over the linker (-0.603 V, designated with DFT [12]), where holes are formed, implying linker-to-linker charge transfer (LLCT). The designated value of LUCO is close to the potential of CO_2 reduction reaction to HCOOH (-0.61 V (*vs.* NHE, pH = 7)). The apparent incompatibility of the calculated value may be due to the approximations used in the modeling (phenomenon explained in detail in [12]). Additionally, the deficiency created in the MOF structure may lead to alternation of the frontiers orbitals [7], what was considered in other calculations by Luna-Triguero and Vicent-Luna, reported in [12].

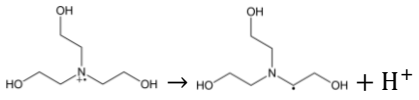
Subsequently, the molecules of CO_2 adsorbed on MOF are reduced by the photogenerated electrons from LUCO to produce $^{\bullet}COO^-$ species (Eq. 9). At the same time TEOA gets oxidized by the created at the beginning hole (Eq. 10). Next, a proton is generated (Eq. 11) as a result of possible structural rearrangement of $TEOA^{\bullet+}$ [388]. It is directly consumed for protonation of $^{\bullet}COO^-$ to give $HCOO^{\bullet}$ (Eq. 12), which is further transformed into HCOOH upon reaction with proton and electron (Eq. 13) [80]. Simultaneously $TEOA^{\bullet}$ radical, being a reactive reductant, reacts with holes from the excited MOF (Eq. 14) leading to the definite decomposition of TEOA, ending with creation of hydroxyacetaldehyde [388] or acetaldehyde [80,389]. Basing on the above description, following reaction equations of the CO_2 photoreduction by NH_2-UiO-66(Zr) can be listed:

$$\mathrm{MOF} + \mathrm{h}\nu \rightarrow h^+ + e^- \qquad \textit{Eq. 8}$$

$$CO_2 + e^- \rightarrow {}^{\bullet}CO_2^- \qquad \textit{Eq. 9}$$



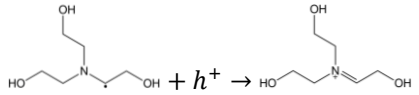
Eq. 10



Eq. 11

$${}^{\bullet}CO_2^- + H^+ \rightarrow HCOO^{\bullet} \qquad \textit{Eq. 12}$$

$$HCOO^{\bullet} + H^+ + e^- \rightarrow HCOOH \qquad \textit{Eq. 13}$$



Eq. 14

According to the DFT studies performed by Luna-Triguero and Vicent-Luna and described in [12], the position of HOCO in Co_{dep}-NUiO shifts. From the primary location at linker it is transferred in the direction of the introduced by photodeposition Co atom and its nearest environment, becoming an important CO_2 adsorption site [390]. LUCO position is changing as well due to introduction of cobalt and extends towards its location. The spread LUCO may contribute two possible pathways of the charge transfer. One of them involves charge transfer from the Zr atom and its closest surroundings to Co atom, indicating possibility of metal-to-metal charge transfer (MMCT) occurrence. Alternatively, linker-to-metal charge transfer (LMCT) characteristic for defected NH_2-UiO-66 [7] may be facilitated to impede the e^--h^+ recombination rate. Two potential pathways of charge transfer improve the efficiency of the photocatalyst as the closest to cobalt Zr atom in Zr-O cluster loses its charge in favor of Co [12]. Creation of defect state in d orbital of Zr related to the missing-linker deficiency was indicated in the literature to improve the LMCT pathway [7]. It is consistent with the fact that, Cu_{dep}-NUiO and Co_{dep}-NUiO which yielded the highest amount of formic acid, at the same time possessed the highest number of ML and balanced content of MC compared to the pristine sample. This also highlights the importance of selecting the proper non-noble metal, which has been shown to be substantial in terms of the type of defect created, and of the resulting photocatalytic activity itself as shown on the example of Ni_{dep}-NUiO. The mentioned sample possessed highest content of missing cluster defects, while the decay time designated with PL lifetime analysis (Figure 8.12) suggested elongated lifetime of the electron-hole pairs. Even though, the defectivity was found to be crucial in terms of photocatalytic activity (Figure 8.14), the amount of the introduced metal was also indicated as important. In the case of Ni_{dep}-NUiO, the content of the modifying metal was an order of magnitude lower in comparison with the values designated for Cu_{dep}-NUiO and Co_{dep}-NUiO (Figure 8.1e,f,g, Table 8.3). Most positions in the literature focuses on the influence of structural defectivity on photocatalytic activity of MOFs in gas-solid photoconversion system. Most often, the missing linker defects turned out to have an even greater impact on photocatalytic activity than herein [7,273]. This indicates that the induction of structural

defectivity in terms of photocatalytic properties should be evaluated more carefully and in more detail regarding the specific types of defects and their relative content.

8.5. Summary

This part of study provides an insight into possibility of UiO-66(Zr) and NH_2-UiO-66(Zr) MOFs modification with three different non-noble metals (Cu, Co, Ni) with two different methods – synthetical and post-synthetical. The amount of introduced structural defects in correlation with metal type and introduction method were evaluated regarding the photocatalytic capability of the obtained materials towards CO_2 reduction. It was established that the highest efficiency of 73.33 $\mu mol \cdot g^{-1}$ formic acid produced was reached by NH_2-UiO-66(Zr) modified by photodeposition of cobalt. There was no effect of CO_2 sorption capacity on the material's ability to reduce it under light irradiation. Compared to the unmodified MOFs, the presence of non-noble metal complexes and the caused defectivity was crucial to improve the photocatalytic efficiency even by 35%. The impact of defects type was assessed by performing quantitative analysis. The sufficiently high content of both missing cluster (relative percentage of about 14 %) and missing linker (0.7-0.9 defects per structural unit) defects was found to boost the photocatalytic performance under UV-Vis irradiation in the case of NH_2-UiO-66(Zr). Compared to the performance under UV-Vis light, under irradiation limited to visible light, the efficiency of two best samples was decreased by about 50%. The most noticeable increase of defects content was observed for both NH_2-UiO-66(Zr) and UiO-66(Zr) after the photodeposition of nickel. Respectively the content of missing-cluster defects content was increased by almost 18 % and 19.5 %, however at the same time the efficiency of photocatalytic CO_2 reduction under UV-Vis light was decreased by 13.7 and 19.6 $\mu mol \cdot g^{-1}$, respectively, in comparison with pristine materials. Even though, the sufficient stability of the crystal structure was determined after five consecutive cycles of CO_2 photoconversion, the yield of the process was diminished by 70% compared to first use of the sample.

The performed cooperation joint studies, including the computational modeling helped to confirm, that introduction of Co by photodeposition on NH_2-UiO-66(Zr) structure can preferentially modify its electronic structure. The change of HOCO and LUCO location and value, as well as introduction of new adsorption sites for CO_2, were found important aspects of boosting MOFs ability to reduce CO_2 under light irradiation. The additional research conducted by the modelling team also allowed to conclude that the functional groups in MOF structure contribute bonding of non-noble metal with metal cluster and linker, and thus generating additional pathway of charge transfer between zirconium and cobalt – MMCT.

Even though the selected method of modification was found successful in the case of boosting the photocatalytic abilities of NH_2-UiO-66(Zr) in the range of UV-Vis light, the same effect was not observed regarding the efficiency under visible light. In the case of most samples, the yield of CO_2 photoreduction was comparable or lower than for the unmodified material, except of one sample. Therefore, another approach of modification was indicated as potential solution for this problem, *i.e.* creation of the MOF-MOF composite and attempt of its additional modification with the use of IL.

9. UiO-67(Zr)-NH_2-MIL-125(Ti) composites modified with ionic liquid for CO_2 photoreduction

Five pathways were investigated to receive the MOF-MOF composites consisting of UiO-67(Zr) acting as a carrier for NH_2-MIL-125(Ti). Four of the materials were obtained by introducing [EMIM][Cl] during synthetical (**1**, **3**), mid-synthetical (**2**) or post-synthetical (**5**) approaches. Material **5** was obtained on the basis of material **4**, not modified with IL. When introducing the IL to the synthesis medium of UiO-67(Zr) (sample **1**) and NH_2-MIL-125(Ti) (sample **3**) molar ratio of metal precursor ($ZrCl_4$ or TTIP, respectively) to [EMIM][Cl] was equal to 1:0.25. In the case of **2** and **5,** 10% w/w of IL in relation to solid MOF mass was used for impregnation to prevent the probability of pore clogging of the resulting structure. Light yellow powders, indistinguishable to the naked eye, were obtained after all five attempts of the MOF-MOF composites synthesis. Graphical representation of the experimental pathways is shown in Figure 9.1.

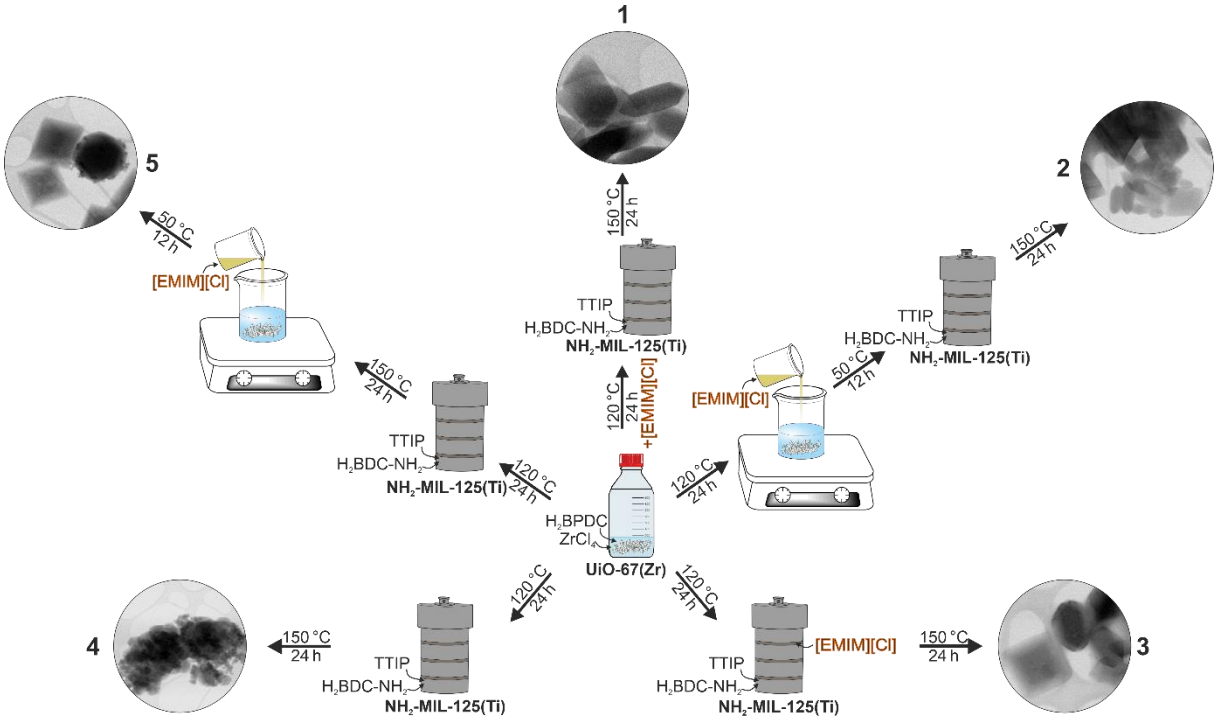


Figure 9.1 Schematical representation of five different MOF-MOF composite materials synthesis pathways.

9.1. Structure of the MOF-MOF composites

The morphology of the obtained pristine MOFs and combined materials was examined by the SEM and TEM techniques (Figure 9.2). Characteristic shape of octahedrons was acquired for both MOFs when synthesized independently. The measured particles of UiO-67(Zr) were 0.45-0.58 μm wide and 0.80-0.86 μm high, while NH_2-MIL-125(Ti) octahedrons were 0.62-0.75 μm wide and 0.97-1.09 μm high.

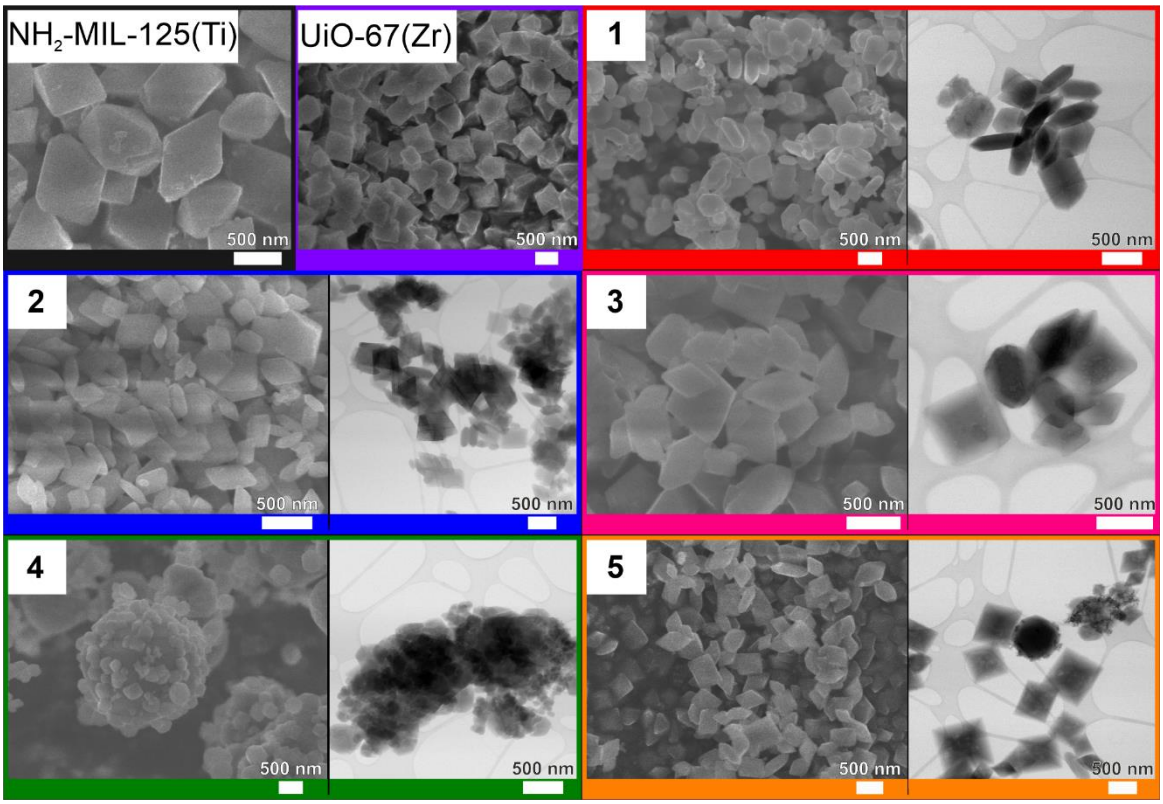


*Figure 9.2 SEM and TEM micrographs of the obtained materials: NH_2-MIL-125(Ti) (black bar), UiO-67(Zr) (violet bar), **1** (red bar), **2** (blue bar), **3** (pink bar), **4** (green bar), **5** (orange bar). In the case of MOF-MOF composites, the SEM images are on the left side, while TEMs are on the right side.*

Different morphologies can be observed among the obtained the MOF-MOF composite. In the case of **4** (for which [EMIM][Cl] was not used), presence of intergrown crystals of UiO-67(Zr) and NH_2-MIL-125(Ti) was revealed (Figure 9.2_**4**). Elemental mapping (Figure 9.3_**4**) and line scanning spectra collected with TEM-EDX (Figure 9.4) clearly confirm, that the obtained structures, being about the size of 2.5 μm (almost 3 times higher than for pristine sample), consist of the inner UiO-67(Zr) octahedron and finer crystals of NH_2-MIL-125(Ti) (0.35-0.50 μm) covering its surface. Interestingly, the deposited NH_2-MIL-125(Ti) crystals are approx. two-three times smaller in comparison with the pristine MOF. These specific structures, however, are not visible in the case of sample **5**, which was created basing on **4**, by simple impregnation with IL. The content of the elements of both MOFs was confirmed by performing TEM-EDX in several areas of each sample (Table 9.1). In the case of **5**, single octahedrons of 0.35-0.50 μm size and mainly containing Ti can be clearly observed (Figure 9.2_**5**). This indicates that probably the unchanged NH_2-MIL-125(Ti) crystals detached from the UiO-67(Zr) surface. In turn, zirconium was detected mainly in crystals with the form of rounded octahedrons of about 0.7-0.8 μm size (TEM micrograph in Figure 9.2_**5**, Figure 9.3_**5**). Such change may indicate that during impregnation with the ionic liquid partial dissolution of UiO-67(Zr) takes place, and thus NH_2-MIL-125(Ti) octahedrons are detaching from its surface.

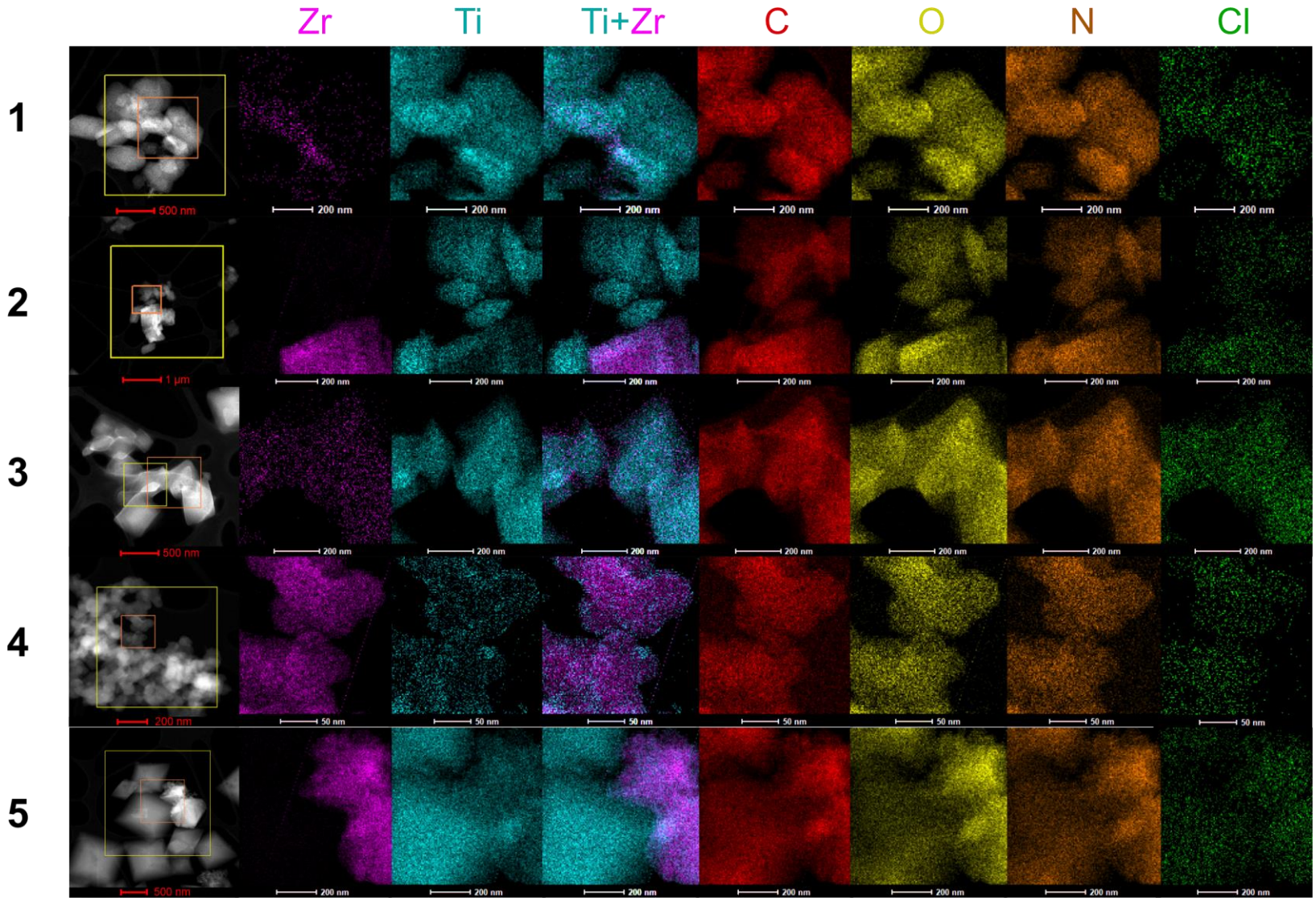


*Figure 9.3 STEM images and elemental mapping of MOF-MOF composites **1-5***

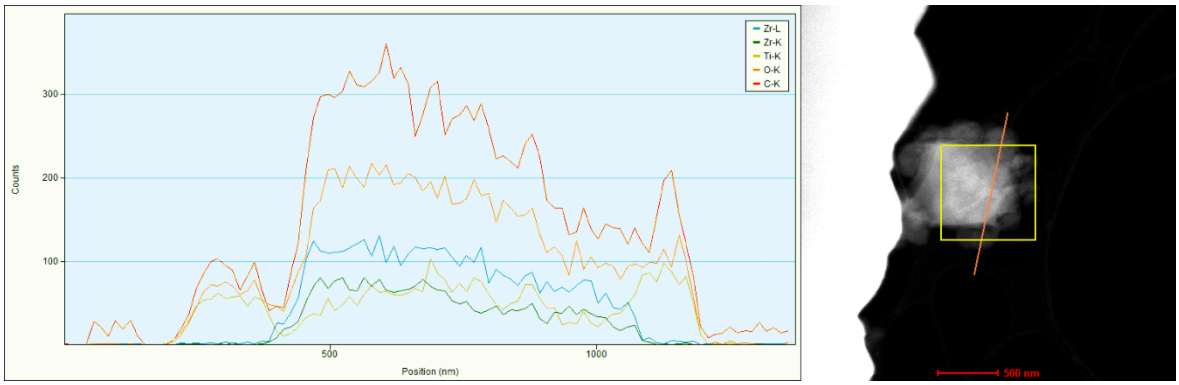


*Figure 9.4 Line scanning spectra of elements distribution in **4***

Table 9.1 Atomic content of elements in MOF-MOF composites designated by TEM-EDX

Sample label	Area	Atomic content (%)					
		C	N	O	Cl	Ti	Zr
1	1	71.18	6.56	18.74	0.00	3.50	0.00
	2	69.71	5.46	19.91	0.05	4.66	0.19
2	1	77.65	5.63	13.91	0.03	1.51	1.24
	2	78.79	1.67	16.65	0.02	0.76	2.08
3	1	60.94	7.27	25.63	0.57	2.33	0.23
	2	59.49	10.80	25.57	0.45	3.67	0.00
4	1	71.04	4.43	20.12	0.00	0.29	4.09
	2	64.88	5.40	24.75	0.01	0.37	4.57
5	1	75.52	4.11	11.46	0.00	8.90	0.00
	2	61.45	7.48	24.83	0.07	1.99	4.15

The imaging of **1** and **2** revealed creation of octahedrons, like in the case of the pristine samples. However, their sizes were reduced in comparison with both single MOFs (mainly height of about 0.52-0.67 μm and width of about 0.33-0.50 μm, but the presence of fraction of about 0.12-0.25 μm in size can be also distinguished). Elemental mapping (Figure 9.3_**1-2**) revealed that zirconium and titanium occur separately in both samples and no evidence of MOFs fusion can be found (no visible aggregated structures disclosed). Very low content of Zr in **1** was disclosed by TEM-EDX (Table 9.1). Additionally, for both **1** and **2**, the particles in the shape of truncated octahedrons (0.55-0.80 μm wide, 0.2-0.3 μm high) were revealed. Probably, the truncated structures are NH_2-MIL-125(Ti) crystals with exposed {001} facets. According to the literature such structures can be created when changes in the composition of the reaction environment are introduced [321]. Herein, IL-decorated UiO-67(Zr) (synthetically or post-synthetically, respectively for **1** and **2**) was introduced to the reaction medium. The IL could desorb from Zr-based MOF surface when introduced to the liquid environment of the Ti-MOF synthesis, and then get adsorbed on the growing crystals of NH_2-MIL-125(Ti). The IL chains could then act as a structure directing agent, blocking the growth of {111} facets and exposing {001} facets [391]. In the case of **3**, the elemental mapping shows that Zr and Ti are relatively evenly distributed in the created crystallites. The observed octahedral structures significantly vary in sizes (Figure 9.2_**3**). Their height varies greatly between about 0.1 and 0.8 μm, thus makes some fraction of them several times smaller compared to pristine MOFs. This suggests size-controlling effect of [EMIM][Cl] when added to the synthesis environment of NH_2-MIL-125(Ti). Presence of IL may influence the viscosity of the synthesis environment [149], which impedes the movement of the forming particles and thus

prevents the aggregation and subsequently confines the size of the MOF. [EMIM][Cl] may also play the role of a capping agent [352] *i.e.* adsorb at the edges of the growing crystals and block their further expansion.

Figure 9.5a shows the PXRD patterns of the obtained samples of pristine UiO-67(Zr) and NH_2-MIL-125(Ti) as well as the MOF-MOF composites. Location of reflexes of the pure MOFs are corresponding to the literature data [392,393], confirming creation of both MOFs for all synthetic pathways with no by-products. Basing on the relative intensity of reflexes, it can be stated that the content of individual MOFs was varying among samples – the content of UiO-67(Zr) was decreasing with the following order **4** (unmodified)>**3**>**2**>**5**>**1**. NH_2-MIL-125(Ti) can be distinguished by the presence of a single peak at about 6.8°, clearly indicating presence of (101) plane, and two overlapping signals at about 9.4° and 9.6°, which can be assigned to (200) and (002) planes, while the next reflex at 11.6° corresponds to plane (211). In the case of **4**, the highest reflex characteristic for NH_2-MIL-125(Ti) is probably overlapping with the signal characteristic for UiO-67(Zr) *i.e.* corresponding to the plane (020) at 6.6° (Figure 9.5b). However, other reflexes are distinguishable, for example at 16.6° and 17.9° corresponding to the (222) and (312) planes, respectively. Presence of UiO-67 can be indicated by the presence of the reflex at 5.7°, characteristic for the (111) plane, clearly visible for **3** and **4**. For **1, 2** and **5** only faint outline of this reflex can be observed. In the case of these three samples, other reflexes characteristic for UiO-67(Zr), which are much lower in intensity than the reflex attributed to the (111) plane, are not visible or overlap with the signals characteristic for NH_2-MIL-125(Ti). It can suggest creation of MOF-MOF composites [233]. Additionally, as it was already indicated by several researchers, introduction of ILs to MOF structure, both synthetically [299] and post-synthetically [307,394], may decrease the intensity of the reflexes appearing on the PXRD spectrum.

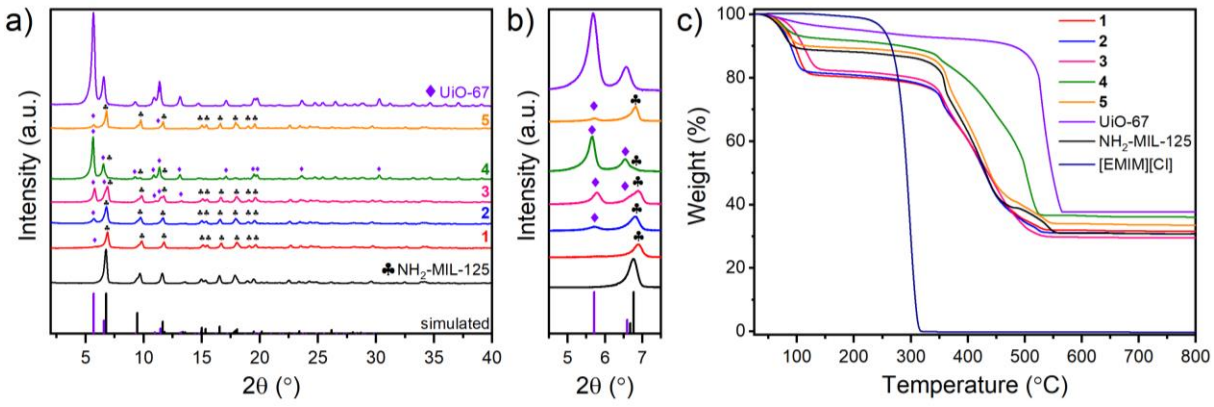


Figure 9.5 a) Full range and b) magnification of PXRD patterns of the obtained MOFs and composites; c) TGA curves of the obtained MOFs and composites.

The varying composition of the as-obtained materials stands in agreement with the TGA results (Figure 9.5c). The degradation of single MOFs begins at approximately 350 °C for NH_2-MIL-125(Ti) and at around 500 °C for UiO-67(Zr) as can be seen for **4** as two separate deflections. In the case of the IL-modified MOF-MOF composites the course of curves is more similar to the curve of pure NH_2-MIL-125(Ti) what is consistent with the XRD patterns, elucidating the role of IL in

creating MOF-MOF composites. The slightly lower temperature of decomposition may also be related to the lower crystallinity of the samples in comparison with pristine MOFs [395]. For all samples the initial mass loss at around 100-150 °C was observed, which can be related to adsorbed moisture and residual methanol evaporation. It has to be underlined that specific degradation step related to IL was not observed for any sample. The maintaining thermal stability after introduction of ILs illustrates its successful integration with the MOF-MOF composite structure [307].

The spectra recorded by *in situ* DRIFTS confirmed vibration of bonds characteristic for both MOFs in the obtained materials (Figure 9.6). Measurements were carried out at 150 °C to eliminate bands originating from adsorbed water or methanol residues present in the MOF pores. Regardless of the synthesis method, the presence of a signal at about 3665 cm^{-1}, indicates successful creation of the MOF-MOF composite. It was created by overlapping two separate bands, originally located at 3655 cm^{-1} and 3670 cm^{-1}. Both bands are related to the stretching vibrations of μ_2-OH and μ_3-OH in the metallic nodes of NH_2-MIL-125(Ti) [396] and UiO-67(Zr) [397], respectively. This overlap is the most pronounced for **1**, **2** and **5**. Apart from that, bands corresponding to individual MOFs structure were exposed, regardless of the synthesis method. Two signals located in close proximity, at 3515 cm^{-1} and 3380 cm^{-1}, can be clearly assigned to the titanium MOF. Their presence refers to the asymmetric and symmetric stretching vibrations of amino group attached to the linker [396]. In the 1800-1000 cm^{-1} region, typical bands associated with both linkers present in the samples were observed. Among them, bands at 1540 cm^{-1} (stretching mode) and 1435 cm^{-1} (bending mode), as well as at 1590 cm^{-1} (stretching mode) correspond to the vibrations of the carboxylic groups respectively of NH_2-MIL-125(Ti) [398] and UiO-67(Zr) [399]. Vibrations of N-H and C-N bands can be also observed at 1625 cm^{-1} (bending mode) and 1255 cm^{-1} (stretching mode), respectively [398,400]. The linkage of metals – titanium and zirconium – with oxygen is represented by signals in the range of 800-650 cm^{-1} [398,399]. The bands associated with [EMIM][Cl] are not visible for samples **1**, **2**, **3** and **5,** as they may overlap with the bands characteristic for both MOFs. The intensity of bands related to IL may be also indistinguishable due to the fact that only a small amount of it was added.

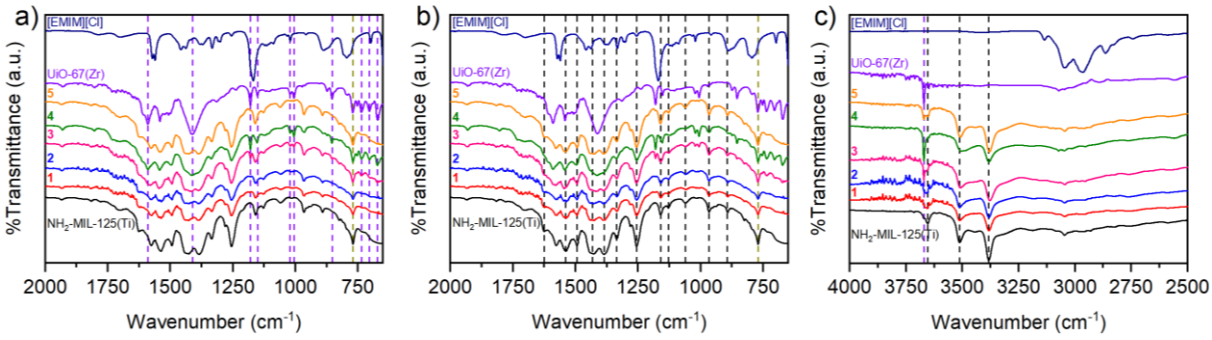


Figure 9.6 Close-up of different ranges of in situ DRIFTS spectra of obtained materials: a) 2000-650 cm^{-1} with marked bands referring to UiO-67(Zr), b) 2000-650 cm^{-1} with marked bands referring to NH_2-MIL-125(Ti), c) 4000-3150 cm^{-1} with marked bands referring to both pristine MOFs.

9.2. Sorption properties

To further explore the properties of the obtained MOF-MOF composites and get deeper insight into IL influence on their structures, N_2 and CO_2 adsorption studies were performed (full isotherms are depicted in Figure 9.7). The specific surface area (S_{BET}) of parent MOFs reached 2170 $m^2 \cdot g^{-1}$ and 1254 $m^2 \cdot g^{-1}$, respectively for UiO-67(Zr) and NH_2-MIL-125(Ti). All obtained samples, including parent MOFs, had microporous structure and almost all MOF-MOF composites are characterized by the S_{BET} lower than both pristine MOFs (Figure 9.2). The course of pore size distribution curve designated with Hovarth-Kawazoe (H-K) method (Figure 9.8) revealed existence of two maxima at about 0.55 and 0.75 nm, characteristic for NH_2-MIL-125(Ti) and UiO-67(Zr), respectively. This confirms, that no new kind of structure was formed and both MOFs are characterized with their original structure. Among MOF-MOF composites, the highest S_{BET} can be observed for **4**, presumably due to the most pronounced structure UiO-67(Zr), as evidenced by PXRD, as well as this may also be due to the lack of ionic liquid added to the structure. In this case, however, particles have a form of aggregates (Figure 9.2), which can explain the lowered value of S_{BET} in comparison to the pristine sample. The MOF-MOF structures obtained by Elsaidi and co-workers [158] were characterized by specific surface within the range of values between both parent MOFs similarly to **4**. For example, SIFSIX-3-Ni@SIFSIX-1-Cu material reached the S_{BET} of 748 $m^2 \cdot g^{-1}$ while the separate structures – 356 and 1294 $m^2 \cdot g^{-1}$, respectively.

Table 9.2 BET surface area, porosity characterization and CO_2 sorption capacity of the obtained materials.

Entry	S_{BET} ($m^2 \cdot g^{-1}$)	Total pore volume[(a)] ($cm^3 \cdot g^{-1}$)	Micropore Surface Area ($m^2 \cdot g^{-1}$) T-Plot	Micropore volume ($cm^3 \cdot g^{-1}$) T-Plot	Dominating pore sizes[(b)] (nm)	CO_2 sorption capacity ($mmol \cdot g^{-1}$)		Average heat of CO_2 adsorption ($kJ \cdot mol^{-1}$)
						At 0 °C	At 25 °C	
UiO-67(Zr)	2170	0.88	2146	0.83	0.7-0.8	2.63	1.55	20.90
NH_2-MIL-125(Ti)	1254	0.58	1189	0.46	0.55-0.60	4.71	2.61	23.04
1	1020	0.64	928	0.37	0.45-0.6	3.87	2.24	22.41
2	1087	0.56	958	0.37	0.45-0.6	3.78	2.21	22.22
3	1168	0.61	1083	0.42	0.55-0.60; 0.7-0.8	3.67	2.04	24.60
4	1283	0.59	1238	0.49	0.55-0.60; 0.7-0.8	2.69	1.60	21.05
5	950	0.50	864	0.34	0.55-0.60	3.71	2.12	22.71

[(a)] Measured at P/P_0=0.990, for pore size diameter < 195.6 nm; [(b)] designated with Hovarth-Kawazoe method

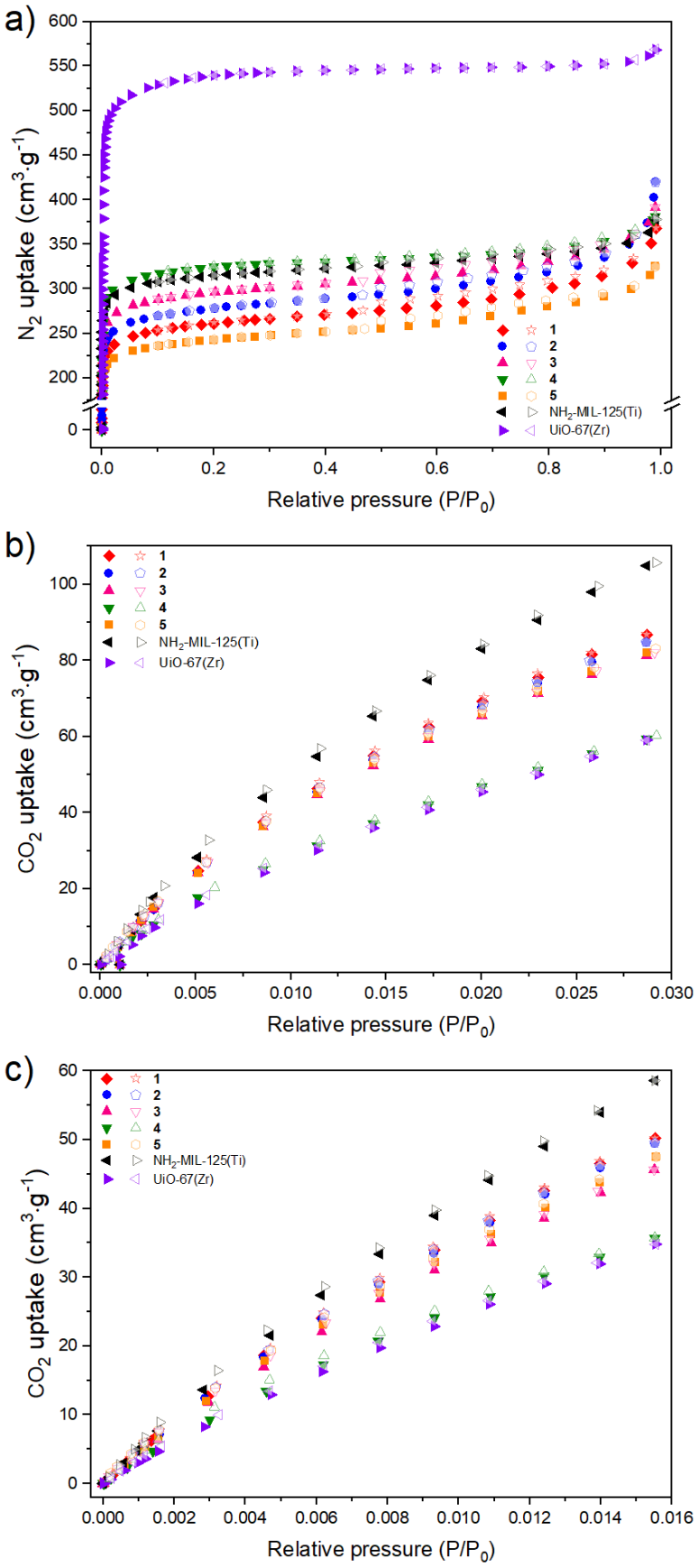


Figure 9.7 N_2 and CO_2 Adsorption isotherms of: a) N_2 at -196 °C, b) CO_2 at 0 °C, c) CO_2 at 25 °C,

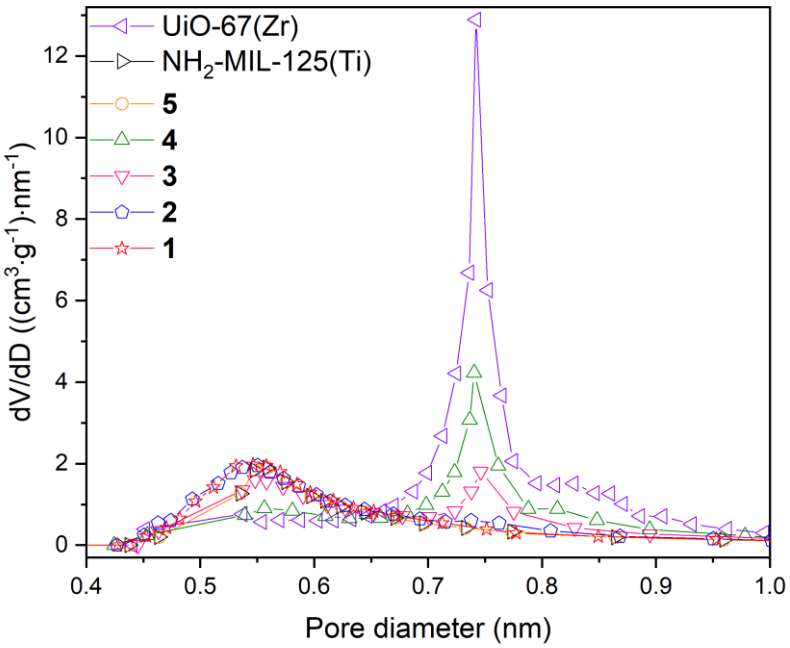


Figure 9.8 Pore size distribution profile designated by H-K method

The addition of IL into the MOF-MOF structure has further decreased the S_{BET}, while the lowest value was registered for post-synthetically modified sample **5**. As mentioned in the PXRD results discussion, IL addition caused crystallinity loss which has direct effect on S_{BET}. The another effect of IL on the MOF-MOF composites structure can be the pore clogging, evidenced by lowered micropore surface area. In the case of **5** (post-synthetical modification) and **2** (mid-synthetical modification, which in a sense can be also described as post-synthetical modification in relation to UiO-67(Zr)), the value of S_{BET} of as obtained samples is consistent with the literature. For example, Sezginel *et al.* reported that impregnation of Cu-BTC with increasing amount of 1-butyl-3-methylimidazolium tetrafluoroborate [BMIM][BF_4], *i.e.* 5, 20 and 30 wt%, was leading to progressively decreasing value of the S_{BET} in comparison with the unmodified MOF by respectively 10, 47 and 82%, as the introduced IL occupied the pores of MOF [300]. Analogous observations were also presented by Xia and co-workers for UiO-66 and NU-1000 impregnated with 5, 10 and 30 wt% of 1-ethyl-3-methylimidazolium glycinate [EMIM][Gly] [307]. For both MOFs, post-synthetical introduction of [EMIM][Gly] effected in S_{BET} decreased by about 27 and 42%, when 5 and 10 wt% was applied, and by nearly 80 and 90% for UiO-66 and NU-1000 when 30 wt% of IL was used.

A limited number of works regarding small amounts of ILs application as modulators in the MOF synthesis can be found in the literature. Usually ILs constitute the main part of the reaction environment in pathways like ionothermal synthesis [88,313], emulsion synthesis [149,150] or electrochemical synthesis [84,85], it is hard to find straightforward**.** One of the very few reference points for results obtained for **1** and **3**, is the addition of 1-(3-Aminopropyl)-3-(2-bromoethyl)imidazole [NAIM][Br] to the synthesis environment of ZIF-67 (molar ratio of components n_{linker}:$n_{metal\ salt}$:n_{IL} = 40:10:1). It have effected in negligible decrease of S_{BET} (about 0.5% in comparison with non-modified sample) with the simultaneous diminishing of the average pore size

from 1.67 to 1.53 nm [299], explained as an effect of complexation of amino groups of IL by cobalt ions leading to settlement of IL on the surface of MOF. It is in a way similar to herein reported **3**, which is characterized by surface area lower by 7% than the NH_2-MIL-125(Ti) (to synthesis of which, the IL was added).

A different trend than in the case of specific surface can be observed considering the CO_2 sorption capacity measured at 25 °C and 0 °C. Herein, all IL-mediated MOF-MOF structures are characterized with comparable values at both temperatures. The measured CO_2 uptake for IL-modified MOF-MOF composites are not close to any of the pristine MOF, but are placed approximately halfway between them. It means, therefore, that compared with pristine UiO-67(Zr), the values of CO_2 uptake increased by about 40-50% (at 0 °C) and 30-15% (at 25 °C). The exception is **4** (sample without IL addition), which shows the comparable with UiO-67(Zr), further supporting the domination of this component in the obtained structure. It is worth underlining, that this is the first work utilizing IL *via* either synthetical, post- or mid-synthetical way in the combined MOF-MOF material synthesis procedure. Therefore, a direct comparison of the literature data to the materials reported in this work is impossible. However, a number of the MOF-MOF composites were obtained without employing ILs and characterized in terms of the CO_2 adsorption. Similarly to the aforementioned S_{BET} value of the SIFSIX-3-Ni@SIFSIX-1-Cu, the value of CO_2 uptake at 1 bar, 25 °C reached intermediate value in relation to the pristine MOFs (2.9 $mmol \cdot g^{-1}$ for SIFSIX-3-Ni *vs.* 4.9 $mmol \cdot g^{-1}$ SIFSIX-1-Cu *vs.* 3.9 $mmol \cdot g^{-1}$ for MOF-MOF composite material) [158]. Interestingly, in the same conditions, the analogous SIFSIX-3-Ni@HKUST-1 have shown better sorption performance than both parent MOFs (increase by nearly 54% and 11% in comparison with pristine SIFSIX-3-Ni and HKUST-1 respectively). Yu *et al.* have obtained NH_2-MIL-125@NTU-9 characterized by the level of CO_2 sorption capacity at 25 °C slightly exceeding pristine NTU-9 (increase from 0.63 $mmol \cdot g^{-1}$ to 0.79-1.02 $mmol \cdot g^{-1}$, growing with decreasing NTU-9 content), but still remaining lower than 50% of CO_2 uptake measured for NH_2-MIL-125 [233]. In turn, in the case of single MOFs subjected to an impregnation with ILs, next to the decreasing S_{BET}, decreasing affinity to CO_2 adsorption was observed as well, especially with the increasing content of introduced IL [300,307]. However, in other cases, the sorption capacity was revealed to increase only in a limited pressure range, especially at lower pressures, especially below 1 bar [296,305].

For all samples, the heat of adsorption (HoA) was designated by using Clausius-Clapeyron equation for CO_2 adsorption isotherms at 0 and 25 °C fitted with Single-site Langmuir-Freundlich model (SLF) (fitting parameters available in Table 9.3). The values of HoA have decreased within the range of adsorbed CO_2 quantity from 0 to about 40 $cm^3 \cdot g^{-1}$ (Figure 9.9). Of the two analyzed pristine MOFs, NH_2-MIL-125(Ti) was characterized with higher mean value of HoA by about 2 $kJ \cdot mol^{-1}$. Additionally, it was characterized by sharp decrease of the curve in the range of 0-20 $cm^3 \cdot g^{-1}$ which then stabilized at about 23 $kJ \cdot mol^{-1}$. As for UiO-67(Zr), despite its initial high HoA (about 28 $kJ \cdot mol^{-1}$), even sharper decrease was noticed, where HoA stabilized at around 20 $kJ \cdot mol^{-1}$, when the CO_2 quantity adsorbed reached 40 $cm^3 \cdot g^{-1}$. **4** was characterized with HoA trend similar to pristine UiO-67(Zr), which stands in line with the PXRD, revealing it mainly consisted of Zr-based

MOF. Similarly, comparable shape of the HoA curve (as well as its mean value) designated for **1** and **2** recalls characteristics of pristine NH_2-MIL-125(Ti) (as for PXRD). The highest values of HoA in the whore range of adsorbed CO_2 quantity, and thus the highest affinity towards CO_2 adsorption, were observed for **3**. This material was characterized by significant amounts of both MOFs. Exceptional behavior can be also observed for **5,** showing the smallest difference of HoA between extreme points of CO_2 adsorbed quantity (only about 1 $kJ \cdot mol^{-1}$) and also the lack of an upward trend in the ending part of the curve. The above data clearly indicates that presence of NH_2-MIL-125(Ti) is significant in terms of increasing the affinity towards CO_2 adsorption. Interestingly, the highest HoA was calculated for **3**, which according to PXRD has the most balanced composition in terms of both MOFs.

Table 9.3 Single-site Langmuir-Freundlich fitting parameters for pure CO_2 isotherms of the obtained materials at 0 and 25 °C, where Q_{sat} – monolayer saturated adsorption capacity, b – Langmuir constant, c – constant.

Sample label	0 °C			25 °C		
	Q_{sat} ($cm^3 \cdot g^{-1}$)	*b*	*c*	Q_{sat} ($cm^3 \cdot g^{-1}$)	*b*	*c*
UiO-67(Zr)	296.3488	0.247080	0.849125	204.4224	0.204527	0.932585
NH_2-MIL-125(Ti)	302.2881	0.529725	0.941584	270.8891	0.275784	0.970446
1	240.4227	0.565448	0.929816	208.7817	0.316952	0.954778
2	238.2648	0.552451	0.922984	199.6387	0.330008	0.960241
3	217.9690	0.595398	0.909331	187.9080	0.320853	0.950951
4	217.3989	0.375989	0.864392	176.3045	0.254121	0.923560
5	217.1454	0.607981	0.920205	218.8316	0.279097	0.926777

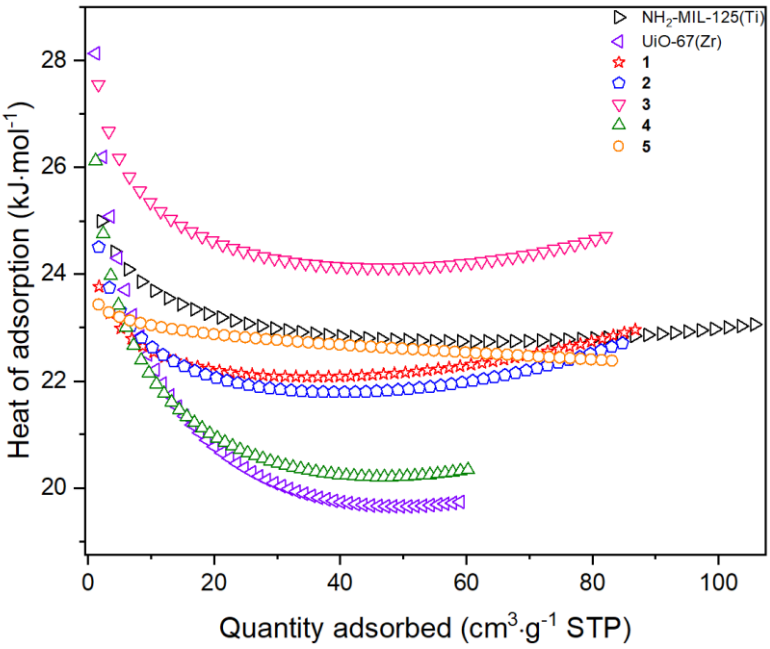


Figure 9.9 Heat of CO_2 adsorption as a function of the amount of the adsorbed gas in the range of 0–110 $cm^3 \cdot g^{-1}$ based on the isotherms collected at 0 and 25 °C (calculated by SLF model) for pristine MOFs and MOF-MOF composites.

All of the prepared samples indicate the photocurrent response under full range of 150 W Xe lamp illumination (Figure 9.10). Immediate growing and dropping current density was recorded for light being respectively turned on and off alternately. As expected, the weakest response for light was observed for pure UiO-67(Zr), while the content of NH_2-MIL-125(Ti) seem to improve the sensitivity of prepared materials. This stands in agreement with the photoluminescence

spectroscopy (Figure 9.11), which revealed much higher PL intensity suggesting very fast recombination of electron-hole pairs regarding pristine UiO-67(Zr) in comparison to any of the MOF-MOF composites. Samples **1**, **4** and **5** have shown similar photocurrent response to the non-modified Ti-MOF, while **3** has shown more pronounced and **2** less pronounced response (Figure 9.10). In the case of **1** this may be due to the fact, that the content of UiO-67(Zr) is relatively the lowest among MOF-MOF composites (confirmed by PXRD), therefore it has no significant impact on this feature.

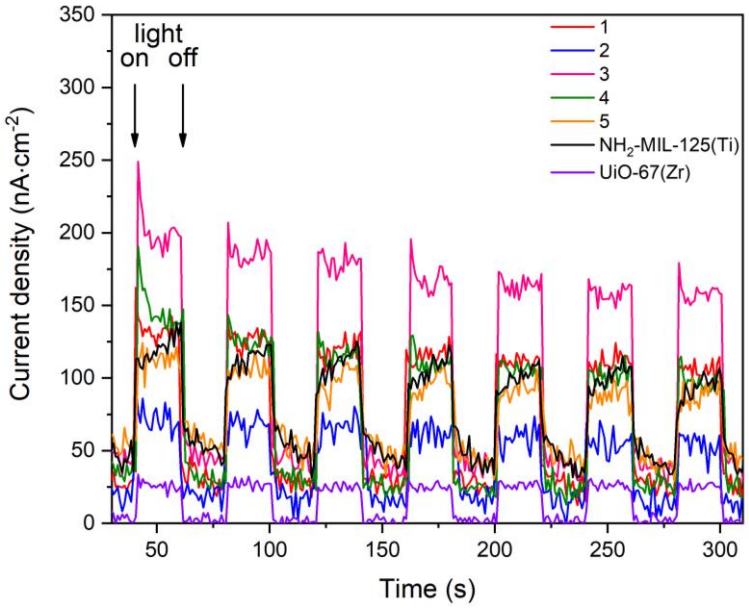


Figure 9.10 Photocurrent response of obtained MOFs and composites.

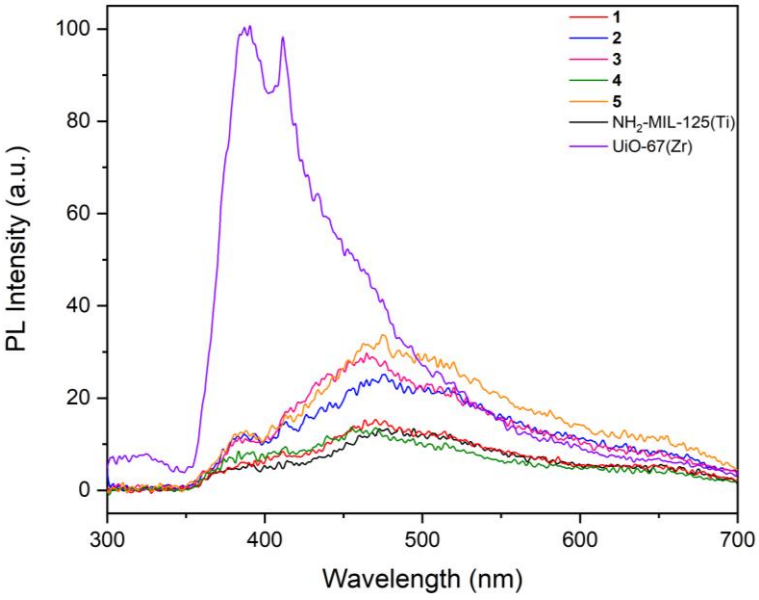


Figure 9.11 PL spectra of parent MOFs and MOF-MOF composites

For **2**, in accordance with elemental mapping (Figure 9.3), revealing presence of separate crystals of both MOFs, the values of induced photocurrents took on intermediate values between both parent MOFs. In turn, sample **3**, in structure of which mutually distributed Ti and Zr elements were mapped, the highest values of the photocurrent density were measured, even though it

contains relatively high amount of UiO-67(Zr) (Figure 9.5a). Such result can be also related to the pathway of its synthesis. In contrast to **1** and **2,** in the case of **3**, [EMIM][Cl] was added to the synthesis environment of NH_2-MIL-125(Ti) separately, not coupled with UiO-67(Zr) in previous steps, which could probably facilitate the formation of combined structure, and thus decrease the recombination of e^--h^+ pairs. Comparing samples **4** and **5,** the another direct positive influence of IL on the optical properties of material can be observed. Although for both, the photocurrent response was similar to NH_2-MIL-125(Ti) (Figure 9.10), for **5** the IL addition caused increased light absorbance by around 30% (Figure 9.12). Overall, **3** and **5**, where IL directly interacted with the NH_2-MIL-125(Ti), were characterized with the most favorable optical properties.

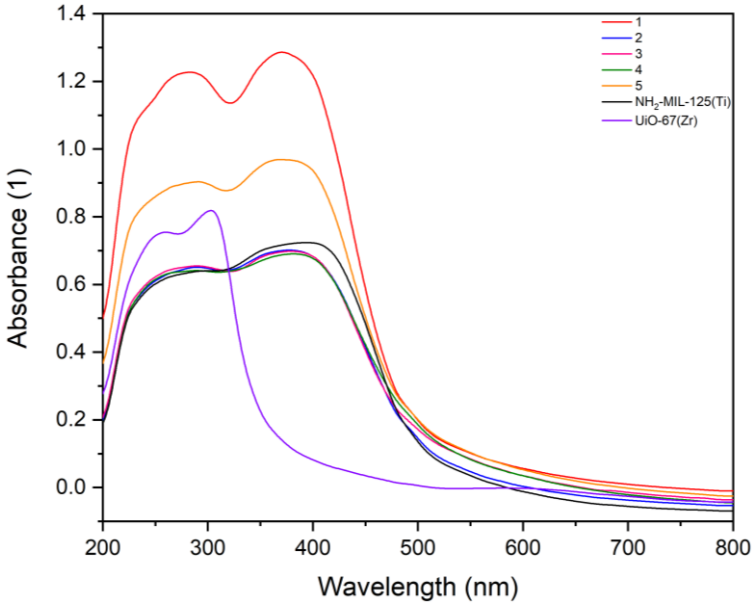


Figure 9.12 DRS spectra of parent MOFs and MOF-MOF composites

9.3. Photocatalytic performance

The effect of the chosen ionic liquid and the method of its introduction to the synthesis procedure of the MOF-MOF composite materials on the ability to convert CO_2 under light illumination was examined. The photocatalytic process was carried out in the solid-liquid system under visible light irradiation, analogously to the procedure described in Chapter 8. Apart from analyzing pure MeCN/TEOA mixture without using MOF for the presence of $HCOO^-$ after light irradiation, the additional experiment with addition of [EMIM][Cl] to the liquid phase was carried out. In this case, no product was also detected as well, confirming that $HCOO^-$ was not originating from the ionic liquid.

Figure 9.13a shows the results of the visible light-driven CO_2 reduction, where the aliquots were sampled every hour during the four hours of process duration. As expected, no formic acid was detected for pristine UiO-67(Zr) under Vis light irradiation, as it absorbs light only up to about 330 nm basing on the DRS spectrum (Figure 9.12). For pristine NH_2-MIL-125(Ti), up to 67.4 $\mu mol \cdot g^{-1}$ of $HCOO^-$ after 4 hours was detected, which corresponds with the results reported previously [80]. Regarding the MOF-MOF composites, the highest amount of formic acid was detected for **5,**

reaching 86.7 μmol·g^{-1} of HCOOH, giving almost 30% of generation improvement in comparison with pristine NH_2-MIL-125(Ti). Similar relative enhancement (about 30%) for this sample was also observed with light absorbance measured by DRS method (Figure 9.12). Interestingly, this sample was characterized by closest values of average HoA to Ti-MOF (about 22.7 and 23 kJ·mol^{-1}, respectively). On the other hand, very poor performance can be observed for other MOF-MOF structures. Even though **1** shows almost doubled light absorption and similar value of the generated photocurrent to the pristine NH_2-MIL-125(Ti) the lowered efficiency by almost 80% was observed. It may be related to the truncated shape of the obtained NH_2-MIL-125(Ti) crystals present in the sample, which was reported to considerably influence the photocatalytic activity [321]. The low efficiency of **2** was expected, as this sample had also the lowest photocurrent density among the MOF-MOF samples and, similarly to **1**, it contains crystals with exposed planes that are not favorable in terms of photocatalytic CO_2 reduction towards formic acid. The low efficiency of **3** and **4** can be attributed to the relatively highest amounts of UiO-67(Zr) among the MOF-MOF composites, even though according to DRS spectra (Figure 9.12), both samples exhibited absorption of the visible light.

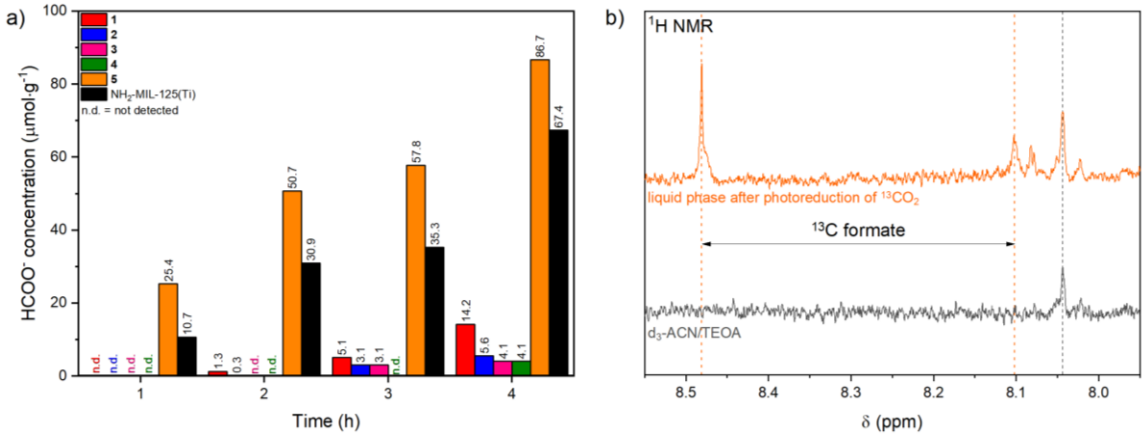


*Figure 9.13 a) Concentration of generated HCOOH under Vis irradiation using as-obtained materials (Xe lamp; environment: 10%TEOA/MeCN). No formic acid was detected for pristine UiO-67(Zr) during experiment (not included on the graph); b) ^{1}H NMR spectra of pure 10%TEOA/d_3-MeCN and of the products obtained via photoconversion under Vis light using $^{13}CO_2$ and **5** (24 hours, Xe lamp; environment: 10%TEOA/d_3-ACN)*

Additionally, in order to evidence the formation of HCOOH from the dosed CO_2 and exclude its other potential sources, experiment with $^{13}CO_2$ was performed. The procedure involved conducting of an experiment analogous to the primary one in the solid-liquid system, exchanging the gas to $^{13}CO_2$ and replacing of acetonitrile with its deuterated form (d_3-MeCN). This enabled the execution of the NMR analysis (Figure 9.13b) by directly sampling an aliquot from the liquid environment. Presence of isotopic H^{13}COO$^-$ created from $^{13}CO_2$ was clearly confirmed by revealing presence of two peaks located at 8.10 ppm and 8.48 ppm [380,381]. Although the presence of a signal at 8.04 ppm may suggest formation of regular H^{12}COOH, the presence of identical signal was detected for pure 10%TEOA/d_3-MeCN, thus it cannot be attributed to the H^{12}COOH.

As presented herein, the literature data confirms that UiO-67(Zr) is photocatalytically inactive in the visible light range and no gaseous or liquid products are observed, when no

modification is performed [401]. Introduction of photosensitizing agent – $Ru(bpy)_3$ – to the liquid environment of reaction arouse the photocatalytic abilities of UiO-67(Zr) to the level of 14.7 $\mu mol \cdot h^{-1} \cdot g^{-1}$ of HCOOH [402]. On the other hand, NH_2-MIL-125(Ti) is widely known for its photocatalytic activity in visible light at similar level (for example, efficiency of 14.65 $\mu mol \cdot h^{-1} \cdot g^{-1}$ of HCOOH was reported by Baluk *et al.* [80]), even without previous modification or introduction of photosensitizers.

In the literature there is very limited data regarding MOF-MOF composites for CO_2 photoreduction (Table 4.1). In one study, Yu *et al.* [233] obtained NH_2-MIL-125@NTU-9 creating a homophase junction, resulting in abundant increase of $HCOO^-$ production under visible light irradiation to reach even up to 72.5 $\mu mol \cdot g^{-1} \cdot h^{-1}$. It gives about a four-fold boost in comparison with the parent MOFs *i.e.* NH_2-MIL-125(Ti) (15.2 $\mu mol \cdot g^{-1} \cdot h^{-1}$ $HCOO^-$) and NTU-9 (19 $\mu mol \cdot g^{-1} \cdot h^{-1}$ $HCOO^-$), another titanium based MOF with 2,5-dihydroxyterephthalic acid acting as linker. Sample **4** corresponding to MOF-MOF composites reported in Yu's work, as it was not modified by IL, achieved very low HCOOH generation efficiency reaching only 1 $\mu mol \cdot g^{-1} \cdot h^{-1}$. However, due to differences in the experimental conditions like higher temperature of the reaction (25 °C), different composition of the liquid environment (60 mL of 5/1 v:v MeCN/TEOA per 50 mg of the sample), longer total time of the process (10 hours), lower lamp power (500 W), these results should not be directly compared. In other study on MOF-MOF composites, CuTCPP⊂UiO-66 (CTU) obtained by Wang and co-workers [234] generated 1.09 $\mu mol \cdot g^{-1} \cdot h^{-1}$ of CO at room temperature in water environment under irradiation with light characterized by wavelength > 300 nm. The structure merges copper-based CuTCPP with tetra(4-carboxylphenyl)porphyrin as linker immobilized on zirconium-based UiO-66 possessing terephthalic acid in its structure. However, creation of such structure only slightly improved the performance comparing with both pristine MOFs *i.e.* from about 0.5 and 1 $\mu mol \cdot g^{-1} \cdot h^{-1}$ of CO for UiO-66 and CuTCPP, respectively. The further combination of CTU with titanium dioxide resulted in nearly 30 times improvement of photocatalytic CO generation in comparison with pure CTU. Although the authors indicate activity in visible light, it should be noted that the wavelength they used includes part of the UV light spectrum, which could have influenced the obtained results.

9.4. Discussion over the possible mechanism of CO_2 photoreduction

The performed experiments do not provide clear explanation of the underlying nature of the observed photocatalytic activity changes in the tested MOF-MOF composites. Thus, the exact role of IL and interactions between MOFs is still unknown, and the possible mechanism presented here is based mostly on the theoretical background. The extensive review published by Pancielejko *et al.* [403], discussing the influence of ILs on the photocatalytic abilities of different semiconductors, clearly indicates that there are several possible mechanisms related to ILs contributing increased photocatalytic activity. Among such considerations, introduction of doping elements, defect surface formation, growth of specific planes, thickness control, surface development or creation of heterojunctions can be listed as examples.

Taking into consideration, that the synthesis pathway of **4** was analogous to **5** (without the additional step of post-synthetic modification), and that the photocatalytic efficiency of **4** was significantly deteriorated (by 95% compared to pristine NH_2-MIL-125(Ti)), the eventual creation of heterojunction or only the presence of NH_2-MIL-125(Ti) could not be treated as the standalone explanation of the performance of **5**. The results of PL showed the spectral intensity of **5** higher than for other MOF-MOF composite structures and NH_2-MIL-125(Ti) MOF alone (Figure 9.11). Additionally, the photogenerated current density was close to the pristine Ti-MOF (Figure 9.10). Both results do not indicate the slowed down recombination of the electron-hole pairs, which suggests the essential role of [EMIM][Cl] in the photocatalytic process. It is likely that the adsorbed on the surface of **5** the ionic liquid affected the interactions between the MOF-MOF surface and the components of the photocatalytic reaction environment [403].

As it was already reported by other researchers, imidazolium-based ILs are not only stable under light irradiation, but also promote activation of CO_2 to radical form [404] *via* gas sorption and creation of a neutral zwitterion [$EMIM^+$-COO^-] [405], which is further released in form of $CO_2^{\bullet-}$. Several different pathways employing varying intermediates were presented in [406], confirming significant role of hydrogen atom at C2 in the imidazolium cation in creation of a reactive site, capable of bonding CO_2, which is possible especially when an electron is donated to the imidazolium cation of IL. (Figure 9.14). Such phenomenon was in particular described for ILs possessing imidazolium cations paired with phenolate or carboxylic anions. According to the theoretical study conducted by Wang *et al.* [406], 1-ethyl-3-methylimidazolium tetrafluoroborate [EMIM][BF_4] may actively take part in the process of CO_2 reduction *via* electrochemical approach. This thus suggests probability that similar interactions may be also contributing in halide-based ILs, as reported herein.

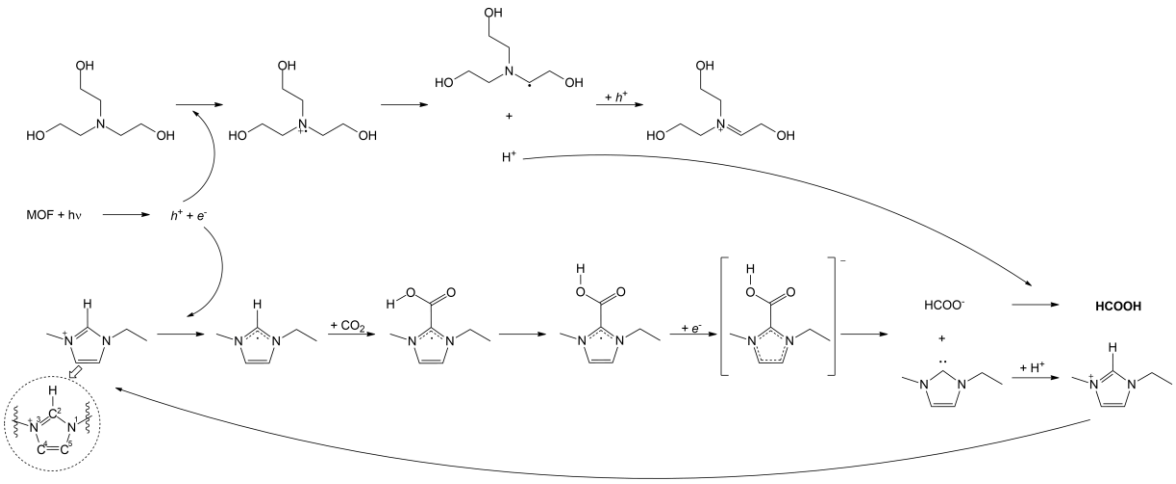


*Figure 9.14 Proposed role of [EMIM][Cl] in the mechanism of CO_2 photoreduction under visible light irradiation using **5** in TEOA/MeCN environment*

Considering the above discussion and the result obtained for **5,** it is possible, that the key importance of the probable explanation of its increased photocatalytic activity may lay in the creation of heterojunction or alternatively, if the heterojunction was not formed – in the nature of NH_2-MIL-125(Ti). Regardless of the actual factor related to the MOF-MOF composite itself, it was concluded

that the IL's presence may play crucial role, which will be speculated herein. The plausible mechanisms for CO_2 photoreduction by pristine NH_2-MIL-125(Ti) was already described in details in previous co-authored work [80]. As it was described by Wang *et al.* [406], it is assumed that [EMIM][Cl] present on the surface of the MOF-MOF composite receives the photogenerated electron from the excited NH_2-MIL-125(Ti) (Figure 9.14). At the same time, the photogenerated hole is captured by the TEOA which, *via* forming intermediates, leads to formation of protons, necessary for the photocatalytic reaction progress [12]. The electron transfer from MOF-MOF composite to imidazolium cation enables attachment of the CO_2 at the active C2 site [406]. Further isomerization of C–OH bond rotation and electron transfer enable a fission, creating imidazolium carbene and carboxylic anion. As the reaction environment is polar (mixture of MeCN and TEOA), it facilitates the creation of $HCOO^-$ as a more favorable photoreduction product than $OCHO^-$ (leading to creation of CO) [407]. In the final step, the proton created by the TEOA is donated to the carboxylate anion, producing formic acid, while the imidazolium cation is restored, presumably by an acidic proton originating from another C2-H of imidazolium ring.

The above discussed possibilities of mechanism routes are only an attempt of theoretical explanation of the of CO_2 light driven reduction by **5** and the extended research (including experimental and computational techniques to verify the above assumptions) should be performed. In the regard of CO_2 photoreduction reaction mechanism, the first matter that should be explored in details is the question of heterojunction formation. It should be verified carefully whether the electronic structure pristine MOFs were jointed and altered in a way that enables the light-driven reduction of CO_2 to HCOOH. It could be indirectly confirmed or negated by performing XPS and Mott-Schottky measurements. Additional support would be electrochemical impedance spectroscopy (EIS), time-resolved PL or electron paramagnetic resonance (EPR). Regardless of the mentioned experiments, it is clear that the presence of IL is the crucial factor that boosts the photocatalytic activity.

9.5. Summary

A new facile and time-efficient approach on synthesis of MOF-MOF composite materials, focusing on utilization of IL as the modifying agent was presented in this research. UiO-67(Zr), MOF inactive under visible light irradiation, was utilized as a substrate for NH_2-MIL-125(Ti) – an effective photocatalyst in these conditions and ionic liquid was introduced to facilitate the creation of MOF-MOF composite. Among four different approaches of [EMIM][Cl] introduction *i.e.* synthetical, mid-synthetical and post-synthetical, the latter – impregnation with IL of material consisting of UiO-67(Zr) and NH_2-MIL-125(Ti) obtained *via* a two-step synthesis – was found the be the most effective method. It resulted in 30% improved photocatalytic ability to reduce CO_2 to HCOOH in comparison with pristine NH_2-MIL-125(Ti) and more than 21-fold increment compared to the unmodified MOF-MOF material. The observed enhancement is corresponding to a similar, ~30% increase in light absorption. Interestingly, based on the experimental evidence, this improvement cannot be assigned to either increased photoinduced generation of electron-hole pairs or increased surface

charge generated during light irradiation. Thus, it is hypothesized that the imidazolium-based IL present on the surface of the MOF-MOF composite structure improves the activity by participation in the CO_2 photoreduction process, boosting the observed NH_2-MIL-125(Ti) photoactivity. However, the actual mechanism for this particular system remains experimentally unverified. Although other strategies (synthetical and mid-synthetical) resulted in lower photocatalytic activity than NH_2-MIL-125(Ti), it has to be underlined that for all created materials the visible light sensitization of UiO-67(Zr) was achieved. Additionally, it was found that the ionic liquid introduced into the synthesis environment acted as a modulator on the developing MOF structure and influenced the shape, size and sorption properties of the forming crystals. Depending on the moment of [EMIM][Cl] introduction it was possible to obtain material characterized by higher CO_2 uptake, higher photocurrent generation or with higher electron-hole pair photogeneration, allowing a kind of material customization. The results of this work show potential of creating efficient photocatalytic materials utilizing simple, cheap and time-efficient modification methods. Application of IL in the MOF synthesis and post-synthetical modifications is still vastly unexplored area and deeper research has to be performed to unveil underlying mechanisms of MOF-IL interactions.

10. Conclusions and future outlook

The literature review gathered in this work clearly demonstrates that metal-organic frameworks are very universal and prone to modification compounds. Firstly, there are multiple possibilities of merging different linker and metal pairs in one structure. What is more, by the adjustment of the synthesis conditions (temperature, solvent, time of reaction), the use of the primarily used precursors can result in obtainment of MOFs with different structural architectures. Secondly, numerous pathways of structural modifications can be taken to adapt MOFs towards different potential applications and the implied conditions of their use. Among others, such modifications can concern the functionalization of linkers or mixing different precursors (either linkers or metals) to boost the chosen characteristic like affinity to specific gas. Additionally, morphology as well as the defectivity of the MOF structure can be influenced by the introduction of different modulators to the synthesis environment e.g., acids, surfactants or ionic liquids. Simultaneously, these materials' characteristics can be influenced post synthesis *via* facile approaches like impregnation, exchange of components or use of the pending functionalities to bind additional moieties. Another pathway also worthy of attention, is combining MOFs with other materials like other MOFs, semiconductors or metals to obtain a derivative that will bear the characteristics of both native materials. Gradual theoretical review into the subject of CO_2 capture, storage and utilization methods, as well as of MOFs and their practical applications, allowed to identify several major research gaps. Firstly, detailed reports concerning the practical application of MOFs in real-life scale are not available. Secondly, the existing research lacks in full-scale and long term load tests regarding the practical use of MOFs (*i.e.* 5 cycles *vs* 5000 cycles). Another aspect is the common consensus that the efficiency of the standalone MOFs is too low for practical use. Thus, very complicated and expensive methods of modifications (*i.e.* introduction of noble metals, complex photosensitizers based on rare elements or use of linkers characterized by sophisticated architecture) are usually employed to boost performance of these materials. In consequence relatively low focus is placed on finding financially and ecologically reasonable methods of MOFs modification that would boost their performance.

To address the last mentioned research gap, the following hypothesis was proposed: MOF properties – especially related to carbon dioxide selective adsorption and its reduction under light illumination – can be tuned by subjecting the material (or the pathway of its synthesis) to different modifications. It was also postulated that depending on the type of modifying agent used, the method of its introduction will have a crucial influence on the final properties of as-obtained MOFs. To verify it, six different MOFs – two copper-based, three zirconium-based and one titanium-based – were selected and subjected to modifications at different stages to improve their CO_2 related characteristics *i.e.* adsorption capacity and ability to reduce it under light irradiation. In order to achieve that, four main tasks were implemented in the research. The synthesis conditions of the first MOF – Cu-TDPAT – were varied in order to determine the influence of different synthesis aspects on the properties of resulting material. The second MOF, namely HKUST-1 was modified using two approaches – synthetical and post-synthetical – by introducing five different ionic liquids

(four of them were amino acid ionic liquids). The sorption properties of resulting materials were characterized. The third task included modification of the two analogous MOFs, *i.e.* UiO-66(Zr) and NH_2-UiO-66(Zr), with three different non-noble metals (Cu, Co, Ni). Two different approaches of these metals introduction were investigated, namely incorporation to the synthesis environment and post-synthetical deposition assisted with the light irradiation (photodeposition). The investigation focused on the aspect of defect engineering and improvement of the photocatalytic performance in light-driven CO_2 reduction. Slightly different approach was applied for the last two MOFs – UiO-67(Zr) and NH_2-MIL-125(Ti). Attempt of merging these two MOFs to obtain a composite was undertaken by simple two-step solvothermal synthesis, which was additionally accompanied by introduction of ionic liquid at four different stages of the binary material synthesis. The influence on the photocatalytic CO_2 reduction was studied to validate the effectiveness and rationale of the chosen modification approach. The implementation of the designated research allowed for the confirmation of both the main and auxiliary hypotheses.

The research described in Chapter 6 validated the influence of seven different factors on the formation of Cu-TDPAT MOF. Among the variating conditions type of solvent, temperature and time of the reaction, presence of modulator, molar ratio of precursors, the type of metal precursor and reaction vessel were utilized in different combinations. Among thirty performed experiments, six did not result in formation of any solid (due to too low temperature, too low concentration of metal precursor or too high concentration of the modulator), while the other twenty four resulted in obtainment of products of varying characteristics. A wide range of pure MOF products was obtained differentiated with specific surface areas in range of several square meters per gram up to values exceeding 2200 $m^2 \cdot g^{-1}$ for DD-95C. For several variants of the chosen synthesis conditions, in addition to the MOF of different crystallinity degree, by-products were also obtained. These experiments demonstrated that the properties of MOFs can be tuned in a facile way and do not require the use of highly complex or energy-intensive approaches, enabling design of tailored products in accordance with the requirements of applications. However, at the same time, results indicate that minor changes in the synthesis environment (especially considering the purity of the precursors and solvents) can disrupt the synthesis process and lead to alterations in the properties of the final product. This especially affects MOFs with more complex linkers or metals more susceptible to various side reactions like the presented Cu-TDPAT. The observed aspects, playing the crucial role in the stability and practical usability of MOFs, could be a viable insight in the context of designing new MOF synthesis or modification routes. Special consideration should be given to source of metal, liquid environment of synthesis as well as the temperature of reaction, as these parameters were found to have the highest impact in the final material properties.

Due to proven complexity of the MOF synthesis process, compounds with simpler structure were therefore chosen to develop a facile and efficient modification method to maximize the structure's performance. Thus, Chapter 7 provided an insight into two methods of ionic liquids introduction into HKUST-1 - synthetical and post-synthetical. As expected, presence of ILs, even of those with relatively small size, did decrease the specific surface area of obtained modified MOFs.

At the same time, the capacity towards CO_2 sorption was significantly improved up to 43% for 0.25[EMIM][Pro]/HKUST-1 compared to bare MOF, when ILs were introduced to the synthesis medium of MOF. More importantly, introduction of IL to the synthesis medium did not disrupt the complicated synthesis process, allowing to obtain pure, CO_2-targeted product characterized by favorable properties in accordance with the assumption. The specific performance of the obtained materials depended on the structure of the selected modifiers *i.e.* on the type of anion and the length of the cation's side chain, as well as on the route of introduction and the selected amount. However, taking into consideration the seriously diminished specific surface area of the IL-modified materials, special attention should be given to the interactions between the structure of MOF and the introduced IL. As the TSILs possess functional groups attractive to water, it should be underlined that side reactions may occur, leading to deterioration of the primary MOF crystal structure.

As the example of utilizing defect engineering route, introduction of three different metals with two approaches to UiO-66(Zr) and its aminated analogue – NH_2-UiO-66(Zr) –was described in Chapter 8. The facile way was successfully implemented, resulting in boosted photocatalytic performance of two samples under UV-Vis light and one under the visible light. The used modification method was found especially beneficial for the second MOF. The key aspects influencing the modification viability were found to be the types of defects introduced, their total and relative content, and also the type of the introduced metal itself. Although the improvement in the photocatalytic properties – even for the best material Co_{dep}-NUiO – was rather moderate (about 35%), it was demonstrated that the structure could be modified using simple methods to achieve it. When intentionally introducing defects, care should be taken to ensure the degree of deficiency not too excessive. Otherwise, the weakened structure can collapse, particularly during cyclic use of the sample, or too many active sites may be removed from the structure (for example open metal sites when missing cluster deficiency is significant).

The other approach of MOFs modification – creation of the MOF-MOF composite in the presence of IL – that was studied in Chapter 9, indicated the importance of coupling the method and moment of introduction of the modifying agent. The relatively efficient standalone photocatalyst for CO_2 reduction – NH_2-MIL-125(Ti) – was deposited on the surface of UiO-67(Zr), which is characterized by poor photocatalytic performance, but at the same time with high specific surface area. Both approaches of IL introduction, synthetical and mid-synthetical, were found to deteriorate the photocatalytic abilities of the obtained materials, when compared to the bare NH_2-MIL-125(Ti). Even though the relative distribution of both MOFs in the resulting composite was the most homogeneous when no IL was used, the yield of photogenerated HCOOH was no higher than the IL-modified composites. Only when sample impregned with IL post synthesis (**5**), was characterized by about 30% increase of photocatalytic yield. Given the limited ability to validate the reaction mechanism – specifically, to conclusively determine whether it stems from the presence of the ionic liquid on the material's surface, the formation of a junction between the MOFs, or a combination of both mechanisms – further research should be conducted to resolve these uncertainties. Apart from that, additional focus should be placed on achieving homogeneous distribution of both IL on the

surface of the composite and different MOFs in the resulting complex structure. Addressing these aspects could be valuable in further optimalization of the resulting composite properties.

The herein presented research clearly indicates that modification of the targeted material properties of MOFs can be achieved with diverse methods, and there is no single method that can be designated the most efficient. Even the simple methods, like impregnation with ionic liquid or introduction of small amounts of additional metals, can significantly change the characteristics of MOFs, confirming the research hypotheses. The presented study addressed specific gaps identified in the literature, which served as the foundation for this work. In conclusion, the hypothesis formulated at the beginning of the research has been confirmed. The results consistently showed that the properties of MOFs like – CO_2 adsorption capacity and photoreduction ability – can be readily alternated by subjecting the synthesis environment of MOF or the structure itself to simple modification methods. Different chosen modifying agents had a crucial influence on different aspects of the final properties of as-obtained MOFs considering the morphology, crystallinity or optical properties among others.

Some aspects of herein reported research were investigated for the first time, often due to the missing testing methodologies or usage of the alternative equipment than described in the literature. Among others, the influence of different non-noble metals and the method of their introduction on the defectivity of MOFs was studied, especially concerning their influence on the photocatalytic ability to reduce CO_2 to HCOOH. Another aspect regarded the research on the influence of various synthesis factors at once on the MOF formation. Regarding the use of ionic liquids, new fields were explored as well. Firstly, it is the first work, that directly compared two different approaches of four AAILs introduction to MOF and their effect on gas sorption properties was studied. Additionally, a direct comparison with the influence of a common, simple, non-functionalized IL was provided. In turn, MOF-MOF composite was for the first time synthesized in the presence of ionic liquid introduced at different stages of the synthesis procedure. Therefore, the development of new methods connected with solving problems and complications, which were impossible to foresee at the study conceptualization stage, constituted a substantial body of the presented work.

This work offers an extensive perspective on the limitations of MOFs, while at the same time outlines the path that must be taken to find practical application for these structures in everyday life. Due to extensive characteristics of this dissertation, a broader overview of the research should be performed to deeply verify general trends and assumptions made throughout the presented research work. While the research included in this dissertation yielded numerous results and conclusions, it also unveiled new research gaps that could – and indeed should – be explored, given their significance for the industrial-scale application of MOFs. These significant areas requiring further attention from the scientific community include e.g., moisture resistance, long-term structural stability, reusability or cost-effectiveness. In the next steps, deeper overview of the ecological aspect of using MOFs should also be considered carefully. The surge after the material durability (low-energy regeneration) and its efficiency (stably uniform) should also concern the

ecological cost of synthesis, environmental burden during the material's use, as well as the burden associated with the spent material storage or disposal.

11. SCIENTIFIC ACHIEVEMENTS

Table 11.1 Summary of author's achievements; Scopus (Status as of 19.09.2026)

Parameter	Value
Publications in journals from JCR list	10
Publications in journals outside of JCR list	0
Summarized IF of publications	118.6
Book chapters	0
Scientific conferences participation	4
Patents	0
Patent applications	0
Total citations without self-citations	480
Hirsch index	6

List of publications:

- Mousavi Khadem, S.S., Dell'Angelo, D., Baluk, M., **Kroczewska-Gnatowska**, M., Marzec, M., Badawi, M., Sayede, A., Zaleska-Medynska, A., Łuczak, J. (2026). *Engineering Redox–Transport Balance in Cobalt-Metalated Al-PMOFs for CO_2 Photoreduction*. ACS APPL. MATER. INTERFACES, 18 (36): 48918–48932, doi: 10.1021/acsami.6c07492 ($MNiSW_{2024}$: 200, IF_{2025}: 7.8)
- **Kroczewska-Gnatowska, M.,** Baluk, M., Luna-Triguero, A., Vicent-Luna, J. M., Pieczyńska, A., Matus, K., Zaleska-Medynska, A., & Łuczak, J. (2026). *The influence of non-noble metal-induced MOF defectivity on light-driven CO2 reduction.* JOURNAL OF CO2 UTILIZATION, 107, 103409, doi: 10.1016/j.jcou.2026.103409 ($MNiSW_{2024}$: 140, IF_{2025}: 8.6);
- Baluk, M., Pieczyńska, A., Mazierski, P., **Kroczewska-Gnatowska, M.,** Nikiforow, K., Mikolajczyk, A., Hoang, K., Tolba, S. A., Pawlyta, M., Dołżonek, J., Kuila, A., Paz, Y., Łuczak, J., & Zaleska-Medynska, A. (2026). *A new strategy for designing porphyrin-based Cu-modified MOFs for CO2-to-solar fuels conversion under visible light.* APPLIED SURFACE SCIENCE, 735, 166696, doi: 10.1016/j.apsusc.2026.166696 ($MNiSW_{2024}$: 140, IF_{2025}: 6.6);
- Gontarek-Castro, E., Pancielejko, A., Baluk, M., **Kroczewska-Gnatowska, M.**, Gnatowski, P., Matus, K., Łuczak, J., & Zaleska-Medynska, A. (2025). *Photocatalytic membranes based on Cu–NH2-MIL-125(Ti) protected by poly(vinylidene fluoride) for high and stable hydrogen production.* MATERIALS HORIZONS, 12, 1504-1515, doi: 10.1039/d4mh01397b ($MNiSW_{2024}$: 200, IF_{2025}: 11.4);
- Pancielejko, A., **Kroczewska-Gnatowska, M.**, Mazierski, P., Łuczak, J., & Zaleska-Medynska, A. (2024). *The effect of ionic liquids on the surface and photocatalytic properties of semiconducting materials.* CHEMICAL ENGINEERING JOURNAL, 498, 155274. doi: 10.1016/j.cej.2024.155274; ($MNiSW_{2024}$: 200, IF_{2024}: 13.2, IF_{2025}: 12.5);
- Baluk, M.A., Pieczyńska, A., Mazierski, P., **Kroczewska, M.**, Nikiforow, K., Mikolajczyk, A., Dołżonek, J., Łuczak, J., & Zaleska-Medynska, A. (2024) *Effect of copper and silver modification of NH2-MIL-125(Ti) on the photoreduction of carbon dioxide to formic acid over this framework under visible-light irradiation*, APPLIED CATALYSIS B:

ENVIRONMENT AND ENERGY, 354, 124107, doi: 10.1016/j.apcatb.2024.124107; ($MNiSW_{2024}$: 200, IF_{2024}: 21.1, IF_{2025}: 19.7)I

- Baluk, M.A., Pieczyńska, A., **Kroczewska, M.,** Łuczak, J., Matus, K., Nikiforow, K., & Zaleska-Medynska, A. (2024) *Efficient method for octahedral NH2-MIL-125 (Ti) synthesis: Fast and mild conditions*, CHEMICAL ENGINEERING JOURNAL, 492, 152313, doi: 10.1016/j.cej.2024.152313 ($MNiSW_{2024}$: 200, IF_{2024}: 13.2, IF_{2025}: 12.5)
- Baluk, M.A., Jutrzenka Trzebiatowska, P., Pieczyńska, A., Makowski, D**., Kroczewska, M.,** Łuczak, J., & Zaleska-Medynska, A. (2024). *A new strategy for PET depolymerization: Application of bimetallic MOF-74 as a selective catalyst*, JOURNAL OF ENVIRONMENTAL MANAGEMENT, 363, 121360. doi: 10.1016/j.jenvman.2024.121360, ($MNiSW_{2024}$: 200, IF_{2024}: 8.4, IF_{2025}: 9.2);
- Łuczak J., **Kroczewska M.**, Baluk M., Sowik J., Mazierski P., & Zaleska-Medynska A., (2023), *Morphology control through the synthesis of metal-organic frameworks*, ADVANCES IN COLLOID AND INTERFACE SCIENCE, 314, 102864-, doi: 10.1016/j.cis.2023.102864, ($MNiSW_{2024}$: 200, IF_{2023}: 15.9, IF_{2025}: 23.7);
- Wilczewska, P., Pancielejko, A., Łuczak, J., **Kroczewska, M**., Lisowski, W., & Siedlecka, E. (2022). *The influence of ILs on TiO2 microspheres activity towards 5-FU removal under artificial sunlight irradiation.* APPLIED SURFACE SCIENCE, 573, 151431, doi: 10.1016/j.apsusc.2021.151431, ($MNiSW_{2024}$: 140, IF_{2022}: 6.7,IF_{2025}: 6.6).

Scientific conferences participation:

- 51st International Conference of the Slovak Society of Chemical Engineering, Slovak Society of Chemical Engineering, Jasna, Slovakia, 27-30.05.2025, Active participation; Title of poster: *Influence of amino acid ionic liquids on morphology and sorption properties of HKUST-1*;
- 49th International Conference of SSCHE 2023; Tatranské Matliare, Slovakia, 15.05-18.05.2023, Active participation; Title of presentation: *The importance of the selection of synthesis conditions of copper-based Metal-Organic Frameworks*
- 8th International Conference on Metal-Organic Frameworks and Open Framework Compounds; DECHEMA, Dresden, Germany, 04.09-07.09.2022, Active participation; Title of poster: *The influence of synthesis conditions on Metal-Organic Frameworks*
- 23rd International Conference Materials, Methods & Technologies, International Scientific Events Bulgaria, Burgas, Bulgaria, 19-22.08.2021, Active participation; Title of poster: *Metal-Organic Frameworks activation using different approaches*;

Scientific internships

- NOVA School Of Science And Technology, Universidade NOVA de Lisboa, Caparica, Portugal. 15.09-15.12.2024; financed from the project funds „Gdańsk Tech Doctoral School closer to Europe" co-financed by the Polish National Agency for Academic Exchange (NAWA), Supervisors: Isabel A.A.C. Esteves, José M.S.S. Esperança

Other achievements:

- IDUB Francium Supporting Outstanding Doctoral Candidates 2023/2024 scholarship in Gdańsk University of Technology;
- Five times awarded with IDUP Nitrogenium Supporting Excellence In Publishing award;
- Award for obtaining *Highly Cited Paper* status on Web of Science;
- PhD student position in the project OPUS-21 project No. 2021/41/B/ST4/00849 “The role of ionic liquids in CO_2 photoconversion” (2022-2026);
- Member of Organizing Committee of „IV Pomorskie Studenckie Sympozjum Chemiczne”, 23-24.04.2022, on-line
- Member of Organizing Committee of „III Pomorskie Studenckie Sympozjum Chemiczne”, 18-19.09.2021, on-line

12. REFERENCES

[1] R.A. Eggleton, A Short Introduction to Climate Change, Illustrate, Cambridge University Press, 2012.

[2] J.W. Maina, C. Pozo-Gonzalo, L. Kong, J. Schütz, M. Hill, L.F. Dumée, Metal organic framework based catalysts for CO 2 conversion, Mater. Horizons 4 (2017) 345–361. https://doi.org/10.1039/C6MH00484A.

[3] D. Li, M. Kassymova, X. Cai, S.-Q. Zang, H.-L. Jiang, Photocatalytic CO2 reduction over metal-organic framework-based materials, Coord. Chem. Rev. 412 (2020) 213262. https://doi.org/10.1016/j.ccr.2020.213262.

[4] J.-R. Li, R.J. Kuppler, H.-C. Zhou, Selective gas adsorption and separation in metal–organic frameworks, Chem. Soc. Rev. 38 (2009) 1477. https://doi.org/10.1039/b802426j.

[5] O.M. Yaghi, M.J. Kalmutzki, C.S. Diercks, Introduction to Reticular Chemistry, Wiley, 2019. https://doi.org/10.1002/9783527821099.

[6] R. Li, W. Zhang, K. Zhou, Metal–Organic-Framework-Based Catalysts for Photoreduction of CO 2, Adv. Mater. 30 (2018) 1705512. https://doi.org/10.1002/adma.201705512.

[7] S.-Q. Wang, X. Gu, X. Wang, X.-Y. Zhang, X.-Y. Dao, X.-M. Cheng, J. Ma, W.-Y. Sun, Defect-engineering of Zr(IV)-based metal-organic frameworks for regulating CO2 photoreduction, Chem. Eng. J. 429 (2022) 132157. https://doi.org/10.1016/j.cej.2021.132157.

[8] S.-Q. Wang, X. Wang, X.-Y. Zhang, X.-M. Cheng, J. Ma, W.-Y. Sun, Effect of the Defect Modulator and Ligand Length of Metal–Organic Frameworks on Carbon Dioxide Photoreduction, ACS Appl. Mater. Interfaces 13 (2021) 61578–61586. https://doi.org/10.1021/acsami.1c21663.

[9] M. Aghaie, N. Rezaei, S. Zendehboudi, A systematic review on CO2 capture with ionic liquids: Current status and future prospects, Renew. Sustain. Energy Rev. 96 (2018) 502–525. https://doi.org/10.1016/j.rser.2018.07.004.

[10] H. Ohno, K. Fukumoto, Amino Acid Ionic Liquids, Acc. Chem. Res. 40 (2007) 1122–1129. https://doi.org/10.1021/ar700053z.

[11] J. Łuczak, M. Kroczewska, M. Baluk, J. Sowik, P. Mazierski, A. Zaleska-Medynska, Morphology control through the synthesis of metal-organic frameworks, Adv. Colloid Interface Sci. 314 (2023) 102864. https://doi.org/10.1016/j.cis.2023.102864.

[12] M. Kroczewska-Gnatowska, M.A. Baluk, A. Luna-Triguero, J.M. Vicent-Luna, A. Pieczyńska, K. Matus, A. Zaleska-Medynska, J. Łuczak, The influence of non-noble metal-induced MOF defectivity on light-driven CO2 reduction, J. CO2 Util. 107 (2026) 103409. https://doi.org/10.1016/j.jcou.2026.103409.

[13] P. Friedlingstein, M. O'Sullivan, M.W. Jones, R.M. Andrew, J. Hauck, P. Landschützer, C. Le Quéré, H. Li, I.T. Luijkx, A. Olsen, G.P. Peters, W. Peters, J. Pongratz, C. Schwingshackl, S. Sitch, J.G. Canadell, P. Ciais, R.B. Jackson, S.R. Alin, A. Arneth, V. Arora, N.R. Bates, M. Becker, N. Bellouin, C.F. Berghoff, H.C. Bittig, L. Bopp, P. Cadule, K. Campbell, M.A. Chamberlain, N. Chandra, F. Chevallier, L.P. Chini, T. Colligan, J. Decayeux, L.M. Djeutchouang, X. Dou, C. Duran Rojas, K. Enyo, W. Evans, A.R. Fay, R.A. Feely, D.J. Ford, A. Foster, T. Gasser, M. Gehlen, T. Gkritzalis, G. Grassi, L. Gregor, N. Gruber, Ö. Gürses, I. Harris, M. Hefner, J. Heinke, G.C. Hurtt, Y. Iida, T. Ilyina, A.R. Jacobson, A.K. Jain, T. Jarníková, A. Jersild, F. Jiang, Z. Jin, E. Kato, R.F. Keeling, K. Klein Goldewijk, J. Knauer, J.I. Korsbakken, X. Lan, S.K. Lauvset, N. Lefèvre, Z. Liu, J. Liu, L. Ma, S. Maksyutov, G. Marland, N. Mayot, P.C. McGuire, N. Metzl, N.M. Monacci, E.J. Morgan, S.-I. Nakaoka, C. Neill, Y. Niwa, T. Nützel, L. Olivier, T. Ono, P.I. Palmer, D. Pierrot, Z. Qin, L. Resplandy, A. Roobaert, T.M. Rosan, C. Rödenbeck, J. Schwinger, T.L. Smallman, S.M. Smith, R. Sospedra-Alfonso, T. Steinhoff, Q. Sun, A.J. Sutton, R. Séférian, S. Takao, H. Tatebe, H. Tian, B. Tilbrook, O. Torres, E. Tourigny, H. Tsujino, F. Tubiello, G. van der Werf, R. Wanninkhof, X. Wang, D. Yang, X. Yang, Z. Yu, W. Yuan, X. Yue, S. Zaehle, N. Zeng, J. Zeng, Global Carbon Budget 2024, Earth Syst. Sci. Data 17 (2025) 965–1039. https://doi.org/10.5194/essd-17-965-2025.

[14] P. Friedlingstein, M. O'Sullivan, M.W. Jones, R.M. Andrew, D.C.E. Bakker, J. Hauck, P. Landschützer, C. Le Quéré, H. Li, I.T. Luijkx, G.P. Peters, W. Peters, J. Pongratz, C. Schwingshackl, S. Sitch, J.G. Canadell, P. Ciais, K. Aas, S.R. Alin, P. Anthoni, L. Barbero, N.R. Bates, N. Bellouin, A. Benoit-Cattin, C.F. Berghoff, R. Bernardello, L. Bopp, I.B.M. Brasika, M.A. Chamberlain, N. Chandra, F. Chevallier, L.P. Chini, N.O. Collier, T.H. Colligan, M. Cronin, L.M. Djeutchouang, X. Dou, M.P. Enright, K. Enyo, M. Erb, W. Evans, R.A. Feely, L. Feng, D.J. Ford, A. Foster, F. Fransner, T. Gasser, M. Gehlen, T. Gkritzalis, J. Goncalves De Souza, G. Grassi, L. Gregor, N. Gruber, B. Guenet, Ö. Gürses, K. Harrington, I. Harris, J. Heinke, G.C. Hurtt, Y. Iida, T. Ilyina, A. Ito, A.R. Jacobson, A.K. Jain, T. Jarníková, A. Jersild, F. Jiang, S.D. Jones, E. Kato, R.F. Keeling, K. Klein Goldewijk, J. Knauer, Y. Kong, J.I. Korsbakken, C. Koven, T. Kunimitsu, X. Lan, J. Liu, Z. Liu, Z. Liu, C. Lo Monaco, L. Ma, G. Marland, P.C. McGuire, G.A. McKinley, J.R. Melton, N. Monacci, E. Monier, E.J. Morgan, D.R. Munro, J.D. Müller, S.-I. Nakaoka, L.R. Nayagam, Y. Niwa, T. Nutzel, A. Olsen, A.M. Omar, N. Pan, S. Pandey, D. Pierrot, Z. Qin, P. Regnier, G. Rehder, L. Resplandy, A. Roobaert, T.M. Rosan, C. Rödenbeck, J. Schwinger, I. Skjelvan, T.L. Smallman, V. Spada, M.G. Sreeush, Q. Sun, A.J. Sutton, C. Sweeney, D. Swingedouw, R. Séférian, S. Takao, H. Tatebe, H. Tian, X. Tian, B. Tilbrook, H. Tsujino, F. Tubiello, E. van Ooijen, G.R. van der Werf, S.J. van de Velde, A.P. Walker, R. Wanninkhof, X. Yang, W. Yuan, X. Yue, J. Zeng, Global Carbon Budget 2025, Earth Syst. Sci. Data 18 (2026) 3211–3288. https://doi.org/10.5194/essd-18-3211-2026.

[15] Rekordowy rok dla OZE, (n.d.). https://www.gov.pl/web/klimat/polska-osiaga-50-mocy-z-

oze--historyczny-przelom (accessed August 6, 2026).

[16] Regulation (EU) 2021/1119 of the European Parliament and of the Council of 30 June 2021 establishing the framework for achieving climate neutrality and amending Regulations (EC) No 401/2009 and (EU) 2018/1999 ('European Climate Law'), (2021) 1–17. http://data.europa.eu/eli/reg/2021/1119/oj.

[17] J.R. Fanchi, C.J. Fanchi, Energy In The 21St Century, 4th editio, Wsp, 2016.

[18] S. Topham, A. Bazzanella, S. Schiebahn, S. Luhr, L. Zhao, A. Otto, D. Stolten, Carbon Dioxide, in: Ullmann's Encycl. Ind. Chem., Wiley-VCH Verlag GmbH & Co. KGaA, Weinheim, Germany, 2014: pp. 1–43. https://doi.org/10.1002/14356007.a05_165.pub2.

[19] E. Hanson, C. Nwakile, V.O. Hammed, Carbon capture, utilization, and storage (CCUS) technologies: Evaluating the effectiveness of advanced CCUS solutions for reducing CO2 emissions, Results in Surfaces and Interfaces 18 (2025) 100381. https://doi.org/10.1016/j.rsurfi.2024.100381.

[20] J. Wang, L. Li, G. Qu, M. Cheng, Y. Ren, P. Lu, T. Zhang, Y. Wang, F. Wu, Advanced materials for CO2 capture and storage: A comprehensive review of current progress and future prospects, J. Environ. Chem. Eng. 13 (2025) 115881. https://doi.org/10.1016/j.jece.2025.115881.

[21] G.T. Rochelle, Amine Scrubbing for CO2 Capture, Science (80-.). 325 (2009) 1652–1654. https://doi.org/10.1126/science.1176731.

[22] F.A. Chowdhury, H. Yamada, T. Higashii, K. Goto, M. Onoda, CO 2 Capture by Tertiary Amine Absorbents: A Performance Comparison Study, Ind. Eng. Chem. Res. 52 (2013) 8323–8331. https://doi.org/10.1021/ie400825u.

[23] B.F. Goodrich, J.C. de la Fuente, B.E. Gurkan, D.J. Zadigian, E.A. Price, Y. Huang, J.F. Brennecke, Experimental Measurements of Amine-Functionalized Anion-Tethered Ionic Liquids with Carbon Dioxide, Ind. Eng. Chem. Res. 50 (2011) 111–118. https://doi.org/10.1021/ie101688a.

[24] Y. Qu, J. Lan, Y. Chen, J. Sun, Amino acid ionic liquids as efficient catalysts for CO 2 capture and chemical conversion with epoxides under metal/halogen/cocatalyst/solvent-free conditions, Sustain. Energy Fuels 5 (2021) 2494–2503. https://doi.org/10.1039/D1SE00060H.

[25] B.F. Goodrich, J.C. de la Fuente, B.E. Gurkan, Z.K. Lopez, E.A. Price, Y. Huang, J.F. Brennecke, Effect of Water and Temperature on Absorption of CO 2 by Amine-Functionalized Anion-Tethered Ionic Liquids, J. Phys. Chem. B 115 (2011) 9140–9150. https://doi.org/10.1021/jp2015534.

[26] F.-F. Chen, K. Huang, Y. Zhou, Z.-Q. Tian, X. Zhu, D.-J. Tao, D. Jiang, S. Dai, Multi-Molar Absorption of CO 2 by the Activation of Carboxylate Groups in Amino Acid Ionic Liquids,

Angew. Chemie Int. Ed. 55 (2016) 7166–7170. https://doi.org/10.1002/anie.201602919.

[27] R. Wanison, W.N. Hadi Syahputra, N. Kammuang-lue, P. Sakulchangsatjatai, P. Terdtoon, N. Tippayawong, P. Suttakul, Y. Mona, A review of cryogenic carbon capture research: Experimental studies, simulations, and application potential, Therm. Sci. Eng. Prog. 61 (2025) 103562. https://doi.org/10.1016/j.tsep.2025.103562.

[28] Z. Dai, L. Deng, Membranes for CO2 capture and separation: Progress in research and development for industrial applications, Sep. Purif. Technol. 335 (2024) 126022. https://doi.org/10.1016/j.seppur.2023.126022.

[29] J.Y. Lai, L.H. Ngu, S.S. Hashim, A review of CO 2 adsorbents performance for different carbon capture technology processes conditions, Greenh. Gases Sci. Technol. 11 (2021) 1076–1117. https://doi.org/10.1002/ghg.2112.

[30] R.W. Broach, D. Jan, D.A. Lesch, S. Kulprathipanja, E. Roland, P. Kleinschmit, Zeolites, in: Ullmann's Encycl. Ind. Chem., Wiley, 2012. https://doi.org/10.1002/14356007.a28_475.pub2.

[31] E.A.P. Dias, D.G. da Silva, M. da C. Amaral, L. dos S. Pereira, D.C. de Melo, W.L. Vasconcelos, CO2 adsorption by zeolites: State-of-Art, techniques and emerging trends, Microporous Mesoporous Mater. 400 (2026) 113904. https://doi.org/10.1016/j.micromeso.2025.113904.

[32] D.G. Boer, J. Langerak, P.P. Pescarmona, Zeolites as Selective Adsorbents for CO 2 Separation, ACS Appl. Energy Mater. 6 (2023) 2634–2656. https://doi.org/10.1021/acsaem.2c03605.

[33] K.-D. Henning, H. von Kienle, Carbon, 5. Activated Carbon, in: Ullmann's Encycl. Ind. Chem., Wiley-VCH Verlag GmbH & Co. KGaA, Weinheim, Germany, 2010. https://doi.org/10.1002/14356007.n05_n04.

[34] H. Hekmatmehr, A. Esmaeili, M. Pourmahdi, S. Atashrouz, A. Abedi, M. Ali Abuswer, D. Nedeljkovic, M. Latifi, S. Farag, A. Mohaddespour, Carbon capture technologies: A review on technology readiness level, Fuel 363 (2024) 130898. https://doi.org/10.1016/j.fuel.2024.130898.

[35] S.-Y. Lee, S.-J. Park, A review on solid adsorbents for carbon dioxide capture, J. Ind. Eng. Chem. 23 (2015) 1–11. https://doi.org/10.1016/j.jiec.2014.09.001.

[36] K.S. Song, P.W. Fritz, A. Coskun, Porous organic polymers for CO 2 capture, separation and conversion, Chem. Soc. Rev. 51 (2022) 9831–9852. https://doi.org/10.1039/D2CS00727D.

[37] J.C.S. Terra, A. Moores, F.C.C. Moura, Amine-Functionalized Mesoporous Silica as a Support for on-Demand Release of Copper in the A 3 -Coupling Reaction: Ultralow Concentration Catalysis and Confinement Effect, ACS Sustain. Chem. Eng. 7 (2019) 8696–

8705. https://doi.org/10.1021/acssuschemeng.9b00576.

[38] D. Golomb, S. Pennell, Ocean sequestration of carbon dioxide (CO2), in: Dev. Innov. Carbon Dioxide Capture Storage Technol., Elsevier, 2010: pp. 304–323. https://doi.org/10.1533/9781845699581.3.304.

[39] C.-H. Lee, A. V. Subhas, J.-H. Kim, K. Lee, Ocean Carbon Dioxide Removal and Storage, Chem. Rev. 126 (2026) 1110–1144. https://doi.org/10.1021/acs.chemrev.5c00433.

[40] C.A. Ehlig-Economides, Geologic carbon dioxide sequestration methods, opportunities, and impacts, Curr. Opin. Chem. Eng. 42 (2023) 100957. https://doi.org/10.1016/j.coche.2023.100957.

[41] T. Ajayi, J.S. Gomes, A. Bera, A review of CO2 storage in geological formations emphasizing modeling, monitoring and capacity estimation approaches, Pet. Sci. 16 (2019) 1028–1063. https://doi.org/10.1007/s12182-019-0340-8.

[42] J. Huang, J.C. Worch, A.P. Dove, O. Coulembier, Update and Challenges in Carbon Dioxide-Based Polycarbonate Synthesis, ChemSusChem 13 (2020) 469–487. https://doi.org/10.1002/cssc.201902719.

[43] J. Langanke, A. Wolf, J. Hofmann, K. Böhm, M.A. Subhani, T.E. Müller, W. Leitner, C. Gürtler, Carbon dioxide (CO 2) as sustainable feedstock for polyurethane production, Green Chem. 16 (2014) 1865–1870. https://doi.org/10.1039/C3GC41788C.

[44] Z. He, J. Wang, Y. Li, Recent advances in microalgae-driven carbon capture, utilization, and storage: Strain engineering through adaptive laboratory evolution and microbiome optimization, Green Carbon 3 (2025) 74–99. https://doi.org/10.1016/j.greenca.2024.10.001.

[45] Z. Zhang, S.-Y. Pan, H. Li, J. Cai, A.G. Olabi, E.J. Anthony, V. Manovic, Recent advances in carbon dioxide utilization, Renew. Sustain. Energy Rev. 125 (2020) 109799. https://doi.org/10.1016/j.rser.2020.109799.

[46] S. Valluri, V. Claremboux, S. Kawatra, Opportunities and challenges in CO2 utilization, J. Environ. Sci. 113 (2022) 322–344. https://doi.org/10.1016/j.jes.2021.05.043.

[47] H.O. LeClerc, H.C. Erythropel, A. Backhaus, D.S. Lee, D.R. Judd, M.M. Paulsen, M. Ishii, A. Long, L. Ratjen, G. Gonsalves Bertho, C. Deetman, Y. Du, M.K.M. Lane, P. V. Petrovic, A.T. Champlin, A. Bordet, N. Kaeffer, G. Kemper, J.B. Zimmerman, W. Leitner, P.T. Anastas, The CO 2 Tree: The Potential for Carbon Dioxide Utilization Pathways, ACS Sustain. Chem. Eng. 13 (2025) 5–29. https://doi.org/10.1021/acssuschemeng.4c07582.

[48] J. Schneider, M. Matsuoka, M. Takeuchi, J. Zhang, Y. Horiuchi, M. Anpo, D.W. Bahnemann, Understanding TiO 2 Photocatalysis: Mechanisms and Materials, Chem. Rev. 114 (2014) 9919–9986. https://doi.org/10.1021/cr5001892.

[49] H. Sibum, V. Güther, O. Roidl, F. Habashi, H. Uwe Wolf, C. Siemers, Titanium, Titanium Alloys, and Titanium Compounds, in: Ullmann's Encycl. Ind. Chem., Wiley-VCH Verlag

GmbH & Co. KGaA, Weinheim, Germany, 2017: pp. 1–35. https://doi.org/10.1002/14356007.a27_095.pub2.

[50] M. Esmat, E. Doustkhah, M. Abdelbar, R. Tahawy, H. El-Hosainy, M. Abdelhameed, Y. Ide, N. Fukata, Structural Conversion of Cu-Titanate into Photoactive Plasmonic Cu-TiO 2 for H 2 Generation in Visible Light, ACS Sustain. Chem. Eng. 10 (2022) 4143–4151. https://doi.org/10.1021/acssuschemeng.1c07555.

[51] Y. Yalçın, M. Kılıç, Z. Çınar, The Role of Non-Metal Doping in TiO2 Photocatalysis, J. Adv. Oxid. Technol. 13 (2010). https://doi.org/10.1515/jaots-2010-0306.

[52] G. Li, Z. Lian, X. Li, Y. Xu, W. Wang, D. Zhang, F. Tian, H. Li, Ionothermal synthesis of black Ti 3+ -doped single-crystal TiO 2 as an active photocatalyst for pollutant degradation and H 2 generation, J. Mater. Chem. A 3 (2015) 3748–3756. https://doi.org/10.1039/C4TA02873B.

[53] E. Can, B. Uralcan, R. Yildirim, Enhancing Charge Transfer in Photocatalytic Hydrogen Production over Dye-Sensitized Pt/TiO 2 by Ionic Liquid Coating, ACS Appl. Energy Mater. 4 (2021) 10931–10939. https://doi.org/10.1021/acsaem.1c01553.

[54] I.A. Bangash, M.S. Shaharun, B.V. Ayodele, S.A. Ali, M.R. Atta, I.U. Din, Photoelectrocatalytic CO 2 Reduction Using g-C 3 N 4 Hybrids: Review and Perspectives, Energy & Fuels 39 (2025) 11504–11535. https://doi.org/10.1021/acs.energyfuels.5c01356.

[55] H. Song, L. Liu, B. Feng, H. Wang, M. Xiao, H. Gai, Y. Tang, X. Qu, T. Huang, Modified g-C3N4 derived from ionic liquid and urea for promoting visible-light photodegradation of organic pollutants, Chinese J. Chem. Eng. 40 (2021) 293–303. https://doi.org/10.1016/j.cjche.2021.06.021.

[56] Y.O. Waidi, Q.A. Drmosh, A. Hezam, Recent progress in materials design strategies for efficient CO2 photocatalytic conversion, Nano-Structures & Nano-Objects 42 (2025) 101489. https://doi.org/10.1016/j.nanoso.2025.101489.

[57] M. Ji, J. Di, Y. Ge, J. Xia, H. Li, 2D-2D stacking of graphene-like g-C 3 N 4 /Ultrathin Bi 4 O 5 Br 2 with matched energy band structure towards antibiotic removal, Appl. Surf. Sci. 413 (2017) 372–380. https://doi.org/10.1016/j.apsusc.2017.03.287.

[58] D. Bhanderi, P. Lakhani, C.K. Modi, Graphitic carbon nitride (g-C 3 N 4) as an emerging photocatalyst for sustainable environmental applications: a comprehensive review, RSC Sustain. 2 (2024) 265–287. https://doi.org/10.1039/D3SU00382E.

[59] S.S.M. Bhat, G.K. S., Recent advances in interface engineering of bismuth-based materials for photocatalytic CO 2 reduction, RSC Appl. Interfaces 2 (2025) 1507–1526. https://doi.org/10.1039/D5LF00154D.

[60] Q. Pan, Y. Wu, X. Su, Y. Yin, S. Shi, O. Oderinde, G. Yui, C. Zhang, Y. Zhang, A review on the recent development of bismuth-based catalysts for CO2 photoreduction, J. Mol. Struct. 1294 (2023) 136404. https://doi.org/10.1016/j.molstruc.2023.136404.

[61] Z. Dong, B. Li, Y. Zhu, W. Guo, Metal halide perovskites for CO 2 photoreduction: recent advances and future perspectives, EES Catal. 2 (2024) 448–474. https://doi.org/10.1039/D3EY00187C.

[62] J. Kaur, S.C. Peter, Two-Dimensional Perovskites for Photocatalytic CO 2 Reduction, Angew. Chemie Int. Ed. 64 (2025). https://doi.org/10.1002/anie.202418708.

[63] I.I. Alkhatib, C. Garlisi, M. Pagliaro, K. Al-Ali, G. Palmisano, Metal-organic frameworks for photocatalytic CO2 reduction under visible radiation: A review of strategies and applications, Catal. Today 340 (2020) 209–224. https://doi.org/10.1016/j.cattod.2018.09.032.

[64] L. Zhang, J. Zhang, Metal-organic frameworks for CO2 photoreduction, Front. Energy 13 (2019) 221–250. https://doi.org/10.1007/s11708-019-0629-8.

[65] Y. He, C. Li, X. Chen, H. Rao, Z. Shi, S. Feng, Critical Aspects of Metal–Organic Framework-Based Materials for Solar-Driven CO 2 Reduction into Valuable Fuels, Glob. Challenges 5 (2021). https://doi.org/10.1002/gch2.202000082.

[66] B. Li, Z. Zhang, Y. Li, K. Yao, Y. Zhu, Z. Deng, F. Yang, X. Zhou, G. Li, H. Wu, N. Nijem, Y.J. Chabal, Z. Lai, Y. Han, Z. Shi, S. Feng, J. Li, Enhanced Binding Affinity, Remarkable Selectivity, and High Capacity of CO2 by Dual Functionalization of a rht-Type Metal-Organic Framework, Angew. Chemie Int. Ed. 51 (2012) 1412–1415. https://doi.org/10.1002/anie.201105966.

[67] G.C. Shearer, S. Chavan, J. Ethiraj, J.G. Vitillo, S. Svelle, U. Olsbye, C. Lamberti, S. Bordiga, K.P. Lillerud, Tuned to Perfection: Ironing Out the Defects in Metal–Organic Framework UiO-66, Chem. Mater. 26 (2014) 4068–4071. https://doi.org/10.1021/cm501859p.

[68] H. Li, M. Eddaoudi, M. O'Keeffe, O.M. Yaghi, Design and synthesis of an exceptionally stable and highly porous metal-organic framework, Nature 402 (1999) 276–279. https://doi.org/10.1038/46248.

[69] R. Sabouni, H. Kazemian, S. Rohani, A novel combined manufacturing technique for rapid production of IRMOF-1 using ultrasound and microwave energies, Chem. Eng. J. 165 (2010) 966–973. https://doi.org/10.1016/j.cej.2010.09.036.

[70] J. Hynek, P. Brázda, J. Rohlíček, M.G.S. Londesborough, J. Demel, Phosphinic Acid Based Linkers: Building Blocks in Metal-Organic Framework Chemistry, Angew. Chemie Int. Ed. 57 (2018) 5016–5019. https://doi.org/10.1002/anie.201800884.

[71] K. Wang, X.-L. Lv, D. Feng, J.-R. Li, S. Chen, J. Sun, L. Song, Y. Xie, J.-R. Li, H.-C. Zhou, Pyrazolate-Based Porphyrinic Metal–Organic Framework with Extraordinary Base-Resistance, J. Am. Chem. Soc. 138 (2016) 914–919. https://doi.org/10.1021/jacs.5b10881.

[72] A. Mariyam, M. Shahid, M. I., M.S. Khan, M.S. Ahmad, Tetrazole Based Porous Metal Organic Framework (MOF): Topological Analysis and Dye Adsorption Properties, J. Inorg.

Organomet. Polym. Mater. 30 (2020) 1935–1943. https://doi.org/10.1007/s10904-019-01334-6.

[73] L. Wang, Y. Sun, H. Sun, Incorporating magnesium and calcium cations in porous organic frameworks for high-capacity hydrogen storage, Faraday Discuss. 151 (2011) 143. https://doi.org/10.1039/c0fd90025g.

[74] K.S. Park, Z. Ni, A.P. Côté, J.Y. Choi, R. Huang, F.J. Uribe-Romo, H.K. Chae, M. O'Keeffe, O.M. Yaghi, Exceptional chemical and thermal stability of zeolitic imidazolate frameworks, Proc. Natl. Acad. Sci. 103 (2006) 10186–10191. https://doi.org/10.1073/pnas.0602439103.

[75] A.M.P. Peedikakkal, A.A. Jimoh, M.N. Shaikh, B. El Ali, Mixed-Metal Metal–Organic Frameworks as Catalysts for Liquid-Phase Oxidation of Toluene and Cycloalkanes, Arab. J. Sci. Eng. 42 (2017) 4383–4390. https://doi.org/10.1007/s13369-017-2452-z.

[76] A. Schejn, L. Balan, V. Falk, L. Aranda, G. Medjahdi, R. Schneider, Controlling ZIF-8 nano- and microcrystal formation and reactivity through zinc salt variations, CrystEngComm 16 (2014) 4493–4500. https://doi.org/10.1039/C3CE42485E.

[77] M. Haouas, C. Volkringer, T. Loiseau, G. Férey, F. Taulelle, In situ NMR, ex situ XRD and SEM study of the hydrothermal crystallization of nanoporous aluminum trimesates MIL-96, MIL-100, and MIL-110, Chem. Mater. 24 (2012) 2462–2471. https://doi.org/10.1021/cm300439e.

[78] C. Xu, M. Bao, J. Ren, Z. Zhang, NH 2 -MIL-88B (Fe α In 1−α) mixed-MOFs designed for enhancing photocatalytic Cr(vi) reduction and tetracycline elimination, RSC Adv. 10 (2020) 39080–39086. https://doi.org/10.1039/D0RA07487J.

[79] A. Schaate, P. Roy, A. Godt, J. Lippke, F. Waltz, M. Wiebcke, P. Behrens, Modulated Synthesis of Zr-Based Metal–Organic Frameworks: From Nano to Single Crystals, Chem. – A Eur. J. 17 (2011) 6643–6651. https://doi.org/10.1002/chem.201003211.

[80] M.A. Baluk, A. Pieczyńska, P. Mazierski, M. Kroczewska, K. Nikiforow, A. Mikolajczyk, J. Dołżonek, J. Łuczak, A. Zaleska-Medynska, Effect of copper and silver modification of NH2-MIL-125(Ti) on the photoreduction of carbon dioxide to formic acid over this framework under visible-light irradiation, Appl. Catal. B Environ. Energy 354 (2024) 124107. https://doi.org/10.1016/j.apcatb.2024.124107.

[81] R.-J. Wei, M. Xie, R.-Q. Xia, J. Chen, H.-J. Hu, G.-H. Ning, D. Li, Gold(I)-Organic Frameworks as Catalysts for Carboxylation of Alkynes with CO 2, J. Am. Chem. Soc. 145 (2023) 22720–22727. https://doi.org/10.1021/jacs.3c08262.

[82] L. Yang, Y. Dou, Z. Zhou, D. Zhang, S. Wang, A Versatile Porous Silver-Coordinated Material for the Heterogeneous Catalysis of Chemical Conversion with Propargylic Alcohols and CO2, Nanomaterials 9 (2019) 1566. https://doi.org/10.3390/nano9111566.

[83] K. Dedecker, M. Drobek, V. Rouessac, A. Julbe, A Palladium-Based MOF for the

Preferential Sorption of Benzene, ACS Appl. Mater. Interfaces 15 (2023) 6831–6838. https://doi.org/10.1021/acsami.2c20034.

[84] H.M. Yang, X.L. Song, T.L. Yang, Z.H. Liang, C.M. Fan, X.G. Hao, Electrochemical synthesis of flower shaped morphology MOFs in an ionic liquid system and their electrocatalytic application to the hydrogen evolution reaction, RSC Adv. 4 (2014) 15720–15726. https://doi.org/10.1039/C3RA47744D.

[85] A. Singh, R. Vedarajan, N. Matsumi, Modified Metal Organic Frameworks (MOFs)/Ionic Liquid Matrices for Efficient Charge Storage, J. Electrochem. Soc. 164 (2017) H5169–H5174. https://doi.org/10.1149/2.0191708jes.

[86] W.-J. Son, J.J. Kim, J.J. Kim, W.-S. Ahn, Sonochemical synthesis of MOF-5, Chem. Commun. (2008) 6336. https://doi.org/10.1039/b814740j.

[87] X.-J. Hong, T.-X. Tan, Y.-K. Guo, X.-Y. Tang, J.-Y. Wang, W. Qin, Y.-P. Cai, Confinement of polysulfides within bi-functional metal–organic frameworks for high performance lithium–sulfur batteries, Nanoscale 10 (2018) 2774–2780. https://doi.org/10.1039/C7NR07118C.

[88] Y. Wang, Y. Xu, D. Li, H. Liu, X. Li, S. Tao, Z. Tian, Ionothermal synthesis of zeolitic imidazolate frameworks and the synthesis dissolution-crystallization mechanism, Chinese J. Catal. 36 (2015) 855–865. https://doi.org/10.1016/S1872-2067(14)60278-3.

[89] A. Carné-Sánchez, I. Imaz, M. Cano-Sarabia, D. Maspoch, A spray-drying strategy for synthesis of nanoscale metal–organic frameworks and their assembly into hollow superstructures, Nat. Chem. 5 (2013) 203–211. https://doi.org/10.1038/nchem.1569.

[90] H. Ali-Moussa, R. Navarro Amador, J. Martinez, F. Lamaty, M. Carboni, X. Bantreil, Synthesis and post-synthetic modification of UiO-67 type metal-organic frameworks by mechanochemistry, Mater. Lett. 197 (2017) 171–174. https://doi.org/10.1016/j.matlet.2017.03.140.

[91] H. YANG, X. LIU, X. SONG, T. YANG, Z. LIANG, C. FAN, In situ electrochemical synthesis of MOF-5 and its application in improving photocatalytic activity of BiOBr, Trans. Nonferrous Met. Soc. China 25 (2015) 3987–3994. https://doi.org/10.1016/S1003-6326(15)64047-X.

[92] M.J. Cliffe, W. Wan, X. Zou, P.A. Chater, A.K. Kleppe, M.G. Tucker, H. Wilhelm, N.P. Funnell, F.-X. Coudert, A.L. Goodwin, Correlated defect nanoregions in a metal–organic framework, Nat. Commun. 5 (2014) 4176. https://doi.org/10.1038/ncomms5176.

[93] G.C. Shearer, S. Chavan, S. Bordiga, S. Svelle, U. Olsbye, K.P. Lillerud, Defect Engineering: Tuning the Porosity and Composition of the Metal–Organic Framework UiO-66 via Modulated Synthesis, Chem. Mater. 28 (2016) 3749–3761. https://doi.org/10.1021/acs.chemmater.6b00602.

[94] R. Luebke, J.F. Eubank, A.J. Cairns, Y. Belmabkhout, L. Wojtas, M. Eddaoudi, The unique rht-MOF platform, ideal for pinpointing the functionalization and CO 2 adsorption

relationship, Chem. Commun. 48 (2012) 1455–1457. https://doi.org/10.1039/C1CC15962C.

[95] S. Sharma, M. Yawer, M. Kariem, H.N. Sheikh, Solvothermal synthesis and structure of 3D frameworks of Nd(III) and Y(III) with thiophene-2,5-dicarboxylate and N,N′-diethylformamide, J. Mol. Struct. 1118 (2016) 241–249. https://doi.org/10.1016/j.molstruc.2016.04.017.

[96] P. Howlader, P.S. Mukherjee, Solvent Directed Synthesis of Molecular Cage and Metal Organic Framework of Copper(II) Paddlewheel Cluster, Isr. J. Chem. 59 (2019) 292–298. https://doi.org/10.1002/ijch.201800155.

[97] D.-W. Jung, D.-A. Yang, J.J. Kim, J.J. Kim, W.-S. Ahn, Facile synthesis of MOF-177 by a sonochemical method using 1-methyl-2-pyrrolidinone as a solvent, Dalt. Trans. 39 (2010) 2883. https://doi.org/10.1039/b925088c.

[98] X. Feng, T. Wu, M.A. Carreon, Synthesis of ZIF-67 and ZIF-8 crystals using DMSO (Dimethyl Sulfoxide) as solvent and kinetic transformation studies, J. Cryst. Growth 455 (2016) 152–156. https://doi.org/10.1016/j.jcrysgro.2016.10.016.

[99] A.M. Ploskonka, S.E. Marzen, J.B. DeCoste, Facile Synthesis and Direct Activation of Zirconium Based Metal–Organic Frameworks from Acetone, Ind. Eng. Chem. Res. 56 (2017) 1478–1484. https://doi.org/10.1021/acs.iecr.6b04361.

[100] L.A. Lozano, C.M. Iglesias, B.M.C. Faroldi, M.A. Ulla, J.M. Zamaro, Efficient solvothermal synthesis of highly porous UiO-66 nanocrystals in dimethylformamide-free media, J. Mater. Sci. 53 (2018) 1862–1873. https://doi.org/10.1007/s10853-017-1658-5.

[101] S. Leubner, R. Stäglich, J. Franke, J. Jacobsen, J. Gosch, R. Siegel, H. Reinsch, G. Maurin, J. Senker, P.G. Yot, N. Stock, Solvent Impact on the Properties of Benchmark Metal–Organic Frameworks: Acetonitrile-Based Synthesis of CAU-10, Ce-UiO-66, and Al-MIL-53, Chem. – A Eur. J. 26 (2020) 3877–3883. https://doi.org/10.1002/chem.201905376.

[102] M.S. Biserčić, B. Marjanović, B.N. Vasiljević, S. Mentus, B.A. Zasońska, G. Ćirić-Marjanović, The quest for optimal water quantity in the synthesis of metal-organic framework MOF-5, Microporous Mesoporous Mater. 278 (2019) 23–29. https://doi.org/10.1016/j.micromeso.2018.11.005.

[103] G. Lee, J. Hwang, Direct Synthesis of Mixed-Metal Paddle-Wheel Metal–Organic Frameworks with Controlled Metal Ratios under Ambient Conditions, Inorg. Chem. 62 (2023) 19457–19465. https://doi.org/10.1021/acs.inorgchem.3c02400.

[104] E.D. Bloch, D. Britt, C. Lee, C.J. Doonan, F.J. Uribe-Romo, H. Furukawa, J.R. Long, O.M. Yaghi, Metal Insertion in a Microporous Metal−Organic Framework Lined with 2,2′-Bipyridine, J. Am. Chem. Soc. 132 (2010) 14382–14384. https://doi.org/10.1021/ja106935d.

[105] H.S. Jena, A.M. Kaczmarek, C. Krishnaraj, X. Feng, K. Vijayvergia, H. Yildirim, S.-N. Zhao, R. Van Deun, P. Van Der Voort, White Light Emission Properties of Defect Engineered

Metal–Organic Frameworks by Encapsulation of Eu 3+ and Tb 3+, Cryst. Growth Des. 19 (2019) 6339–6350. https://doi.org/10.1021/acs.cgd.9b00824.

[106] E. Biemmi, S. Christian, N. Stock, T. Bein, High-throughput screening of synthesis parameters in the formation of the metal-organic frameworks MOF-5 and HKUST-1, Microporous Mesoporous Mater. 117 (2009) 111–117. https://doi.org/10.1016/j.micromeso.2008.06.040.

[107] A. Martinez Joaristi, J. Juan-Alcañiz, P. Serra-Crespo, F. Kapteijn, J. Gascon, Electrochemical Synthesis of Some Archetypical Zn 2+ , Cu 2+ , and Al 3+ Metal Organic Frameworks, Cryst. Growth Des. 12 (2012) 3489–3498. https://doi.org/10.1021/cg300552w.

[108] U. Mueller, M. Schubert, F. Teich, H. Puetter, K. Schierle-Arndt, J. Pastré, Metal–organic frameworks—prospective industrial applications, J. Mater. Chem. 16 (2006) 626–636. https://doi.org/10.1039/B511962F.

[109] H.K. Kim, W.S. Yun, M.-B. Kim, J.Y. Kim, Y.-S. Bae, J. Lee, N.C. Jeong, A Chemical Route to Activation of Open Metal Sites in the Copper-Based Metal–Organic Framework Materials HKUST-1 and Cu-MOF-2, J. Am. Chem. Soc. 137 (2015) 10009–10015. https://doi.org/10.1021/jacs.5b06637.

[110] D. Sun, W. Liu, M. Qiu, Y. Zhang, Z. Li, Introduction of a mediator for enhancing photocatalytic performance via post-synthetic metal exchange in metal–organic frameworks (MOFs), Chem. Commun. 51 (2015) 2056–2059. https://doi.org/10.1039/C4CC09407G.

[111] E. Haque, N.A. Khan, J.E. Lee, S.H. Jhung, Facile Purification of Porous Metal Terephthalates with Ultrasonic Treatment in the Presence of Amides, Chem. - A Eur. J. 15 (2009) 11730–11736. https://doi.org/10.1002/chem.200902036.

[112] E.J. Lee, J. Bae, K.M. Choi, N.C. Jeong, Exploiting Microwave Chemistry for Activation of Metal–Organic Frameworks, ACS Appl. Mater. Interfaces 11 (2019) 35155–35161. https://doi.org/10.1021/acsami.9b12201.

[113] J. Espín, L. Garzón-Tovar, A. Carné-Sánchez, I. Imaz, D. Maspoch, Photothermal Activation of Metal–Organic Frameworks Using a UV–Vis Light Source, ACS Appl. Mater. Interfaces 10 (2018) 9555–9562. https://doi.org/10.1021/acsami.8b00557.

[114] O.K. Farha, A. Özgür Yazaydın, I. Eryazici, C.D. Malliakas, B.G. Hauser, M.G. Kanatzidis, S.T. Nguyen, R.Q. Snurr, J.T. Hupp, De novo synthesis of a metal–organic framework material featuring ultrahigh surface area and gas storage capacities, Nat. Chem. 2 (2010) 944–948. https://doi.org/10.1038/nchem.834.

[115] H. Furukawa, N. Ko, Y.B. Go, N. Aratani, S.B. Choi, E. Choi, A.Ö. Yazaydin, R.Q. Snurr, M. O'Keeffe, J. Kim, O.M. Yaghi, Ultrahigh Porosity in Metal-Organic Frameworks, Science (80-.). 329 (2010) 424–428. https://doi.org/10.1126/science.1192160.

[116] L. Ma, A. Jin, Z. Xie, W. Lin, Freeze Drying Significantly Increases Permanent Porosity and

Hydrogen Uptake in 4,4-Connected Metalâ€“Organic Frameworks, Angew. Chemie Int. Ed. 48 (2009) 9905–9908. https://doi.org/10.1002/anie.200904983.

[117] Y.-P. He, Y.-X. Tan, J. Zhang, Comparative Study of Activation Methods on Tuning Gas Sorption Properties of a Metal–Organic Framework with Nanosized Ligands, Inorg. Chem. 51 (2012) 11232–11234. https://doi.org/10.1021/ic3017529.

[118] Z. Hu, A. Nalaparaju, Y. Peng, J. Jiang, D. Zhao, Modulated Hydrothermal Synthesis of UiO-66(Hf)-Type Metal–Organic Frameworks for Optimal Carbon Dioxide Separation, Inorg. Chem. 55 (2016) 1134–1141. https://doi.org/10.1021/acs.inorgchem.5b02312.

[119] M. Taddei, D. Tiana, N. Casati, J.A. van Bokhoven, B. Smit, M. Ranocchiari, Mixed-linker UiO-66: structure–property relationships revealed by a combination of high-resolution powder X-ray diffraction and density functional theory calculations, Phys. Chem. Chem. Phys. 19 (2017) 1551–1559. https://doi.org/10.1039/C6CP07801J.

[120] Z. Hu, Y. Peng, Z. Kang, Y. Qian, D. Zhao, A Modulated Hydrothermal (MHT) Approach for the Facile Synthesis of UiO-66-Type MOFs, Inorg. Chem. 54 (2015) 4862–4868. https://doi.org/10.1021/acs.inorgchem.5b00435.

[121] M. Zeama, M. Morsy, S. Abdel-Azeim, M. Abdelnaby, A. Alloush, Z. Yamani, Photophysical and photocatalytic properties of structurally modified UiO-66, Inorganica Chim. Acta 501 (2020) 119287. https://doi.org/10.1016/j.ica.2019.119287.

[122] X. Zeng, Y. Zhang, J. Zhang, H. Hu, X. Wu, Z. Long, X. Hou, Facile colorimetric sensing of Pb 2+ using bimetallic lanthanide metal-organic frameworks as luminescent probe for field screen analysis of lead-polluted environmental water, Microchem. J. 134 (2017) 140–145. https://doi.org/10.1016/j.microc.2017.05.011.

[123] M. Liu, S. Li, N. Tang, Y. Wang, X. Yang, S. Wang, Highly efficient capture of phosphate from water via cerium-doped metal-organic frameworks, J. Clean. Prod. 265 (2020) 121782. https://doi.org/10.1016/j.jclepro.2020.121782.

[124] W. Morris, B. Volosskiy, S. Demir, F. Gándara, P.L. McGrier, H. Furukawa, D. Cascio, J.F. Stoddart, O.M. Yaghi, Synthesis, Structure, and Metalation of Two New Highly Porous Zirconium Metal–Organic Frameworks, Inorg. Chem. 51 (2012) 6443–6445. https://doi.org/10.1021/ic300825s.

[125] M.J. Katz, Z.J. Brown, Y.J. Colón, P.W. Siu, K.A. Scheidt, R.Q. Snurr, J.T. Hupp, O.K. Farha, A facile synthesis of UiO-66, UiO-67 and their derivatives, Chem. Commun. 49 (2013) 9449. https://doi.org/10.1039/c3cc46105j.

[126] Z. Liang, Y. Ou, E.-S.M. El-Sayed, K. Su, W. Wang, D. Yuan, Effect of Functional Groups on Low-Concentration Carbon Dioxide Capture in UiO-66 -Type Metal–Organic Frameworks, Inorg. Chem. 62 (2023) 8309–8314. https://doi.org/10.1021/acs.inorgchem.3c00821.

[127] D. Sun, Y. Fu, W. Liu, L. Ye, D. Wang, L. Yang, X. Fu, Z. Li, Studies on Photocatalytic CO 2 Reduction over NH2-UiO-66(Zr) and Its Derivatives: Towards a Better Understanding of Photocatalysis on Metal–Organic Frameworks, Chem. – A Eur. J. 19 (2013) 14279–14285. https://doi.org/10.1002/chem.201301728.

[128] K. Koh, A.G. Wong-Foy, A.J. Matzger, Coordination Copolymerization Mediated by Zn 4 O(CO 2 R) 6 Metal Clusters: a Balancing Act between Statistics and Geometry, J. Am. Chem. Soc. 132 (2010) 15005–15010. https://doi.org/10.1021/ja1065009.

[129] S. Mahdian, M.R. Naimi-Jamal, L. Panahi, Activity of M 2 (BDC) 2 (DABCO) (M= Co, Ni, Cu and Zn) Metal-Organic Frameworks Prepared via Ball-Milling Solvent-Free Method in Acylation of Alcohols, Amines and Aldehydes, ChemistrySelect 3 (2018) 11223–11229. https://doi.org/10.1002/slct.201801585.

[130] C. Wang, Z. Xie, K.E. DeKrafft, W. Lin, Doping Metal–Organic Frameworks for Water Oxidation, Carbon Dioxide Reduction, and Organic Photocatalysis, J. Am. Chem. Soc. 133 (2011) 13445–13454. https://doi.org/10.1021/ja203564w.

[131] Z.-Q. Li, L.-G. Qiu, W. Wang, T. Xu, Y. Wu, X. Jiang, Fabrication of nanosheets of a fluorescent metal–organic framework [Zn(BDC)(H2O)] (BDC = 1,4-benzenedicarboxylate): Ultrasonic synthesis and sensing of ethylamine, Inorg. Chem. Commun. 11 (2008) 1375–1377. https://doi.org/10.1016/j.inoche.2008.09.010.

[132] J. Zhuang, D. Ceglarek, S. Pethuraj, A. Terfort, Rapid Room-Temperature Synthesis of Metal–Organic Framework HKUST-1 Crystals in Bulk and as Oriented and Patterned Thin Films, Adv. Funct. Mater. 21 (2011) 1442–1447. https://doi.org/10.1002/adfm.201002529.

[133] P. Chowdhury, C. Bikkina, D. Meister, F. Dreisbach, S. Gumma, Comparison of adsorption isotherms on Cu-BTC metal organic frameworks synthesized from different routes, Microporous Mesoporous Mater. 117 (2009) 406–413. https://doi.org/10.1016/j.micromeso.2008.07.029.

[134] T. Rodenas, I. Luz, G. Prieto, B. Seoane, H. Miro, A. Corma, F. Kapteijn, F.X. Llabrés i Xamena, J. Gascon, Metal–organic framework nanosheets in polymer composite materials for gas separation, Nat. Mater. 14 (2015) 48–55. https://doi.org/10.1038/nmat4113.

[135] N. Missaoui, A. Chrouda, F. Bourguiba, J. Serafin, Impact of metal precursor and molar ratios on adsorption and separation of CO2 and CH4 by SOD-ZIF-67 prepared using green solvent-free synthesis, Fuel 378 (2024) 132840. https://doi.org/10.1016/j.fuel.2024.132840.

[136] B. Shan, S.M. McIntyre, M.R. Armstrong, Y. Shen, B. Mu, Investigation of Missing-Cluster Defects in UiO-66 and Ferrocene Deposition into Defect-Induced Cavities, Ind. Eng. Chem. Res. 57 (2018) 14233–14241. https://doi.org/10.1021/acs.iecr.8b03516.

[137] S. Yuan, J.-S. Qin, H.H.-Q. Xu, J. Su, D. Rossi, Y. Chen, L. Zhang, C. Lollar, Q. Wang, H.-L. Jiang, D.H. Son, H.H.-Q. Xu, Z. Huang, X. Zou, H.-C. Zhou, [Ti 8 Zr 2 O 12 (COO) 16] Cluster: An Ideal Inorganic Building Unit for Photoactive Metal–Organic Frameworks, ACS

Cent. Sci. 4 (2018) 105–111. https://doi.org/10.1021/acscentsci.7b00497.

[138] F. Vermoortele, B. Bueken, G. Le Bars, B. Van de Voorde, M. Vandichel, K. Houthoofd, A. Vimont, M. Daturi, M. Waroquier, V. Van Speybroeck, C. Kirschhock, D.E. De Vos, Synthesis Modulation as a Tool To Increase the Catalytic Activity of Metal–Organic Frameworks: The Unique Case of UiO-66(Zr), J. Am. Chem. Soc. 135 (2013) 11465–11468. https://doi.org/10.1021/ja405078u.

[139] P.B.S. Rallapalli, M.C. Raj, S. Senthilkumar, R.S. Somani, H.C. Bajaj, HF-free synthesis of MIL-101(Cr) and its hydrogen adsorption studies, Environ. Prog. Sustain. Energy 35 (2016) 461–468. https://doi.org/10.1002/ep.12239.

[140] F. Wang, H. Guo, Y. Chai, Y. Li, C. Liu, The controlled regulation of morphology and size of HKUST-1 by “coordination modulation method,” Microporous Mesoporous Mater. 173 (2013) 181–188. https://doi.org/10.1016/j.micromeso.2013.02.023.

[141] J. Cravillon, R. Nayuk, S. Springer, A. Feldhoff, K. Huber, M. Wiebcke, Controlling Zeolitic Imidazolate Framework Nano- and Microcrystal Formation: Insight into Crystal Growth by Time-Resolved In Situ Static Light Scattering, Chem. Mater. 23 (2011) 2130–2141. https://doi.org/10.1021/cm103571y.

[142] M.-H. Pham, G.-T. Vuong, F.-G. Fontaine, T.-O. Do, Rational Synthesis of Metal–Organic Framework Nanocubes and Nanosheets Using Selective Modulators and Their Morphology-Dependent Gas-Sorption Properties, Cryst. Growth Des. 12 (2012) 3091–3095. https://doi.org/10.1021/cg300297p.

[143] H. Guo, Y. Zhu, S. Wang, S. Su, L. Zhou, H. Zhang, Combining Coordination Modulation with Acid–Base Adjustment for the Control over Size of Metal–Organic Frameworks, Chem. Mater. 24 (2012) 444–450. https://doi.org/10.1021/cm202593h.

[144] J.-M. Yang, Q. Liu, Y.-S. Kang, W.-Y. Sun, Controlled growth and gas sorption properties of IRMOF-3 nano/microcrystals, Dalt. Trans. 43 (2014) 16707–16712. https://doi.org/10.1039/C4DT02429J.

[145] S. Wang, Y. Lv, Y. Yao, H. Yu, G. Lu, Modulated synthesis of monodisperse MOF-5 crystals with tunable sizes and shapes, Inorg. Chem. Commun. 93 (2018) 56–60. https://doi.org/10.1016/j.inoche.2018.05.010.

[146] A. Umemura, S. Diring, S. Furukawa, H. Uehara, T. Tsuruoka, S. Kitagawa, Morphology Design of Porous Coordination Polymer Crystals by Coordination Modulation, J. Am. Chem. Soc. 133 (2011) 15506–15513. https://doi.org/10.1021/ja204233q.

[147] P. Sarawade, H. Tan, V. Polshettiwar, Shape- and Morphology-Controlled Sustainable Synthesis of Cu, Co, and In Metal Organic Frameworks with High CO 2 Capture Capacity, ACS Sustain. Chem. Eng. 1 (2013) 66–74. https://doi.org/10.1021/sc300036p.

[148] X. Kang, Q. Zhu, X. Sun, J. Hu, J. Zhang, Z. Liu, B. Han, Highly efficient electrochemical

reduction of CO 2 to CH 4 in an ionic liquid using a metal–organic framework cathode, Chem. Sci. 7 (2016) 266–273. https://doi.org/10.1039/C5SC03291A.

[149] C. Huang, X. Su, D. Zhang, X. Gu, R. Liu, H. Zhu, Co-MOF nanocatalysts of tunable shape and size for selective aerobic oxidation of toluene, Inorganica Chim. Acta 510 (2020) 119737. https://doi.org/10.1016/j.ica.2020.119737.

[150] X. qiang Cao, X. Wang, M. Chen, F. Xiao, Y. meng Huang, X. jun Lyu, Synthesis of nanoscale zeolitic imidazolate framework-8 (ZIF-8) using reverse micro-emulsion for Congo red adsorption, Sep. Purif. Technol. 260 (2021) 118062. https://doi.org/10.1016/j.seppur.2020.118062.

[151] Y. Shan, G. Zhang, Y. Shi, H. Pang, Synthesis and catalytic application of defective MOF materials, Cell Reports Phys. Sci. 4 (2023) 101301. https://doi.org/10.1016/j.xcrp.2023.101301.

[152] M. Khan, Z. Akmal, M. Tayyab, S. Mansoor, A. Zeb, Z. Ye, J. Zhang, S. Wu, L. Wang, MOFs materials as photocatalysts for CO2 reduction: Progress, challenges and perspectives, Carbon Capture Sci. Technol. 11 (2024) 100191. https://doi.org/10.1016/j.ccst.2024.100191.

[153] L. Li, S. Shen, W. Ai, S. Song, Y. Bai, H. Liu, Facilely synthesized Eu3+ post-functionalized UiO-66-type metal-organic framework for rapid and highly selective detection of Fe3+ in aqueous solution, Sensors Actuators B Chem. 267 (2018) 542–548. https://doi.org/10.1016/j.snb.2018.04.064.

[154] B. Rungtaweevoranit, J. Baek, J.R. Araujo, B.S. Archanjo, K.M. Choi, O.M. Yaghi, G.A. Somorjai, Copper Nanocrystals Encapsulated in Zr-based Metal–Organic Frameworks for Highly Selective CO 2 Hydrogenation to Methanol, Nano Lett. 16 (2016) 7645–7649. https://doi.org/10.1021/acs.nanolett.6b03637.

[155] Q. Yang, W. Liu, B. Wang, W. Zhang, X. Zeng, C. Zhang, Y. Qin, X. Sun, T. Wu, J. Liu, F. Huo, J. Lu, Regulating the spatial distribution of metal nanoparticles within metal-organic frameworks to enhance catalytic efficiency, Nat. Commun. 8 (2017) 14429. https://doi.org/10.1038/ncomms14429.

[156] S.-Q. Wang, X.-Y. Zhang, X.-Y. Dao, X.-M. Cheng, W.-Y. Sun, Cu 2 O@Cu@UiO-66-NH 2 Ternary Nanocubes for Photocatalytic CO 2 Reduction, ACS Appl. Nano Mater. 3 (2020) 10437–10445. https://doi.org/10.1021/acsanm.0c02312.

[157] K.A. McDonald, J.I. Feldblyum, K. Koh, A.G. Wong-Foy, A.J. Matzger, Polymer@MOF@MOF: “grafting from” atom transfer radical polymerization for the synthesis of hybrid porous solids, Chem. Commun. 51 (2015) 11994–11996. https://doi.org/10.1039/C5CC03027G.

[158] S.K. Elsaidi, S.R. Venna, M.H. Mohamed, M.J. Gipple, D.P. Hopkinson, Dual-Layer MOF Composite Membranes with Tuned Interface Interaction for Postcombustion Carbon Dioxide

Separation, Cell Reports Phys. Sci. 1 (2020) 100059. https://doi.org/10.1016/j.xcrp.2020.100059.

[159] M. Zhang, D. Wu, Y. Ye, L. Wu, Z. Yao, X. Ma, L. Wang, Z. Zhang, S. Xiang, Thermal Conversion of MOF@MOF: Synthesis of an N-Doped Carbon Material with Excellent ORR Performance, Chempluschem 83 (2018) 1044–1051. https://doi.org/10.1002/cplu.201800392.

[160] A. Melillo, M. Cabrero-Antonino, B. Ferrer, A. Dhakshinamoorthy, H.G. Baldoví, S. Navalón, MOF-on-MOF Composites with UiO-66-Based Materials as Photocatalysts for the Overall Water Splitting under Sunlight Irradiation, Energy & Fuels 37 (2023) 5457–5468. https://doi.org/10.1021/acs.energyfuels.3c00309.

[161] T.T.Y. Tan, J.T.M. Cham, M.R. Reithofer, T.S. Andy Hor, J.M. Chin, Motorized Janus metal organic framework crystals, Chem. Commun. 50 (2014) 15175–15178. https://doi.org/10.1039/C4CC06952H.

[162] Q. Zha, F. Yuan, G. Qin, Y. Ni, Cobalt-Based MOF-on-MOF Two-Dimensional Heterojunction Nanostructures for Enhanced Oxygen Evolution Reaction Electrocatalytic Activity, Inorg. Chem. 59 (2020) 1295–1305. https://doi.org/10.1021/acs.inorgchem.9b03011.

[163] C. Liu, Q. Sun, L. Lin, J. Wang, C. Zhang, C. Xia, T. Bao, J. Wan, R. Huang, J. Zou, C. Yu, Ternary MOF-on-MOF heterostructures with controllable architectural and compositional complexity via multiple selective assembly, Nat. Commun. 11 (2020) 4971. https://doi.org/10.1038/s41467-020-18776-z.

[164] L. Liu, L. Zhang, F. Wang, K. Qi, H. Zhang, X. Cui, W. Zheng, Bi-metal–organic frameworks type II heterostructures for enhanced photocatalytic styrene oxidation, Nanoscale 11 (2019) 7554–7559. https://doi.org/10.1039/C9NR00790C.

[165] C. Liu, L. Lin, Q. Sun, J. Wang, R. Huang, W. Chen, S. Li, J. Wan, J. Zou, C. Yu, Site-specific growth of MOF-on-MOF heterostructures with controllable nano-architectures: beyond the combination of MOF analogues, Chem. Sci. 11 (2020) 3680–3686. https://doi.org/10.1039/D0SC00417K.

[166] Y. Gu, Y. Wu, L. Li, W. Chen, F. Li, S. Kitagawa, Controllable Modular Growth of Hierarchical MOF-on-MOF Architectures, Angew. Chemie Int. Ed. 56 (2017) 15658–15662. https://doi.org/10.1002/anie.201709738.

[167] Y. Lee, S. Kim, H. Fei, J.K. Kang, S.M. Cohen, Photocatalytic CO 2 reduction using visible light by metal-monocatecholato species in a metal–organic framework, Chem. Commun. 51 (2015) 16549–16552. https://doi.org/10.1039/C5CC04506A.

[168] H. Fei, S.M. Cohen, Metalation of a Thiocatechol-Functionalized Zr(IV)-Based Metal–Organic Framework for Selective C–H Functionalization, J. Am. Chem. Soc. 137 (2015) 2191–2194. https://doi.org/10.1021/ja5126885.

[169] S. Yuan, W. Lu, Y.-P. Chen, Q. Zhang, T.-F. Liu, D. Feng, X. Wang, J. Qin, H.-C. Zhou, Sequential Linker Installation: Precise Placement of Functional Groups in Multivariate Metal–Organic Frameworks, J. Am. Chem. Soc. 137 (2015) 3177–3180. https://doi.org/10.1021/ja512762r.

[170] S. Han, D. Kim, S. Lee, H. Choi, S.W. Moon, A. Sharma, J. Seong, J. Lim, S. Jeong, S. Bin Baek, Y.S. Kim, C.S. Kim, S.K. Min, M.S. Lah, Symmetry-Mismatched SBU Transformation in MOFs: Postsynthetic Metal Exchange from Zn to Fe and Its Effects on Gas Adsorption and Dye Selectivity, ACS Appl. Mater. Interfaces 15 (2023) 48406–48415. https://doi.org/10.1021/acsami.3c10943.

[171] Y. Lee, S. Kim, J.K. Kang, S.M. Cohen, Photocatalytic CO 2 reduction by a mixed metal (Zr/Ti), mixed ligand metal–organic framework under visible light irradiation, Chem. Commun. 51 (2015) 5735–5738. https://doi.org/10.1039/C5CC00686D.

[172] M. Kim, J.F. Cahill, H. Fei, K.A. Prather, S.M. Cohen, Postsynthetic Ligand and Cation Exchange in Robust Metal–Organic Frameworks, J. Am. Chem. Soc. 134 (2012) 18082–18088. https://doi.org/10.1021/ja3079219.

[173] J. Baek, B. Rungtaweevoranit, X. Pei, M. Park, S.C. Fakra, Y.-S. Liu, R. Matheu, S.A. Alshmimri, S. Alshehri, C.A. Trickett, G.A. Somorjai, O.M. Yaghi, Bioinspired Metal–Organic Framework Catalysts for Selective Methane Oxidation to Methanol, J. Am. Chem. Soc. 140 (2018) 18208–18216. https://doi.org/10.1021/jacs.8b11525.

[174] I.S. Kim, J. Borycz, A.E. Platero-Prats, S. Tussupbayev, T.C. Wang, O.K. Farha, J.T. Hupp, L. Gagliardi, K.W. Chapman, C.J. Cramer, A.B.F. Martinson, Targeted Single-Site MOF Node Modification: Trivalent Metal Loading via Atomic Layer Deposition, Chem. Mater. 27 (2015) 4772–4778. https://doi.org/10.1021/acs.chemmater.5b01560.

[175] H. Wang, Z. Shi, J. Yang, T. Sun, B. Rungtaweevoranit, H. Lyu, Y. Zhang, O.M. Yaghi, Docking of Cu I and Ag I in Metal–Organic Frameworks for Adsorption and Separation of Xenon, Angew. Chemie Int. Ed. 60 (2021) 3417–3421. https://doi.org/10.1002/anie.202015262.

[176] X. Liu, Y. Xu, Q. Liu, W. Zhang, 8-Hydroxyquinoline and Eu 3+ Incorporated Metal–Organic Framework Nanosystems with Tunable Emissions for White Light and Anticounterfeiting Applications, ACS Appl. Nano Mater. 4 (2021) 313–321. https://doi.org/10.1021/acsanm.0c02671.

[177] Z. Xiaoxiong, Z. Wenjun, L. Cuiliu, Q. Xiaohong, Z. Chengyu, Eu 3+ -Postdoped UIO-66-Type Metal–Organic Framework as a Luminescent Sensor for Hg 2+ Detection in Aqueous Media, Inorg. Chem. 58 (2019) 3910–3915. https://doi.org/10.1021/acs.inorgchem.8b03555.

[178] M. Kaposi, M. Cokoja, C.H. Hutterer, S.A. Hauser, T. Kaposi, F. Klappenberger, A. Pöthig, J. V. Barth, W.A. Herrmann, F.E. Kühn, Immobilisation of a molecular epoxidation catalyst

on UiO-66 and -67: the effect of pore size on catalyst activity and recycling, Dalt. Trans. 44 (2015) 15976–15983. https://doi.org/10.1039/C5DT01340B.

[179] S. Sadeghi, M. Jafarzadeh, A. Reza Abbasi, K. Daasbjerg, Incorporation of CuO NPs into modified UiO-66-NH 2 metal–organic frameworks (MOFs) with melamine for catalytic C–O coupling in the Ullmann condensation, New J. Chem. 41 (2017) 12014–12027. https://doi.org/10.1039/C7NJ02114C.

[180] R. Kardanpour, S. Tangestaninejad, V. Mirkhani, M. Moghadam, I. Mohammadpoor-Baltork, F. Zadehahmadi, Anchoring of Cu(II) onto surface of porous metal-organic framework through post-synthesis modification for the synthesis of benzimidazoles and benzothiazoles, J. Solid State Chem. 235 (2016) 145–153. https://doi.org/10.1016/j.jssc.2015.11.019.

[181] R. Kardanpour, S. Tangestaninejad, V. Mirkhani, M. Moghadam, I. Mohammadpoor-Baltork, F. Zadehahmadi, Efficient alkene epoxidation catalyzed by molybdenyl acetylacetonate supported on aminated UiO-66 metal−organic framework, J. Solid State Chem. 226 (2015) 262–272. https://doi.org/10.1016/j.jssc.2014.11.020.

[182] Y. Zhou, B. Yan, Lanthanides post-functionalized nanocrystalline metal–organic frameworks for tunable white-light emission and orthogonal multi-readout thermometry, Nanoscale 7 (2015) 4063–4069. https://doi.org/10.1039/C4NR06873D.

[183] V. Nevruzoglu, S. Demir, G. Karaca, M. Tomakin, N. Bilgin, F. Yilmaz, Improving the stability of solar cells using metal–organic frameworks, J. Mater. Chem. A 4 (2016) 7930–7935. https://doi.org/10.1039/C6TA02609E.

[184] M.T. Huxley, C.J. Coghlan, W.M. Bloch, A. Burgun, C.J. Doonan, C.J. Sumby, X-ray crystallographic insights into post-synthetic metalation products in a metal–organic framework, Philos. Trans. R. Soc. A Math. Phys. Eng. Sci. 375 (2017) 20160028. https://doi.org/10.1098/rsta.2016.0028.

[185] J. Wang, T. Li, Z. Zhao, X. Zhang, W. Pang, Pd Nanoparticles Embedded Into MOF-808: Synthesis, Structural Characteristics, and Catalyst Properties for the Suzuki–Miyaura Coupling Reaction, Catal. Letters 152 (2022) 1545–1554. https://doi.org/10.1007/s10562-021-03731-4.

[186] J. Liu, D.M. Strachan, P.K. Thallapally, Enhanced noble gas adsorption in Ag@MOF-74Ni, Chem. Commun. 50 (2014) 466–468. https://doi.org/10.1039/C3CC47777K.

[187] T.J. Ferreira, C. Cabral, T.O. Carvalho, J. Pais, L.M. Esteves, L.P.C. Silva, P.M. Reis, J.M.S.S. Esperança, I.A.A.C. Esteves, Cationic effect study in acetate-based ionic liquids/ZIF-8 composites for CO2 sorption, Sustain. Mater. Technol. 42 (2024) e01122. https://doi.org/10.1016/j.susmat.2024.e01122.

[188] T.J. Ferreira, B.A. de Moura, L.M. Esteves, P.M. Reis, J.M.S.S. Esperança, I.A.A.C. Esteves, Biocompatible ammonium-based ionic liquids/ZIF-8 composites for CO2/CH4 and CO2/N2 separations, Sustain. Mater. Technol. 35 (2023) e00558.

https://doi.org/10.1016/j.susmat.2022.e00558.

[189] T.J. Ferreira, R.P.P.L. Ribeiro, J.P.B. Mota, L.P.N. Rebelo, J.M.S.S. Esperança, I.A.A.C. Esteves, Ionic Liquid-Impregnated Metal–Organic Frameworks for CO 2 /CH 4 Separation, ACS Appl. Nano Mater. 2 (2019) 7933–7950. https://doi.org/10.1021/acsanm.9b01936.

[190] A. Aijaz, T. Akita, H. Yang, Q. Xu, From ionic-liquid@metal–organic framework composites to heteroatom-decorated large-surface area carbons: superior CO2 and H2 uptake, Chem. Commun. 50 (2014) 6498. https://doi.org/10.1039/c4cc02459a.

[191] F.A. Philip, A. Henni, Enhancement of post-combustion CO2 capture capacity by incorporation of task-specific ionic liquid into ZIF-8, Microporous Mesoporous Mater. 330 (2022) 111580. https://doi.org/10.1016/j.micromeso.2021.111580.

[192] D. Li, A. Yadav, H. Zhou, K. Roy, P. Thanasekaran, C. Lee, Advances and Applications of Metal-Organic Frameworks (MOFs) in Emerging Technologies: A Comprehensive Review, Glob. Challenges 8 (2024). https://doi.org/10.1002/gch2.202300244.

[193] M.S. Khan, Y. Li, D.-S. Li, J. Qiu, X. Xu, H.Y. Yang, A review of metal–organic framework (MOF) materials as an effective photocatalyst for degradation of organic pollutants, Nanoscale Adv. 5 (2023) 6318–6348. https://doi.org/10.1039/D3NA00627A.

[194] T. Yang, H. Zhang, B. Pang, J.W.C. Wong, Recent Advances in Transition Metal-Based Metal-Organic Frameworks for Hydrogen Production, Small Sci. 5 (2025). https://doi.org/10.1002/smsc.202400446.

[195] B. Saboorizadeh, R. Zare-Dorabei, M. Safavi, V. Safarifard, Applications of Metal–Organic Frameworks (MOFs) in Drug Delivery, Biosensing, and Therapy: A Comprehensive Review, Langmuir 40 (2024) 22477–22503. https://doi.org/10.1021/acs.langmuir.4c02795.

[196] Z.A. Sandhu, M.A. Raza, N.S. Awwad, H.A. Ibrahium, U. Farwa, S. Ashraf, A. Dildar, E. Fatima, S. Ashraf, F. Ali, Metal–organic frameworks for next-generation energy storage devices; a systematic review, Mater. Adv. 5 (2024) 30–50. https://doi.org/10.1039/D3MA00822C.

[197] L. Jimenez-Lopez, R. Morales Ospino, L.G. de Araujo, A. Celzard, V. Fierro, Latest developments in the synthesis of metal–organic frameworks and their hybrids for hydrogen storage, Nanoscale 17 (2025) 6390–6413. https://doi.org/10.1039/D4NR03969F.

[198] Y. Ma, Q. Tang, W.-Y. Sun, Z.-Y. Yao, W. Zhu, T. Li, J. Wang, Assembling ultrafine TiO2 nanoparticles on UiO-66 octahedrons to promote selective photocatalytic conversion of CO2 to CH4 at a low concentration, Appl. Catal. B Environ. 270 (2020) 118856. https://doi.org/10.1016/j.apcatb.2020.118856.

[199] S.R. Firoozabadi, M.R. Khosravi-Nikou, A. Shariati, CO2 photoreduction using TiO2 nanoflower /UiO-66 composite under UV light irradiation, J. Environ. Chem. Eng. 11 (2023) 110978. https://doi.org/10.1016/j.jece.2023.110978.

[200] L. Shi, T. Wang, H. Zhang, K. Chang, J. Ye, Electrostatic Self-Assembly of Nanosized Carbon Nitride Nanosheet onto a Zirconium Metal–Organic Framework for Enhanced Photocatalytic CO 2 Reduction, Adv. Funct. Mater. 25 (2015) 5360–5367. https://doi.org/10.1002/adfm.201502253.

[201] X. Chen, Q. Li, J. Li, J. Chen, H. Jia, Modulating charge separation via in situ hydrothermal assembly of low content Bi2S3 into UiO-66 for efficient photothermocatalytic CO2 reduction, Appl. Catal. B Environ. 270 (2020) 118915. https://doi.org/10.1016/j.apcatb.2020.118915.

[202] D. Li, B. Zhu, Z. Sun, Q. Liu, L. Wang, H. Tang, Construction of UiO-66/Bi4O5Br2 Type-II Heterojunction to Boost Charge Transfer for Promoting Photocatalytic CO2 Reduction Performance, Front. Chem. 9 (2021). https://doi.org/10.3389/fchem.2021.804204.

[203] M. Bhattacharya, K.J. Chandler, J. Geary, C.T. Saouma, The role of leached Zr in the photocatalytic reduction of CO 2 to formate by derivatives of UiO-66 metal organic frameworks, Dalt. Trans. 49 (2020) 4751–4757. https://doi.org/10.1039/D0DT00524J.

[204] Q. Niu, S. Dong, J. Tian, G. Huang, J. Bi, L. Wu, Rational Design of Novel COF/MOF S-Scheme Heterojunction Photocatalyst for Boosting CO 2 Reduction at Gas–Solid Interface, ACS Appl. Mater. Interfaces 14 (2022) 24299–24308. https://doi.org/10.1021/acsami.2c02439.

[205] H.-N. Wang, Y.-H. Zou, Y.-M. Fu, X. Meng, L. Xue, H.-X. Sun, Z.-M. Su, Integration of zirconium-based metal–organic framework with CdS for enhanced photocatalytic conversion of CO 2 to CO, Nanoscale 13 (2021) 16977–16985. https://doi.org/10.1039/D1NR04417F.

[206] H. Zhao, X. Yang, R. Xu, J. Li, S. Gao, R. Cao, CdS/NH 2 -UiO-66 hybrid membrane reactors for the efficient photocatalytic conversion of CO 2, J. Mater. Chem. A 6 (2018) 20152–20160. https://doi.org/10.1039/C8TA05970E.

[207] X. Su, T. Xu, R. Ye, C. Guo, S.M. Wabaidur, D.-L. Chen, S. Aftab, Y. Zhong, Y. Hu, One-pot solvothermal synthesis of In-doped amino-functionalized UiO-66 Zr-MOFs with enhanced ligand-to-metal charge transfer for efficient visible-light-driven CO2 reduction, J. Colloid Interface Sci. 646 (2023) 129–140. https://doi.org/10.1016/j.jcis.2023.05.041.

[208] A. Crake, K.C. Christoforidis, A. Kafizas, S. Zafeiratos, C. Petit, CO 2 capture and photocatalytic reduction using bifunctional TiO 2 /MOF nanocomposites under UV–vis irradiation, Appl. Catal. B Environ. 210 (2017) 131–140. https://doi.org/10.1016/j.apcatb.2017.03.039.

[209] X. Wang, Y. Wang, G. Chai, G. Yang, C. Wang, W. Yan, Poly (triphenylamine)-decorated UIO-66-NH2 mesoporous architectures with enhanced photocatalytic activity for CO2 reduction and H2 evolution, J. CO2 Util. 51 (2021) 101654. https://doi.org/10.1016/j.jcou.2021.101654.

[210] X. Wang, G. Yang, G. Chai, M.S. Nasir, S. Wang, X. Zheng, C. Wang, W. Yan, Fabrication

of heterostructured UIO-66-NH2 /CNTs with enhanced activity and selectivity over photocatalytic CO2 reduction, Int. J. Hydrogen Energy 45 (2020) 30634–30646. https://doi.org/10.1016/j.ijhydene.2020.08.273.

[211] Y. Wang, L. Guo, Y. Zeng, H. Guo, S. Wan, M. Ou, S. Zhang, Q. Zhong, Amino-Assisted NH 2 -UiO-66 Anchored on Porous g-C 3 N 4 for Enhanced Visible-Light-Driven CO 2 Reduction, ACS Appl. Mater. Interfaces 11 (2019) 30673–30681. https://doi.org/10.1021/acsami.9b04302.

[212] X. Wang, X. Zhao, D. Zhang, G. Li, H. Li, Microwave irradiation induced UIO-66-NH2 anchored on graphene with high activity for photocatalytic reduction of CO2, Appl. Catal. B Environ. 228 (2018) 47–53. https://doi.org/10.1016/j.apcatb.2018.01.066.

[213] L. Hong, R. Guo, Z. Zhang, Y. Yuan, X. Ji, Z. Lin, W. Pan, Fabrication of porous octahedron-flowerlike microsphere NH2-UiO-66/CdIn2S4 heterojunction photocatalyst for enhanced photocatalytic CO2 reduction, J. CO2 Util. 51 (2021) 101650. https://doi.org/10.1016/j.jcou.2021.101650.

[214] G. Wang, C.-T. He, R. Huang, J. Mao, D. Wang, Y. Li, Photoinduction of Cu Single Atoms Decorated on UiO-66-NH 2 for Enhanced Photocatalytic Reduction of CO 2 to Liquid Fuels, J. Am. Chem. Soc. 142 (2020) 19339–19345. https://doi.org/10.1021/jacs.0c09599.

[215] Y.-C. Hao, L.-W. Chen, J. Li, Y. Guo, X. Su, M. Shu, Q. Zhang, W.-Y. Gao, S. Li, Z.-L. Yu, L. Gu, X. Feng, A.-X. Yin, R. Si, Y.-W. Zhang, B. Wang, C.-H. Yan, Metal-organic framework membranes with single-atomic centers for photocatalytic CO2 and O2 reduction, Nat. Commun. 12 (2021) 2682. https://doi.org/10.1038/s41467-021-22991-7.

[216] H. Zhang, J. Wei, J. Dong, G. Liu, L. Shi, P. An, G. Zhao, J. Kong, X. Wang, X. Meng, J. Zhang, J. Ye, Efficient Visible-Light-Driven Carbon Dioxide Reduction by a Single-Atom Implanted Metal-Organic Framework, Angew. Chemie Int. Ed. 55 (2016) 14310–14314. https://doi.org/10.1002/anie.201608597.

[217] N. Li, J. Liu, J. Liu, L. Dong, Z. Xin, Y. Teng, Y. Lan, Adenine Components in Biomimetic Metal–Organic Frameworks for Efficient CO 2 Photoconversion, Angew. Chemie Int. Ed. 58 (2019) 5226–5231. https://doi.org/10.1002/anie.201814729.

[218] D. Chen, H. Xing, C. Wang, Z. Su, Highly efficient visible-light-driven CO 2 reduction to formate by a new anthracene-based zirconium MOF via dual catalytic routes, J. Mater. Chem. A 4 (2016) 2657–2662. https://doi.org/10.1039/C6TA00429F.

[219] X.-X. Li, J. Liu, L. Zhang, L.-Z. Dong, Z.-F. Xin, S.-L. Li, X.-Q. Huang-Fu, K. Huang, Y.-Q. Lan, Hydrophobic Polyoxometalate-Based Metal-Organic Framework for Efficient CO 2 Photoconversion, ACS Appl. Mater. Interfaces 11 (2019) 25790–25795. https://doi.org/10.1021/acsami.9b03861.

[220] X.-K. Wang, J. Liu, L. Zhang, L.-Z. Dong, S.-L. Li, Y.-H. Kan, D.-S. Li, Y.-Q. Lan, Monometallic Catalytic Models Hosted in Stable Metal–Organic Frameworks for Tunable

CO 2 Photoreduction, ACS Catal. 9 (2019) 1726–1732. https://doi.org/10.1021/acscatal.8b04887.

[221] Q. Liu, Z.-X. Low, L. Li, A. Razmjou, K. Wang, J. Yao, H. Wang, ZIF-8/Zn2GeO4 nanorods with an enhanced CO2 adsorption property in an aqueous medium for photocatalytic synthesis of liquid fuel, J. Mater. Chem. A 1 (2013) 11563. https://doi.org/10.1039/c3ta12433a.

[222] S. Wang, W. Yao, J. Lin, Z. Ding, X. Wang, Cobalt Imidazolate Metal-Organic Frameworks Photosplit CO 2 under Mild Reaction Conditions, Angew. Chemie Int. Ed. 53 (2014) 1034–1038. https://doi.org/10.1002/anie.201309426.

[223] Y. Fu, D. Sun, Y. Chen, R. Huang, Z. Ding, X. Fu, Z. Li, An Amine-Functionalized Titanium Metal-Organic Framework Photocatalyst with Visible-Light-Induced Activity for CO2 Reduction, Angew. Chemie Int. Ed. 51 (2012) 3364–3367. https://doi.org/10.1002/anie.201108357.

[224] D. Wang, R. Huang, W. Liu, D. Sun, Z. Li, Fe-Based MOFs for Photocatalytic CO 2 Reduction: Role of Coordination Unsaturated Sites and Dual Excitation Pathways, ACS Catal. 4 (2014) 4254–4260. https://doi.org/10.1021/cs501169t.

[225] Y. Xie, Z. Fang, L. Li, H. Yang, T.-F. Liu, Creating Chemisorption Sites for Enhanced CO 2 Photoreduction Activity through Alkylamine Modification of MIL-101-Cr, ACS Appl. Mater. Interfaces 11 (2019) 27017–27023. https://doi.org/10.1021/acsami.9b09436.

[226] B. Han, X. Ou, Z. Deng, Y. Song, C. Tian, H. Deng, Y. Xu, Z. Lin, Nickel Metal–Organic Framework Monolayers for Photoreduction of Diluted CO 2 : Metal-Node-Dependent Activity and Selectivity, Angew. Chemie Int. Ed. 57 (2018) 16811–16815. https://doi.org/10.1002/anie.201811545.

[227] H.-Q. Xu, J. Hu, D. Wang, Z. Li, Q. Zhang, Y. Luo, S.-H. Yu, H.-L. Jiang, Visible-Light Photoreduction of CO 2 in a Metal–Organic Framework: Boosting Electron–Hole Separation via Electron Trap States, J. Am. Chem. Soc. 137 (2015) 13440–13443. https://doi.org/10.1021/jacs.5b08773.

[228] L. Wang, P. Jin, J. Huang, H. She, Q. Wang, Integration of Copper(II)-Porphyrin Zirconium Metal–Organic Framework and Titanium Dioxide to Construct Z-Scheme System for Highly Improved Photocatalytic CO 2 Reduction, ACS Sustain. Chem. Eng. 7 (2019) 15660–15670. https://doi.org/10.1021/acssuschemeng.9b03773.

[229] N. Sadeghi, S. Sharifnia, T.-O. Do, Enhanced CO 2 photoreduction by a graphene–porphyrin metal–organic framework under visible light irradiation, J. Mater. Chem. A 6 (2018) 18031–18035. https://doi.org/10.1039/C8TA07158F.

[230] J. Zhao, Q. Wang, C. Sun, T. Zheng, L. Yan, M. Li, K. Shao, X. Wang, Z. Su, A hexanuclear cobalt metal–organic framework for efficient CO 2 reduction under visible light, J. Mater. Chem. A 5 (2017) 12498–12505. https://doi.org/10.1039/C7TA02611K.

[231] S. Zhang, L. Li, S. Zhao, Z. Sun, M. Hong, J. Luo, Hierarchical metal–organic framework nanoflowers for effective CO 2 transformation driven by visible light, J. Mater. Chem. A 3 (2015) 15764–15768. https://doi.org/10.1039/C5TA03322E.

[232] J.F. Kurisingal, Y. Rachuri, Y. Gu, G.-H. Kim, D.-W. Park, Binary metal-organic frameworks: Catalysts for the efficient solvent-free CO2 fixation reaction via cyclic carbonates synthesis, Appl. Catal. A Gen. 571 (2019) 1–11. https://doi.org/10.1016/j.apcata.2018.11.035.

[233] Y. Yu, S. Li, L. Huang, J. Yu, H. Zhang, S. Song, T. Zeng, Solar-driven CO2 conversion promoted by MOF − on − MOF homophase junction, Catal. Commun. 150 (2021) 106270. https://doi.org/10.1016/j.catcom.2020.106270.

[234] L. Wang, P. Jin, S. Duan, H. She, J. Huang, Q. Wang, In-situ incorporation of Copper(II) porphyrin functionalized zirconium MOF and TiO2 for efficient photocatalytic CO2 reduction, Sci. Bull. 64 (2019) 926–933. https://doi.org/10.1016/j.scib.2019.05.012.

[235] T.G. Grissom, D.M. Driscoll, D. Troya, N.S. Sapienza, P.M. Usov, A.J. Morris, J.R. Morris, Molecular-Level Insight into CO 2 Adsorption on the Zirconium-Based Metal–Organic Framework, UiO-66: A Combined Spectroscopic and Computational Approach, J. Phys. Chem. C 123 (2019) 13731–13738. https://doi.org/10.1021/acs.jpcc.9b02513.

[236] A. Kazemi, F. Moghadaskhou, M.A. Pordsari, F. Manteghi, A. Tadjarodi, A. Ghaemi, Enhanced CO2 capture potential of UiO-66-NH2 synthesized by sonochemical method: experimental findings and performance evaluation, Sci. Rep. 13 (2023) 19891. https://doi.org/10.1038/s41598-023-47221-6.

[237] S. Couck, J.F.M. Denayer, G. V. Baron, T. Rémy, J. Gascon, F. Kapteijn, An Amine-Functionalized MIL-53 Metal−Organic Framework with Large Separation Power for CO 2 and CH 4, J. Am. Chem. Soc. 131 (2009) 6326–6327. https://doi.org/10.1021/ja900555r.

[238] R. Vaidhyanathan, S.S. Iremonger, K.W. Dawson, G.K.H. Shimizu, An amine-functionalized metal organic framework for preferential CO2 adsorption at low pressures, Chem. Commun. (2009) 5230. https://doi.org/10.1039/b911481e.

[239] R. Vaidhyanathan, S.S. Iremonger, G.K.H. Shimizu, P.G. Boyd, S. Alavi, T.K. Woo, Direct Observation and Quantification of CO 2 Binding Within an Amine-Functionalized Nanoporous Solid, Science (80-.). 330 (2010) 650–653. https://doi.org/10.1126/science.1194237.

[240] P.D.C. Dietzel, R.E. Johnsen, H. Fjellvåg, S. Bordiga, E. Groppo, S. Chavan, R. Blom, Adsorption properties and structure of CO2 adsorbed on open coordination sites of metal–organic framework Ni2(dhtp) from gas adsorption, IR spectroscopy and X-ray diffraction, Chem. Commun. (2008) 5125. https://doi.org/10.1039/b810574j.

[241] J. Yu, P.B. Balbuena, Water Effects on Postcombustion CO 2 Capture in Mg-MOF-74, J. Phys. Chem. C 117 (2013) 3383–3388. https://doi.org/10.1021/jp311118x.

[242] C. Serre, S. Bourrelly, A. Vimont, N.A. Ramsahye, G. Maurin, P.L. Llewellyn, M. Daturi, Y. Filinchuk, O. Leynaud, P. Barnes, G. Férey, An Explanation for the Very Large Breathing Effect of a Metal–Organic Framework during CO2 Adsorption, Adv. Mater. 19 (2007) 2246–2251. https://doi.org/10.1002/adma.200602645.

[243] C. Chen, N. Feng, Q. Guo, Z. Li, X. Li, J. Ding, L. Wang, H. Wan, G. Guan, Surface engineering of a chromium metal-organic framework with bifunctional ionic liquids for selective CO2 adsorption: Synergistic effect between multiple active sites, J. Colloid Interface Sci. 521 (2018) 91–101. https://doi.org/10.1016/j.jcis.2018.03.029.

[244] S. Xian, Y. Wu, J. Wu, X. Wang, J. Xiao, Enhanced Dynamic CO 2 Adsorption Capacity and CO 2 /CH 4 Selectivity on Polyethylenimine-Impregnated UiO-66, Ind. Eng. Chem. Res. 54 (2015) 11151–11158. https://doi.org/10.1021/acs.iecr.5b03517.

[245] B. Arstad, H. Fjellvåg, K.O. Kongshaug, O. Swang, R. Blom, Amine functionalised metal organic frameworks (MOFs) as adsorbents for carbon dioxide, Adsorption 14 (2008) 755–762. https://doi.org/10.1007/s10450-008-9137-6.

[246] C. Chen, H. Zhu, B. Li, S. Zhu, Structuring Metal–Organic Framework Materials into Hierarchically Porous Composites through One-Pot Fabrication Strategy, Chem. – A Eur. J. 26 (2020) 3358–3363. https://doi.org/10.1002/chem.201905260.

[247] J.-S. Lee, J.-H. Kim, J.-T. Kim, J.-K. Suh, J.-M. Lee, C.-H. Lee, Adsorption Equilibria of CO 2 on Zeolite 13X and Zeolite X/Activated Carbon Composite, J. Chem. Eng. Data 47 (2002) 1237–1242. https://doi.org/10.1021/je020050e.

[248] S.-Y. Lee, S.-J. Park, Determination of the optimal pore size for improved CO2 adsorption in activated carbon fibers, J. Colloid Interface Sci. 389 (2013) 230–235. https://doi.org/10.1016/j.jcis.2012.09.018.

[249] J. Silvestre-Albero, A. Wahby, A. Sepúlveda-Escribano, M. Martínez-Escandell, K. Kaneko, F. Rodríguez-Reinoso, Ultrahigh CO2 adsorption capacity on carbon molecular sieves at room temperature, Chem. Commun. 47 (2011) 6840. https://doi.org/10.1039/c1cc11618e.

[250] R.W. Flaig, T.M. Osborn Popp, A.M. Fracaroli, E.A. Kapustin, M.J. Kalmutzki, R.M. Altamimi, F. Fathieh, J.A. Reimer, O.M. Yaghi, The Chemistry of CO 2 Capture in an Amine-Functionalized Metal–Organic Framework under Dry and Humid Conditions, J. Am. Chem. Soc. 139 (2017) 12125–12128. https://doi.org/10.1021/jacs.7b06382.

[251] W. Zhang, H. Huang, C. Zhong, D. Liu, Cooperative effect of temperature and linker functionality on CO2 capture from industrial gas mixtures in metal–organic frameworks: a combined experimental and molecular simulation study, Phys. Chem. Chem. Phys. 14 (2012) 2317. https://doi.org/10.1039/c2cp23839j.

[252] T.K. Vo, V.C. Nguyen, D.T. Quang, B.J. Park, J. Kim, Formation of structural defects within UiO-66(Zr)-(OH)2 framework for enhanced CO2 adsorption using a microwave-assisted continuous-flow tubular reactor, Microporous Mesoporous Mater. 312 (2021) 110746.

https://doi.org/10.1016/j.micromeso.2020.110746.

[253] W.L. Queen, M.R. Hudson, E.D. Bloch, J.A. Mason, M.I. Gonzalez, J.S. Lee, D. Gygi, J.D. Howe, K. Lee, T.A. Darwish, M. James, V.K. Peterson, S.J. Teat, B. Smit, J.B. Neaton, J.R. Long, C.M. Brown, Comprehensive study of carbon dioxide adsorption in the metal–organic frameworks M 2 (dobdc) (M = Mg, Mn, Fe, Co, Ni, Cu, Zn), Chem. Sci. 5 (2014) 4569–4581. https://doi.org/10.1039/C4SC02064B.

[254] M.A. Tekalgne, H.H. Do, A. Hasani, Q. Van Le, H.W. Jang, S.H. Ahn, S.Y. Kim, Two-dimensional materials and metal-organic frameworks for the CO2 reduction reaction, Mater. Today Adv. 5 (2020) 100038. https://doi.org/10.1016/j.mtadv.2019.100038.

[255] A. Kidanemariam, J. Lee, J. Park, Recent Innovation of Metal-Organic Frameworks for Carbon Dioxide Photocatalytic Reduction, Polymers (Basel). 11 (2019) 2090. https://doi.org/10.3390/polym11122090.

[256] H.L. Nguyen, T.T. Vu, D. Le, T.L.H. Doan, V.Q. Nguyen, N.T.S. Phan, A Titanium–Organic Framework: Engineering of the Band-Gap Energy for Photocatalytic Property Enhancement, ACS Catal. 7 (2017) 338–342. https://doi.org/10.1021/acscatal.6b02642.

[257] H.Q. Pham, T. Mai, N.-N. Pham-Tran, Y. Kawazoe, H. Mizuseki, D. Nguyen-Manh, Engineering of Band Gap in Metal–Organic Frameworks by Functionalizing Organic Linker: A Systematic Density Functional Theory Investigation, J. Phys. Chem. C 118 (2014) 4567–4577. https://doi.org/10.1021/jp405997r.

[258] C.H. Hendon, D. Tiana, M. Fontecave, C. Sanchez, L. D'arras, C. Sassoye, L. Rozes, C. Mellot-Draznieks, A. Walsh, Engineering the Optical Response of the Titanium-MIL-125 Metal–Organic Framework through Ligand Functionalization, J. Am. Chem. Soc. 135 (2013) 10942–10945. https://doi.org/10.1021/ja405350u.

[259] A. Aziz, A.R. Ruiz-Salvador, N.C. Hernández, S. Calero, S. Hamad, R. Grau-Crespo, Porphyrin-based metal-organic frameworks for solar fuel synthesis photocatalysis: band gap tuning via iron substitutions, J. Mater. Chem. A 5 (2017) 11894–11904. https://doi.org/10.1039/C7TA01278K.

[260] L.-M. Yang, G.-Y. Fang, J. Ma, R. Pushpa, E. Ganz, Halogenated MOF-5 variants show new configuration, tunable band gaps and enhanced optical response in the visible and near infrared, Phys. Chem. Chem. Phys. 18 (2016) 32319–32330. https://doi.org/10.1039/C6CP06981A.

[261] Y. Xi, X. Zhang, Y. Shen, W. Dong, Z. Fan, K. Wang, S. Zhong, S. Bai, Aspect ratio dependent photocatalytic enhancement of CsPbBr3 in CO2 reduction with two-dimensional metal organic framework as a cocatalyst, Appl. Catal. B Environ. 297 (2021) 120411. https://doi.org/10.1016/j.apcatb.2021.120411.

[262] D. Sun, W. Liu, Y. Fu, Z. Fang, F. Sun, X. Fu, Y. Zhang, Z. Li, Noble Metals Can Have Different Effects on Photocatalysis Over Metal-Organic Frameworks (MOFs): A Case Study

on M/NH 2 -MIL-125(Ti) (M=Pt and Au), Chem. - A Eur. J. 20 (2014) 4780–4788. https://doi.org/10.1002/chem.201304067.

[263] P. Lu, Y. Wu, H. Kang, H. Wei, H. Liu, M. Fang, What can pK a and NBO charges of the ligands tell us about the water and thermal stability of metal organic frameworks?, J. Mater. Chem. A 2 (2014) 16250–16267. https://doi.org/10.1039/C4TA03154G.

[264] K. Tan, N. Nijem, Y. Gao, S. Zuluaga, J. Li, T. Thonhauser, Y.J. Chabal, Water interactions in metal organic frameworks, CrystEngComm 17 (2015) 247–260. https://doi.org/10.1039/C4CE01406E.

[265] W. Zhang, Y. Hu, J. Ge, H.-L. Jiang, S.-H. Yu, A Facile and General Coating Approach to Moisture/Water-Resistant Metal–Organic Frameworks with Intact Porosity, J. Am. Chem. Soc. 136 (2014) 16978–16981. https://doi.org/10.1021/ja509960n.

[266] Z.-P. Qi, J.-M. Yang, Y.-S. Kang, F. Guo, W.-Y. Sun, Facile water-stability evaluation of metal–organic frameworks and the property of selective removal of dyes from aqueous solution, Dalt. Trans. 45 (2016) 8753–8759. https://doi.org/10.1039/C6DT00886K.

[267] R. Hariri, S. Dehghanpour, Effective visible-light CO2 photoreduction over (metallo)porphyrin-based metal–organic frameworks to achieve useful hydrocarbons, Appl. Organomet. Chem. 35 (2021). https://doi.org/10.1002/aoc.6422.

[268] A. Angulo-Ibáñez, M. Perfecto-Irigaray, I. Merino-Garcia, N. Luengo, A.M. Goitandia, J. Albo, E. Aranzabe, G. Beobide, O. Castillo, S. Pérez-Yáñez, Metal-organic aerogels based on titanium(IV) for visible-light conducted CO2 photoreduction to alcohols, Mater. Today Energy 30 (2022) 101178. https://doi.org/10.1016/j.mtener.2022.101178.

[269] Z.-B. Fang, T.-T. Liu, J. Liu, S. Jin, X.-P. Wu, X.-Q. Gong, K. Wang, Q. Yin, T.-F. Liu, R. Cao, H.-C. Zhou, Boosting Interfacial Charge-Transfer Kinetics for Efficient Overall CO 2 Photoreduction via Rational Design of Coordination Spheres on Metal–Organic Frameworks, J. Am. Chem. Soc. 142 (2020) 12515–12523. https://doi.org/10.1021/jacs.0c05530.

[270] C. Liu, T.R. Cundari, A.K. Wilson, CO 2 Reduction on Transition Metal (Fe, Co, Ni, and Cu) Surfaces: In Comparison with Homogeneous Catalysis, J. Phys. Chem. C 116 (2012) 5681–5688. https://doi.org/10.1021/jp210480c.

[271] S. Chen, G. Hai, H. Gao, X. Chen, A. Li, X. Zhang, W. Dong, Modulation of the charge transfer behavior of Ni(II)-doped NH2-MIL-125(Ti): Regulation of Ni ions content and enhanced photocatalytic CO2 reduction performance, Chem. Eng. J. 406 (2021) 126886. https://doi.org/10.1016/j.cej.2020.126886.

[272] Y. Ma, J. Du, Y. Fang, X. Wang, Encapsulation of Cobalt Oxide into Metal-Organic Frameworks for an Improved Photocatalytic CO 2 Reduction, ChemSusChem 14 (2021) 946–951. https://doi.org/10.1002/cssc.202002656.

[273] S.-Q. Wang, X. Wang, X.-M. Cheng, J. Ma, W.-Y. Sun, Tailoring defect-type and ligand-vacancies in Zr(IV) frameworks for CO2 photoreduction, J. Mater. Chem. A 10 (2022) 16396–16402. https://doi.org/10.1039/D2TA04528A.

[274] M.J. Earle, J.M.S.S. Esperança, M.A. Gilea, J.N. Canongia Lopes, L.P.N. Rebelo, J.W. Magee, K.R. Seddon, J.A. Widegren, The distillation and volatility of ionic liquids, Nature 439 (2006) 831–834. https://doi.org/10.1038/nature04451.

[275] G.W. Meindersma, M. Maase, A.B. De Haan, Ionic Liquids, in: Ullmann's Encycl. Ind. Chem., Wiley, 2007. https://doi.org/10.1002/14356007.l14_l01.

[276] X. Zhang, F. Huo, Z. Liu, W. Wang, W. Shi, E.J. Maginn, Absorption of CO 2 in the Ionic Liquid 1- n -Hexyl-3-methylimidazolium Tris(pentafluoroethyl)trifluorophosphate ([hmim][FEP]): A Molecular View by Computer Simulations, J. Phys. Chem. B 113 (2009) 7591–7598. https://doi.org/10.1021/jp900403q.

[277] W. Shi, C.R. Myers, D.R. Luebke, J.A. Steckel, D.C. Sorescu, Theoretical and Experimental Studies of CO 2 and H 2 Separation Using the 1-Ethyl-3-methylimidazolium Acetate ([emim][CH 3 COO]) Ionic Liquid, J. Phys. Chem. B 116 (2012) 283–295. https://doi.org/10.1021/jp205830d.

[278] D. Almantariotis, T. Gefflaut, A.A.H. Pádua, J.-Y. Coxam, M.F. Costa Gomes, Effect of Fluorination and Size of the Alkyl Side-Chain on the Solubility of Carbon Dioxide in 1-Alkyl-3-methylimidazolium Bis(trifluoromethylsulfonyl)amide Ionic Liquids, J. Phys. Chem. B 114 (2010) 3608–3617. https://doi.org/10.1021/jp912176n.

[279] S.N.V.K. Aki, B.R. Mellein, E.M. Saurer, J.F. Brennecke, High-Pressure Phase Behavior of Carbon Dioxide with Imidazolium-Based Ionic Liquids, J. Phys. Chem. B 108 (2004) 20355–20365. https://doi.org/10.1021/jp046895+.

[280] M.J. Muldoon, S.N.V.K. Aki, J.L. Anderson, J.K. Dixon, J.F. Brennecke, Improving Carbon Dioxide Solubility in Ionic Liquids, J. Phys. Chem. B 111 (2007) 9001–9009. https://doi.org/10.1021/jp071897q.

[281] S.K. Shukla, S.G. Khokarale, T.Q. Bui, J.-P.T. Mikkola, Ionic Liquids: Potential Materials for Carbon Dioxide Capture and Utilization, Front. Mater. 6 (2019). https://doi.org/10.3389/fmats.2019.00042.

[282] C. Wang, S.M. Mahurin, H. Luo, G.A. Baker, H. Li, S. Dai, Reversible and robust CO2 capture by equimolar task-specific ionic liquid–superbase mixtures, Green Chem. 12 (2010) 870. https://doi.org/10.1039/b927514b.

[283] C. Wang, H. Luo, H. Li, X. Zhu, B. Yu, S. Dai, Tuning the Physicochemical Properties of Diverse Phenolic Ionic Liquids for Equimolar CO2 Capture by the Substituent on the Anion, Chem. - A Eur. J. 18 (2012) 2153–2160. https://doi.org/10.1002/chem.201103092.

[284] P.J. Carvalho, V.H. Álvarez, B. Schröder, A.M. Gil, I.M. Marrucho, M. Aznar, L.M.N.B.F.

Santos, J.A.P. Coutinho, Specific Solvation Interactions of CO 2 on Acetate and Trifluoroacetate Imidazolium Based Ionic Liquids at High Pressures, J. Phys. Chem. B 113 (2009) 6803–6812. https://doi.org/10.1021/jp901275b.

[285] M.B. Shiflett, A. Yokozeki, Phase Behavior of Carbon Dioxide in Ionic Liquids: [emim][Acetate], [emim][Trifluoroacetate], and [emim][Acetate] + [emim][Trifluoroacetate] Mixtures, J. Chem. Eng. Data 54 (2009) 108–114. https://doi.org/10.1021/je800701j.

[286] L.M. Galán Sánchez, G.W. Meindersma, A.B. de Haan, Solvent Properties of Functionalized Ionic Liquids for CO2 Absorption, Chem. Eng. Res. Des. 85 (2007) 31–39. https://doi.org/10.1205/cherd06124.

[287] B.E. Gurkan, J.C. de la Fuente, E.M. Mindrup, L.E. Ficke, B.F. Goodrich, E.A. Price, W.F. Schneider, J.F. Brennecke, Equimolar CO 2 Absorption by Anion-Functionalized Ionic Liquids, J. Am. Chem. Soc. 132 (2010) 2116–2117. https://doi.org/10.1021/ja909305t.

[288] K. Fukumoto, M. Yoshizawa, H. Ohno, Room Temperature Ionic Liquids from 20 Natural Amino Acids, J. Am. Chem. Soc. 127 (2005) 2398–2399. https://doi.org/10.1021/ja043451i.

[289] B. Lv, Y. Xia, Y. Shi, N. Liu, W. Li, S. Li, A novel hydrophilic amino acid ionic liquid [C2OHmim][Gly] as aqueous sorbent for CO2 capture, Int. J. Greenh. Gas Control 46 (2016) 1–6. https://doi.org/10.1016/j.ijggc.2015.12.029.

[290] N. Noorani, A. Mehrdad, R. Zarei diznab, Thermodynamic study on carbon dioxide absorption in vinyl imidazolium–amino acid ionic liquids, Fluid Phase Equilib. 557 (2022) 113433. https://doi.org/10.1016/j.fluid.2022.113433.

[291] Y.S. Sistla, A. Khanna, CO2 absorption studies in amino acid-anion based ionic liquids, Chem. Eng. J. 273 (2015) 268–276. https://doi.org/10.1016/j.cej.2014.09.043.

[292] T.J. Ferreira, T.O. Carvalho, J. Pais, L.M. Esteves, L.P.C. Silva, P.M. Reis, J.M.S.S. Esperança, I.A.A.C. Esteves, Boosting CO2 selectivity by mono- and dicarboxylate-based ionic liquids impregnation into ZIF-8 for post-combustion separation, Carbon Capture Sci. Technol. 13 (2024) 100282. https://doi.org/10.1016/j.ccst.2024.100282.

[293] F.P. Kinik, C. Altintas, V. Balci, B. Koyuturk, A. Uzun, S. Keskin, [BMIM][PF 6] Incorporation Doubles CO 2 Selectivity of ZIF-8: Elucidation of Interactions and Their Consequences on Performance, ACS Appl. Mater. Interfaces 8 (2016) 30992–31005. https://doi.org/10.1021/acsami.6b11087.

[294] Y. Ban, Z. Li, Y. Li, Y. Peng, H. Jin, W. Jiao, A. Guo, P. Wang, Q. Yang, C. Zhong, W. Yang, Confinement of Ionic Liquids in Nanocages: Tailoring the Molecular Sieving Properties of ZIF-8 for Membrane-Based CO 2 Capture, Angew. Chemie Int. Ed. 54 (2015) 15483–15487. https://doi.org/10.1002/anie.201505508.

[295] B. Koyuturk, C. Altintas, F.P. Kinik, S. Keskin, A. Uzun, Improving Gas Separation Performance of ZIF-8 by [BMIM][BF 4] Incorporation: Interactions and Their Consequences

on Performance, J. Phys. Chem. C 121 (2017) 10370–10381. https://doi.org/10.1021/acs.jpcc.7b00848.

[296] M. Mohamedali, H. Ibrahim, A. Henni, Incorporation of acetate-based ionic liquids into a zeolitic imidazolate framework (ZIF-8) as efficient sorbents for carbon dioxide capture, Chem. Eng. J. 334 (2018) 817–828. https://doi.org/10.1016/j.cej.2017.10.104.

[297] M. Zeeshan, S. Keskin, A. Uzun, Enhancing CO2/CH4 and CO2/N2 separation performances of ZIF-8 by post-synthesis modification with [BMIM][SCN], Polyhedron 155 (2018) 485–492. https://doi.org/10.1016/j.poly.2018.08.073.

[298] J. Avila, L.F. Lepre, C.C. Santini, M. Tiano, S. Denis-Quanquin, K. Chung Szeto, A.A.H. Padua, M. Costa Gomes, High-Performance Porous Ionic Liquids for Low-Pressure CO 2 Capture**, Angew. Chemie Int. Ed. 60 (2021) 12876–12882. https://doi.org/10.1002/anie.202100090.

[299] X. Song, J. Yu, M. Wei, R. Li, X. Pan, G. Yang, H. Tang, Ionic Liquids-Functionalized Zeolitic Imidazolate Framework for Carbon Dioxide Adsorption, Materials (Basel). 12 (2019) 2361. https://doi.org/10.3390/ma12152361.

[300] K.B. Sezginel, S. Keskin, A. Uzun, Tuning the Gas Separation Performance of CuBTC by Ionic Liquid Incorporation, Langmuir 32 (2016) 1139–1147. https://doi.org/10.1021/acs.langmuir.5b04123.

[301] F.W.M. da Silva, G.M. Magalhães, E.O. Jardim, J. Silvestre-Albero, A. Sepúlveda-Escribano, D.C.S. de Azevedo, S.M.P. de Lucena, CO 2 Adsorption on Ionic Liquid—Modified Cu-BTC: Experimental and Simulation Study, Adsorpt. Sci. Technol. 33 (2015) 223–242. https://doi.org/10.1260/0263-6174.33.2.223.

[302] X. Xia, W. Li, S. Li, On the water stability of ionic liquids/Cu-BTC composites: an experimental study, J. Nanoparticle Res. 21 (2019) 39. https://doi.org/10.1007/s11051-019-4475-8.

[303] H.M. Polat, M. Zeeshan, A. Uzun, S. Keskin, Unlocking CO2 separation performance of ionic liquid/CuBTC composites: Combining experiments with molecular simulations, Chem. Eng. J. 373 (2019) 1179–1189. https://doi.org/10.1016/j.cej.2019.05.113.

[304] V. Nozari, M. Zeeshan, S. Keskin, A. Uzun, Effect of methylation of ionic liquids on the gas separation performance of ionic liquid/metal–organic framework composites, CrystEngComm 20 (2018) 7137–7143. https://doi.org/10.1039/C8CE01364K.

[305] F.A. Philip, A. Henni, Incorporation of Amino Acid-Functionalized Ionic Liquids into Highly Porous MOF-177 to Improve the Post-Combustion CO2 Capture Capacity, Molecules 28 (2023) 7185. https://doi.org/10.3390/molecules28207185.

[306] J. Ma, Y. Ying, X. Guo, H. Huang, D. Liu, C. Zhong, Fabrication of mixed-matrix membrane containing metal–organic framework composite with task-specific ionic liquid for efficient CO

2 separation, J. Mater. Chem. A 4 (2016) 7281–7288. https://doi.org/10.1039/C6TA02611G.

[307] X. Xia, G. Hu, W. Li, S. Li, Understanding Reduced CO 2 Uptake of Ionic Liquid/Metal–Organic Framework (IL/MOF) Composites, ACS Appl. Nano Mater. 2 (2019) 6022–6029. https://doi.org/10.1021/acsanm.9b01538.

[308] C. Zhao, X. Li, G. Liu, X. Wang, Selective adsorption of trace CO2 by immobilized amino acid ionic liquids with ultra-micropores based on amino MOFs, Sep. Purif. Technol. 356 (2025) 129742. https://doi.org/10.1016/j.seppur.2024.129742.

[309] W.-L. Xue, L. Wang, Y.K. Li, H. Chen, K.X. Fu, F. Zhang, T. He, Y.H. Deng, J.R. Li, C.-Q. Wan, Reticular Chemistry for Ionic Liquid-Functionalized Metal–Organic Frameworks with High Selectivity for CO 2, ACS Sustain. Chem. Eng. 8 (2020) 18558–18567. https://doi.org/10.1021/acssuschemeng.0c06551.

[310] L.G. Ding, B.J. Yao, W.L. Jiang, J.T. Li, Q.J. Fu, Y.A. Li, Z.H. Liu, J.P. Ma, Y. Bin Dong, Bifunctional Imidazolium-Based Ionic Liquid Decorated UiO-67 Type MOF for Selective CO2 Adsorption and Catalytic Property for CO2 Cycloaddition with Epoxides, Inorg. Chem. 56 (2017) 2337–2344. https://doi.org/10.1021/acs.inorgchem.6b03169.

[311] S. Mehra, V. Polisetti, K. Damarla, P. Ray, A. Kumar, Ionic Liquid-Based Colloidal Formulations for the Synthesis of Nano-MOFs: Applications in Gas Adsorption and Water Desalination, ACS Appl. Mater. Interfaces 13 (2021) 41249–41261. https://doi.org/10.1021/acsami.1c10184.

[312] R. Lin, L. Ge, H. Diao, V. Rudolph, Z. Zhu, Ionic liquids as the MOFs/polymer interfacial binder for efficient membrane separation, ACS Appl. Mater. Interfaces 8 (2016) 32041–32049. https://doi.org/10.1021/acsami.6b11074.

[313] C. Liu, B. Zhang, J. Zhang, L. Peng, X. Kang, B. Han, T. Wu, X. Sang, X. Ma, Gas promotes the crystallization of nano-sized metal-organic frameworks in ionic liquid, Chem. Commun. 51 (2015) 11445–11448. https://doi.org/10.1039/c5cc02503f.

[314] W.L. Xue, W.H. Deng, H. Chen, R.H. Liu, J.M. Taylor, Y. kun Li, L. Wang, Y.H. Deng, W.H. Li, Y.Y. Wen, G.E. Wang, C.Q. Wan, G. Xu, MOF-Directed Synthesis of Crystalline Ionic Liquids with Enhanced Proton Conduction, Angew. Chemie Int. Ed. 60 (2021) 1290–1297. https://doi.org/10.1002/anie.202010783.

[315] M. Ermer, J. Mehler, M. Kriesten, Y.S. Avadhut, P.S. Schulz, M. Hartmann, Synthesis of the novel MOF hcp UiO-66 employing ionic liquids as a linker precursor, Dalt. Trans. 47 (2018) 14426–14430. https://doi.org/10.1039/C8DT02999G.

[316] Y. Sun, H. Huang, H. Vardhan, B. Aguila, C. Zhong, J.A. Perman, A.M. Al-Enizi, A. Nafady, S. Ma, Facile Approach to Graft Ionic Liquid into MOF for Improving the Efficiency of CO 2 Chemical Fixation, ACS Appl. Mater. Interfaces 10 (2018) 27124–27130. https://doi.org/10.1021/acsami.8b08914.

[317] J. Li, J. Liang, W. Wu, S. Zhang, K. Zhang, H. Zhou, AuCl4−-responsive self-assembly of ionic liquid block copolymers for obtaining composite gold nanoparticles and polymeric micelles with controlled morphologies, New J. Chem. 38 (2014) 2508. https://doi.org/10.1039/c4nj00128a.

[318] H. Zhu, J.F. Huang, Z. Pan, S. Dai, Ionothermal synthesis of hierarchical ZnO nanostructures from ionic-liquid precursors, Chem. Mater. 18 (2006) 4473–4477. https://doi.org/10.1021/cm060472y.

[319] S. Hsu, Synthesis of Gold Nanosheets through Thermolysis of Mixtures of Long Chain 1-Alkylimidazole and Hydrogen Tetrachloroaurate (III), (2009) 98–106.

[320] Y. Zhang, J. Di, W. Tong, X. Chen, J. Zhao, P. Ding, S. Yin, J. Xia, H. Li, Controllable synthesis of FeWO4/BiOBr in reactive ionic liquid with effective charge separation towards photocatalytic pollutant removal, Res. Chem. Intermed. 45 (2019) 437–451. https://doi.org/10.1007/s11164-018-3610-y.

[321] X.-M. Cheng, X.-Y. Dao, S.-Q. Wang, J. Zhao, W.-Y. Sun, Enhanced Photocatalytic CO 2 Reduction Activity over NH 2 -MIL-125(Ti) by Facet Regulation, ACS Catal. 11 (2021) 650–658. https://doi.org/10.1021/acscatal.0c04426.

[322] L.M. Esteves, T.J. Ferreira, A. Keba, J.M.S.S. Esperança, I.A.A.C. Esteves, Carbon materials derived from cyano-based IL@ZIF-8 composites for CO2 sorption separation systems, Mater. Today Sustain. 22 (2023) 100353. https://doi.org/10.1016/j.mtsust.2023.100353.

[323] I.A.A.C. Esteves, M.S.S. Lopes, P.M.C. Nunes, J.P.B. Mota, Adsorption of natural gas and biogas components on activated carbon, Sep. Purif. Technol. 62 (2008) 281–296. https://doi.org/10.1016/j.seppur.2008.01.027.

[324] S. Gumma, O. Talu, Net Adsorption: A Thermodynamic Framework for Supercritical Gas Adsorption and Storage in Porous Solids, Langmuir 26 (2010) 17013–17023. https://doi.org/10.1021/la102186q.

[325] J. Strunk, Separating fiction from fact for photocatalytic CO2 reduction, Nat. Chem. 15 (2023) 1209–1211. https://doi.org/10.1038/s41557-023-01293-z.

[326] S. Yang, L. Peng, D.T. Sun, M. Asgari, E. Oveisi, O. Trukhina, S. Bulut, A. Jamali, W.L. Queen, A new post-synthetic polymerization strategy makes metal–organic frameworks more stable, Chem. Sci. 10 (2019) 4542–4549. https://doi.org/10.1039/C9SC00135B.

[327] N. Zhang, Q. Guan, C. Liu, Y. Sun, B. Li, Y. Xing, F. Bai, A rht-Type Luminescent Zn (II)-MOF Constructed by Triazine Hexacarboxylate Ligand: Tunable Luminescent Performance and White-light Emission Regulation through doping Eu 3+ /Tb 3+, Appl. Organomet. Chem. 34 (2020). https://doi.org/10.1002/aoc.5506.

[328] C.-Y. Wang, Q. Gong, Y. Zhao, J. Li, A.D. Lueking, Stability and hydrogen adsorption of

metal–organic frameworks prepared via different catalyst doping methods, J. Catal. 318 (2014) 128–142. https://doi.org/10.1016/j.jcat.2014.07.010.

[329] C.-Y. Wang, J.L. Gray, Q. Gong, Y. Zhao, J. Li, E. Klontzas, G. Psofogiannakis, G. Froudakis, A.D. Lueking, Hydrogen Storage with Spectroscopic Identification of Chemisorption Sites in Cu-TDPAT via Spillover from a Pt/Activated Carbon Catalyst, J. Phys. Chem. C 118 (2014) 26750–26763. https://doi.org/10.1021/jp507395p.

[330] C. Li, T. Zhang, J. Zhao, H. Liu, B. Zheng, Y. Gu, X. Yan, Y. Li, N. Lu, Z. Zhang, G. Feng, Boosted Sensor Performance by Surface Modification of Bifunctional rht -Type Metal–Organic Framework with Nanosized Electrochemically Reduced Graphene Oxide, ACS Appl. Mater. Interfaces 9 (2017) 2984–2994. https://doi.org/10.1021/acsami.6b13788.

[331] B. He, D. Yan, Au/ERGO nanoparticles supported on Cu-based metal-organic framework as a novel sensor for sensitive determination of nitrite, Food Control 103 (2019) 70–77. https://doi.org/10.1016/j.foodcont.2019.04.001.

[332] S. Menzel, S. Höfert, S. Öztürk, A. Schmitz, C. Janiak, A mixed-valence copper(I/II) coordination polymer directed with a bifunctional soft-hard pyrazolate−carboxylate ligand, Zeitschrift Für Anorg. Und Allg. Chemie 647 (2021) 803–808. https://doi.org/10.1002/zaac.202000428.

[333] A. Sahai, N. Goswami, S.D. Kaushik, S. Tripathi, Cu/Cu2O/CuO nanoparticles: Novel synthesis by exploding wire technique and extensive characterization, Appl. Surf. Sci. 390 (2016) 974–983. https://doi.org/10.1016/j.apsusc.2016.09.005.

[334] X. Cao, H. Li, J. Yi, F. Zhao, Y. Hao, Recent advances for water-stable metal-organic frameworks (MOFs), J. Phys. Conf. Ser. 2478 (2023) 062029. https://doi.org/10.1088/1742-6596/2478/6/062029.

[335] S. Øien-Ødegaard, K. Lillerud, Twinning in Zr-Based Metal-Organic Framework Crystals, Chemistry (Easton). 2 (2020) 777–786. https://doi.org/10.3390/chemistry2030050.

[336] S. Øien-Ødegaard, G.C. Shearer, D.S. Wragg, K.P. Lillerud, Pitfalls in metal–organic framework crystallography: towards more accurate crystal structures, Chem. Soc. Rev. 46 (2017) 4867–4876. https://doi.org/10.1039/C6CS00533K.

[337] E. Sletten, L.H. Jensen, The crystal structure of dimethylammonium copper(II) formate, NH2(CH2)2[Cu(OOCH)3], Acta Crystallogr. Sect. B Struct. Crystallogr. Cryst. Chem. 29 (1973) 1752–1756. https://doi.org/10.1107/s0567740873005480.

[338] R. Scatena, R.D. Johnson, P. Manuel, P. Macchi, Formate-mediated magnetic superexchange in the model hybrid perovskite [(CH3)2NH2]Cu(HCOO)3, J. Mater. Chem. C 8 (2020) 12840–12847. https://doi.org/10.1039/d0tc03913f.

[339] I.E. Collings, M. Bykov, E. Bykova, M. Hanfland, S. Van Smaalen, L. Dubrovinsky, N. Dubrovinskaia, Disorder-order transitions in the perovskite metal-organic frameworks

[(CH3)2NH2][M(HCOO)3] at high pressure, CrystEngComm 20 (2018) 3512–3521. https://doi.org/10.1039/c8ce00617b.

[340] B. Baumgartner, K. Ikigaki, K. Okada, M. Takahashi, Infrared crystallography for framework and linker orientation in metal–organic framework films, Chem. Sci. 12 (2021) 9298–9308. https://doi.org/10.1039/D1SC02370E.

[341] S.A. Mohamed, Y. Kim, J. Lee, W. Choe, J. Kim, Understanding the Structural Collapse during Activation of Metal–Organic Frameworks with Copper Paddlewheels, Inorg. Chem. 61 (2022) 9702–9709. https://doi.org/10.1021/acs.inorgchem.2c01171.

[342] R. Pang, K. Teramura, H. Asakura, S. Hosokawa, T. Tanaka, Role of Bicarbonate Ions in Aqueous Solution as a Carbon Source for Photocatalytic Conversion of CO 2 into CO, ACS Appl. Energy Mater. 2 (2019) 5397–5405. https://doi.org/10.1021/acsaem.9b00093.

[343] S. Goyal, M.S. Shaharun, C.F. Kait, B. Abdullah, M. Ameen, Photoreduction of Carbon Dioxide to Methanol over Copper Based Zeolitic Imidazolate Framework-8: A New Generation Photocatalyst, Catalysts 8 (2018) 581. https://doi.org/10.3390/catal8120581.

[344] Z. Wang, J. Yang, J. Cao, W. Chen, G. Wang, F. Liao, X. Zhou, F. Zhou, R. Li, Z.-Q. Yu, G. Zhang, X. Duan, Y. Wu, Room-Temperature Synthesis of Single Iron Site by Electrofiltration for Photoreduction of CO2 into Tunable Syngas, ACS Nano 14 (2020) 6164–6172. https://doi.org/10.1021/acsnano.0c02162.

[345] M.P. Singh, N.R. Dhumal, H.J. Kim, J. Kiefer, J.A. Anderson, Influence of Water on the Chemistry and Structure of the Metal–Organic Framework Cu 3 (btc) 2, J. Phys. Chem. C 120 (2016) 17323–17333. https://doi.org/10.1021/acs.jpcc.6b02906.

[346] B. Sen, J.C.C. Santos, R. Haldar, Q. Zhang, T. Hashem, P. Qin, Y. Li, F. Kirschhöfer, G. Brenner-Weiss, H. Gliemann, L. Heinke, C. Barner-Kowollik, A. Knebel, C. Wöll, Introducing electrical conductivity to metal–organic framework thin films by templated polymerization of methyl propiolate, Nanoscale 12 (2020) 24419–24428. https://doi.org/10.1039/D0NR06848A.

[347] N.R. Dhumal, M.P. Singh, J.A. Anderson, J. Kiefer, H.J. Kim, Molecular Interactions of a Cu-Based Metal–Organic Framework with a Confined Imidazolium-Based Ionic Liquid: A Combined Density Functional Theory and Experimental Vibrational Spectroscopy Study, J. Phys. Chem. C 120 (2016) 3295–3304. https://doi.org/10.1021/acs.jpcc.5b10123.

[348] M.P. Singh, N.R. Dhumal, H.J. Kim, J. Kiefer, J.A. Anderson, Removal of Confined Ionic Liquid from a Metal Organic Framework by Extraction with Molecular Solvents, J. Phys. Chem. C 121 (2017) 10577–10586. https://doi.org/10.1021/acs.jpcc.7b02289.

[349] W. Feng, Y. Lu, Y. Chen, Y. Lu, T. Yang, Thermal stability of imidazolium-based ionic liquids investigated by TG and FTIR techniques, J. Therm. Anal. Calorim. 125 (2016) 143–154. https://doi.org/10.1007/s10973-016-5267-3.

[350] X. Sang, J. Zhang, J. Xiang, J. Cui, L. Zheng, J. Zhang, Z. Wu, Z. Li, G. Mo, Y. Xu, J. Song, C. Liu, X. Tan, T. Luo, B. Zhang, B. Han, Ionic liquid accelerates the crystallization of Zr-based metal–organic frameworks, Nat. Commun. 8 (2017) 175. https://doi.org/10.1038/s41467-017-00226-y.

[351] J. Yuan, H. Liu, H. Wei, J. Guo, Y. Chen, A. Wang, W. Yan, C. Liu, S. Peng, Z. Jiang, Green and Scalable Synthesis of Metal–Organic Framework via a Two-Stage Crystallization Approach, Small 21 (2025). https://doi.org/10.1002/smll.202509238.

[352] L. Gong, J. Bai, C. Wang, Z. Li, L. Shan, Precisely tuning morphology and size of ZIF-67-based nanosheets in mixed matrix membranes for advanced CO2/CH4 separation, Microporous Mesoporous Mater. 400 (2026) 113915. https://doi.org/10.1016/j.micromeso.2025.113915.

[353] W. Shang, X. Kang, H. Ning, J. Zhang, X. Zhang, Z. Wu, G. Mo, X. Xing, B. Han, Shape and Size Controlled Synthesis of MOF Nanocrystals with the Assistance of Ionic Liquid Mircoemulsions, Langmuir 29 (2013) 13168–13174. https://doi.org/10.1021/la402882a.

[354] W. Zhang, Z. Lu, R. Liu, L. Ji, B. Nian, Y. Hu, Ionic liquid modulation of metal-organic framework immobilized laccase and boosted its catalytic performance for organic pollutants removal, J. Environ. Chem. Eng. 11 (2023) 110880. https://doi.org/10.1016/j.jece.2023.110880.

[355] M.. Donohue, G.. Aranovich, Classification of Gibbs adsorption isotherms, Adv. Colloid Interface Sci. 76–77 (1998) 137–152. https://doi.org/10.1016/S0001-8686(98)00044-X.

[356] D.D. Do, Adsorption Analysis: Equilibria and Kinetics, PUBLISHED BY IMPERIAL COLLEGE PRESS AND DISTRIBUTED BY WORLD SCIENTIFIC PUBLISHING CO., 1998. https://doi.org/10.1142/p111.

[357] L. Valenzano, B. Civalleri, S. Chavan, S. Bordiga, M.H. Nilsen, S. Jakobsen, K.P. Lillerud, C. Lamberti, Disclosing the Complex Structure of UiO-66 Metal Organic Framework: A Synergic Combination of Experiment and Theory, Chem. Mater. 23 (2011) 1700–1718. https://doi.org/10.1021/cm1022882.

[358] L. Jin, H. Liu, A. Xu, Y. Wu, J. Lu, J. Liu, S. Xie, Y. Yao, L. Dong, M. Zhang, S. Kai, M. Fan, Defective UiO-66-NH2 (Zr/Ce) catalyzes the synthesis of propylene carbonate under mild conditions, Microporous Mesoporous Mater. 317 (2021) 110997. https://doi.org/10.1016/j.micromeso.2021.110997.

[359] S. Øien, D. Wragg, H. Reinsch, S. Svelle, S. Bordiga, C. Lamberti, K.P. Lillerud, Detailed Structure Analysis of Atomic Positions and Defects in Zirconium Metal–Organic Frameworks, Cryst. Growth Des. 14 (2014) 5370–5372. https://doi.org/10.1021/cg501386j.

[360] R. Yuniasari, F. Amri, S.A. Abrori, N.L.W. Septiani, M. Rezki, Irzaman, M.Z. Fahmi, B. Yuliarto, A graphene-modified Co-BDC metal-organic frameworks (Co-MOF) for electrochemical non-enzymatic glucose sensing, IOP Conf. Ser. Mater. Sci. Eng. 1045

(2021) 012010. https://doi.org/10.1088/1757-899X/1045/1/012010.

[361] J. Cheng, Y. Shao, H. Guo, Z. Zhang, Y. Mao, L. Qian, K. Xin, W. Yang, Ni-based metal–organic frameworks prepared with terephthalic acid hydroxylation converted methyl palmitate into jet-fuel range hydrocarbons in CO2 atmosphere, Fuel 318 (2022) 123679. https://doi.org/10.1016/j.fuel.2022.123679.

[362] Y.A. Patil, G.S. Shankarling, Deep eutectic solvent-mediated, energy-efficient synthesis of copper terephthalate metal-organic framework and its application in degradation of an azo dye, Chem. Eng. J. Adv. 3 (2020) 100032. https://doi.org/10.1016/j.ceja.2020.100032.

[363] L.A. Lozano, L.A.S. Hoyos, B.M.C. Faroldi, J.M. Zamaro, Enhancement in the CO2 uptake of UiO-66 by a simple exposure to ultraviolet light, Mater. Today Commun. 31 (2022) 103540. https://doi.org/10.1016/j.mtcomm.2022.103540.

[364] M.C. Biesinger, Advanced analysis of copper X-ray photoelectron spectra, Surf. Interface Anal. 49 (2017) 1325–1334. https://doi.org/10.1002/sia.6239.

[365] E. Cano, C.L. Torres, J.M. Bastidas, An XPS study of copper corrosion originated by formic acid vapour at 40% and 80% relative humidity, Mater. Corros. 52 (2001) 667–676. https://doi.org/10.1002/1521-4176(200109)52:9<667::AID-MACO667>3.0.CO;2-H.

[366] T.M. Ivanova, K.I. Maslakov, A.A. Sidorov, M.A. Kiskin, R.V. Linko, S.V. Savilov, V.V. Lunin, I.L. Eremenko, XPS detection of unusual Cu(II) to Cu(I) transition on the surface of complexes with redox-active ligands, J. Electron Spectros. Relat. Phenomena 238 (2020) 146878. https://doi.org/10.1016/j.elspec.2019.06.010.

[367] M.C. Biesinger, B.P. Payne, A.P. Grosvenor, L.W.M. Lau, A.R. Gerson, R.S.C. Smart, Resolving surface chemical states in XPS analysis of first row transition metals, oxides and hydroxides: Cr, Mn, Fe, Co and Ni, Appl. Surf. Sci. 257 (2011) 2717–2730. https://doi.org/10.1016/j.apsusc.2010.10.051.

[368] S. Wang, Y. Hou, X. Wang, Development of a Stable MnCo2O4 Cocatalyst for Photocatalytic CO 2 Reduction with Visible Light, ACS Appl. Mater. Interfaces 7 (2015) 4327–4335. https://doi.org/10.1021/am508766s.

[369] Q. Jia, C. Wang, J. Liu, X. Cai, L. Zhong, S. Chen, T. Li, G. Yu, L. Wu, D. Duan, Synergistic Effect of Sr-O Divacancy and Exposing Facets in SrTiO 3 Micro/Nano Particle: Accelerating Exciton Formation and Splitting, Highly Efficient Co 2+ Photooxidation, Small 18 (2022). https://doi.org/10.1002/smll.202202659.

[370] T. Ivanova, A. Naumkin, A. Sidorov, I. Eremenko, M. Kiskin, X-ray photoelectron spectra and electron structure of polynuclear cobalt complexes, J. Electron Spectros. Relat. Phenomena 156–158 (2007) 200–203. https://doi.org/10.1016/j.elspec.2006.12.005.

[371] X. Chen, Y. Cai, R. Liang, Y. Tao, W. Wang, J. Zhao, X. Chen, H. Li, D. Zhang, NH2-UiO-66(Zr) with fast electron transfer routes for breaking down nitric oxide via photocatalysis,

Appl. Catal. B Environ. 267 (2020) 118687. https://doi.org/10.1016/j.apcatb.2020.118687.

[372] Y. Zhu, J. Zheng, J. Ye, Y. Cui, K. Koh, L. Kovarik, D.M. Camaioni, J.L. Fulton, D.G. Truhlar, M. Neurock, C.J. Cramer, O.Y. Gutiérrez, J.A. Lercher, Copper-zirconia interfaces in UiO-66 enable selective catalytic hydrogenation of CO2 to methanol, Nat. Commun. 11 (2020) 5849. https://doi.org/10.1038/s41467-020-19438-w.

[373] D.G. Brown, U. Weser, XPS Spectra of Spin-Triplet Cobalt(III) Complexes, Zeitschrift Für Naturforsch. B 34 (1979) 1468–1470. https://doi.org/10.1515/znb-1979-1027.

[374] J. Klein, L. Kampermann, B. Mockenhaupt, M. Behrens, J. Strunk, G. Bacher, Limitations of the Tauc Plot Method, Adv. Funct. Mater. 33 (2023). https://doi.org/10.1002/adfm.202304523.

[375] A. Cybula, M. Klein, A. Zaleska, Methane formation over TiO2-based photocatalysts: Reaction pathways, Appl. Catal. B Environ. 164 (2015) 433–442. https://doi.org/10.1016/j.apcatb.2014.09.038.

[376] J. Zhang, J. Yu, M. Jaroniec, J.R. Gong, Noble Metal-Free Reduced Graphene Oxide-Zn x Cd 1– x S Nanocomposite with Enhanced Solar Photocatalytic H 2 -Production Performance, Nano Lett. 12 (2012) 4584–4589. https://doi.org/10.1021/nl301831h.

[377] A. Kudo, Y. Miseki, Heterogeneous photocatalyst materials for water splitting, Chem. Soc. Rev. 38 (2009) 253–278. https://doi.org/10.1039/B800489G.

[378] B. Ohtani, Photocatalysis A to Z-What we know and what we do not know in a scientific sense, J. Photochem. Photobiol. C Photochem. Rev. 11 (2010) 157–178. https://doi.org/10.1016/j.jphotochemrev.2011.02.001.

[379] X. Chen, C. Li, M. Grätzel, R. Kostecki, S.S. Mao, Nanomaterials for renewable energy production and storage, Chem. Soc. Rev. 41 (2012) 7909. https://doi.org/10.1039/c2cs35230c.

[380] K.P. Kuhl, T. Hatsukade, E.R. Cave, D.N. Abram, J. Kibsgaard, T.F. Jaramillo, Electrocatalytic Conversion of Carbon Dioxide to Methane and Methanol on Transition Metal Surfaces, J. Am. Chem. Soc. 136 (2014) 14107–14113. https://doi.org/10.1021/ja505791r.

[381] R. Hudson, R. de Graaf, M. Strandoo Rodin, A. Ohno, N. Lane, S.E. McGlynn, Y.M.A. Yamada, R. Nakamura, L.M. Barge, D. Braun, V. Sojo, CO 2 reduction driven by a pH gradient, Proc. Natl. Acad. Sci. 117 (2020) 22873–22879. https://doi.org/10.1073/pnas.2002659117.

[382] N. Mina-Camilde, C. Manzanares I., J.F. Caballero, Molecular Constants of Carbon Monoxide at v = 0, 1, 2, and 3: A Vibrational Spectroscopy Experiment in Physical Chemistry, J. Chem. Educ. 73 (1996) 804. https://doi.org/10.1021/ed073p804.

[383] F.C. Meunier, Relevance of IR Spectroscopy of Adsorbed CO for the Characterization of Heterogeneous Catalysts Containing Isolated Atoms, J. Phys. Chem. C 125 (2021) 21810–

21823. https://doi.org/10.1021/acs.jpcc.1c06784.

[384] W. Zhou, Z. Ma, S. Guo, M. Wang, J. Wang, M. Xia, L. Jia, B. Hou, D. Li, Y. Zhao, Comparative study of CO adsorption on zirconia polymorphs with DRIFT and transmission FT-IR spectroscopy, Appl. Surf. Sci. 427 (2018) 867–873. https://doi.org/10.1016/j.apsusc.2017.08.113.

[385] Y. Tang, Z. Yang, C. Guo, H. Han, Y. Jiang, Z. Wang, J. Liu, L. Wu, F. Wang, Encapsulating Ir nanoparticles into UiO-66 for photo-thermal catalytic CO 2 methanation under ambient pressure, J. Mater. Chem. A 10 (2022) 12157–12167. https://doi.org/10.1039/D2TA00933A.

[386] L. Wang, B. Cheng, L. Zhang, J. Yu, In situ Irradiated XPS Investigation on S-Scheme TiO 2 @ZnIn 2 S 4 Photocatalyst for Efficient Photocatalytic CO 2 Reduction, Small 17 (2021). https://doi.org/10.1002/smll.202103447.

[387] M. Wang, M. Shen, X. Jin, J. Tian, M. Li, Y. Zhou, L. Zhang, Y. Li, J. Shi, Oxygen Vacancy Generation and Stabilization in CeO 2– x by Cu Introduction with Improved CO 2 Photocatalytic Reduction Activity, ACS Catal. 9 (2019) 4573–4581. https://doi.org/10.1021/acscatal.8b03975.

[388] Y.-L. Men, Y. You, Y.-X. Pan, H. Gao, Y. Xia, D.-G. Cheng, J. Song, D.-X. Cui, N. Wu, Y. Li, S. Xin, J.B. Goodenough, Selective CO Evolution from Photoreduction of CO 2 on a Metal-Carbide-Based Composite Catalyst, J. Am. Chem. Soc. 140 (2018) 13071–13077. https://doi.org/10.1021/jacs.8b08552.

[389] M.A. Baluk, P. Mazierski, A. Pieczyńska, K. Nikiforow, G. Trykowski, T. Klimczuk, A. Zaleska-Medynska, MOF/TiO 2 erythrocyte-like heterostructures decorated by noble metals for use in hydrogen photogeneration and pollutant photodegradation, Catal. Sci. Technol. 13 (2023) 5033–5047. https://doi.org/10.1039/D3CY00531C.

[390] K.L. Svane, J.K. Bristow, J.D. Gale, A. Walsh, Vacancy defect configurations in the metal–organic framework UiO-66: energetics and electronic structure, J. Mater. Chem. A 6 (2018) 8507–8513. https://doi.org/10.1039/C7TA11155J.

[391] S.J. Shah, R. Wang, Z. Gao, Y. Muhammad, H. Zhang, Z. Zhang, Z. Chu, Z. Zhao, Z. Zhao, IL-assisted synthesis of defect-rich polyaniline/NH2-MIL-125 nanohybrids with strengthened interfacial contact for ultra-fast photocatalytic degradation of acetaldehyde under high humidity, Chem. Eng. J. 411 (2021) 128590. https://doi.org/10.1016/j.cej.2021.128590.

[392] A.P. Smalley, D.G. Reid, J.C. Tan, G.O. Lloyd, Alternative synthetic methodology for amide formation in the post-synthetic modification of Ti-MIL125-NH2, CrystEngComm 15 (2013) 9368. https://doi.org/10.1039/c3ce41332b.

[393] N. Ko, J. Hong, S. Sung, K.E. Cordova, H.J. Park, J.K. Yang, J. Kim, A significant enhancement of water vapour uptake at low pressure by amine-functionalization of UiO-67, Dalt. Trans. 44 (2015) 2047–2051. https://doi.org/10.1039/C4DT02582B.

[394] L.G. da Trindade, K.M.N. Borba, L. Zanchet, D.W. Lima, A.B. Trench, F. Rey, U. Diaz, E. Longo, K. Bernardo-Gusmão, E.M.A. Martini, SPEEK-based proton exchange membranes modified with MOF-encapsulated ionic liquid, Mater. Chem. Phys. 236 (2019) 121792. https://doi.org/10.1016/j.matchemphys.2019.121792.

[395] E. V. Shaw, A.M. Chester, G.P. Robertson, C. Castillo-Blas, T.D. Bennett, Synthetic and analytical considerations for the preparation of amorphous metal–organic frameworks, Chem. Sci. 15 (2024) 10689–10712. https://doi.org/10.1039/D4SC01433B.

[396] V. Kavun, E. Uslamin, B. van der Linden, S. Canossa, A. Goryachev, E.E. Bos, J. Garcia Santaclara, G. Smolentsev, E. Repo, M.A. van der Veen, Promoting Photocatalytic Activity of NH 2 -MIL-125(Ti) for H 2 Evolution Reaction through Creation of Ti III - and Co I -Based Proton Reduction Sites, ACS Appl. Mater. Interfaces 15 (2023) 54590–54601. https://doi.org/10.1021/acsami.3c15490.

[397] V. Swaroopa Datta Devulapalli, R.P. McDonnell, J.P. Ruffley, P.B. Shukla, T. Luo, M.L. De Souza, P. Das, N.L. Rosi, J. Karl Johnson, E. Borguet, Identifying UiO-67 Metal-Organic Framework Defects and Binding Sites through Ammonia Adsorption, ChemSusChem 15 (2022). https://doi.org/10.1002/cssc.202102217.

[398] D. Jin, Q. Xu, L. Yu, X. Hu, Photoelectrochemical detection of the herbicide clethodim by using the modified metal-organic framework amino-MIL-125(Ti)/TiO2, Microchim. Acta 182 (2015) 1885–1892. https://doi.org/10.1007/s00604-015-1505-9.

[399] J. Zhang, X. Gao, W. Guo, Z. Wu, Y. Yin, Z. Li, Enhanced photocatalytic activity of TiO 2 /UiO-67 under visible-light for aflatoxin B1 degradation, RSC Adv. 12 (2022) 6676–6682. https://doi.org/10.1039/D1RA09441F.

[400] S. Liu, Q. Zou, Y. Ma, W. Sun, Y. Li, J. Zhang, C. Zhang, L. He, Y. Sun, Q. Chen, B. Liu, H. Zhang, K. Zhang, A novel amorphous CoSx/NH2-MIL-125 composite for photocatalytic degradation of rhodamine B under visible light, J. Mater. Sci. 55 (2020) 16171–16183. https://doi.org/10.1007/s10853-020-05210-4.

[401] X. Gao, B. Guo, C. Guo, Q. Meng, J. Liang, J. Liu, Zirconium-Based Metal–Organic Framework for Efficient Photocatalytic Reduction of CO 2 to CO: The Influence of Doped Metal Ions, ACS Appl. Mater. Interfaces 12 (2020) 24059–24065. https://doi.org/10.1021/acsami.0c05631.

[402] M. Asiri, F.M.A. Altalbawy, F.F. Sead, J. Makasana, R. M M, P.K. Pathak, B. Juneja, A. Kumar, S. Saydaxmetova, Hetero bimetallic Zr–O–Cu in UiO-67 MOF for selective and efficient CO2 photoreduction to ethylene, J. Mol. Struct. 1328 (2025) 141306. https://doi.org/10.1016/j.molstruc.2024.141306.

[403] A. Pancielejko, M. Kroczewska-Gnatowska, P. Mazierski, J. Łuczak, A. Zaleska-Medynska, The effect of ionic liquids on the surface and photocatalytic properties of semiconducting materials, Chem. Eng. J. 498 (2024) 155274. https://doi.org/10.1016/j.cej.2024.155274.

[404] M.I. Qadir, J. Dupont, Thermo- and Photocatalytic Activation of CO 2 in Ionic Liquids Nanodomains, Angew. Chemie Int. Ed. 62 (2023). https://doi.org/10.1002/anie.202301497.

[405] L. Eisele, K. Bica-Schröder, Photocatalytic Carbon Dioxide Reduction with Imidazolium-Based Ionic Liquids, ChemSusChem 18 (2025). https://doi.org/10.1002/cssc.202402626.

[406] Y. Wang, M. Hatakeyama, K. Ogata, M. Wakabayashi, F. Jin, S. Nakamura, Activation of CO 2 by ionic liquid EMIM–BF 4 in the electrochemical system: a theoretical study, Phys. Chem. Chem. Phys. 17 (2015) 23521–23531. https://doi.org/10.1039/C5CP02008E.

[407] T. Baran, S. Wojtyła, A. Dibenedetto, M. Aresta, W. Macyk, Zinc sulfide functionalized with ruthenium nanoparticles for photocatalytic reduction of CO2, Appl. Catal. B Environ. 178 (2015) 170–176. https://doi.org/10.1016/j.apcatb.2014.09.052.

List of Figures

Figure 1.1 Schematic representation of the roles that can be performed by MOFs in the light-driven CO_2 reduction: a) photocatalysts, b) cocatalysts and c) photocatalytic hosts. Gray balls denote materials of other type in MOF-based photocatalysts (reproduced with permission from [6]). 13

Figure 4.1 Different materials for potential use in CO_2 adsorption (reproduced with permission from [29]); ACF – activated carbon fiber, CMS – carbon molecular sieves, COF – covalent-organic frameworks. 20

Figure 4.2. Possible pathways of CO_2 copolymerization (reproduced with permission from [42]) 23

Figure 4.3. Examples of carious carboxylate linkers with different topology: a) 1,4-benzenedicarboxylic acid, b) naphthalene-2,6-dicarboxylic acid, c) [1,1′-biphenyl]-3,4′,5-tricarboxylic acid, d) 4,4′,4″,4‴-(porphyrin-5,10,15,20-tetrayl)tetrabenzoic acid, e) 4′,4‴,4⁗,4⁗′-methanetetrayltetrakis (([1,1′-biphenyl]-4-carboxylic acid)), f) 4,4′-((2,5-dimethoxy-1,4-phenylene)bis(ethyne-2,1-diyl))dibenzoic acid 27

Figure 4.4. Structures of organic solvents used in MOFs synthesis 29

Figure 4.5. Schematical representation of MOF activation 30

Figure 4.6. Structures of H_2BDC and different H_2BDC-derived linkers 33

Figure 4.7. Structure of acetic modulators: a) organic, b) inorganic 35

Figure 4.8 Schematical representation of MOF with ideal and defected structure 36

Figure 4.9. TEM images of different location of Au NPs incorporated into ZIF-8(Zn) supported on ZnO depending on synthesis conditions: a) high concentration of linker, b) low concentration of linker. Scale bar represents 100 nm (adapted from [155] under CC-BY-4.0 license). 37

Figure 4.10. Scheme of MOF-303 modification with Cu atoms (reproduced with permission from [175]) 38

Figure 4.11. Structure of UiO-66(Zr) with intentionally incorporated defects of structure and its post-synthetic metalation with Eu^{3+} (reproduced with permission from [153]) 39

Figure 4.12 MOF-808(Zr): a) pristine (SEM image), b)-f) with embedded Pt NPs (TEM images) (reproduced with permission from [185]) 40

Figure 4.13. Exemplary scheme of CO_2 photoreduction reaction over NH_2-MIL-125(Ti) (reproduced with permission from [6]) 53

Figure 4.14. Chemical absorption of CO_2 by ILs with NH_2-functionalized: a) cation, b) anion. 57

Figure 4.15. Possible structures of AAILs 58

Figure 5.1 FTIR spectra of prepared AAILs in comparison with primary commercial ILs; methodology was described in Subsection 5.6.9; 73

Figure 6.1 Photographs of Cu-TDPAT(DD) a) before activation, b) after activation, c) after activation and contact with air; SEM images of: d) Cu-TDPAT(DD), e) Cu-TDPAT(DWE); f) Cu-TDPAT(DMF) g) optical micrograph of Cu-TDPAT(DMF); Photographs of reaction solutions of: h) Cu-TDPAT(DMF/DMSO), i) DMF/DMSO-0A; SEM images of j) Cu-TDPAT(DMF/DMSO), k) DMF/DMSO-0A..... 87

Figure 6.2 Comparison of PXRD patterns of the Cu-TDPAT samples synthesized: a) in the primary conditions in different solvents; b) in DMA/DMSO; c) in DMF; d) in other solvent mixtures. 88

Figure 6.3 Comparison of N_2 adsorption-desorption curves at -196 °C; b) CO_2 at 0 °C c) CO_2 at 25 °C of the Cu-TDPAT samples..... 89

Figure 6.4 Comparison of CO_2 adsorption-desorption curves of the Cu-TDPAT samples measured at 0 °C..... 90

Figure 6.5 Comparison of CO_2 adsorption-desorption curves of the Cu-TDPAT samples measured at 25 °C..... 91

Figure 6.6 Comparison of TGA curves of the Cu-TDPAT samples synthesized: a) in the primary conditions in different solvents; b) in DMA/DMSO; c) in DMF; d) in other solvent mixtures. 92

Figure 6.7 Comparison DRIFTs spectra of Cu-TDPAT(DD) recorded at RT in air atmosphere and at 150 °C under N_2 flow 92

Figure 6.8. Comparison of FTIR spectra of the Cu-TDPAT samples synthesized: a) in the primary conditions in different solvents; b) in DMA/DMSO; c) in DMF; d) in other solvent mixtures 93

Figure 6.9 Comparison of PXRD patterns of: a) Cu-TDPAT(DMF/DMSO), Cu and Cu_2O; b) Cu-TDPAT(DMF/DMSO) with simulated Cu-TDPAT data in 2-30° range 95

Figure 6.10 FTIR spectrum comparison of Cu-TDPAT(DMF/DMSO), Cu_2O and DMF 96

Figure 6.11 SEM images of a) DD-R and b) DMF-R..... 97

Figure 6.12 Comparison of PXRD patterns of: a) DMF-0.5A, DMF-0A, Cu and Cu_2O; b) DMF-0.5A and DMF-0A with simulated Cu-TDPAT data in 2-30° range. 98

Figure 6.13 SEM images of a) DMF-0A and b) DMF-0.5A 99

Figure 6.14 Comparison of PXRD patterns of: a) DMF-65C (before and after activation with MeOH and water), DMF-75C and DMACuF; b) DMF-65C and DMF-75C with simulated Cu-TDPAT data in 2-12° range. 101

Figure 6.15 Digital images of a) DMF-65C and b) DMF-75C; SEM images of c) DMF-65C, d) DMF-75C, e) DD-95C and f) DMF-95C 102

Figure 6.16 Comparison of PXRD patterns of: a) DMF-95C and by-products (Cu and Cu_2O) general overview; b) DMF-95C and simulated Cu-TDPAT data in 2-30° range..... 103

Figure 6.17 SEM images of a) DMF-3/1 and b) DD-3/1 104

Figure 6.18 Comparison of PXRD patterns of DMF-3/1, DMF-3/1-HNO_3 and by-products (Cu and Cu_2O): a) general overview, b) DMF-3/1-HNO_3 and simulated Cu-TDPAT data in 2-30° range; c) SEM image of DMF-3/1-HNO_3 105

Figure 6.19 SEM images of a) DD-BF_4, b) DD-AcO, c) DD-AcO-3/1, d) DD-AcO-R, e) DD-95C-AcO, f) DMF-AcO, g) DMF-AcO-3/1 107

Figure 6.20 Comparison of PXRD patterns of DMF-AcO, DMF-AcO-3/1 and by-products (Cu and Cu_2O) 108

Figure 6.21 Relative changes observed for the fully analyzed Cu-TDPAT samples and summary of others. Each asterisk symbol stands for the factor that was changed for the actual synthesis compared to the reference sample (* - one factor changed, ** - two factors changed, *** - three factors changed). Diamond (◊) symbolizes formation of by-products. 110

Figure 6.22 Relationship graph between S_{BET} and CO_2 uptake (at 0 °C). Colors and shapes were assigned to type of changed factor and number of changed factors for the specific sample. Asterisk symbol was assigned to the reference sample for clarity. 112

Figure 6.23 PXRD patterns of Cu-TDPAT after treatment with different liquid environments 114

Figure 7.1 Chemical structures of: a) 1-Butyl-3-methylimidazolium bromide [BMIM][Br], b) 1-Butyl-3-methylimidazolium histidinate [BMIM][His], c) 1-Butyl-3-methylimidazolium prolinate [BMIM][Pro], d) 1-Ethyl-3-methylimidazolium histidinate [EMIM][His], e) 1-Ethyl-3-methylimidazolium prolinate [EMIM][Pro]. 116

Figure 7.2 Schematical representation of: a) pristine HKUST-1 synthesis; b) synthetical AAIL introduction, c) post-synthetical AAIL impregnation. 117

Figure 7.3 PXRD of the HKUST-1 samples: a) post-synthetically impregned with 1% of ILs or synthesized in presence of 0.1 mole equivalents of ILs, b) post-synthetically impregnated with 10 wt% of ILs or synthesized in presence of 0.25 mole equivalents of ILs; c) comparison of DRIFT spectra of HKUST-1 at RT and at 150 °C 119

Figure 7.4 Comparison of FTIR spectra of :a) all MOF samples; samples modified with: b) [BMIM][Br], c) [BMIM][Pro], d) [BMIM][His], e) [EMIM][Pro], f) [EMIM][His]; the red dashed lines refer to the signals assigned to the ionic liquids 120

Figure 7.5 SEM images and EDX mapping of: a) HKUST-1, b) 10%EP, c) 0.25EP 123

Figure 7.6 SEM images of: a) HKUST-1; samples modified post synthesis with [EMIM]-based ILs: b) 1%EP, c) 1%EH, d) 10%EP, e) 10%EP (magnification on finer fraction), f)10%EH, the samples modified with [EMIM]-based ILs during the synthesis: g) 0.1EP, h) 0.1EH, i) 0.25EP, j) 0.25EP (magnification on finer fraction), k) 0.25EH. 124

Figure 7.7 SEM images of: a) HKUST-1 samples modified post synthesis with [BMIM]-based ILs: b) 10%BB, c) 10%BP, d) 10%BH, e) 10%BH (magnification on finer fraction), the samples modified

with [BMIM]-based ILs during the synthesis:, f) 0.25BB, g) 0.25BP, h) 0.25BH, i) 0.25BH (magnification on finer fraction). 125

Figure 7.8 TGA curves of: a) HKUST-1 samples post-synthetically impregned with 1% of ILs or synthesized in presence of 0.1 mole equivalents of ILs, b) HKUST-1 samples post-synthetically impregnated with 10 wt% of ILs or synthesized in presence of 0.25 mole equivalents of ILs; c) ionic liquids. 126

Figure 7.9 Relative change of S_{BET} and CO_2 sorption capacity at 25 °C of samples modified: a) during synthesis, b) post-synthetically (calculated basing on Table 7.1); c) schematical representation of anion and cation influence on S_{BET} and CO_2 uptake of modified HKUST-1 samples 127

Figure 7.10 N_2, CH_4 and CO_2 adsorption/desorption equilibrium isotherms at 25 °C for HKUST-1 and AAILs-modified composites in full and low-pressure region (insets). Closed and open symbols denote the adsorption and desorption data, respectively. Lines represent the Sips (left) and Toth (right) adsorption isotherm model fitting 132

Figure 7.11 Ideal selectivity of HKUST-1 and AAIL-modified samples based on experimental data fitted with a) Sips and b) Toth models 133

Figure 8.1. SEM images of: a) UiO-66, b) NH_2-UiO-66; TEM images of: c) Cu_{dep}-NUiO, d) Co_{dep}-NUiO; EDS mapping of: e) Cu_{dep}-NUiO, f) Co_{dep}-NUiO, g) Ni_{dep}-NUiO; 137

Figure 8.2 SEM images of metal-modified NH_2-UiO-66(Zr) and UiO-66(Zr) samples; scale bars represent 100 nm. 138

Figure 8.3 DRIFTs spectra of UiO-66(Zr) and NH_2-UiO-66(Zr) after activation at 150 °C under N_2 flow. 139

Figure 8.4.The XRD patterns of: a) UiO after photodeposition of Cu/Ni/Co, b) NH_2-UiO-66 after photodeposition of Cu/Ni/Co; low 2θ region of diffraction pattern of: c) UiO after photodeposition d) NH_2-UiO-66 after photodeposition; e) UiO after incorporation of Cu/Ni/Co, f) NH_2-UiO-66 after incorporation of Cu/Ni/Co; low 2θ region of diffraction pattern of: g) UiO after incorporation h) NH_2-UiO-66 after incorporation; comparison of MC defects in obtained UiO-66 and NH_2-UiO-66 samples after: i) incorporation, j) photodeposition 140

Figure 8.5 TGA curves of: a) UiO-66(Zr) after incorporation, b) UiO-66(Zr) after photodeposition, c) NH_2-UiO-66(Zr) after incorporation, d) NH_2-UiO-66(Zr) after photodeposition; comparison of the TGA curves of: e) H_2BDC and UiO-66(Zr), f) NH_2- H_2BDC and NH_2-UiO-66(Zr); Comparison of missing-linker defects in obtained UiO-66(Zr) and NH_2-UiO-66(Zr) samples after: g) incorporation, h) photodeposition 142

Figure 8.6 Survey spectra of UiO-66(Zr), NH_2-UiO-66(Zr) and samples after photodeposition of Co and Cu 144

Figure 8.7 High-resolution spectra of Co 2p and Cu 2p of UiO-66(Zr) and NH_2-UiO-66(Zr) modified by photodeposition 145

Figure 8.8 High resolution spectra of O 1s and N 1s (where applicable) of UiO-66(Zr), NH_2-UiO-66(Zr) and samples modified by photodeposition of Cu and Co..... 145

Figure 8.9 DRS spectra of a) UiO-66(Zr) after incorporation and photodeposition and c) NH_2-UiO-66(Zr) after incorporation and photodeposition; Tauc plots of b) UiO-66(Zr) after incorporation and d) NH_2-UiO-66(Zr) after incorporation 146

Figure 8.10 a) Concentration of generated HCOOH by UiO-66(Zr) and NH_2-UiO-66(Zr) under UV-Vis irradiation (Xe lamp; environment: 10%TEOA/MeCN); b) Concentration of generated HCOOH after 4 hours under UV-Vis irradiation for: NH_2-UiO-66(Zr) after photodeposition and incorporation, UiO-66(Zr) after photodeposition and incorporation, as well as under Vis irradiation for: NH_2-UiO-66(Zr) after photodeposition and incorporation, (Xe lamp; environment: 10% TEOA/MeCN); c) Action spectra for HCOOH generation vs. absorption spectrum of Co_{dep}-NUiO 149

Figure 8.11 PL spectra of a) UiO-66(Zr) and b) NH_2-UiO-66(Zr) after Cu, Co or Ni incorporation and photodeposition..... 151

Figure 8.12 Time-resolved photoluminescence decay spectra of NH_2-UiO-66(Zr) and samples via photodeposition approach. Spectra were recorded under 330 nm excitation and monitored at the emission maximum wavelength. 151

Figure 8.13 ^1H NMR spectra of pure 10%TEOA/d_3-MeCN and of the liquid phase after photoconversion under UV-Vis light using $^{13}CO_2$ and Co_{dep}-NUiO (24 hours, Xe lamp). 153

Figure 8.14 Quantitative analysis of ML or MC content influence on the photocatalytic activity of MOFs. The black fitted curves consider all data points, red curves – data sets after exclusion of outlying points (also marked with red). Polynomial fit was distinguished with dashed lines. 155

Figure 8.15 Stability test of Co_{dep}-NUiO photocatalyst: a) concentration of HCOOH after 4 hours irradiation under UV-Vis (Xe lamp; environment: 10%TEOA/MeCN); b) XRD patterns and S_{BET} values of Co_{dep}-NUiO before and after 5 cycles of photocatalytic CO_2 reduction; c) TGA curves of Co_{dep}-NUiO before and after 5 cycles of photocatalytic CO_2 reduction 156

Figure 8.16 In situ DRIFTs spectra recorded for Cu_{dep}-NUiO: a) time-resolved difference spectra of MOF exposed to CO_2 flow; b) time-resolved difference spectra of MOF exposed to UV light and steady CO_2/H_2 flow; c) stability of CO generation during three cycles of photoreduction; d) comparison of spectra during CO flow, CO_2 flow and during CO_2 photoreduction..... 157

Figure 8.17 Time-resolved In situ DRIFTs spectra of Cu_{dep}-NUiO during gas-solid CO_2 photoconversion..... 158

Figure 9.1 Schematical representation of five different MOF-MOF composite materials synthesis pathways. 161

Figure 9.2 SEM and TEM micrographs of the obtained materials: NH_2-MIL-125(Ti) (black bar), UiO-67(Zr) (violet bar), **1** (red bar), **2** (blue bar), **3** (pink bar), **4** (green bar), **5** (orange bar). In the case of MOF-MOF composites, the SEM images are on the left side, while TEMs are on the right side. 162

Figure 9.3 STEM images and elemental mapping of MOF-MOF composites **1-5** 163

Figure 9.4 Line scanning spectra of elements distribution in **4** 164

Figure 9.5 a) Full range and b) magnification of PXRD patterns of the obtained MOFs and composites; c) TGA curves of the obtained MOFs and composites. 165

Figure 9.6 Close-up of different ranges of in situ DRIFTS spectra of obtained materials: a) 2000-650 cm^{-1} with marked bands referring to UiO-67(Zr), b) 2000-650 cm^{-1} with marked bands referring to NH_2-MIL-125(Ti), c) 4000-3150 cm^{-1} with marked bands referring to both pristine MOFs. 166

Figure 9.7 N_2 and CO_2 Adsorption isotherms of: a) N_2 at -196 °C, b) CO_2 at 0 °C, c) CO_2 at 25 °C, ... 168

Figure 9.8 Pore size distribution profile designated by H-K method 169

Figure 9.9 Heat of CO_2 adsorption as a function of the amount of the adsorbed gas in the range of 0–110 $cm^3 \cdot g^{-1}$ based on the isotherms collected at 0 and 25 °C (calculated by SLF model) for pristine MOFs and MOF-MOF composites. 171

Figure 9.10 Photocurrent response of obtained MOFs and composites. 172

Figure 9.11 PL spectra of parent MOFs and MOF-MOF composites 172

Figure 9.12 DRS spectra of parent MOFs and MOF-MOF composites 173

Figure 9.13 a) Concentration of generated HCOOH under Vis irradiation using as-obtained materials (Xe lamp; environment: 10%TEOA/MeCN). No formic acid was detected for pristine UiO-67(Zr) during experiment (not included on the graph); b) ^1H NMR spectra of pure 10%TEOA/d_3-MeCN and of the products obtained via photoconversion under Vis light using $^{13}CO_2$ and **5** (24 hours, Xe lamp; environment: 10%TEOA/d_3-ACN) 174

Figure 9.14 Proposed role of [EMIM][Cl] in the mechanism of CO_2 photoreduction under visible light irradiation using **5** in TEOA/MeCN environment 176

List of Tables

Table 4.1. Application of MOFs for CO_2 sorption and photoconversion 42

Table 4.2 Standard potentials of CO_2 reduction in aqueous solution at 25 °C 52

Table 4.3. Absorption capacity of CO_2 in different AAILs and values of viscosity before and after saturation with the gas 58

Table 4.4. Application of ionic liquids for MOFs modification (to enhance CO_2 binding); the full names of the listed ILs symbols are listed below the table in alphabetical order. 60

Table 5.1 Details of synthesis reagents calculated per 100 mL of the reaction vessel volume 70

Table 6.1 Yield and visual product assessment of prepared Cu-TDPAT samples and their BET surface area, porosity characterization and CO_2 sorption capacity of the obtained materials. 85

Table 6.2 Comparison of Cu-TDPAT sample presence after the next steps of CO_2 photoconversion procedure 113

Table 7.1 Sample labels, method of ILs introduction, amount and name of ILs, CO_2 sorption capacity (measured by volumetric method, at p~99 kPa) and BET surface area of HKUST-1 samples. Sample symbols consist of the IL amount introduced (0.1 and 0.25 for synthetical approach. 1% and 10% for post-synthetical approach), first letter of cation side chain (B – butyl, E – ethyl) and first letter of anion name (B – bromide, H – histidinate, P – prolinate). 117

Table 7.2 Average elements content designated by SEM-EDX 121

Table 7.3 Elements concentration designated by CHN elemental analysis, normalized 121

Table 7.4 Sips and Toth model fitting parameters for N_2, CH_4, and CO_2 on HKUST-1 samples. For Sips equation: q_s – saturation concentration, b – isotherm constant, n – heterogeneity factor; for Toth equation: q_s – saturation concentration, b – isotherm constant, t – heterogeneity factor. For both models: ARE – absolute relative error. 131

Table 8.1 Sample codes and synthesis conditions of the UiO-66(Zr) and NH_2-UiO-66(Zr) samples; inc – incorporation, dep – photodeposition, BDC – terephthalic acid, NH_2-BDC – 2-aminoterephthalic acid, mol_{Zr}% – amount of the modifying metal in relation to the number of moles of the zirconium precursor, wt_{MOF}% – amount of the modifying metal in relation to the mass of MOF to be modified..... 136

Table 8.2 Atomic concentration of elements analyzed with XPS..... 143

Table 8.3 Actual content of the non-noble metals (ICP-OES), specific surface area, CO_2 sorption capacity, enthalpy of adsorption, band gap values and HCOOH formation efficiency of UiO-66(Zr)- and NH_2-UiO-66(Zr)-based samples..... 148

Table 9.1 Atomic content of elements in MOF-MOF composites designated by TEM-EDX 164

Table 9.2 BET surface area, porosity characterization and CO_2 sorption capacity of the obtained materials. 167

Table 9.3 Single-site Langmuir-Freundlich fitting parameters for pure CO_2 isotherms of the obtained materials at 0 and 25 °C, where Q_{sat} – monolayer saturated adsorption capacity, b – Langmuir constant, c – constant. 171

Table 11.1 Summary of author's achievements; Scopus (Status as of 19.09.2026) 184